ABSTRACT

Title of Dissertation: AN EFFECTIVE MEXICAN-HAT BAND FOR ULTRACOLD ATOMS IN A TIME-MODULATED OPTICAL LATTICE

Carlos A. Bracamontes
Doctor of Philosophy, 2022

Dissertation Directed by: Professor James V. Porto
Joint Quantum Institute,
National Institute of Standards and Technology
and
University of Maryland Department of Physics

Ring-shaped energy bands, where a continuum of degenerate minima lie along a closed loop in momentum space, are of interest in ultracold fermionic and bosonic gases since the associated singularity in the density of states is expected to stabilize unconventional phases of matter. These moatlike dispersions are also linked to enhanced properties in solid-state materials. This thesis describes the realization and characterization of a Mexican-hat band generated with an amplitude modulated double-well optical lattice, where the effective static Hamiltonian giving rise to the moat band can be understood using a Floquet analysis. Since our experimental approach allowed for the coherent preparation of Bose condensed (BEC) clouds in this hybridized ring-shaped band, we also examined the stability of BEC dressed states in the presence of the moatlike dispersion, which we modeled using a linear stability analysis of the mean-field solutions to the driven Gross-Pitaevskii equation. Our observations are in fair agreement with the theoretical prediction that a single-momentum BEC at the minimum of a moatlike band (which

is a competing bosonic ground state in several interesting phase diagrams associated with ring-shaped dispersions) lies at the edge of an instability region and should, hence, be unstable in any realistic scenario.

Motivated by the necessity to understand and mitigate dissipative mechanisms that curtail the applicability of Floquet engineering in bosonic optical lattices, this thesis also discusses a framework to model drive-induced instabilities in condensates subject to time-modulated lattice potentials. A linear stability analysis, similar to the one employed to model the BEC stability in the presence of the effective moat band, leads to parametric instabilities. Unlike the moat-induced instability, which is inherent to the Floquet generated effective static band, these instabilities are coupled via the modulation, and depend on the details of the modulation parameters. The predictions of this model are contrasted with the results from an experimental investigation of the condensate depletion in shaken optical lattices, as a function of the modulation parameters, from which we assess the validity and limitations of the theory.

AN EFFECTIVE MEXICAN-HAT BAND FOR ULTRACOLD ATOMS IN A TIME-MODULATED OPTICAL LATTICE

by

Carlos A. Bracamontes

Dissertation submitted to the Faculty of the Graduate School of the
University of Maryland, College Park in partial fulfillment
of the requirements for the degree of
Doctor of Philosophy
2022

Advisory Committee:
Professor Norbert Linke, Chair
Dr. James V. (Trey) Porto, Advisor
Dr. Ian B. Spielman
Professor Wendell T. Hill
Professor Yanne K. Chembo, Dean's representative

Acknowledgments

I would like to begin by thanking my two main mentors, Trey Porto and Alessandro Restelli, to whom I owe a significant part of my professional growth. Your kindness, expertise and abundant patience supported me for many years, and were crucial to overcome the countless hurdles I faced as a graduate student. I appreciate the devoted and selfless guidance you both offer to all your mentees and, partly for this reason, I consider it appropriate to apologize for the times I disappointed you.

I am also grateful to Professor Luis Orozco for his invaluable assistance during the year I started my PhD program. Without his initial support, I am certain I would not have the opportunity to write this list of acknowledgements.

As an experimental graduate student, I was helped by and learnt (sometimes inadvertently) lessons from all the labmates I had the opportunity to collaborate with. I acknowledge the importance of those interactions. Some of them exposed the many misconceptions and the unfortunate disregard I had for the social aspect of experimental research, and have strongly reshaped my vision on what an ideal teammate should be. Special thanks to James Maslek, who was the only other labmate during the final years of the RbI lab; I sincerely wish you, your family and your team at OpenBB all the best. I also owe some gratitude to Sarthak Subhankar for several pleasant conversations, and for his genuine interest and trust in the DDS devices that Alessandro and I worked on. The latter meant a lot to me. You are an incredibly talented experimentalist and I

hope you fulfill your academic goals.

My time outside the lab was filled with great experiences by other graduate students, post-docs and friends who, like me, came to Maryland after growing up south of the Tropic of Cancer: Alejandra, Ana, Dalia, David, Héctor, Israel, Kristel, Maggie, Pablo and Paco. I hold many cherished memories from the time you were all in Maryland, including Cafe Tacvba and "Shakira" concerts, Thanksgivings, volleyball and tennis matches, and the eternal debate with Paco on whether San Luis is part of central or northern Mexico. I am inspired by the successful careers you are all building.

I consider myself lucky to have met valuable friends when I was an undergrad in Mexico City: Adolfo, Alfonsina, Arnaldo, Caro, Chinitos, Claudia, Erick, Eulogio, Julián, Luciano, Manuel, Mónica, Oscarito, Pepe, Reyna, Theurel and Wilfrido. I appreciate being in contact with you, rediscovering your personalities, and sharing good memories at different stages of my PhD.

Lastly, but certainly not least, I am thankful for all the support I have received from my family. This includes the beloved memory of those that passed away while I was a PhD student, and the four-legged creatures that inhabit my parents' house. Your presence, even if only by phone, has been extremely important (no words would do justice), particularly in the hard times.

Table of Contents

List of Figures

List of Abbreviations

BEC	Bose-Einstein condensate
BdG	Bogoliubov-de Gennes
BZ	Brillouin Zone
CF	Composite fermion
DOS	Density of states
EOM	Electro-Optic Modulator
FBdG	Floquet Bogoliubov-de Gennes
FGR	Fermi's Golden Rule
GP	Gross-Pitaevskii
HV	High-vacuum
MH	Mexican-hat
MI	Mott insulator
MOT	Magneto-optical trap
PC	Pockels cell
RF	Radio frequency
SF	Superfluid
SOC	Spin-orbit coupling
TOF	Time-of-flight
TiSub	Titanium Sublimation
Ti:sapph	Titanium-sapphire
UHV	Ultra-high vacuum

Chapter 1: Introduction

Optical lattices [1–5], the physical system I studied as a PhD student, have been systematically employed in atomic physics laboratories since the early 1990s [6, 7] and their implementation with ultracold neutral atoms continues to be a rewarding platform for the study of quantum many-body physics [8–12]. The appeal of this experimental resource stems to a large extent from its relatively high dynamic manipulability and the flexible probing techniques available in cold atomic gases. Nearly every property of cold atoms in optical lattices is controllable, from the lattice structure to the interaction strength (including sign). In the past quarter-century, these properties have facilitated the observation of numerous interesting quantum phenomena in optical lattices, some of which are challenging to realize in other systems such as solid-state electronic materials. Among these nonclassical effects are the generation of different strongly correlated states associated with the Hubbard model [13–20], the observation of interesting phases in reduced dimensions such as the stabilization of a Tonks-Girardeau gas [21, 22] (a fermionized phase of a 1D Bose gas predicted in 1960 [23]) and the Berezinskii-Kosterlitz-Thouless (BKT) transition to a quasicondensate [24, 25] in 2D Bose gases, the production of superfluidity possessing an unconventional orbital degree of freedom [26, 27], and the emulation of the Harper Hamiltonian [28, 29] that describes the evolution of charged particles in crystals and large magnetic fields. In addition, the coherence of cold atom systems and the ability to isolate them from

the environment allows for the production of non-equilibrium states that are completely unavailable in traditional condensed matter contexts. One example being the realization of the highly excited so-called "super-Tonks-Girardeau" gas [30–32], a correlated highly excited many-body state that is essentially impossible to realize in traditional solid-state materials.

The capabilities that optical lattices offer to realize unconventional phases of matter can be further expanded using Floquet engineering [33–35] techniques, whereby the Hamiltonian of a system is modified via a periodic time modulation of the parameters in the equations of motion. This Floquet approach, which relies on the restriction Floquet's theorem imposes on the form of the solutions to linear ordinary differential equations with periodic coefficients, is an attractive technique in quantum simulation using ultracold atoms, as it allows forging effective Hamiltonians which are expected to have exotic ground states. In optical lattices, proposed and successful applications of Floquet engineering include the creation of topological bands [36, 37], the transformation of antiferromagnetic correlations into magnetic correlations [38], the generation of tunable artificial gauge fields [39, 40], and the production of low-energy single-particle states with large degeneracy [41].

One approach to producing novel, strongly correlated ground phases of matter consists in synthesizing interacting many-body systems whose low energy single-particle states exhibit a large degeneracy, which enhances the role that interactions play in lifting the degeneracy, and stabilizing unconventional states. This strong influence that interactions have in the determination of the ground state can take place even when the degeneracy occurs only at a couple of points in phase space, as experimentally demonstrated in the observation of a chiral $p_x \pm ip_y$ superfluid order [26, 42], the emergence of ferromagnetic domains in a BEC in the presence of a double-well energy band [43], and the formation of a stripe phase in the double-well dispersion of spin-orbit-

coupled BECs [44–46]. Not surprisingly, a continuous degeneracy in the single-particle ground states causes interacting systems to exhibit exotic nonclassical behavior. An example is the fractional quantum Hall effect, observed in 2D gases of interacting electrons that occupy an infinitely degenerate lowest Landau level in the presence of a uniform magnetic field [47]. Another example is given by systems with flat Bloch bands, whose high degeneracy is also expected to favor the emergence of supersolid phases [48] and fractional anomalous quantum Hall states in the absence of external magnetic fields [49–51]. Accordingly, there is significant interest in engineering such continuous ground state degeneracy.

Such degeneracies arise in moatlike dispersions, where a continuum of nearly degenerate minima lie along a closed loop in reciprocal space. This type of dispersion will be termed, somewhat interchangeably, as Mexican-hat (MH), ring-shaped, Rashba-like or moat band. Central to this thesis is the idea that MH dispersions can be "Floquet-engineered" for ultracold atoms (both bosons and fermions) by periodically modulating an optical lattice [41].

In fermionic systems, a MH dispersion arises in some 2D electron gases with Rashba spin-orbit coupling (SOC). It has been argued that low-density cold fermionic possessing the Rashba-type dispersion may exhibit interesting, competing low-energy states, such as the Wigner crystal, spin-density waves and ferromagnetic nematic phases [52–54]. A Rashba SOC may also boost the formation of bound states in an interacting 2D Fermi gas, inducing a BKT transition from a BCS superfluid state to a BEC of molecules [55].

In bosonic systems, the determination of the interacting many-body ground state for the moatlike degeneracy remains an interesting problem [41, 56–62]. Even in the weakly interacting, mean field limit, where strong correlations are not expected, the nature of the low energy states is unclear. For noninteracting bosons in 3D with a ring-shaped dispersion, the density of states

is two-dimensional at low energy, and Bose-Einstein condensation at finite temperature is not expected. Interactions play an important role in the condensate stability, however, and BEC at finite temperature has been predicted for the interacting system [63, 64]. It has been argued [41, 59–61] that the low density ground state in a moatlike dispersion is a composite-fermion-like state leading to a chiral spin liquid.

In a more practical context, the pronounced rise in the density of states (DOS), commonly referred to as van Hove singularity in condensed matter physics, that occurs at the lowest energy of MH bands is connected to appealing properties in some two-dimensional materials composed of a few monolayers. In tunnel field-effect transistors built with 2D graphene bilayer [65, 66], for example, this DOS enhancement has been predicted to enable a steep, more efficient current switching [67], an improved feature that would aid in reducing the power dissipation in integrated circuits composed of a large number of transistors. The band flatness in the emergence of a MH band, as measured via photoemission spectroscopy in Ref. [68], has also been proposed as a mechanism to attain high-temperature superconductivity in bilayer graphene. In addition, calculations based on density functional theory indicate that these van Hove singularities could magnify the thermoelectric properties (such as the Seebeck coefficient) in van der Waals materials [69], improving, for example, the efficiency of power generators installed in satellites [70]. Monolayer and bilayer materials with MH bands also exhibit an inherent controllable magnetism since they are unstable toward a ferromagnetic ground state [71–73], and constitute a potential platform for the development of 2D spintronic devices [74].

Unfortunately, and in spite of the large number of experiments that have successfully employed Floquet engineering in interacting ultracold gases [28, 43, 75, 76], heating caused by the interaction-induced and uncontrolled feeding of energy into the system (via the periodic drive)

remains a common limitation in experimental realizations of low-energy phases of matter when using Floquet methods. This problem has motivated numerous theoretical [77–82] and experimental [83–88] studies aimed at understanding the origin and potential mitigation of the dissipative mechanisms inherent to the Floquet technique. Since a full treatment of periodically interacting systems typically leads to intractable calculations, the analytical and numerical treatments of periodically driven interacting systems commonly resort to approximate approaches, such as the Truncated Wigner approximation (TWA) [89], high-frequency expansions, Fermi's Golden Rule (FGR) [90] and the weak-coupling conserving approximation. Feedback from experiments is thus a valuable asset to determine the validity of the approximations adopted in such models and to suggest more sophisticated ones. Given the importance of heating to Floquet systems, we carried out experiments to study heating in the context of BECs in driven lattices.

Numerous studies [91–95] have been dedicated to enhance the controllability and tunability in optical lattice setups, as well as to improve the associated detection procedures [96–100]. Examples of projects that were carried out with such intents by past members in my experimental group, some of which were essential for the work described here, are: (i) the manipulation of the internal spin of atoms with a subwavelength resolution (i.e., in a scale below the unit cell of the lattice potential) for both field-sensitive [101] and field-insensitive states [102], (ii) the design and construction of a single-beam retro-reflected double well lattice potential [103] that is impervious to the phase noise generated by the vibrations of mirrors along the path of the lattice light, and where features of the double well remain dynamically tunable, (iii) the cancellation of differential Stark shifts, that cause inhomogeneous (generally unwanted) broadening in atomic transitions, by finding "magic" wavelengths [104, 105], and (iv) the design and inclusion of low-steering kinematic mirrors that allowed to controllably modulate the position of the optical lattice [106].

The contents of this thesis are organized as follows. Chapter 2 briefly describes the main elements of the experimental apparatus I worked with on a daily basis; this chapter includes a concise review of the functional form and the typical calibration procedure of our double-well optical lattice. The remaining three chapters deal with our work on Floquet engineering. A review of both Floquet theory and the numerical solution of the Bogoliubov-deGennes equations, tailored to the needs of the last two chapters is contained in Chapter 3. This review starts with the single-particle Floquet framework, and expands it to incorporate the nonlinear Gross-Pitaevskii equation and the linear stability of its solutions. Chapter 4 describes a thorough investigation of condensate heating in a regime where parametric instabilities, arising from the interplay between the modulation and the interactions, constitute the main cause of condensate depletion in shaken optical lattices. (A peer-reviewed report of these results can be found in Ref. [86].) Finally, Chapter 5 covers the realization of a MH energy dispersion using a Floquet approach with a checkerboard optical lattice. This chapter recounts different modulation schemes we explored to meet this goal. The chapter then reviews the different experimental probes we employed to demonstrate we had realized a moatlike band, as well as our measurements of the condensate stability in the presence of such ring-shaped dispersion. (Relevant references for this chapter are the articles [41, 107].)

Chapter 2: Apparatus

The current chapter offers a brief account of the hardware I employed routinely to generate and manipulate a cold atomic gas in the presence of a double-well optical lattice. Section 2.1 covers the apparatus that generated the Bose-Einstein condensate (BEC). Section 2.2 describes the setup for the optical lattice. Since some idiosyncrasies of the lattice and their effects on the BEC will become relevant in later chapters of this thesis, the second section also addresses the functional form of the lattice and outlines the numerical procedure to solve the Schrödinger equation with such periodic potential.

2.1 BEC apparatus

Experimental procedures entailed producing an optically trapped BEC [108–112] of ^{87}Rb atoms, which would afterwards be subject to an optical lattice potential [93, 113, 114]. The atoms to be Bose condensed, were cooled and trapped inside an ultra-high vacuum (UHV) chamber (described in section 2.1.1.2) belonging to a larger vacuum structure (section 2.1.1). Electromagnetic radiation in the radiofrequency, microwave, infrared and visible regimes (traversing the windows of the UHV chamber) and magnetic fields (generated by electrical current running through coils surrounding the chamber) interacted with the atoms at different stages of the procedures to manipulate or extract physical information from the cloud. Measurements on the cold

gas were for the most part performed via absorption imaging [115] from a probe laser beam after time-of-flight (see section 2.1.3).

A more detailed account (including part numbers and relevant technical specifications) of the laboratory hardware can be found in Roger Brown's PhD thesis [116]. An older version of the apparatus, having some overlap with the devices here discussed, is contained in John Huckans' PhD thesis [117]. Reference [118] is also helpful as our apparatus design closely followed the one reported in it; a similar implementation of that design has been documented in Ref. [119].

2.1.1 Vacuum system

2.1.1.1 Oven

Atoms for the production of a BEC were optically slowed and captured from a collimated thermal beam of rubidium-87 atoms emanating from a ~ 85 °C source that consisted of a broken glass ampule containing rubidium with natural abundance housed inside a bellows. The thermal source was separated from the "oven" vacuum space by a long tube that acted as a collimator and a differential pressure orifice (see Fig. 2.1). The oven pressure, just above 5×10^{-10} torr, was maintained with an ion pump and measured with a hot-filament ionization gauge [120]. Additionally, the oven contained a cup-like piece of copper with a collimation hole in it. This "cold cup" was cooled down to $\lesssim -10$ °C by contact with an external thermoelectric cooler. The cold cup passively yet uninterruptedly captured on its surface the excess amount of residual rubidium atoms, further collimating the thermal beam and effectively preventing detrimental alkali poisoning of the ion pump.

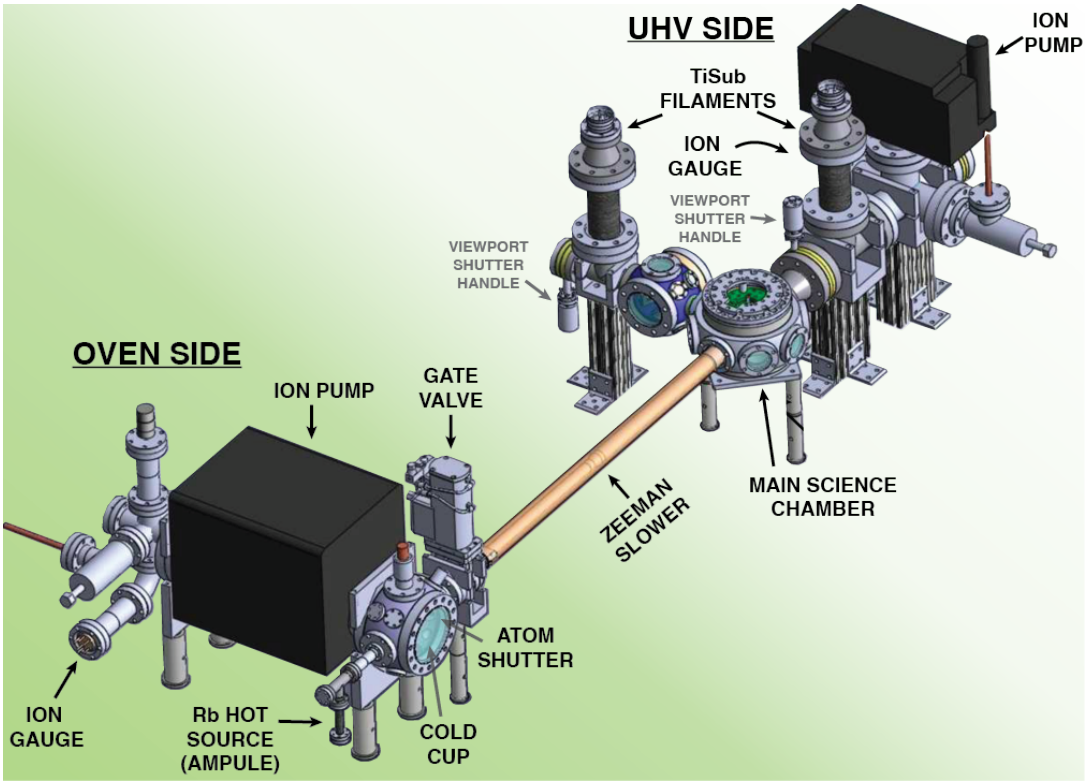

Figure 2.1: Vacuum system diagram. This apparatus comprised two regions: the "oven" and the UHV. A collimated thermal beam of Rb atoms was produced on the oven side and then decelerated as it moved through a Zeeman slower before being collected in a six-beam MOT in the main sience chamber (UHV section). After several stages of evaporation the atoms in the MOT trap were transformed into a BEC. The low pressures were maintained with the assitance of ion pumps, a 'cold cup' and TiSub pumps.

2.1.1.2 UHV

Atoms from the collimated effusive beam produced in the oven were fed into the ultra-high vacuum (UHV) part of the apparatus through a differential pressure tube wrapped with Zeeman slower coils [119, 121]. A commercial *Uniblitz* shutter was attached to the entrance of this differential pumping tube and acted as a gate for the Rb atom beam. To protect the UHV region from potential malfunctions in the oven, a pneumatic gate valve (interlocked to the oven pressure) was installed between the oven and the Zeeman slower tube.

In addition to an ion pump and ion gauge, the UHV part of the vacuum had a pair of titanium sublimation (TiSub) pumps [122], also known as titanium getters. The UHV pressure steadily increased over time and heating of the TiSub filaments every other month or so was needed to bring the pressure back to its optimal value on the order of 1×10^{-10} torr. When the TiSub filaments were heated by driving current through them, harmful coating of the nearby vacuum chamber windows by the sublimated titanium was prevented by closing the vacuum viewport shutters (circular flapper plates mounted on a tangential axis), which were hand-rotatable from the outside via feedthrough knobs.

The main science chamber was a spherical octagon UHV chamber directly attached to the Zeeman slower. After being Zeeman-slowed, atoms from the collimated beam were collected in a six-beam magneto-optical trap (MOT) [123]. The MOT light beams, with relatively large diameters (between 25 mm and 40 mm), entered the main chamber directly after reflection from pneumatically [124] or motorized movable flipper mirrors; these kinematic mirrors would only stay close to the windows of the chamber during the MOT loading phase of the procedure and would be retracted thereafter to provide optical access for other light beams needed at later stages.

Shortly after the MOT gathered a sufficiently large number of atoms (the loading time of the MOT was commonly used to regulate the final atom number in the BEC), the confinement was switched to a magnetic quadrupole trap [125, 126], where the gas underwent forced radiofrequency (RF) evaporation until the phase space density was as high as possible without inducing significant detrimental nonadiabatic (Majorana) spin-flip losses [127] associated with slow moving atoms near the quadrupole zero-field point.

The cloud was then transferred to a cross-beam red-detuned optical dipole trap (ODT) [128] by switching on a pair of infrared (1064 nm) perpendicular dipole beams and slowly ramping the quadrupole field to zero. At the cloud's position, one of the dipole beams (D1) had waists of 30 μm by 80 μm, while the other dipole beam (D2) had waists of 70 μm by 275 μm. Typical trap frequencies in the ODT are 10 Hz along D1, 50 Hz along D2, and 130 Hz vertically. Lastly, intensities of dipole beams were exponentially ramped down for approximately 4 seconds to further evaporate the cloud, yielding a BEC (with minimal thermal component) in the $F = 1$, $m_F = -1$ magnetic state.

2.1.2 Cooling, repump and dipole lasers

Three lasers were employed to produce the cooling and repump light required for the Zeeman slower and the six-beam MOT trap. The cooling laser (Toptica TA pro) was locked near the cycling $F = 2 \rightarrow F' = 3$ hyperfine transition of ^{87}Rb, while the repump (Toptica DL pro) laser was locked near the $F = 1 \rightarrow F' = 2$ hyperfine transition to repump the atoms that escaped the cycling transtion. Both the cooling and repump lasers were locked by beat-note frequency stabilization [129] to a reference (or *master*) laser (New Focus Vortex model 6013). The latter was

locked to the ^{87}Rb $F = 2 \rightarrow F' = 2 - 3$ crossover resonance produced by saturated absorption spectroscopy [130].

The two dipole trap beams, having a 1064 nm wavelength, were generated with a Yb fiber laser (IPG photonics, model YLR-20-1064-LP-S) and delivered to the experimental chamber via crystal photonic fibers. The intensity of each dipole beam was actively stabilized in order to avoid parametric heating of atoms in the trap. This stabilization was performed through a feedback control system by controlling the RF power driving an AOM in the beam path. The error signal in this control loop was constructed from the powers of beam-sampled fractions of the dipole beams, measured at points near the main chamber. This intensity stabilization was not required for the cooling and repump lights.

2.1.3 Imaging system

We used absorptive imaging [115] to measure the integrated column density of the atomic cloud after time of flight along two different directions (see Fig. 2.2):

- The path of one of the probe beams nearly matched the path of one of the dipole beams (differing by $\approx 5^\circ$). With this probe, the cloud was imaged in a plane (y-z plane in Fig. 2.2) perpendicular to the one formed by the dipole beams, with gravity along one of the image axes. Cloud images in this direction were always in focus regardless of the time of flight. For this case, magnification was calibrated using acceleration of atoms due to gravity. The CCD camera used for this probe was a Point Grey Flea 3.

- The path of the other probe beam was orthogonal to both dipole beams, imaging the cloud in the 2D horizontal plane, i.e., the one formed by the dipole beams (x-y plane in Fig. 2.2).

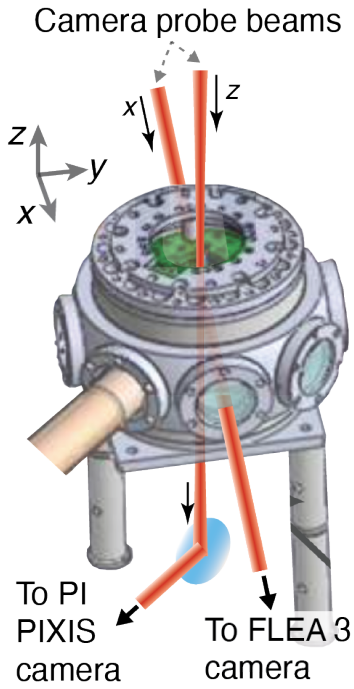

Figure 2.2: Layout of camera probe beams around the main science chamber. The probe beam sent to the PI PIXIS camera imaged the atoms in the x-y plane, while the one sent to the Flea 3 camera did the same in the y-z plane.

Along this direction, the images of the cloud were in focus after approximately 30 ms time of flight. The CCD camera used for this probe was a Princeton Instruments PIXIS.

Both probe beams were drawn from the cooling laser (locked near the $F = 2$ to $F' = 3$ transition) and their intensities were kept below saturation.

2.2 Optical lattice

This section discusses some basic features of the optical lattice apparatus and the functional form of the periodic potential (section 2.2.1), as well as a rough account of its alignment and calibration (section 2.2.3). More in-depth expositions are contained in Refs. [103, 116], with some more concise descriptions in Refs. [101, 131].

2.2.1 Double-well optical lattice

A double-well 2D optical lattice was formed along a horizontal (x-y) plane inside the main science chamber by a retroreflected infrared laser, folded as shown in Fig. 2.3. Lattice light was obtained from a tunable titanium-sapphire laser (pumped by a 532 nm Coherent Verdi laser) whose wavelength λ was almost always set around 813 nm, i.e., 18 nm above (red-detuned in energy) the rubidium 795 nm transition. The lattice beam was retroreflected at the curved mirror M3 (after hitting the plane mirrors M1 and M2) hence traversing the atomic cloud four times, as indicated by the wave-vectors $\boldsymbol{k}_1$, $\boldsymbol{k}_2$, $\boldsymbol{k}_3$ (=$-\boldsymbol{k}_2$) and $\boldsymbol{k}_4$ (=$-\boldsymbol{k}_1$). The four light fields associated with these wave-vectors possessed each a $1/e^2$ radius of approximately 170 μm at the position of the cloud, and their interference in this region gave rise to a periodic potential. The presence of the lattice on top of the dipole trap produced an optical lattice in the x-y plane but a much

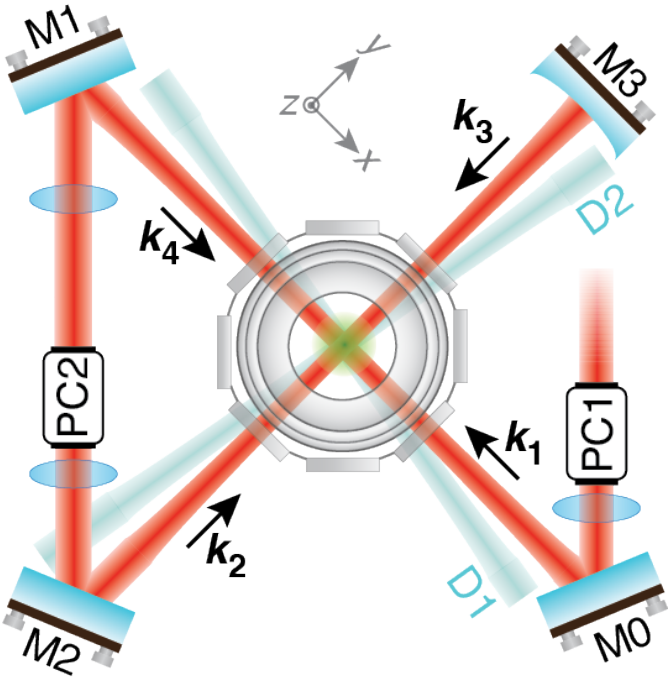

Figure 2.3: Layout, around the main science chamber, of the components used to generate our double-well optical lattice (top view). The periodic potential is formed by retroreflecting a single light beam, indicated in red. In the figure, the beam first enters the main science chamber from the right bottom corner (as indicated by the arrow $\boldsymbol{k}_1$). It is then successively deflected by mirrors M1 and M2, eventually hitting the curved mirror M3 where it is reflected back into its original path. The lattice beam crosses the cloud four times as specified by the wave-vectors $\boldsymbol{k}_{1,2,3,4}$. The pair of dipole beams D1 and D2 forming a cross-beam optical dipole trap are depicted in light blue. The Pockels cell PC1 controls the relative intensity between the in-plane (x-y) and out-of-plane (z) polarization components of the lattice light reaching the atomic cloud. The Pockels cell PC2 tunes the path length difference between the out-of-plane and in-plane polarization components without altering their relative intensities.

weaker ($\sim$130 Hz) confinement along z causing the atomic gas to adopt a distribution of an array of elongated tubes.

A property of this lattice configuration is that the phase of the $\boldsymbol{k}_4$ field was determined by the phases of the $\boldsymbol{k}_1$, $\boldsymbol{k}_2$ and $\boldsymbol{k}_3$ fields alone as no new optical path length was traversed by $\boldsymbol{k}_4$ when it reached the cloud. In other words, only three of the four beams inducing the two-dimensional lattice were phase independent. Because of this, and as pointed out in references [103, 132], the shape (or "topology") of the double-well lattice potential produced under this folded retroreflected configuration was unaffected by most sources of phase noise in the four laser fields. The lattice was, nonetheless, still affected by global translations caused by phase noise. These (most likely acoustic) displacements were, in general, unlikely to have major harmful effects on the atoms due to the broad bandwidth and relatively low power of their spectra (i.e., low power spectral density). In contrast, rapid changes in the shape of the lattice would translate into substantial nonadiabatic variations (quenches) in the band structure experienced by the atoms, naturally leading to excitations into excited states. For this reason, it was advantageous to work with an optical lattice whose "topology" is intrinsically insensitive to phase noise. Contrastingly, other double-well lattice configurations [133], where more than three beams are phase independent, require active phase stabilization by interferometric methods in order to avoid rapid uncontrolled changes in the lattice topology.

As shown in Fig. 2.3, two Pockels cells (LINOS Pockels cell driven by a Trek high-voltage amplifier), denoted PC1 and PC2, lay along the path of the lattice beam. These two devices allowed for dynamical variation of (i) the relative intensity between the out-of-plane (z) and in-plane (x-y) lattice light polarization components at the cloud's position and (ii) the relative phase between those polarization components. Different values of parameters (i) and (ii) corresponded

to lattices with distinct shapes. To be more precise about the effects of PC1 and PC2:

- The input Pockels cell PC1 had its fast axis oriented 45° with respect to the nearly perfectly horizontal polarization of the inciding beam, making it possible to dynamically switch the polarization from purely horizontal to purely vertical, as well as any intermediate distribution between the polarization components. As the high voltage applied to PC1 moved away from zero volts, the polarization changed from horizontal to elliptical until it turned circular, then back to elliptical as it eventually became completely vertical.

- The Pockels cell PC2 had its fast axis aligned horizontally. When driven, PC2 would produce a relative retardation (or advance) of the in-plane phase with respect to that of the vertical component.

In its most simplified version, the double-well potential is composed of two independent (non-interfering) lattices, namely, the lattice potentials produced by the light shifts from the horizontal and the vertical polarization components of the lattice beam.

Denoting the angular wavenumber of the lattice laser as $k_R\,(=2\pi/\lambda)$, the in-plane polarization component of the lattice beam induces the following square optical lattice

$$V_{\text{ip}}(x,y) = -\frac{V_{\text{ip,0}}}{8}\left[2\cos\left(2k_R x\right) + 2\cos\left(2k_R y\right) + 4\right], \tag{2.1}$$

which we commonly referred to as the 'in-plane', 'short-period' or '$\lambda/2$-' lattice as adjacent minima of V_{ip} are separated by $\lambda/2$ [Fig. 2.4(a)]. The out-of-plane component, on the other

hand, generates the potential

$$V_{\text{op}}(x, y; \theta_z) = -\frac{V_{\text{op},0}}{16} \cos^2\left[\frac{k_R}{2}(x+y) - \frac{\theta_z}{2}\right] \cos^2\left[\frac{k_R}{2}(x-y) - \frac{\theta_z}{2}\right], \tag{2.2}$$

knwon as the 'out-of-plane', 'long-period' or 'λ-' lattice. The last moniker originates from the fact that consecutive minima have a separation of λ along x and y [Fig. 2.4(b)]. Strictly speaking, however, the separation between nearest sites (along $y = \pm x$ direction) is $\lambda/\sqrt{2}$ and not λ. In the equation (2.2), the parameter θ_z is the optical path-length difference produced by PC2; if PC2 is removed from the lattice beam path, $\theta_z = 0$ as no path-length difference is induced. Changing the value of θ_z results in a translation of the lattice along the x direction.

Since the potentials V_{ip} and V_{op} are produced using non-interfering fields with polarizations perpendicular to each other, the full potential V_{LATT} is equal to

$$V_{\text{LATT}}(x, y; \theta_z) = V_{\text{ip}}(x, y) + V_{\text{op}}(x, y; \theta_z). \tag{2.3}$$

Figure 2.4 shows four representative geometries of the double-well potential (2.3). For $\theta_z = 0$ [Fig. 2.4(c)], the lattice displays a checkerboard geometry as the λ lattice induces an energy offset $V_{\text{op},0}$ between neighboring sites of the otherwise balanced $\lambda/2$ lattice. When $\theta_z = \pi/2$ [Fig. 2.4(d)], the lattice displays a dimer geometry with the λ lattice lowering the barrier between every other pair of adjacent minima.

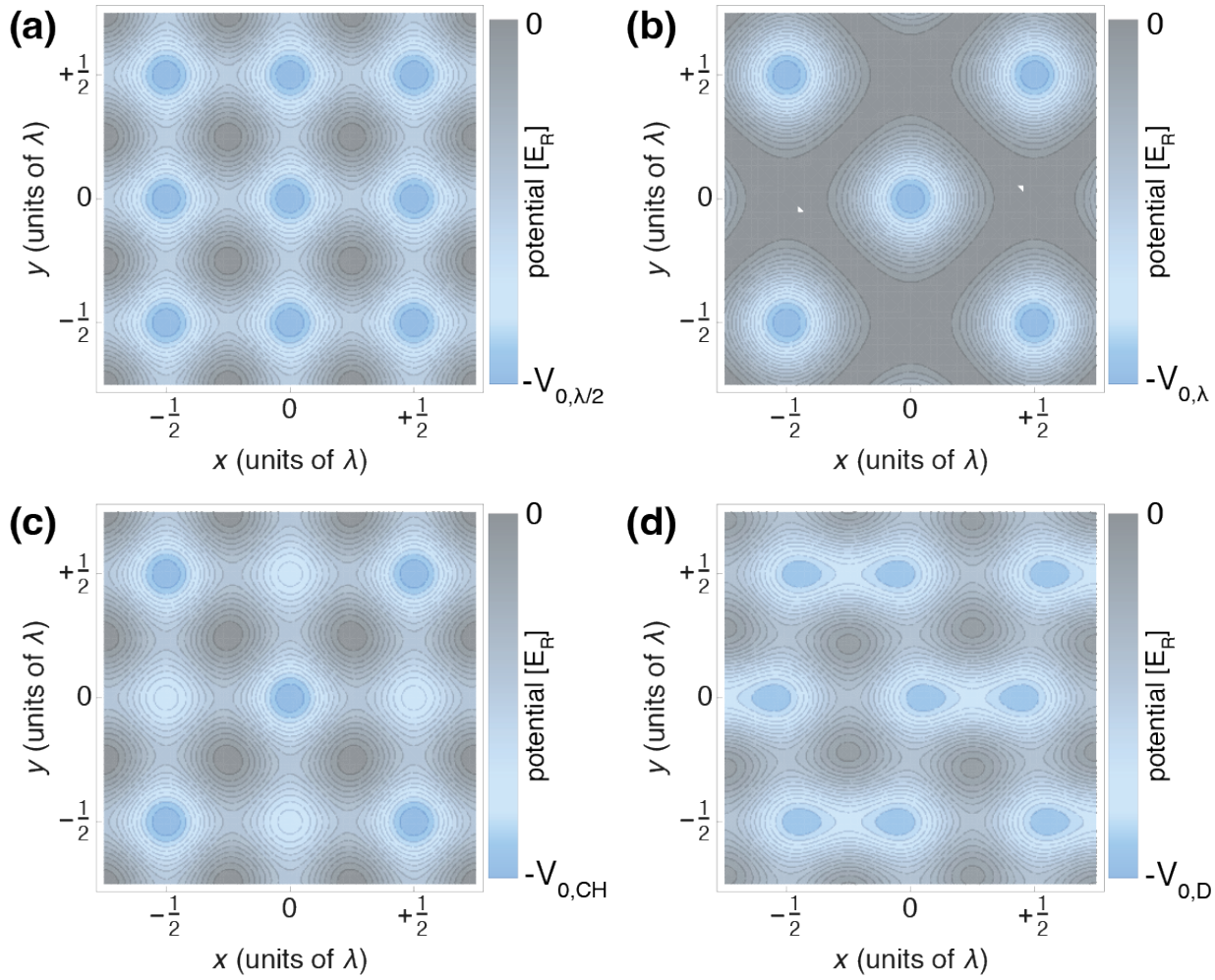

Figure 2.4: Different configurations of our double-well potential V_{LATT}. (a) $\lambda/2$ or 'in-plane', formed when polarization is fully in-plane, i.e., $V_{\text{op},0} = 0$. (b) λ or 'out-of-plane', formed when polarization is fully out-of-plane, i.e., $V_{\text{ip},0} = 0$. (c) Checkerboard lattice, corresponds to $\theta_z = 0$ in Eq. (2.3). In this configuration, minima of out-of-plane potential lie on top of minima of in-plane lattice. (d) Dimer lattice, corresponds to $\theta_z = \pi/2$. Minima of out-of-plane potential lie halfway between adjacent minima of in-plane lattice.

2.2.2 Numerical treatment of Schrödinger's equation

The scalar lattice potentials $V_{\text{ip}}(x,y)$ [Eq. (2.1)] and $V_{\text{op}}(x,y;\theta_z)$ [Eq. (2.2)] can be expanded in plane-wave components using the vectors $\boldsymbol{b}_1 = k_R(\hat{\boldsymbol{e}}_x - \hat{\boldsymbol{e}}_y)$ and $\boldsymbol{b}_2 = k_R(\hat{\boldsymbol{e}}_x + \hat{\boldsymbol{e}}_y)$, namely,

$$V_{\text{ip}}(x,y) = -\frac{V_{\text{ip},0}}{8}\left\{\left[e^{+i(\boldsymbol{b}_2+\boldsymbol{b}_1)\cdot\boldsymbol{r}} + e^{+i(\boldsymbol{b}_2-\boldsymbol{b}_1)\cdot\boldsymbol{r}} + \text{h.c.}\right] + 4\right\} \tag{2.4}$$

and

$$\begin{aligned} V_{\text{op}}(x,y;\theta_z) = -\frac{V_{\text{op},0}}{16}\Big\{4 + 2\left[e^{+i(\boldsymbol{b}_2\cdot\boldsymbol{r}-\theta_z)} + \text{h.c.}\right] + 2\left[e^{+i(\boldsymbol{b}_1\cdot\boldsymbol{r}-\theta_z)} + \text{h.c.}\right] + \\ + \left[e^{+i((\boldsymbol{b}_2+\boldsymbol{b}_1)\cdot\boldsymbol{r}-2\theta_z)} + \text{h.c.}\right] + \left[e^{+i(\boldsymbol{b}_2-\boldsymbol{b}_1)\cdot\boldsymbol{r}} + \text{h.c.}\right]\Big\}. \end{aligned} \tag{2.5}$$

Expressing the lattice potential as a Fourier expansion is convenient when performing computations in a plane-wave basis[1]. The identification of the reciprocal primitive vectors also clarifies the derivation of some mathematical objects naturally related to the periodicity of the potential. Some of these concepts are:

- Reciprocal lattice $\tilde{\mathcal{B}}$. A useful notion nabbed from the diffraction theory in crystallography [134, 135]. For our double-well optical lattice, it is given by $\tilde{\mathcal{B}} = \{n_1\boldsymbol{b}_1 + n_2\boldsymbol{b}_2 | n_1, n_2 \in \mathbb{Z}\}$, where $\boldsymbol{b}_1$ and $\boldsymbol{b}_2$ are the vectors in Eqs. (2.4) and (2.5). For crystallographers, the reciprocal lattice is a convenient tool to transform data inferred from the Bragg peaks, obtained through diffraction techniques, into information related to the (rarely directly accessible) lattice geometry in real space.

[1] Alternative sets of states used as basis to calculate properties of particles in the presence of optical lattices are the Bloch states and the Wannier orbitals (tight-binding approach).

- Bragg *planes*. The planes (in 3D) or lines (in 2D) bisecting the vectors in the lattice $\tilde{\mathcal{B}}$ at right angles.

- Brillouin zones. The first Brillouin zone BZ1 is defined as the Wigner-Seitz cell of $\tilde{\mathcal{B}}$, i.e., set of points in reciprocal space that can be reached from the origin without crossing any Bragg plane. In like manner, the $n-$th Brillouin zone BZn is the set of points in reciprocal space that can be connected to the origin only by crossing no less than n Bragg planes.

- Bravais primitive vectors. For our double-well lattice, these are

$$\boldsymbol{a}_1 = \frac{\lambda}{\sqrt{2}}\frac{\boldsymbol{e}_x - \boldsymbol{e}_y}{\sqrt{2}}, \quad \boldsymbol{a}_2 = \frac{\lambda}{\sqrt{2}}\frac{\boldsymbol{e}_x + \boldsymbol{e}_y}{\sqrt{2}}.$$

  In general, the primitive vectors are found through the relation $\boldsymbol{a}_m \cdot \boldsymbol{b}_n = 2\pi\delta_{mn}$. The Bravais lattice is given by $\mathcal{B} = \{m_1\boldsymbol{b}_1 + m_2\boldsymbol{b}_2 | m_1, m_2 \in \mathbb{Z}\}$, and the unit (or primitive) cell is the parallelogram defined by $\boldsymbol{a}_1$ and $\boldsymbol{a}_2$. The lattice is invariant under any translation by a vector in the discrete set $\mathcal{B}$.

According to Bloch's theorem [136, 137], when the potential V_{latt} is spatially periodic, the stationary states ψ that solve the Schrödringer equation $(-\frac{\hbar^2}{2m}\nabla^2 + V_{\text{LATT}})\psi = E\psi$, have the form

$$\psi_{n\boldsymbol{q}}(\boldsymbol{r}) = e^{i\boldsymbol{q}\cdot\boldsymbol{r}} u_{n\boldsymbol{q}}(\boldsymbol{r}), \tag{2.6}$$

where $\boldsymbol{q}$ is a vector in the Brillouin zone BZ1 and known as *crystal momentum* or *quasimomentum*, n is a discrete index referred to as the *band index* commonly taken to be a natural number, and $u_{n\boldsymbol{q}}(\boldsymbol{r})$ is a spatially periodic function with the same periodicity as the potential. The wavefunctions $\psi_{n\boldsymbol{q}}$ are known as Bloch waves.

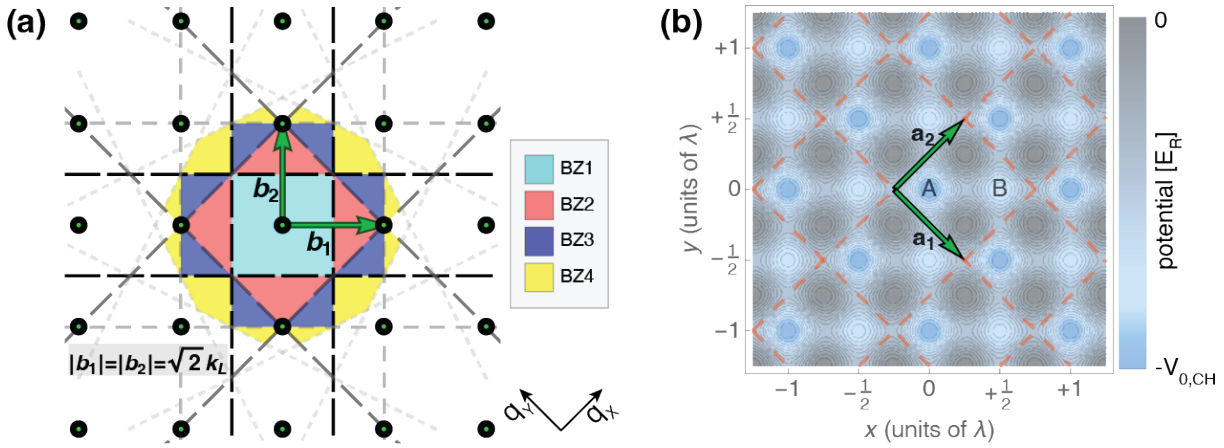

Figure 2.5: Reciprocal and Bravais lattices associated with the double-well lattice V_{LATT} in Eq. (2.3). (a) Reciprocal lattice (dark circles), reciprocal primitive vectors ($\boldsymbol{b}_1$ and $\boldsymbol{b}_2$), Bragg planes (dashed grey lines) and the first four Brillouin zones. (b) Bravais lattice $\mathcal{B}$ and the Bravais primitive vectors $\boldsymbol{a}_1$ and $\boldsymbol{a}_2$ for our double-well lattice. Contour lines in the background correspond to a checkerboard potential like the one shown in Fig. 2.4(c).

Since the function $u_{n\boldsymbol{q}}(\boldsymbol{r})$ is $\mathcal{B}$-periodic, it can be Fourier expanded in the reciprocal lattice $\tilde{\mathcal{B}}$, namely, $u_{n\boldsymbol{q}}(\boldsymbol{r}) = \sum_{\boldsymbol{\mathcal{Q}}\in\tilde{\mathcal{B}}} C_{n,\boldsymbol{q},\boldsymbol{\mathcal{Q}}} e^{i\boldsymbol{\mathcal{Q}}\cdot\boldsymbol{r}}$. From Eqs. (2.4) and (2.5), and inserting $u_{n\boldsymbol{q}}$ as a Fourier expansion into the time-independent Schrödinger equation, one gets the following eigenvalue equation

$$[M_L]\, V_{C,\boldsymbol{q}} = \epsilon_{n,\boldsymbol{q}} V_{C,\boldsymbol{q}} \tag{2.7}$$

where the matrix $[M_L]$ has the following aspect

$$[M_L] = \begin{bmatrix} \ddots & \vdots & \vdots & \vdots & \vdots & \vdots & \vdots & \vdots & \vdots & \vdots & \vdots & \vdots & \iddots \\ \dots & C^* & 0 & 0 & \dots & D^* & 0 & 0 & \dots & A & 0 & 0 & \dots \\ \dots & B^* & C^* & 0 & \dots & (\boldsymbol{q}-\boldsymbol{b}_2)^2 & D^* & 0 & \dots & B & A & 0 & \dots \\ \dots & A^* & B^* & C^* & \dots & D & \boldsymbol{q}^2 & D^* & \dots & C & B & A & \dots \\ \dots & 0 & A^* & B^* & \dots & 0 & D & (\boldsymbol{q}+\boldsymbol{b}_2)^2 & \dots & 0 & C & B & \dots \\ \dots & 0 & 0 & A^* & \dots & 0 & 0 & D & \dots & 0 & 0 & C & \dots \\ \iddots & \vdots & \vdots & \vdots & \vdots & \vdots & \vdots & \vdots & \vdots & \vdots & \vdots & \vdots & \ddots \end{bmatrix} \tag{2.8}$$

with

$$A = -\frac{v_{\text{ip},0}}{8} - \frac{v_{\text{op},0}}{16}e^{i2\theta_z}, \quad B = -\frac{v_{\text{op},0}}{8}e^{i\theta_z}, \quad C = -\frac{v_{\text{ip},0}}{8} - \frac{v_{\text{op},0}}{16}, \quad D = -\frac{v_{\text{op},0}}{8}e^{-i\theta_z}, \tag{2.9}$$

and

$$\begin{aligned} V_{C,\boldsymbol{q}} = [\dots\ & C_{n,\boldsymbol{q},-\boldsymbol{b}_1-2\boldsymbol{b}_2},\ C_{n,\boldsymbol{q},-\boldsymbol{b}_1-\boldsymbol{b}_2},\ C_{n,\boldsymbol{q},-\boldsymbol{b}_1+\boldsymbol{0}},\ C_{n,\boldsymbol{q},-\boldsymbol{b}_1+\boldsymbol{b}_2},\ C_{n,\boldsymbol{q},-\boldsymbol{b}_1+2\boldsymbol{b}_2},\ \dots \\ & \dots\ C_{n,\boldsymbol{q},-2\boldsymbol{b}_2},\ C_{n,\boldsymbol{q},-\boldsymbol{b}_2},\ C_{n,\boldsymbol{q},\boldsymbol{0}},\ C_{n,\boldsymbol{q},+\boldsymbol{b}_2},\ C_{n,\boldsymbol{q},+2\boldsymbol{b}_2},\ \dots \\ & \dots C_{n,\boldsymbol{q},+\boldsymbol{b}_1-2\boldsymbol{b}_2},\ C_{n,\boldsymbol{q},+\boldsymbol{b}_1-\boldsymbol{b}_2},\ C_{n,\boldsymbol{q},+\boldsymbol{b}_1-\boldsymbol{0}},\ C_{n,\boldsymbol{q},+\boldsymbol{b}_1+\boldsymbol{b}_2},\ C_{n,\boldsymbol{q},+\boldsymbol{b}_1+2\boldsymbol{b}_2}, \dots]^T . \end{aligned} \tag{2.10}$$

In Eq. (2.9), lattice parameters have been scaled in units of the single-photon recoil energy $E_R \equiv \hbar^2 k_R^2/2m$: $v_{\text{ip},0} \equiv V_{\text{ip},0}/E_R$, $v_{\text{op},0} \equiv V_{\text{op},0}/E_R$.

The values of the band index n labeling the eigenvalues are chosen so that $\epsilon_{1,\boldsymbol{q}} \leq \epsilon_{2,\boldsymbol{q}} \leq \epsilon_{3,\boldsymbol{q}} \leq \cdots$. Upon taking this convention for n, the eigenenergies $\epsilon_{n,\boldsymbol{q}}$ will depend continuously

on $\boldsymbol{q}$ for a given band index n. The sets $E^{(n)} \equiv \{\epsilon_{n,\boldsymbol{q}} | \boldsymbol{q} \in \text{BZ1}\}$ constitute disjoint intervals with no energies lying outside of them; they are known as energy *bands* and the distances between intervals are called band *gaps*, see Fig. 2.6. As a whole, the relation between $\epsilon_{n,\boldsymbol{q}}$ and the variables n and $\boldsymbol{q}$ is referred to as *band structure* or *band dispersion*. This concept plays an important role in solid-state physics, as several properties of solids can be derived from it, such as band gaps, effective mass, tunneling rates and density of states.

While the eigenvalue equation (2.7) involves matrices and vectors of infinite dimensions, an actual numerical computation of its solution requires proper truncation, keeping only a finite number of P unknown coefficients $C_{n,\boldsymbol{q},\boldsymbol{\mathcal{Q}}}$. Solving the eigenvalue equation reduces then to the diagonalization of a $P \times P$ square matrix $[M_L]_P$. In most cases, one is mainly interested in the lowest lying eigenvalues and their corresponding eigenvectors since the dynamics of atoms loaded in an optical lattice can be expected to involve only the ground states and their first few excited ones. For a sufficiently large matrix order P and appropriate selection of vectors $\boldsymbol{\mathcal{Q}}$ in the reciprocal lattice $\tilde{\mathcal{B}}$, the low lying eigenenergies of $[M_L]_P$ will depend very weakly on the value of P, converging to their respective true numerical values (those obtained without truncating the infiinite matrix) as P approaches infinity. In most of our calculations we use $M = 81$ coefficients ($C_{n,\boldsymbol{q},r\boldsymbol{b}_1+s\boldsymbol{b}_2}$, where integers r and s satisfy $-4 \leq r, s \leq 4$).

Figure 2.6 presents some examples of numerically calculated energy bands and Bloch states for in-plane, checkerboard and dimer lattices.

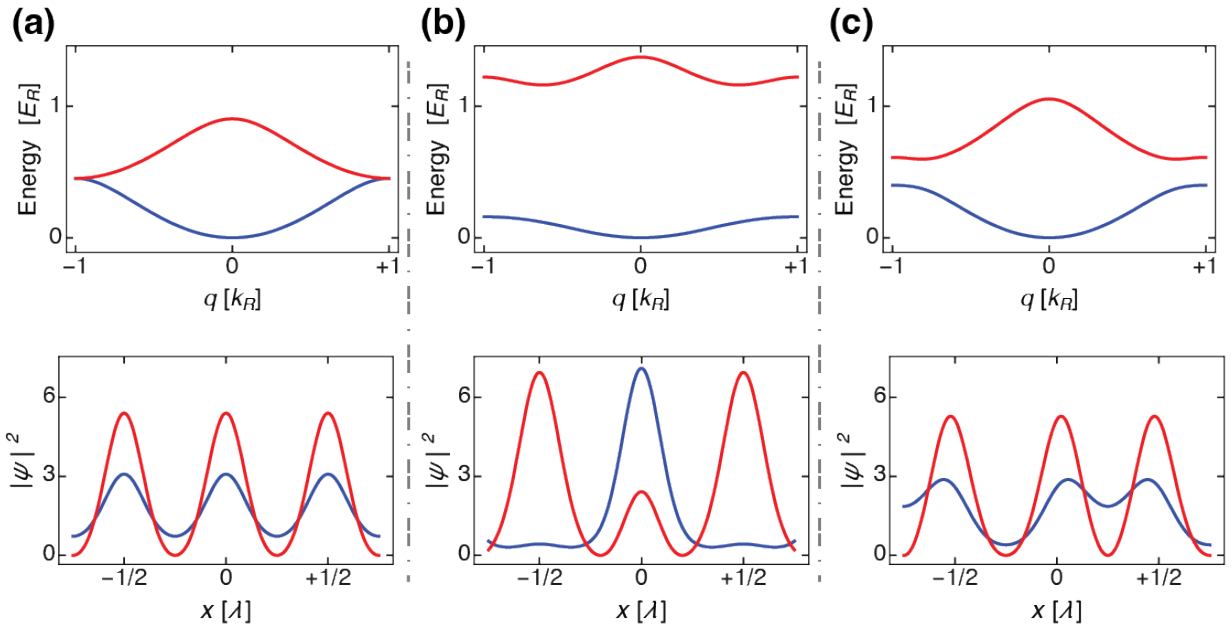

Figure 2.6: Lowest energy bands (upper row) and Bloch wavefunctions at $q = 0$ (lower row) for particular examples of (a) $\lambda/2$, (b) checkerboard and (c) dimer lattices. Blue and red curves indicate, respectively, ground excited bands. The wavefunctions are plotted along the $y = 0$ line in real space. Parameters used for these examples are (a) $V_{\text{ip},0} = 6\ E_R$, $V_{\text{op},0} = 0\ E_R$, (b) $V_{\text{ip},0} = 5.2\ E_R$, $V_{\text{op},0} = 1.6\ E_R$, $\theta_z = 0$, (c) $V_{\text{ip},0} = 5.2\ E_R$, $V_{\text{op},0} = 1.6\ E_R$, $\theta_z = \pi/2$. These three sets of parameters correspond to a lattice beam with the same intensity but with different polarizations.

2.2.3 Calibration and maintenance of lattice alignment

For different reasons, such as long-term drift in the lattice alignment or shifts in the center of the ODT trap, it was necessary to occasionally improve the alignment of the lattice beams. During the first step of this re-alignment process, we blocked the lattice beams $\boldsymbol{k}_{2,3,4}$ (see Fig. 2.3) and tuned the alignment of the $\boldsymbol{k}_1$ beam by finely rotating the mount knobs of the mirror M0 in Fig. 2.3. The proximity of $\boldsymbol{k}_1$ to the cloud was gauged by using the intensity and off-center placement of this lattice beam to 'pull' the atoms, hence causing the (originally at rest) BEC, held by the ODT, to undergo spatial oscillations whose amplitudes were related to how close $\boldsymbol{k}_1$ was to the cloud. Accordingly, this procedure was colloquially known as 'dipole pulling'. If the $\boldsymbol{k}_1$ beam lay close enough to the initially resting BEC, the latter would undergo substantial oscillations detectable in a series of TOF images. To pull the cloud, the intensity of the $\boldsymbol{k}_1$ beam was first rapidly ramped up close to its maximum possible power and then suddenly switched off to let the cloud move in trap. As the $\boldsymbol{k}_1$ beam was moved closer to the ODT center, the amplitude of the oscillations decreased until they became negligible. A drawback of this method was that a low oscillation amplitude was not exclusive of a near-perfect alignment but was also obtained when $\boldsymbol{k}_1$ was sufficiently far from the atoms. Consequently, one had to first identify a narrow range of knob positions where, by tilting the mirror in a single direction, the amplitudes went quickly first down to zero and then up again; the position, within this narrow range, where amplitudes vanished corresponded to near-perfect alignment of $\boldsymbol{k}_1$.

In the rare occasions where $\boldsymbol{k}_1$ was awfully far away from the cloud (something that could occur, for example, if the 'dipole pulling' technique was done carelessly), one would resort to a coarser method by having $\boldsymbol{k}_1$ replace the dipole beam D1 (see figure 2.3) to form a cross-beam

dipole trap with the dipole beam D2. This procedure was known as '$\boldsymbol{k}_1$-D2 trapping'. With this technique, alignment of $\boldsymbol{k}_1$ was optimized based on the number of atoms held by the '$\boldsymbol{k}_1$-D2' trap after zero time of flight (in-situ detection).

Once $\boldsymbol{k}_1$ was satisfactorily lined up, the next step was to tune the alignment of the $\boldsymbol{k}_2$ beam by touching up the position of the mount knobs for mirror M2. To do this, we blocked the curved mirror M3 and formed a 1-dimensional sinusoidal lattice, along the direction of $\boldsymbol{k}_1 + \boldsymbol{k}_2$, caused by the interference between the vertically polarized beams $\boldsymbol{k}_1$ and $\boldsymbol{k}_2$. Vertical polarization of $\boldsymbol{k}_1$ and $\boldsymbol{k}_2$ was obtained by driving the Pockels cell PC1 at its half-wave voltage. Alignment of $\boldsymbol{k}_2$ was improved using the lattice depth obtained from the diffraction technique.

Having aligned $\boldsymbol{k}_1$ and $\boldsymbol{k}_2$, the final part of the alignment procedure consisted in doing the same for $\boldsymbol{k}_3$ and $\boldsymbol{k}_4$. This was performed by touching up the mount knobs of the curved mirror M3 while maximizing the power sent back into the long optical fiber where lattice light originally came from (i.e., the fiber that took light from the Ti:sapph laser into the optical table holding up the vacuum apparatus). To monitor this power, a non-polarizing beamsplitter cube was placed between the Ti:sapph laser and the fiber, which allowed to measure some fixed percentage of the light sent back into this fiber after having hit the mirror M3.

2.2.4 Piezo-driven mirrors

A new design for low-steering piezo-driven mirrors, shown in Fig. 2.7(a), was implemented in our lab to controllably modulate the position of the lattice potential with frequencies up to a few tens of kilohertz and displacements reaching several lattice spacings. In this innovative design, the mirror is translated along its principal axis by three piezoelectric actuators arranged in a tripod

configuration and supported by a steel mount. Slight differences in the enlargements of the three piezoelectric transducers (when driven with the same voltage) caused a significant adverse tilt in the position of the mirror, and were considerably minimized by rescaling the respective voltages driving each actuator via a feed-forward electronic system. The remaining tilt, measured with a beam profiler placed several meters away from the mirror, was 0.6 microradians per micron of displacement when modulating the mirror position at a few kilohertz. The mirror translation as a function of the voltage driving the piezoelectric transducers was calibrated using a Michelson interferometer where the piezo-actuated mirror modified the path length of one of the arms. The largest translation attained with this mount was about 2 μm. Harmful mechanical resonances in this device appear only for frequencies above 50 kHz, as indicated by the open loop Bode plot shown in Fig. 2.7(b), obtained with the signal from the Michelson interferometer. A more detailed account of the design and characterization of these kinematic mirrors, including the actual effects of the tilt on the depth of the lattice as measured by Kapitza-Dirac diffraction, can be found in Ref. [106].

Our optical lattice was shaken using a pair of the piezo-actuated mirrors [M1 and M3 in Fig. 2.8(a)]. Translation of mirror M1 alone moved the lattice along the x-only direction; translation of mirror M3 alone moved the lattice along the diagonal $y = -x$ direction. Arbitrary trajectories (with amplitudes below the maximum possible displacement of the mirrors) could be tailored by combining the two motions of M1 and M3, and adjusting their relative amplitudes and phases. In our studies of parametric heating (Chapter 4), we explored the three modulation trajectories illustrated in Fig. 2.8(b), namely, x-only, diagonal and circular.

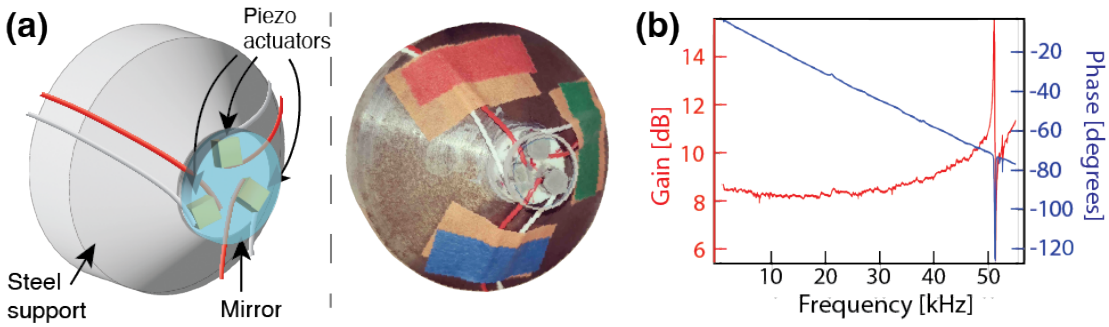

Figure 2.7: (a) Design of the piezo driven mirrors employed to shake our 2D lattice. Left image is a sketch, and right image is a photo of the actual mirror mount used in our experiment. By using three piezoelectric transducers in a tripod arrangement and a feed-forward stabilization system, we attained an acceptably small tilt of 0.6 micro-radians per μm of displacement [106]. (b) Frequency response (Bode plot) obtained from the signal of a Michelson interferometer where the path length of one of the arms was varied by translating the mirror. No detrimental mechanical resonances arose when the mirror position was modulated with frequencies below 50 kHz.

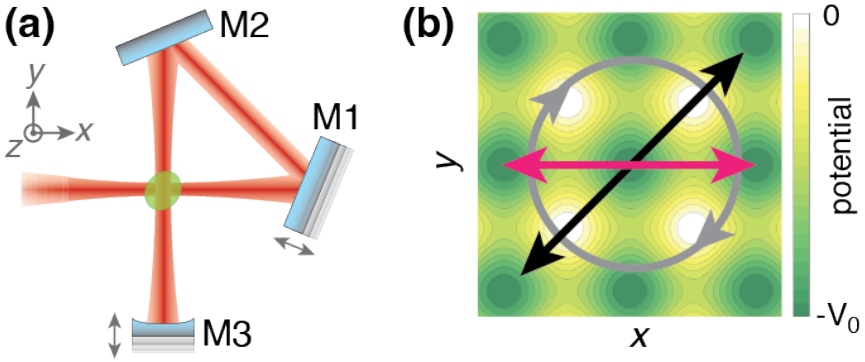

Figure 2.8: Shaken 2D lattice. (a) The lattice, formed from a single retroreflected beam, is translated along the plane defined by the lattice laser beams (x-y plane) using the mirrors M1 and M3. (The mirror M2 is motionless.) (b) Trajectories employed in our study of parametric heating (Chapter 4) sketched on top of a contour plot of the square lattice.

Chapter 3: Floquet-Bogoliubov equations for BECs in optical lattices

This chapter outlines a convenient framework to analyze periodically driven condensates held in optical lattices as well as the properties of the dynamical instabilities arising therein. Section 3.1 covers a few mathematical results and numerical techniques related to the Floquet formalism, whose function in this thesis is to generalize the single-particle Bloch framework (briefly outlined in Chapter 2) to periodically time-modulated lattice potentials. The Floquet theory is illustrated by considering periodically shaken lattices where the frequency is (i) higher than the bandwidth of the static ground band but far from the resonance with the excited bands, and (ii) close to the separation between the first two bands. These two examples will be relevant in chapters 4 and 5. Section 3.2 sums up the theoretical derivation of dynamical instabilities in weakly-interacting BECs held in static optical lattices, as described by a linear stability analysis of the solution to the Gross-Pitaevskii equation. The theoretical approaches presented in the first two sections are then combined in section 3.3, focusing on some aspects of parametric instabilities.

3.1 Single-particle Floquet formalism

Floquet's theorem is a result conventionally discussed in the context of linear ordinary differential equations possessing periodic coefficients [138–140]. The application of this theorem

to time-periodic Hamiltonians leads to results analogous to those of Bloch's theorem when applied to lattice potentials. Both theorems exploit the symmetries of the problem to characterize the solutions to the Schrödinger equation: while Bloch's theorem constrains the eigenstates to be eigenfunctions of space translation operators $\hat{T}(\boldsymbol{\mathcal{R}})$ with $\boldsymbol{\mathcal{R}}$ belonging to the Bravais lattice $\mathcal{B}$, Floquet's theorem restricts the eigenstates to the eigenfunctions of the time translation operator $\hat{T}(T)$, where T is the period of the Hamiltonian. In addition, just as the crystal momentum of a particle (in the presence of a lattice) behaves virtually as its free-particle momentum, an energy-like quantity (to be discussed below) emerges from the Floquet famework that acts as the effective eigenenergy of the particle. This virtual energy is ascribed to an effective time-independent Hamiltonian, whose form can be designed to some extent by tuning the parameters defining the periodic drive; this last remark is the essence of "Floquet engineering" (reviewed in Chapter 1).

3.1.1 Floquet states and quasi-energies

One way to formulate Floquet's theorem [141–145] states that the evolution operator $\hat{U}(t_f, t_i)$ of a time-periodic Hamiltonian $\hat{H}(t)$ with period T can be factorized in the following way

$$\hat{U}(t_f, t_i) = \hat{P}(t_f) \exp\left[-\frac{i}{\hbar}(t_f - t_i)\,\hat{G}\right], \tag{3.1}$$

where the time-dependent operator $\hat{P}(t)$ is unitary, possesses the same periodicity as the Hamiltonian (i.e., $\hat{P}(t+T) = \hat{P}(t)$), and matches the identity operator $\hat{\mathbb{1}}$ when $t = t_i, t_i+T, t_i+2T, \ldots$ (i.e., $\hat{\mathbb{1}} = \hat{P}(t_i) = \hat{P}(t_i + T) = \hat{P}(t_i + 2T) = \cdots$). The time-independent operator $\hat{G}$ inside the exponential is Hermitian and known as the *Floquet Hamiltonian*. Except for $\hat{P}(t)$, equation (3.1)

possesses the same form as that of a system whose (static) Hamiltonian is $\hat{G}$.

As a corollary of Eq. (3.1), if ψ_m and ε_m denote the eigenvectors and eigenenergies of $\hat{G}$, so that ψ_m are eigenvectors of $\exp[-\frac{i}{\hbar}(t_f - t_i)\hat{G}]$ with proper values $e^{-\frac{i}{\hbar}(t_f - t_i)\varepsilon_m}$, then the solution to the Schrödinger equation with inital condition ψ_m at time t_i is

$$\hat{U}(t_f, t_i)\left[\hat{P}(t_i)\psi_m\right] = \hat{U}(t_f, t_i)\psi_m = e^{-i(t_f - t_i)\varepsilon_m}\left[\hat{P}(t_f)\psi_m\right], \tag{3.2}$$

where the relation $\hat{P}(t_i) = \hat{\mathbb{1}}$ has been used. It follows from this equation, and after defining $u_m(t) \equiv \hat{P}(t)\psi_m$, that some solutions to this periodically driven system possess the form

$$\tilde{\psi}_m(t) = e^{-i\,\varepsilon_m\,(t - t_i)}\,u_m(t), \tag{3.3}$$

where $u_m(t)$ is by construction time-periodic with period T, i.e., $u_m(t + T) = u_m(t)$. Equation (3.2) hints at a technique to find both $u_m(t_i + T) = u_m(t_i)$ and ε_m: $u_m(t_i)$ is a solution of the eigenvalue equation

$$\hat{U}(t_i + T, t_i)\,u_m(t_i) = e^{-\frac{i}{\hbar}\varepsilon_m T}\,u_m(t_i), \tag{3.4}$$

and $e^{-\frac{i}{\hbar}\varepsilon_m T}$ is its accompanying eigenvalue. The value of ε_m is determined only up to $\hbar\omega$, where $\omega = \frac{2\pi}{T}$, as $e^{-\frac{i}{\hbar}(\varepsilon_m + \kappa\hbar\omega)T}$ has the same value for any integer κ; this is not a limitation of this method but results from the intrinsic Brillouin zone structure of ε_m [144].

Some authors [144] refer to the one-cycle evolution operator $\hat{U}(t_i + T, t_i)$ as the *monodromy operator* and its eigenvectors $u_m(t_i)$ as *Floquet functions* or *Floquet modes*. The solutions to the time-dependent Schrödinger equation with the form (3.3) are known as *Floquet states*. These

states are not stationary, as they would be if the Hamiltonian was static; however, the phase factor $e^{-\frac{i}{\hbar}\varepsilon_m(t-t_i)}$ resembles the one accompanying the time evolution of stationary states for a time-independent Hamiltonian. States (3.3) represent a generalized version of stationary states, and the quantities ε_m, named *quasienergies* or *Floquet energies*, can be regarded as generalized energies.

3.1.2 Numerical calculation of Floquet spectra

The analytical derivation of the full Floquet Hamiltonian $\hat{G}$, or of its spectrum ε_m, is in general a challenging task. Evaluations of the quasienergy spectra hence resort either to theoretical approximations to $\hat{G}$, as the ones worked out for systems driven at high frequencies [146–148], or to numerical techniques [148, 149], two of which are outlined in this subsection.

Trotter-Suzuki decomposition of time-evolution operator

The major computational difficulty in solving the eigenvalue equation (3.4) is the calculation the one-cycle evolution operator $\hat{U}(t_i+T,t_i)$. The operator $\hat{U}(t_f,t_i)$, evaluated at arbitrary times $t_f > t_i$ and associated with a time-dependent Hamiltonian $\hat{H}(t)$, has a conventional expansion known as the Dyson series [150–152]

$$\begin{aligned}\hat{U}(t_f,t_i) &= \hat{\mathcal{T}}_o \exp\left[-\frac{i}{\hbar}\int_{t_i}^{t_f} d\tau \hat{H}(\tau)\right] = \\ &= \hat{\mathbb{1}} + \sum_{n=1}^{\infty}\left(-\frac{i}{\hbar}\right)^n \int_{t_i}^{t_f} dt_1 \int_{t_i}^{t_1} dt_2 \cdots \int_{t_i}^{t_{n-1}} dt_n\, \hat{H}(t_1)\hat{H}(t_2)\cdots\hat{H}(t_n), \end{aligned} \tag{3.5}$$

where $\hat{\mathcal{T}}_o$ is a time-ordering operator.

(One of the time-dependent Hamiltonians that we will be considering in this thesis is

$$\hat{H}_s(\hat{\boldsymbol{r}}, \hat{\boldsymbol{p}}, t) = \hat{H}_0(\hat{\boldsymbol{r}}, \hat{\boldsymbol{p}}) - \omega_s \left[\Delta_x \cos(\omega t)\hat{p}_x + \Delta_y \cos(\omega t + \theta_s)\hat{p}_y\right], \tag{3.6}$$

which describes a shaken lattice in the comoving frame. In the previous expression (3.6) for the Hamiltonian $\hat{H}_s(\boldsymbol{r}, \boldsymbol{p}, t)$, ω_s is the frequency of the modulation, Δ_x and Δ_y are the spatial amplitudes of the shaking along x and y, and $\hat{H}_0$ is the Hamiltonian in the absence of the drive. The other time-dependent Hamiltonian we will consider is

$$\hat{H}_{\text{am}}(\hat{\boldsymbol{r}}, \hat{\boldsymbol{p}}, t) = \hat{H}_0(\hat{\boldsymbol{r}}, \hat{\boldsymbol{p}}) + \alpha_m \cos(\omega_{\text{am}} t) V_{\text{latt}}^{[\text{um}]}(\boldsymbol{r}), \tag{3.7}$$

which describes an amplitude modulated lattice. In the previous expression (3.7) for the Hamiltonian $\hat{H}_{\text{am}}$, ω_{am} is the frequency of the drive, α_m is the magnitude of the modulation, $\hat{H}_0$ is the unmodulated Hamiltonian, and $V_{\text{latt}}^{[\text{um}]}(\boldsymbol{r})$ is the unmodulated optical lattice.)

It is usually impractical to evaluate $\hat{U}$ using the expansion (3.5). A more practical approach to calculate the one-cycle evolution operator $\hat{U}(t_i + T, t_i)$ appearing in the equation (3.4) begins by approximating $\hat{U}(t_i + T, t_i)$ with a less convoluted time-ordered expression derived from the Lie-Trotter product formula and given by [153–155]

$$\begin{aligned}\hat{U}(t_i + T, t_i) &\approx \prod_{n=1}^{N} e^{-i\frac{T}{N}\hat{H}(t_i + \frac{n}{N}T)} \\ &\approx e^{-i\frac{T}{N}\hat{H}(t_i+T)} e^{-i\frac{T}{N}\hat{H}(t_i+\frac{N-1}{N}T)} \cdots e^{-i\frac{T}{N}\hat{H}(t_i+\frac{2}{N}T)} e^{-i\frac{T}{N}\hat{H}(t_i+\frac{1}{N}T)},\end{aligned} \tag{3.8}$$

where equality is attained as $N \to \infty$.

Exact computation of each exponential $e^{-i\frac{T}{N}\hat{H}(\tau)}$ in Eq. (3.8) is rarely efficient, and approximations are regularly used. While for a sufficiently large N it would be justified to make the first-order approximation $e^{-i\frac{T}{N}\hat{H}(\tau)} \approx \hat{\mathbb{1}} - i\frac{T}{N}\hat{H}(\tau)$, it is more convenient to first decompose (if possible) the Hamiltonian $\hat{H}$ into two components $\hat{H}(t) = \hat{H}_A + \hat{H}_B(t)$ where $\hat{H}_A$ is a time-independent dominant part of the Hamiltonian and $\hat{H}_B$ is expected to be small compared to $\hat{H}_A$. This decomposition is then used along with a Trotter-Suzuki approximant [155] of second order, $e^{-i\frac{T}{N}\hat{H}(\tau)} \approx e^{-i\frac{1}{2}\frac{T}{N}\hat{H}_B(\tau)}e^{-i\frac{T}{N}\hat{H}_A}e^{-i\frac{1}{2}\frac{T}{N}\hat{H}_B(\tau)}$, to obtain

$$\begin{aligned}\hat{U}(t_i+T,t_i) \quad \approx \quad & \left\{e^{-i\frac{1}{2}\frac{T}{N}\hat{H}_B(t_i+T)}e^{-i\frac{T}{N}\hat{H}_A}e^{-i\frac{1}{2}\frac{T}{N}\hat{H}_B(t_i+T)}\right\}\times \\ & \times\left\{e^{-i\frac{1}{2}\frac{T}{N}\hat{H}_B(t_i+\frac{N-1}{N}T)}e^{-i\frac{T}{N}\hat{H}_A}e^{-i\frac{1}{2}\frac{T}{N}\hat{H}_B(t_i+\frac{N-1}{N}T)}\right\}\times\cdots \\ \cdots & \times\left\{e^{-i\frac{1}{2}\frac{T}{N}\hat{H}_B(t_i+\frac{2}{N}T)}e^{-i\frac{T}{N}\hat{H}_A}e^{-i\frac{1}{2}\frac{T}{N}\hat{H}_B(t_i+\frac{2}{N}T)}\right\}\times \\ & \times\left\{e^{-i\frac{1}{2}\frac{T}{N}\hat{H}_B(t_i+\frac{1}{N}T)}e^{-i\frac{T}{N}\hat{H}_A}e^{-i\frac{1}{2}\frac{T}{N}\hat{H}_B(t_i+\frac{1}{N}T)}\right\}. \end{aligned} \tag{3.9}$$

In the expansion (3.9), the time-independent exponential $e^{-i\frac{T}{N}\hat{H}_A}$ need not be computed N times but rather once, while the time-dependent exponential $e^{-i\frac{1}{2}\frac{T}{N}\hat{H}_B(\tau)}$ can be justifiably approximated by $e^{-i\frac{T}{N}\hat{H}_B(\tau)} = \hat{\mathbb{1}} - \frac{i}{\hbar}\frac{T}{N}\hat{H}_B(\tau)$ since N is chosen such that $(T/\hbar N)\hat{H}_B$ is small. (Note that this approximation works even if $(T/\hbar N)\hat{H}_A$ is not small.)

Quasienergies ε_m and the Floquet modes at time t_i, $u_m(t_i)$, are obtained from diagonalizing the product (3.9), which yields as many eigenvalues as the rank of the employed matrix representation for $\hat{H}$. To obtain $u_m(t)$ at arbitrary times $0 < t < T$ (and, hence, the full Floquet state $\tilde{\psi}_m$), one could either compute $\hat{U}(t+T,t)$ within the interval $(0,T)$ or, more efficiently if only a few of the Floquet modes are of interest, by time-evolving Schrödinger's equation using $u_m(t_i)$ as the initial condition. As a final remark, in some cases it might be complicated (even

if possible) to identify within the raw computed quasienergies those who originate from one or more bare (static) energy bands, i.e., those Floquet energies that would continuously transform into a given set of bare bands as the modulation vanishes. One way to sort out this difficulty is to use the overlap between the bare eigenstates and $u_m(t_i)$ as an indicator of what bare state a quasienergy ε_m predominantly descends from.

Extending Hilbert space to include time-periodic functions

An alternative approach (discussed, for example, in Refs. [144, 148, 156]) to calculate the Floquet states and the quasienergy spectrum ε_m circumvents the calculation of time-ordered exponentials, but requires composing and diagonalizing a matrix over an *extended* Hilbert space [157], also known as Floquet-Hilbert space [158], wherein time t is treated as a coordinate. This framework is motivated by the equation

$$\left[\hat{H}(t) - i\hbar\frac{\partial}{\partial t}\right] u_m(t) = \varepsilon_m u_m(t), \tag{3.10}$$

obtained after inserting the expression (3.3) for a Floquet state $\tilde{\psi}_m$ into the Schrödinger equation $i\hbar\frac{\partial}{\partial t}\tilde{\psi}_m = \hat{H}(t)\tilde{\psi}_m$. The unknown Floquet modes $u_m(t)$ in Eq. (3.10) are then expanded in the extended basis $\mathcal{E} \equiv \mathcal{S} \otimes \mathcal{T}$, where $\mathcal{T} = \left\{e^{i\beta\omega t} \,|\, \beta \text{ is an integer and } \omega = \frac{2\pi}{T}\right\}$ is a Fourier basis for time periodic functions with period T and $\mathcal{S} = \{|S_\alpha\rangle\}$ is a basis for the unmodulated Hamiltonian,

$$u_m(t) = \sum_\alpha \tilde{c}_{m,\alpha}(t)\,|S_\alpha\rangle = \sum_{\alpha,\beta} C_{m,\{\alpha,\beta\}}\left(|S_\alpha\rangle \otimes e^{i\beta\frac{2\pi}{T}t}\right), \tag{3.11}$$

where $\tilde{c}_{m,\alpha}(t) \equiv \sum_\beta C_{m,\{\alpha,\beta\}} e^{i\beta\frac{2\pi}{T}t}$ is periodic in time and the indeterminate coefficients $C_{m,\{\alpha,\beta\}}$ do not depend on time. By denoting the p-th time Fourier components of the Hamiltonian as $\hat{H}_p$ (so that $\hat{H}(t) = \sum_p \hat{H}_p e^{ip\omega t}$) it follows from equation (3.10) and the expansion (3.11) that

$$\sum_{\alpha',p} \langle S_\alpha | \, \hat{H}_p \, | S_{\alpha'} \rangle \, C_{m,\{\alpha',\beta-p\}} + \hbar\beta\omega \, C_{m,\{\alpha,\beta\}} = \varepsilon_m \, C_{m,\{\alpha,\beta\}} \tag{3.12}$$

for any value of $\{\alpha, \beta\}$. The equations (3.12) can be recast as the following eigenvalue equation

$$\left(\hat{K}^{[\mathcal{E}]}\right) u_m^{[\mathcal{E}]} = \varepsilon_m \, u_m^{[\mathcal{E}]}, \tag{3.13}$$

where $u_m^{[\mathcal{E}]}$ is the representation of u_m in the $\mathcal{E}$ basis

$$\begin{aligned} u_m^{[\mathcal{E}]} = \{ \; & \ldots, C_{m,\{\alpha=1,\,\beta=-1\}}, C_{m,\{\alpha=2,\,\beta=-1\}}, C_{m,\{\alpha=3,\,\beta=-1\}}, \ldots \\ & \ldots, C_{m,\{\alpha=1,\,\beta=0\}}, C_{m,\{\alpha=2,\,\beta=0\}}, C_{m,\{\alpha=3,\,\beta=0\}}, \ldots \\ & \ldots, C_{m,\{\alpha=1,\,\beta=+1\}}, C_{m,\{\alpha=2,\,\beta=+1\}}, C_{m,\{\alpha=3,\,\beta=+1\}}, \ldots \; \}^T, \end{aligned} \tag{3.14}$$

$\hat{K}^{[\mathcal{E}]}$ is the matrix representation of the operator $\hat{K} = \hat{H}(t) - i\hbar\frac{\partial}{\partial t}$ in the $\mathcal{E}$ basis, block partitioned as follows

$$\hat{K}^{[\mathcal{E}]} = \begin{pmatrix} \ddots & \vdots & \vdots & \vdots & \vdots & \vdots & \iddots \\ \cdots & \hat{H}_0^{[\mathcal{S}]} - 2\hbar\omega & \hat{H}_{-1}^{[\mathcal{S}]} & \hat{H}_{-2}^{[\mathcal{S}]} & \hat{H}_{-3}^{[\mathcal{S}]} & \hat{H}_{-4}^{[\mathcal{S}]} & \cdots \\ \cdots & \hat{H}_{+1}^{[\mathcal{S}]} & \hat{H}_0^{[\mathcal{S}]} - \hbar\omega & \hat{H}_{-1}^{[\mathcal{S}]} & \hat{H}_{-2}^{[\mathcal{S}]} & \hat{H}_{-3}^{[\mathcal{S}]} & \cdots \\ \cdots & \hat{H}_{+2}^{[\mathcal{S}]} & \hat{H}_{+1}^{[\mathcal{S}]} & \hat{H}_0^{[\mathcal{S}]} & \hat{H}_{-1}^{[\mathcal{S}]} & \hat{H}_{-2}^{[\mathcal{S}]} & \cdots \\ \cdots & \hat{H}_{+3}^{[\mathcal{S}]} & \hat{H}_{+2}^{[\mathcal{S}]} & \hat{H}_{+1}^{[\mathcal{S}]} & \hat{H}_0^{[\mathcal{S}]} + \hbar\omega & \left[\hat{H}_{-1}\right]_{\mathcal{S}} & \cdots \\ \cdots & \hat{H}_{+4}^{[\mathcal{S}]} & \hat{H}_{+3}^{[\mathcal{S}]} & \hat{H}_{+2}^{[\mathcal{S}]} & \hat{H}_{+1}^{[\mathcal{S}]} & \hat{H}_0^{[\mathcal{S}]} + 2\hbar\omega & \cdots \\ \iddots & \vdots & \vdots & \vdots & \vdots & \vdots & \ddots \end{pmatrix}, \tag{3.15}$$

with $\hat{H}_p^{[\mathcal{S}]}$ denoting the matrix representation of $\hat{H}_p$ in the $\mathcal{S}$ basis, i.e., $(\hat{H}_p^{[\mathcal{S}]})_{\alpha,\alpha'} = \langle S_\alpha | \hat{H}_p | S_{\alpha'} \rangle$. The matrix (3.15) is truncated in actual computations of its spectrum, keeping only a finite number of block matrices according to the subset of states selected from the extended basis $\mathcal{E}$.

3.1.3 Periodically shaken 1D lattice

This subsection illustrates some results connected with periodically shaken 1D sinusoidal lattices. The following examples consider a lattice with spacing a_ℓ ($= \pi/k_R = \lambda/2$) between neighboring sites and a 7 E_R depth. The three lowest energy bands of the unmodulated potential are depicted as solid lines in Fig. 3.1. The amplitude, period and frequency of the shaking are respectively denoted as ΔL, T_s and ω_s. In the reference frame comoving with the lattice, this

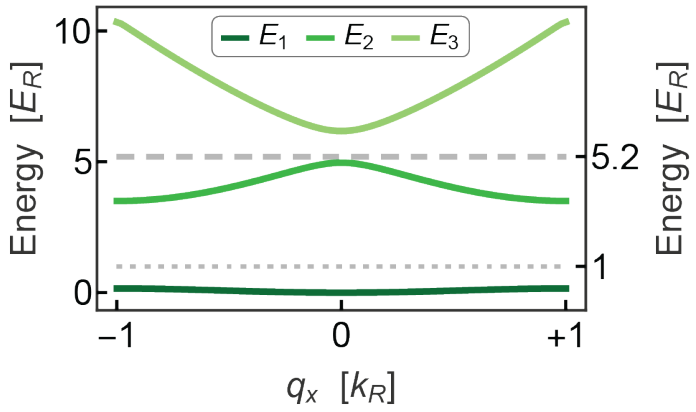

Figure 3.1: Lowest three energy bands (denoted as E_1, E_2 and E_3) of a 1D lattice with a 7 E_R depth. Dashed and dotted lines indicate the frequencies $\omega_s = 1\ E_R/\hbar$ and $\omega_s = 5.2\ E_R/\hbar$.

periodic drive produces an inertial sinusoidal force given by [33, 75, 144]

$$F(t) = m\,(\Delta L)\,\omega_s^2\cos(\omega_s t) = K_0\frac{\hbar\omega_s}{a_\ell}\cos(\omega_s t), \tag{3.16}$$

where the dimensionless parameter K_0, defined as $K_0 = m\,\Delta L\,\omega_s a_\ell/\hbar$, represents the drive strength and will become relevant later when approximate expressions to the Floquet energies and states are presented.

Off-resonance shaking (band renormalization)

As a first example, ω_s is chosen to be $1\ E_R/\hbar$, indicated by the dotted line in Fig. 3.1. This frequency is much smaller than the separation between E_1 and E_2 so that the coupling between the ground and excited bands is not substantial, and much larger than the width of the ground band so that a high-frequency approximation is valid. Under these conditions, and as shown in Fig. 3.2(a), the computed quasienergies ε_1 (corresponding to the Floquet states largely com-

posed of bare ground states) form a band similar to the unmodulated ground band E_1, but whose width first decreases and eventually becomes inverted as ΔL grows. As a matter of fact, in a tight-binding single-band description, in which E_1 is approximated by $E_1(q_x) \approx -2J\cos(q_x a_\ell)$ (where J is the tunneling matrix element between neighboring sites), this time modulated problem is well approximated by an effective Hamiltonian whose tunneling J is merely rescaled by a factor set by the parameter K_0 [75, 159]. This rescaling of J has been used in experiments to observe dynamical localization [75,160] simulate frustrated classical magnetism [161] and create state-dependent lattices [162].

Since ω_s is small compared to the separation between E_1 and E_2, the quasienergies ε_1 do not exhibit significant avoided level crossings with other bands as is the case with the quasienergies ε_2 and ε_3 [see Fig. 3.2(b)]. The dynamics thus takes place predominantly within the ground band E_1, a decent approximation to the spatiotemporal Floquet-Bloch waves with quasimomenta q_x is the Houston state [163]

$$\tilde{\psi}_{q_x}(x,t) \approx \exp\left(-\frac{i}{\hbar}\int_0^t d\tau E_1[\tilde{q}_{q_x}(\tau)]\right)\psi_{q_x}(x), \tag{3.17}$$

where ψ_{q_x} is the ground Bloch state and $\tilde{q}_{q_x}(t)$ is the time-dependent wave number satisfying the semiclassical equation $\hbar[d\tilde{q}_{q_x}(t)/dt] = F(t)$, namely, $\tilde{q}_{q_x}(t) = q_x + (K_0/a_\ell)\sin(\omega_s t + \phi)$. The wavefunctions (3.17) are also known as accelerated Bloch states [164, 165], and are valid for any type of uniform forcing $F(t)$ [160]. The dependence of $\tilde{\psi}_{q_x}$ on time t and modulation strength K_0 is contained in the exponential in Eq. (3.17). Further insight into these scalings is obtained

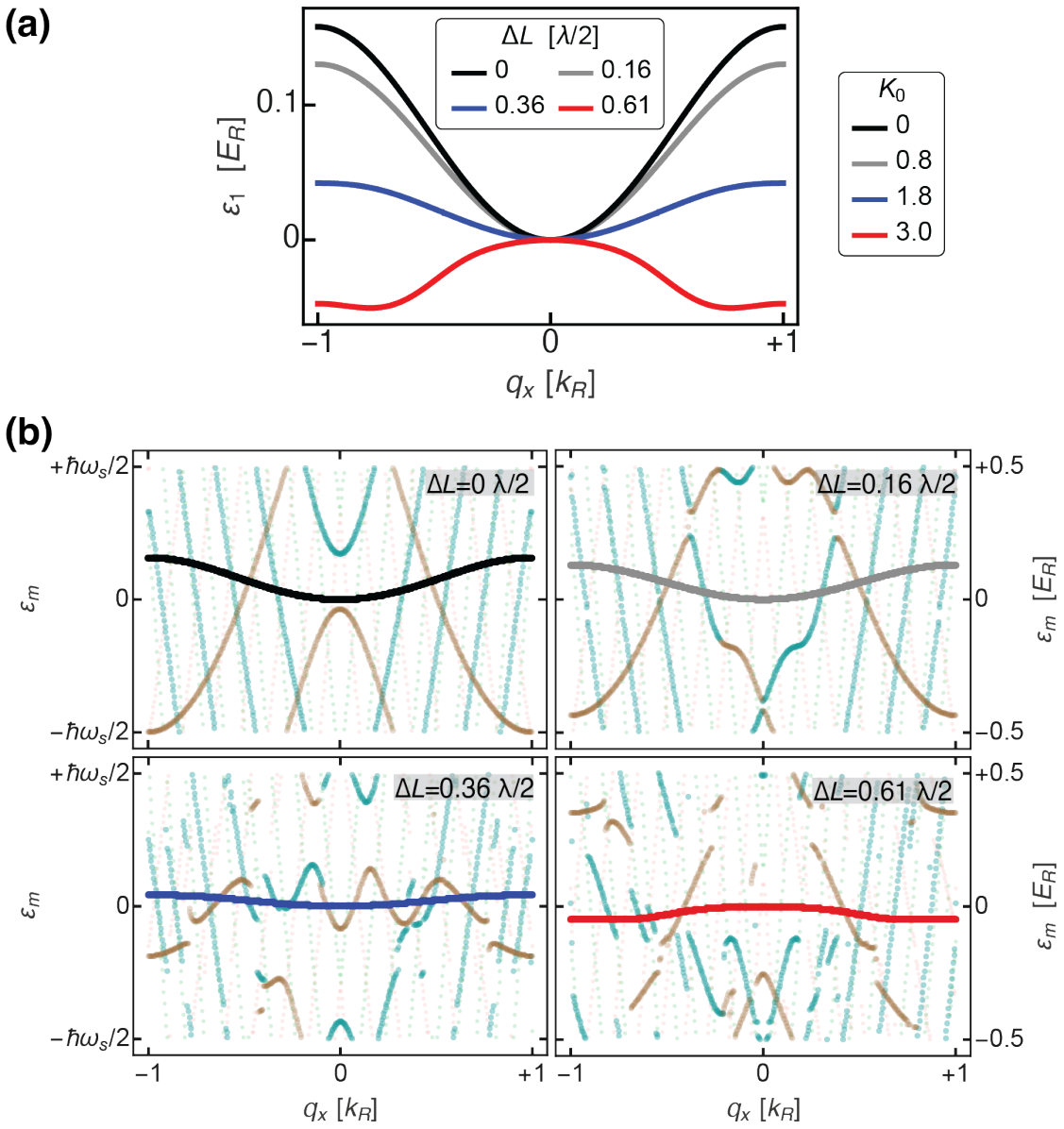

Figure 3.2: Quasienergies vs q_x for a 7 E_R one-dimensional lattice shaken at a frequency $\omega_s = 1\ E_R/\hbar$. (a) Quasienergy ε_1 for different values of the modulation amplitude ΔL (corresponding values of K_0 are also indicated in the figure). These quasienergies form a band whose width is first reduced and then gets inverted as ΔL grows. (b) Quasienergies ε_m plotted within a Floquet Brillouin zone $[-\hbar\omega_s/2, +\hbar\omega_s/2]$ for $1 \leq m \leq 5$. Thickest lines correspond to ε_1, cyan and brown lines indicate $\varepsilon_{2,3}$, and faintest points (in the background) represent $\varepsilon_{4,5}$.

by using the Jacobi-Anger expansion

$$E_1[\tilde{q}_{q_x}(\tau)] \approx -2J\cos[\tilde{q}_{q_x}(\tau)a_\ell] = \\ = -2J\left\{\cos(q_x a_\ell)\left[\mathcal{J}_0(K_0) + \sum_{p=1}^{+\infty} 2\mathcal{J}_{2p}\left(K_0\right)\cos(2p\omega_s\tau)\right]\right. \\ \left. - \sin(q_x a_\ell)\sum_{p=1}^{+\infty} 2\mathcal{J}_{2p-1}\left(K_0\right)\cos[(2p-1)\omega_s\tau]\right\}, \tag{3.18}$$

where $\mathcal{J}_n$ is the n-th Bessel function of the first kind. The accelerated Bloch state then takes the form

$$\tilde{\psi}_{q_x}(x,t) = \exp\left\{-\frac{i}{\hbar}\left[-2J\mathcal{J}_0(K_0)\cos\left(q_x a_\ell\right)\right]t\right\}\times \\ \times\exp\left\{+\frac{i}{\hbar}2J\cos(q_x a_\ell)\sum_{p=1}^{\infty}\frac{1}{p\omega_s}\mathcal{J}_{2p}(K_0)\sin(2p\omega_s t)\right\}\times \\ \times\exp\left\{+\frac{i}{\hbar}2J\sin(q_x a_\ell)\sum_{p=1}^{\infty}\frac{2}{(2p-1)\omega_s}\mathcal{J}_{2p-1}(K_0)\sin[(2p-1)\omega_s t]\right\}\times\psi_{q_x}(x). \tag{3.19}$$

It follows from this expression that the quasienergy ε_1, effectively inducing a net increment in the phase of the wavefunction $\tilde{\psi}_{q_x}$ following a single period T_s of the drive, is approximated by [164]

$$\varepsilon_1(q_x) \approx \frac{1}{T_s}\int_0^{T_s} d\tau E_1(\tilde{q}_{q_x}(t)) = -2J\mathcal{J}_0(K_0)\cos(q_x a_\ell). \tag{3.20}$$

The last relation lends itself to the graphical interpretation illustrated in Fig. 3.3 whereby ε_1 is the time-averaged energy of a wavepacket whose quasimomentum oscillates as $\tilde{q}_{q_x}(t)$. The width of the band ε_1, whose change was illustrated in Fig. 3.2, is then set by the scale factor $\mathcal{J}_0(K_0)$.

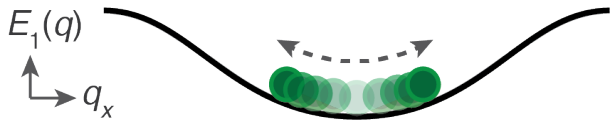

Figure 3.3: The time average of $E_1(\tilde{q}_{q_x}(t))$ for a wavepacket with time-varying quasimomentum $\tilde{q}_{q_x}(t)$ [see equation (3.20)] constitutes a good approximation to the ground-like quasienergy $\varepsilon_1(q_x)$ for a particle in a shaken lattice when the modulation frequency is assumed to be much smaller than the separation between E_1 and the higher bands.

At moderate values of the strength K_0, it is reasonable to neglect Bessel functions of order higher than 2, and the expression (3.19) for the Houston state is then approximated by

$$\begin{aligned}\tilde{\psi}_{q_x}(x,t) \approx \exp\left\{-\frac{i}{\hbar}\varepsilon_1(q_x)t\right\} \times \\ \times \exp\left\{+i\frac{2J}{\hbar\omega_s}\cos(q_x a_\ell)\mathcal{J}_2(K_0)\sin(2\omega_s t)\right\} \times \\ \times \exp\left\{+i\frac{2J}{\hbar\omega_s}\sin(q_x a_\ell)2\mathcal{J}_1(K_0)\sin(\omega_s t)\right\} \times \psi_{q_x}(x)\end{aligned} \tag{3.21}$$

$$\begin{aligned}\tilde{\psi}_{q_x}(x,t) \approx \exp\left\{-\frac{i}{\hbar}\varepsilon_1(q_x)t\right\} \times \\ \times \left[\mathcal{J}_0\left(\frac{2J}{\hbar\omega_s}\cos(q_x a_\ell)\mathcal{J}_2(K_0)\right) + 2i\mathcal{J}_1\left(\frac{2J}{\hbar\omega_s}\cos(q_x a_\ell)\mathcal{J}_2(K_0)\right)\sin(2\omega_s t)\right] \times \\ \times \left[\mathcal{J}_0\left(\frac{2J}{\hbar\omega_s}\sin(q_x a_\ell)2\mathcal{J}_1(K_0)\right) + 2i\mathcal{J}_1\left(\frac{2J}{\hbar\omega_s}\sin(q_x a_\ell)2\mathcal{J}_1(K_0)\right)\sin(\omega_s t)\right] \times \\ \times \psi_{q_x=0}(x),\end{aligned} \tag{3.22}$$

where the Jacobi-Anger expansion has been used again, keeping only its terms up to order 1 since it is assumed J is small compared to $\hbar\omega_s$. The approximation (3.20) has also been used in

Eq. (3.21) to insert ε_1 in the first exponential.

As it will become relevant later in the discussion of parametric instabilities, special attention is given to the form of the Houston states at $q_x = 0$ and $q_x = \pm k$:

- At $q_x = 0$, where the band ε_1 has a minimum for moderate values of the strength K_0 (making this quasimomentum relevant for experiments), only terms with even order Bessel functions appear in Eq. (3.21), and the accelerated Bloch state is

$$\tilde{\psi}_{q_x=0}(x,t) \approx \exp\left\{-\frac{i}{\hbar}\varepsilon_1(q_x=0)t\right\} \times \\ \times \left[\mathcal{J}_0\left(\frac{2J}{\hbar\omega_s}\mathcal{J}_2(K_0)\right) + 2i\mathcal{J}_1\left(\frac{2J}{\hbar\omega_s}\mathcal{J}_2(K_0)\right)\sin(2\omega_s t)\right]\psi_{q_x=0}(x). \tag{3.23}$$

The time-periodic part of $\tilde{\psi}_{q_x=0}(x,t)$ [second exponential in Eq. (3.23)] has a period $T_s/2$ and, hence, only possesses even time Fourier components; this halving of the period is a consequence of the even symmetry of E_1 [as it appears in Eq. (3.17)] around $q_x = 0$. Moreover, since it is assumed $J/\omega_s \ll 1$, and $\mathcal{J}_1(\rho) \approx \rho/2$ for small ρ, one gets

$$\tilde{\psi}_{q_x=0}(x,t) \approx \exp\left\{-\frac{i}{\hbar}\varepsilon_1(q_x=0)t\right\} \times \\ \times \left[\mathcal{J}_0\left(\frac{2J}{\hbar\omega_s}\mathcal{J}_2(K_0)\right) + i\frac{2J}{\hbar\omega_s}\mathcal{J}_2(K_0)\sin(2\omega_s t)\right]\psi_{q_x=0}(x), \tag{3.24}$$

from which it follows that the amplitude of the dominating time oscillating terms in $\tilde{\psi}_{q_x=0}(x,t)$ is proportional to $J\mathcal{J}_2(K_0)/\hbar\omega_s$. Figure 3.4 shows the numerically calculated coefficients $\tilde{c}_{m=1,\alpha}(t)$ [see Eq. (3.11)] of the Floquet state $\tilde{\psi}_{q_x=0}$ corresponding to the $\varepsilon_{m=1}$ bands in Fig. (3.2). As expected from the preceding discussion on the Houston states, the

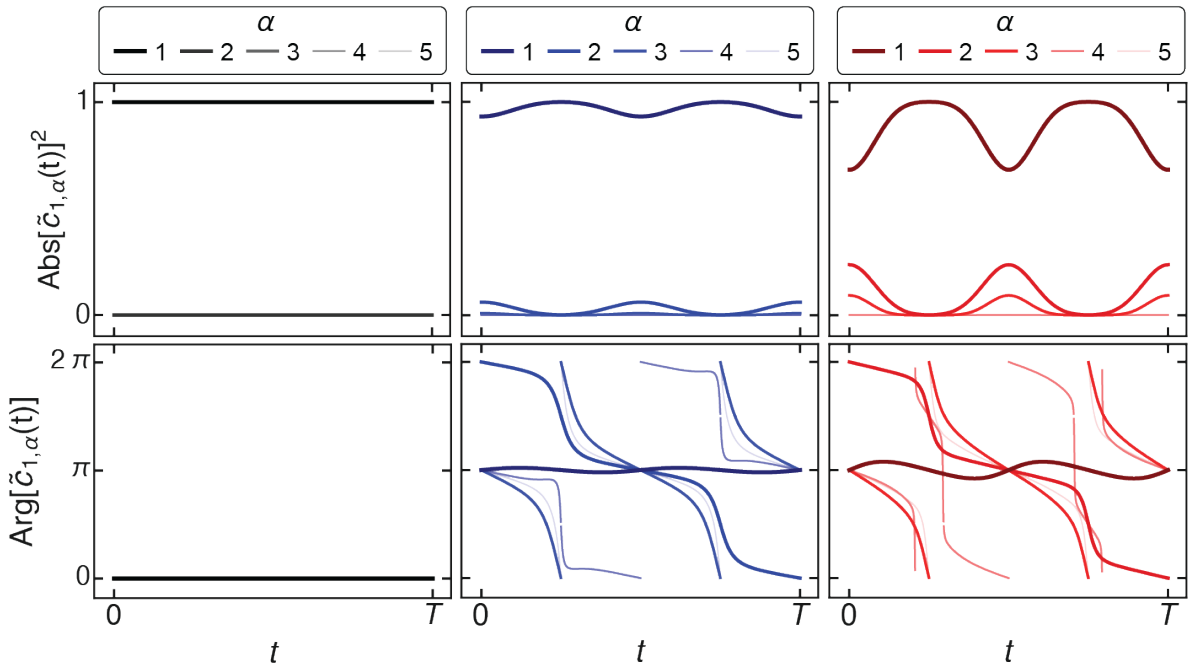

Figure 3.4: Time variation of the numerically calculated complex Floquet coefficients $\tilde{c}_{m=1,\alpha}(t)$, shown for different values of the bare band index α, see Eq. (3.11). The coefficients show here define the states at $q_x = 0\ k_R$ in the $\varepsilon_{m=1}$ bands shown in Fig. 3.2. The modulation frequency is $\omega_s = 1\ E_R/\hbar$, far from any resonance. Left, middle and right panels correspond to $\Delta L/(\lambda/2) = 0$, 0.36 and 0.61 (or, in terms of the dimensionless strength, $K_0 = 0,\ 1.8,\ 3.0$). The $\pm 1\omega$ Fourier terms of the dominating coefficient $\tilde{c}_{m=1,\alpha=1}(t)$ (darkest and thickest lines) vanish. The remaining coefficients $\tilde{c}_{m=1,\alpha\neq 1}$ grow with ΔL.

ground band coefficients $\tilde{c}_{m=1,\alpha=1}(t)$ have a period $T_s/2$.

- At *conjugate* quasimomenta $q_x = \pm k$, the Houston state (3.21) is

$$\begin{aligned}
\tilde{\psi}_{q_x=\pm k}(x,t) \approx \exp\left\{-\frac{i}{\hbar}\varepsilon_1(q_x = \pm k)t\right\} \times \\
\times \left[\mathcal{J}_0\left(\frac{2J}{\hbar\omega_s}\cos(ka_\ell)\mathcal{J}_2(K_0)\right) + 2i\mathcal{J}_1\left(\frac{2J}{\hbar\omega_s}\cos(ka_\ell)\mathcal{J}_2(K_0)\right)\sin(2\omega_s t)\right] \times \\
\times \left[\mathcal{J}_0\left(\frac{2J}{\hbar\omega_s}\sin(ka_\ell)2\mathcal{J}_1(K_0)\right) \pm 2i\mathcal{J}_1\left(\frac{2J}{\hbar\omega_s}\sin(ka_\ell)2\mathcal{J}_1(K_0)\right)\sin(\omega_s t)\right] \times \\
\times \psi_{q_x=0}(x) \approx \\
\approx \exp\left\{-\frac{i}{\hbar}\varepsilon_1(q_x = \pm k)t\right\} \times \\
\times \left[\mathcal{J}_0\left(\frac{2J}{\hbar\omega_s}\cos(ka_\ell)\mathcal{J}_2(K_0)\right) + i\frac{2J}{\hbar\omega_s}\cos(ka_\ell)\mathcal{J}_2(K_0)\sin(2\omega_s t)\right] \times \\
\times \left[\mathcal{J}_0\left(\frac{2J}{\hbar\omega_s}\sin(ka_\ell)2\mathcal{J}_1(K_0)\right) \pm i\frac{2J}{\hbar\omega_s}\sin(ka_\ell)2\mathcal{J}_1(K_0)\sin(\omega_s t)\right] \times \\
\times \psi_{q_x=0}(x), \qquad (3.25)
\end{aligned}$$

where the odd parity of $\mathcal{J}_1$ and the approximation $\mathcal{J}_1(\rho) \approx \rho/2$ have been used.

Near-resonance shaking

As a second example, ω_s is taken to be $5.2\ E_R/\hbar$, a frequency lying near the separation between E_1 and E_2, as indicated by the dashed line in Fig. 3.1. The proximity of the excited band causes ε_1 to display a double-well shape [see Fig. 3.5(a)], a feature that has been used in experiments to simulate domain formation in an effective ferromagnetic system [43], and to generate a roton-maxon excitation spectrum [166].

If ΔL is relatively small, the form of ε_1 in this second example is heavily determined by the coupling between the ground and first-excited states, while the effects due to higher bands can

be neglected. It is then reasonable to use a two-band approximation, in which the Floquet states $\tilde{\psi}_{m=1,q_x}$ and the time-periodic Hamiltonian $\hat{H}(t)$ are accurately represented in a basis composed solely of the (static) Bloch states $\psi_{m=1,q_x}$ and $\psi_{m=2,q_x}$. If, as is the case with shaken lattices, $\hat{H}(t)$ can be split as a sum of a static Hamiltonian $\hat{H}_{q_x,0}$ and a time-dependent part $\hat{H}'_{q_x}(t)$ having the form $\hat{H}'_{q_x}(t) = \cos(\omega_s t + \varphi)\hat{H}'_{q_x,1}$, the representation of $\hat{H}(t)$ in this two-band approximation resembles the Hamiltonian describing a two-state atom whose dipole moment interacts with linearly polarized radiation. This similarity, along with a rotating-wave approximation, leads to the following effective time-independent representation $[H_{q_x}]_{\text{Bloch}}$ of the Hamiltonian for the shaken 1D optical lattice

$$[H_{q_x}]_{\text{Bloch}} = \begin{pmatrix} E_1(q_x) & \Omega_{1,2}(q_x) \\ \Omega^*_{1,2}(q_x) & E_2(q_x) \end{pmatrix} \tag{3.26}$$

where $\Omega_{1,2}(q_x) = \frac{1}{2}e^{i\varphi}\langle\psi_{m=1,q_x}| H'_{q_x} |\psi_{m=2,q_x}\rangle$ is the effective coupling term between the lowest lying states. The eigenvalues of the matrix (3.26)

$$\varepsilon^{\text{dr}}_{\pm}(q_x) = \frac{1}{2}\left(E_1 + E_2 + \hbar\omega_s\right) \pm \frac{1}{2}\sqrt{\delta^2 + 4|\Omega_{1,2}|^2}, \tag{3.27}$$

where $\delta = E_2 - E_1 - \hbar\omega_s$ is the detuning of the modulation frequency ω_s with respect to the energy spacing $E_2(q_x) - E_1(q_x)$. The eigenvalues $\varepsilon^{\text{dr}}_{\pm}$ are known as *dressed energies*, and represent

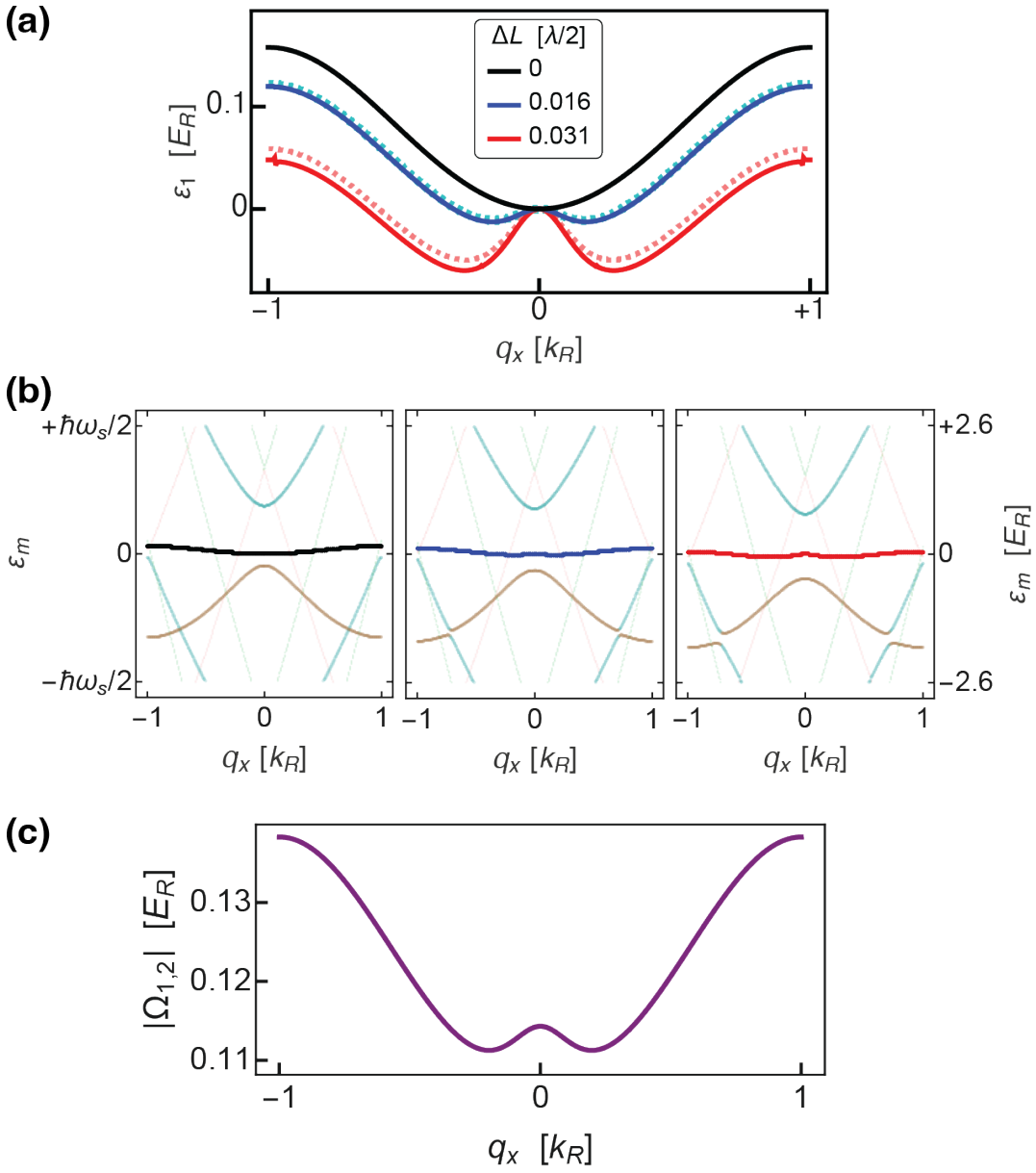

Figure 3.5: Quasienergies plotted vs q_x for a 7 E_R one-dimensional lattice shaken at a frequency $\omega_s = 5.2\ E_R/\hbar$. (a) ε_1 for different values of the modulation amplitude ΔL. Solid lines were computed using the extended Hilbert space. Dashed lines were calculated using the formulas (3.27) for $\varepsilon_{\pm}^{\mathrm{dr}}$ in the two-band approximation. (b) Quasienergies ε_m for $1 \leq m \leq 5$. Thickest lines correspond to ε_1, cyan and brown lines indicate $\varepsilon_{2,3}$, and faintest points in the background represent $\varepsilon_{4,5}$. (c) Absolute value of the effective coupling term $\Omega_{1,2}$ [see Eq. (3.26)] between ground and excited states for $\Delta L = 0.016\ \lambda/2$.

approximations to the Floquet energies ε_1 and ε_2. The eigenvectors of (3.26)

$$w_+ = \frac{1}{\sqrt{|\Omega_{1,2}|^2 + \frac{1}{4}\left(\delta + \sqrt{\delta^2 + 4|\Omega_{1,2}|^2}\right)^2}} \begin{pmatrix} \Omega_{1,2} \\ +\frac{1}{2}\delta + \frac{1}{2}\sqrt{\delta^2 + 4\Omega_{1,2}^2} \end{pmatrix} \tag{3.28}$$

$$w_- = \frac{1}{\sqrt{|\Omega_{1,2}|^2 + \frac{1}{4}\left(\delta + \sqrt{\delta^2 + 4|\Omega_{1,2}|^2}\right)^2}} \begin{pmatrix} -\frac{1}{2}\delta - \frac{1}{2}\sqrt{\delta^2 + 4\Omega_{1,2}^2} \\ \Omega_{1,2}^* \end{pmatrix} \tag{3.29}$$

approximate the Floquet modes u_1 and u_2 with their periodic time dependence (or *micromotion*) contained in the coupling term via the phase φ. Figure 3.5(a) includes the calculated values of $\varepsilon_{\pm}^{\mathrm{dr}}(q_x)$, showing the fair agreement between the full Floquet calculation and the two-band approximation for the parameters chosen in this second example. The profile of $|\Omega_{1,2}|$, whose form induces a double-well shape in ε_1, is displayed in Fig. 3.5(c).

3.2 Weakly-interacting BECs in static optical lattice

The Gross-Pitaevskii (GP) equation [167, 168] describes dilute weakly-interacting BECs at low temperatures in a mean-field approach, where all bosons are assumed to be in the same single-particle state Ψ. The time-dependent GP equation for the order parameter Ψ is [169, 170]

$$i\hbar\frac{\partial\Psi}{\partial t} = \left[-\frac{\hbar^2}{2m}\nabla_{\boldsymbol{r}}^2 + V_{\mathrm{ext}}(\boldsymbol{r}) + g\bar{n}|\Psi|^2\right]\Psi, \tag{3.30}$$

where V_{ext} is an external potential, $g = 4\pi\hbar^2 a_s/m$ is the coupling constant for the interparticle interactions and a_s denotes the s-wave scattering length (the dilute limit corresponds to a_s being much smaller than the mean interparticle separation). Although this nonlinear equa-

tion represents a simplification of the more complicated full many-body Schrödinger problem, it successfully accounts for some interaction-induced effects in BECs such as collective phonon-like excitations [171, 172], the formation of solitons [173], emergence of quantized vortices in rotating gases [174–177] and macroscopic self-trapping between BECs held in a double-well trap [178–180]. The GP equation is used in optical lattices to describe condensate fluctuations (known as dynamical instabilities) that grow exponentially in time [181–183], swallow-tail-shaped loop structures in nonlinear Bloch bands [184–187], which are responsible for nonexponential tunneling probabilities [188]. This subsection summarizes the theory related to dynamical instabilities in optical lattices.

If V_{ext} is a static lattice $V_{\text{latt}}(\boldsymbol{r})$, some stationary solutions Φ_c to the GP equation are single-momentum Bloch states of the form, $\Phi_c(\boldsymbol{r}, t; \boldsymbol{q}_c) = e^{i\boldsymbol{q}_c\cdot\boldsymbol{r} - i\mu_c t} U_c(\boldsymbol{r}; \boldsymbol{q}_c)$, with $\boldsymbol{q}_c$ denoting the condensate quasimomentum. The state Φ_c satisfies the time-independent GP equation $\left[-\frac{\hbar^2}{2m}\nabla^2_{\boldsymbol{r}} + V_{\text{latt}}(\boldsymbol{r}) + 2g\bar{n}|\Phi_c|^2\right]\Phi_c = \mu_c\Phi_c$, where μ_c represents the nonlinear eigenvalue. A linear stability analysis of the state Φ_c begins by including low-energy non-condensed excitations $\delta\phi$ in the order parameter as $\Psi = \Phi_c + \delta\phi$. Next, the perturbed Ψ is inserted into the time-dependent GP equation which, after keeping terms up to first order in $\delta\phi$, gives

$$i\hbar\frac{\partial}{\partial t}\delta\phi = \left[-\frac{\hbar^2}{2m}\nabla^2_{\boldsymbol{r}} + V_{\text{latt}}(\boldsymbol{r}) + 2g\bar{n}\left|\Phi_c\right|^2\right]\delta\phi + g\bar{n}\Phi_c^2\delta\phi^*. \tag{3.31}$$

The fluctuations $\delta\phi$ are then decomposed into modes labeled by $\boldsymbol{q}_c + \boldsymbol{k}$: $\delta\phi(\boldsymbol{r}, t; \boldsymbol{q}_c) = \sum_{\boldsymbol{k}} e^{i(\boldsymbol{q}_c+\boldsymbol{k})\cdot\boldsymbol{r}} e^{-i\mu_c t} v_{\boldsymbol{q}_c+\boldsymbol{k}}(\boldsymbol{r}, t)$, where the perturbation functions $v_{\boldsymbol{\kappa}}$ are periodic in $\boldsymbol{r}$. Using this

decomposition, one gets the linear differential equations

$$i\hbar\frac{\partial}{\partial t}\begin{pmatrix} v_{\boldsymbol{q}_c+\boldsymbol{k}} \\ \\ v^*_{\boldsymbol{q}_c-\boldsymbol{k}} \end{pmatrix} = \sigma_z M(\boldsymbol{k};\boldsymbol{q}_c)\begin{pmatrix} v_{\boldsymbol{q}_c+\boldsymbol{k}} \\ \\ v^*_{\boldsymbol{q}_c-\boldsymbol{k}} \end{pmatrix}, \tag{3.32}$$

with

$$\sigma_z = \begin{pmatrix} 1 & 0 \\ \\ 0 & -1 \end{pmatrix}, \quad M(\boldsymbol{k};\boldsymbol{q}_c) = \begin{pmatrix} \hat{h}_{\boldsymbol{q}_c+\boldsymbol{k}} & g\bar{n}U_c^2 \\ \\ g\bar{n}U_c^{*2} & \hat{h}_{\boldsymbol{q}_c-\boldsymbol{k}} \end{pmatrix}, \tag{3.33}$$

where $\hat{h}_{\boldsymbol{\kappa}} = \frac{\hbar^2}{2m}\left(\boldsymbol{\kappa} - i\nabla_{\boldsymbol{r}}\right)^2 + V_{\text{latt}} - \mu_c + 2g\bar{n}\left|\Phi_c\right|^2$.

The presence of exponentionally growing perturbations around Φ_c, known as dynamical instabilities is inferred from the eigenvalues $\lambda_{\boldsymbol{q}_c}(\boldsymbol{k})$ of the operator $\sigma_z M(\boldsymbol{k};\boldsymbol{q}_c)$. Purely real eigenvalues represent the phonon spectrum of oscillatory modes [181]. In this case, half of the eigenvectors (or modes) $V_{\boldsymbol{k}}$, representing the phonon modes, satisfy the skew normalization condition $V_{\boldsymbol{k}}^\dagger \sigma_z V_{\boldsymbol{k}} = +1$, while the other half, referred to as anti-phonon mode (and providing no more information than already given by the phonon modes), meets the similar condition $V_{\boldsymbol{k}}^\dagger \sigma_z V_{\boldsymbol{k}} = +1$. On the other hand, a complex eigenvalue $\lambda_{\boldsymbol{q}_c}(\boldsymbol{k})$ indicates the corresponding mode is unstable and has an exponential growth rate proportional to $\text{Im}[\lambda_{\boldsymbol{q}_c}]$. Since the $\sigma_z M(\boldsymbol{k};\boldsymbol{q}_c)$ is non-Hermitian and real, the complex eigenvalues always appear in conjugate pairs [181] and, hence, a decaying mode is always accompanied by a growing one.

The dynamical instabilities are closely related to the shape of the energy bands in optical lattices, and are absent if a BEC is in free space. For example, when a mean-field state is a local minimum of the energy dispersion, all eigenvalues $\lambda_{\boldsymbol{q}_c}(\boldsymbol{k})$ are real and collective excita-

tions cause an energy increase, which dynamically stabilizes the state Φ_c against fluctuations. Figure 3.6 shows the calculated $\lambda_{q_{c,x}}$ spectra (only phonon modes) for four different condensate quasimomenta $q_{c,x}$ using a 1D lattice with interaction coupling $g\bar{n} = 0.03\ E_R$. Unstable modes appear in the region $q_{c,x} > 0.5\ k_R$, where the band curvature is concave. No unstable modes are present when the band is convex ($q_{c,x} < 0.5\ k_R$).

3.3 Weakly-interacting BECs in periodically modulated optical lattice

3.3.1 GP equation with a time-periodic lattice

This subsection considers the GP equation when the lattice $V_{\text{latt}}(\boldsymbol{r}, t)$ is time-periodic with period T. Technically, Floquet theorem only holds for linear differential equations, so we should expect attempts to apply Floquet theory to the non-linear, time-periodic GP equation to fail. One sign of this failur is the appearance of imaginary values of λ. A single-momentum ansatz $\tilde{\Phi}_c$ has the Floquet-Bloch form

$$\tilde{\Phi}_c(\boldsymbol{r}, t; \boldsymbol{q}_c) = e^{i\boldsymbol{q}_c\cdot\boldsymbol{r} - i\mu_c t/\hbar} u_c(\boldsymbol{r}, t; \boldsymbol{q}_c), \tag{3.34}$$

where the mode u_c is $\mathcal{B}$- and T- periodic for any value of the condensate momentum $\boldsymbol{q}_c$. Inserting $\tilde{\Phi}_c$ into the GP equation gives

$$i\hbar\frac{\partial}{\partial t}\left(e^{-i\mu_c t}u_c\right) = \left[\frac{\hbar^2}{2m}\left(\boldsymbol{q}_c - i\nabla_{\boldsymbol{r}}\right)^2 + \left(V_{\text{latt}}(\boldsymbol{r}, t) + g\bar{n}|u_c|^2\right)\right]\left(e^{-i\mu_c t}u_c\right). \tag{3.35}$$

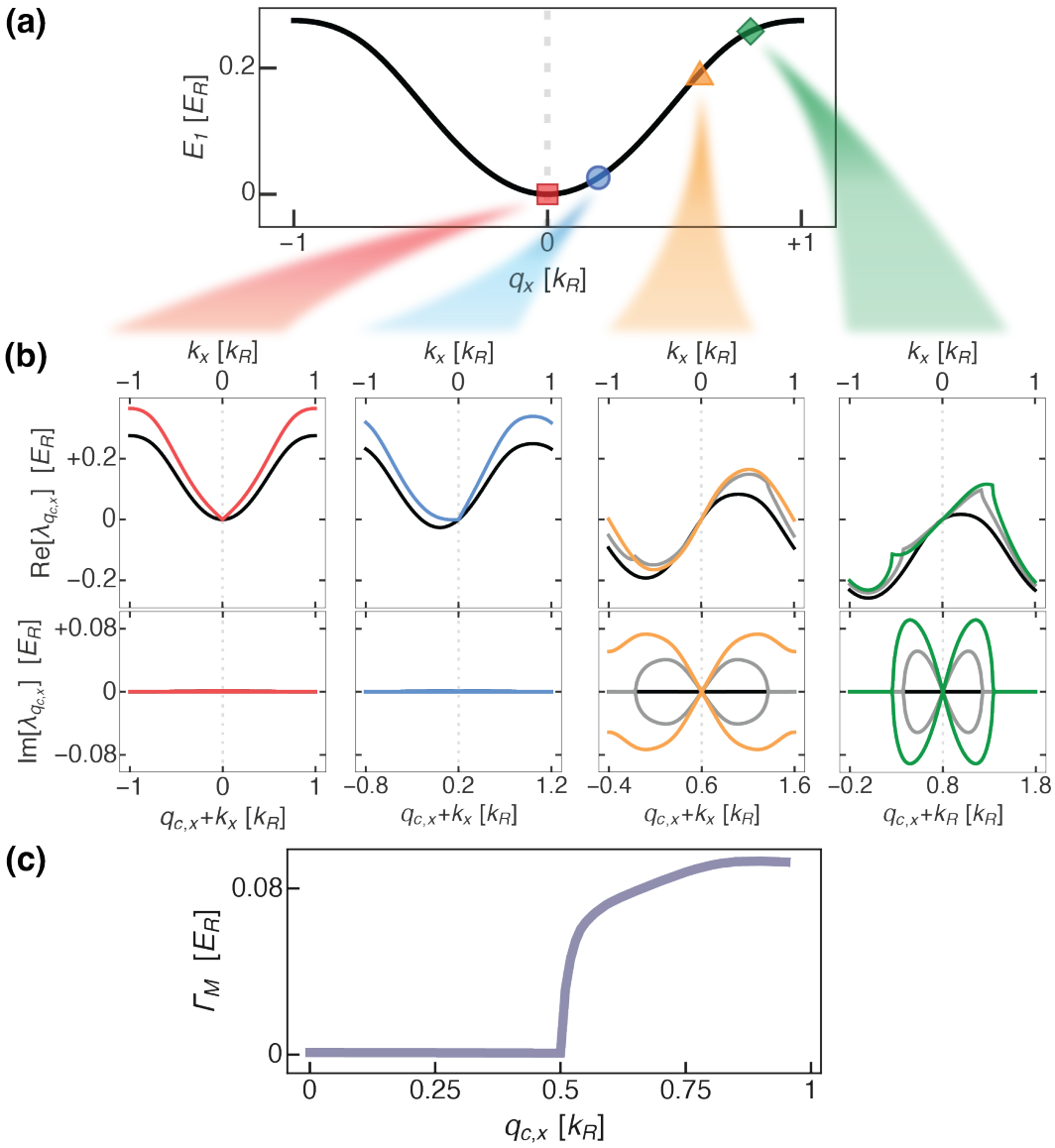

Figure 3.6: Dynamical instabilities in the lowest energy band of a 1D lattice with a 6 E_R depth. (a) Ground band E_1 of a 1D lattice. Square, circle, trangle and diamond markers correspond to quasimomenta 0, 0.2, 0.6 and 0.8 k_R. (b) Real (top) and imaginary (bottom) parts of calculated eigenvalues $\lambda_{q_{c,x}}$ of the matrix $\sigma_z M(k_x; q_{c,x})$ plotted as a function of k_x. Only phonon modes are presented for the real parts. The imaginary parts include both values from the conjugate pairs. From left to right, condensate quasimomentum $q_{c,x}$ is 0, 0.2, 0.6 and 0.8 k_R. The interaction coupling term is $g\bar{n} = 0.03\ E_R$ for all colored lines. Gray lines in the two rightmost panels were obtained with $g\bar{n} = 0.015\ E_R$. Black lines correspond to $g\bar{n} = 0\ E_R$. (c) Maximum value Γ_M (for a fixed $q_{c,x}$) of the imaginary part of $\lambda_{q_{c,x}}(k_x)$, plotted as a function of the condensate quansimomentum $q_{c,x}$. No unstable modes appear if $q_{c,x} < 0.5\ k_R$.

Since the sum $\tilde{V}_{\text{latt}}(u_c) = V_{\text{latt}} + g\bar{n}|u_c|^2$ acts as an effective lattice in Eq. (3.35), a simple numerical method to solve this nonlinear differential equation for $e^{-i\mu_c t}u_c$ is a fixed-point iterative method whereby the $(n+1)$-th order of the iteration $\left(e^{-i\mu_c^{[n+1]}t}u_c^{[n+1]}\right)$ is obtained from the n-th order result $\left(e^{-i\mu_c^{[n]}t}u_c^{[n]}\right)$ by solving the linear Schrödinger equation with the potential $\tilde{V}_{\text{latt}}\left(u_c^{[n]}\right)$

$$i\hbar\frac{\partial}{\partial t}\left(e^{-i\mu_{\boldsymbol{q}_c}^{[n+1]}t}u_c^{[n+1]}\right) = \left[\frac{\hbar^2}{2m}\left(\boldsymbol{q}_c - i\nabla_{\boldsymbol{r}}\right)^2 + V_{\text{latt}} + g\bar{n}\left|u_c^{[n]}\right|^2\right]\left(e^{-i\mu_{\boldsymbol{q}_c}^{[n+1]}t}u_c^{[n+1]}\right). \tag{3.36}$$

One advantage of this approach is that the techniques applicable to solve the single-particle Schrödinger equation with time-periodic V_{latt}, like those described in the subsection 3.1.2, can be readily adapted to include the nonlinear term $g\bar{n}|u_c|^2$.

A different technique, along the lines of the method outlined in the subsubsection 3.1.2, expands the Floquet mode u_c over the extended basis $\mathcal{R}\otimes\mathcal{T}$, where $\mathcal{R} = \{\rho_{m'}(\boldsymbol{r};\boldsymbol{q}_c)\}$ is a basis for the space of spatially $\mathcal{B}$-periodic functions and $\mathcal{T} = \{e^{im''(2\pi/T)t}|m'' \in \mathbb{Z}\}$ is the Fourier basis for time periodic functions with periodic T. $\mathcal{R}$ could, for example, be the set of plane waves $\{e^{i\boldsymbol{\mathcal{Q}}\cdot\boldsymbol{r}}|\boldsymbol{\mathcal{Q}} \in \tilde{\mathcal{B}}\}$, or it might also be the set of Bloch modes at $\boldsymbol{q_c}$ corresponding to the unmodulated lattice. Over a finite subset of M' and M'' elements from $\mathcal{R}$ and $\mathcal{T}$, respectively, the expansion of u_c is

$$u_c(\boldsymbol{r},t;\boldsymbol{q}_c) = \sum_{m'=1}^{M'}\sum_{m''=1}^{M''} c_{m',m''} \times \left[\rho_{m'}(\boldsymbol{r};\boldsymbol{q}_c)\, e^{im''\frac{2\pi}{T}t}\right],$$

with indeterminate coefficients $c_{m',m''}$. Inserting this expansion into Eq. (3.35), followed by grouping and equating those terms corresponding to the same harmonics (i.e., the same product $\rho_{m'}(\boldsymbol{r};\boldsymbol{q}_c)\, e^{im''\frac{2\pi}{T}t}$), yields a set of $M'\times M''$ nonlinear polynomial equations whose $(M'\times M'')+1$

unknowns are the coefficients $c_{m',m''}$ and $\mu_{\boldsymbol{q}_c}$ (an additional constraint being the normalization condition $\|u_c\| = 1$).

3.3.2 Floquet-BdG equations (stability of the mean-field solution)

The linear stability of the calculated $\tilde{\Phi}_c(\boldsymbol{r}, t; \boldsymbol{q}_c)$ is assessed, as was done in the subsection 3.2, by adding fluctuations $\delta\tilde{\varphi}$ on top of $\tilde{\Phi}_c$. These perturbations are expanded as $\delta\tilde{\varphi}(\boldsymbol{r}, t; \boldsymbol{q}_c) = \sum_{\boldsymbol{k}} e^{+i(\boldsymbol{q}_c+\boldsymbol{k})\cdot\boldsymbol{r}} e^{-i\mu_c t/\hbar}\, w_{\boldsymbol{q}_c+\boldsymbol{k}}(\boldsymbol{r}, t)$, with $\boldsymbol{q}_c + \boldsymbol{k}$ indicating the quasimomentum of the excitation and the functions $w_{\boldsymbol{\kappa}}(\boldsymbol{r}, t)$ being $\mathcal{B}$-periodic. Inserting the perturbed order parameter $\tilde{\Phi}_c + \delta\tilde{\varphi}$ into the GP equation, keeping terms up to first order in the perturbation, yields

$$i\hbar\frac{\partial}{\partial t} w_{\boldsymbol{q}_c+\boldsymbol{k}}(\boldsymbol{r}, t) = \left[\frac{\hbar^2}{2m}\left(\boldsymbol{q}_c + \boldsymbol{k} - i\nabla_{\boldsymbol{r}}\right)^2 + V_{\text{latt}}(\boldsymbol{r}, t) - \mu_c + 2g\bar{n}|u_c|^2\right] w_{\boldsymbol{q}_c+\boldsymbol{k}}(\boldsymbol{r}, t) + \\ + g\bar{n}\, u_c^2\, w^*_{\boldsymbol{q}_c-\boldsymbol{k}}(\boldsymbol{r}, t), \quad (3.37)$$

with a similar equation for $w^*_{\boldsymbol{q}_c-\boldsymbol{k}}(\boldsymbol{r}, t)$, leading to the Floquet-BdG equations

$$i\hbar\frac{\partial}{\partial t}\begin{pmatrix} w_{\boldsymbol{q}_c+\boldsymbol{k}} \\ w^*_{\boldsymbol{q}_c-\boldsymbol{k}} \end{pmatrix} = \begin{pmatrix} \hat{h}_{\boldsymbol{q}_c+\boldsymbol{k}} & g\bar{n}u_c^2 \\ -g\bar{n}u_c^{*2} & -\hat{h}_{\boldsymbol{q}_c-\boldsymbol{k}} \end{pmatrix}\begin{pmatrix} w_{\boldsymbol{q}_c+\boldsymbol{k}} \\ w^*_{\boldsymbol{q}_c-\boldsymbol{k}} \end{pmatrix}, \quad (3.38)$$

where $\hat{h}_{\boldsymbol{\kappa}}(\boldsymbol{r}, t) = \frac{\hbar^2}{2m}\left(\boldsymbol{\kappa} - i\nabla_{\boldsymbol{r}}\right)^2 + V_{\text{latt}}(\boldsymbol{r}, t) - \mu_c + 2g\bar{n}|u_c(\boldsymbol{r}, t; \boldsymbol{q}_c)|^2$. To numerically solve Eqs. (3.38), the $\mathcal{B}$-periodic time-dependent functions $w_{\boldsymbol{\kappa}}(\boldsymbol{r}, t)$ are expressed as a linear combination of N' orthogonal states $\{\rho_{m'}(\boldsymbol{r}; \boldsymbol{\kappa})\}$ in a, possibly $\boldsymbol{\kappa}$-dependent, $\mathcal{R}$ basis for spatially periodic functions $w_{\boldsymbol{\kappa}}(\boldsymbol{r}, t) = \sum_{m''=1}^{N'} d_{m''}(t; \boldsymbol{\kappa})\rho_{m''}(\boldsymbol{r}; \boldsymbol{\kappa})$. In terms of the coefficients $d_{m'}$, the

BdG equations (3.38) turn into $2 \times N'$ linear differential equations

$$
\begin{aligned}
& i\hbar \frac{\partial}{\partial t} d_{m'}(t; \boldsymbol{q}_c + \boldsymbol{k}) = \\
& = \sum_{m''=1}^{N'} \left[\frac{1}{V_{\mathrm{BZ}}} \int d\boldsymbol{r}\, \rho^*_{m'}(\boldsymbol{r}; \boldsymbol{q}_c + \boldsymbol{k})\, \hat{h}_{\boldsymbol{q}_c + \boldsymbol{k}}(\boldsymbol{r}, t)\, \rho_{m''}(\boldsymbol{r}; \boldsymbol{q}_c + \boldsymbol{k}) \right] d_{m''}(t; \boldsymbol{q}_c + \boldsymbol{k}) + \\
& \quad + g\bar{n} \sum_{m''=1}^{N'} \left[\frac{1}{V_{\mathrm{BZ}}} \int d\boldsymbol{r}\, \rho^*_{m'}(\boldsymbol{r}; \boldsymbol{q}_c + \boldsymbol{k})\, u_c^2(\boldsymbol{r}, t; \boldsymbol{q}_c)\, \rho^*_{m''}(\boldsymbol{r}; \boldsymbol{q}_c - \boldsymbol{k}) \right] d^*_{m''}(t; \boldsymbol{q}_c - \boldsymbol{k}),
\end{aligned}
\tag{3.39}
$$

$$
\begin{aligned}
& i\hbar \frac{\partial}{\partial t} d^*_{m'}(t; \boldsymbol{q}_c - \boldsymbol{k}) = \\
& = - \sum_{m''=1}^{N'} \left[\frac{1}{V_{\mathrm{BZ}}} \int d\boldsymbol{r}\, \rho^*_{m'}(\boldsymbol{r}; \boldsymbol{q}_c + \boldsymbol{k})\, \hat{h}_{\boldsymbol{q}_c + \boldsymbol{k}}(\boldsymbol{r}, t)\, \rho_{m''}(\boldsymbol{r}; \boldsymbol{q}_c + \boldsymbol{k}) \right] d_{m''}(t; \boldsymbol{q}_c + \boldsymbol{k}) + \\
& \quad - g\bar{n} \sum_{m''=1}^{N'} \left[\frac{1}{V_{\mathrm{BZ}}} \int d\boldsymbol{r}\, \rho^*_{m'}(\boldsymbol{r}; \boldsymbol{q}_c + \boldsymbol{k})\, u_c^2(\boldsymbol{r}, t; \boldsymbol{q}_c)\, \rho^*_{m''}(\boldsymbol{r}; \boldsymbol{q}_c - \boldsymbol{k}) \right] d^*_{m''}(t; \boldsymbol{q}_c - \boldsymbol{k}),
\end{aligned}
\tag{3.40}
$$

where V_{BZ} is the *volume* (or area) of the Brillouin zone. The results from Floquet's theorem [138] apply to this set of equations as all coefficients appearing in them are time-periodic. The Lyapunov exponents $\gamma_{\boldsymbol{k}} = \mathrm{Im}(\lambda_{\boldsymbol{k}})$ are calculated from the eigenvalues $e^{-i\lambda_{\boldsymbol{k}} T/\hbar}$ of the propagator, which is determined by time-evolving the equations over a single period of the drive (at fixed values of $\boldsymbol{q}_c$ and $\boldsymbol{k}$). A nonzero $\gamma_{\boldsymbol{k}}$ implies the collective mode with momentum $\boldsymbol{q}_c + \boldsymbol{k}$ is unstable.

3.3.2.1 Single-band approximation of the Floquet-BdG equations

If only the modes related to the macroscopically occupied Floquet band are expected to be relevant (as would be the case, for example, if the coupling with the other bands is weak), it is reasonable to make a single-band approximation of the BdG equations. In this approximation,

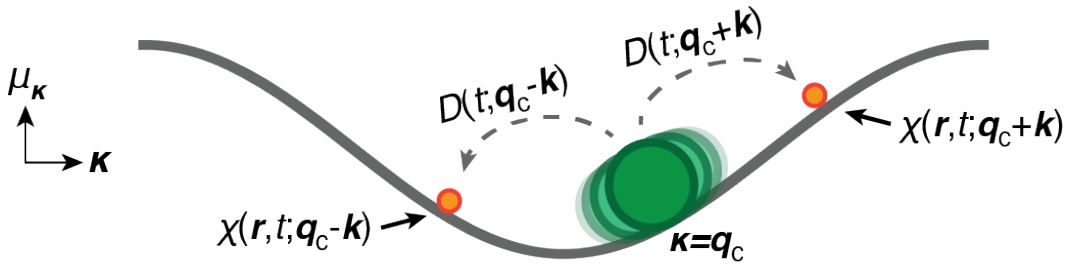

Figure 3.7: Sketch of the single-band approximation to the BdG equations, wherein the BEC fluctuations (represented by the Floquet modes χ) are restricted to the macroscopically occupied band $\mu_{\boldsymbol{\kappa}}$. The coefficients D determine the rate of growth of the unstable modes.

the functions $w_{\boldsymbol{\kappa}}$ in Eqs. (3.37) are expressed as $w_{\boldsymbol{\kappa}}(\boldsymbol{r},t) = D(t;\boldsymbol{\kappa})\chi(\boldsymbol{r},t;\boldsymbol{\kappa})$ where χ is the Floquet mode satisfying the Schrödinger equation with $\tilde{V}_{\text{latt}}\left(u_c(\boldsymbol{r},t;\boldsymbol{q}_c)\right)$ as the potential

$$\mu_{\boldsymbol{\kappa}}\chi(\boldsymbol{r},t;\boldsymbol{\kappa}) + i\hbar\frac{\partial}{\partial t}\chi(\boldsymbol{r},t;\boldsymbol{\kappa}) = \left[\frac{\hbar^2}{2m}(\boldsymbol{\kappa} - i\nabla_{\boldsymbol{r}})^2 + V_{\text{latt}}(\boldsymbol{r},t) + g\bar{n}|u_c|^2\right]\chi(\boldsymbol{r},t;\boldsymbol{\kappa}). \tag{3.41}$$

Substitution of Eq. (3.41) into Eq. (3.37) gives the following pair of equations for the coefficients $D(t;\boldsymbol{q}_c+\boldsymbol{k})$ and $D(t;\boldsymbol{q}_c-\boldsymbol{k})$

$$i\hbar\frac{\partial}{\partial t}\begin{pmatrix} D(t;\boldsymbol{q}_c+\boldsymbol{k}) \\ D^*(t;\boldsymbol{q}_c-\boldsymbol{k}) \end{pmatrix} = \mathcal{M}_2(t;\boldsymbol{k},\boldsymbol{q}_c)\begin{pmatrix} D(t;\boldsymbol{q}_c+\boldsymbol{k}) \\ D^*(t;\boldsymbol{q}_c-\boldsymbol{k}) \end{pmatrix}, \tag{3.42}$$

where

$$\mathcal{M}_2(t;\boldsymbol{k},\boldsymbol{q}_c) = \begin{pmatrix} +(\mu_{\boldsymbol{q}_c+\boldsymbol{k}} - \mu_c) + A_+(t) & B(t;\boldsymbol{q}_c,\boldsymbol{k}) \\ -B^*(t;\boldsymbol{q}_c,\boldsymbol{k}) & -(\mu_{\boldsymbol{q}_c-\boldsymbol{k}} - \mu_c) - A_-(t) \end{pmatrix}, \tag{3.43}$$

and

$$A_{\pm}(t) = g\bar{n} \int d\boldsymbol{r}\, \chi^*(\boldsymbol{r}, t; \boldsymbol{q}_c \pm \boldsymbol{k}) |u_c(\boldsymbol{r}, t; \boldsymbol{q}_c)|^2 \chi(\boldsymbol{r}, t; \boldsymbol{q}_c \pm \boldsymbol{k}), \tag{3.44}$$

$$B(t; \boldsymbol{q}_c, \boldsymbol{k}) = g\bar{n} \int d\boldsymbol{r}\, \chi^*(\boldsymbol{r}, t; \boldsymbol{q}_c + \boldsymbol{k})\, u_c^2(\boldsymbol{r}, t; \boldsymbol{q}_c)\, \chi^*(\boldsymbol{r}, t; \boldsymbol{q}_c - \boldsymbol{k}). \tag{3.45}$$

3.3.3 Drive-induced (parametric) instabilities

The off-diagonal time-periodic terms $B(t; \boldsymbol{q}_c, \boldsymbol{k})$ of $\mathcal{M}_2$ in Eq. (3.43) are typically dominated by the Fourier component of order ν for some integer ν, which is determined by the time dependence of the condensate and excitation modes u_c and χ in Eq. (3.44). An effective time-independent approximation to $\mathcal{M}_2$ in the BdG equations (3.42), after moving to the $\nu\omega$ rotating frame and neglecting fast oscillating terms, is

$$\mathcal{M}_2^{[\mathrm{RWA}]} = \begin{pmatrix} +(\mu_{\boldsymbol{q}_c+\boldsymbol{k}} - \mu_c) & B_{\nu\omega}(\boldsymbol{q}_c, \boldsymbol{k}) \\ -B^*_{\nu\omega}(\boldsymbol{q}_c, \boldsymbol{k}) & -(\mu_{\boldsymbol{q}_c-\boldsymbol{k}} - \mu_c) + \hbar\,\nu\omega \end{pmatrix}, \tag{3.46}$$

where $B_{\nu\omega}$ is the Fourier coefficient of order ν of $B(t)$. The excitation spectrum is inferred from the quadratic characteristic polynomial $\mathcal{P}$ of the matrix (3.46)

$$\mathcal{P}(\eta; \boldsymbol{k}) = \{\eta - (\mu_{\boldsymbol{q}_c+\boldsymbol{k}} - \mu_c)\} \times \{\eta - [-(\mu_{\boldsymbol{q}_c-\boldsymbol{k}} - \mu_c) + \hbar\,\nu\omega]\} + |B_{\nu\omega}|^2. \tag{3.47}$$

The imaginary parts of the roots of $\mathcal{P}(\eta;\boldsymbol{k})$ determine the exponential growth rates (i.e., the Lyapunov exponents) of the unstable modes. For the polynomial $\mathcal{P}(\eta;\boldsymbol{k})$, whose discriminant is

$$\left\{ +(\mu_{\boldsymbol{q}_c+\boldsymbol{k}}-\mu_c)-[-(\mu_{\boldsymbol{q}_c-\boldsymbol{k}}-\mu_c)+\hbar\nu\omega]\right\}^2-4|B_{\nu\omega}|^2, \tag{3.48}$$

to yield roots that are not purely real, the difference between $(\mu_{\boldsymbol{q}_c+\boldsymbol{k}}-\mu_c)$ and $-(\mu_{\boldsymbol{q}_c-\boldsymbol{k}}-\mu_c)+\hbar\,\nu\omega$ should be less than $2|B_{\nu\omega}(\boldsymbol{q}_c,\boldsymbol{k})|$. The fastest growth rate Γ_{M} among all the unstable modes is approximately given by $\Gamma_{\mathrm{M}}=|B_{\nu\omega}(\boldsymbol{q}_c,\boldsymbol{k}_{\mathrm{res}})|$, i.e., the imaginary part of the roots of $\mathcal{P}$ when evaluated at the quasimomenta $\boldsymbol{k}=\pm\boldsymbol{k}_{\mathrm{res}}$ where $(\mu_{\boldsymbol{q}_c+\boldsymbol{k}_{\mathrm{res}}}-\mu_c)$ matches $-(\mu_{\boldsymbol{q}_c-\boldsymbol{k}_{\mathrm{res}}}-\mu_c)+\hbar\,\nu\omega$ (resonance condition).

Although the dynamical instabilities pertaining to BECs in static lattices (reviewed in section 3.2) are associated with the Lyapunov exponents arising from very similar dynamical equations, the unstable modes derived from the spectrum of the matrix (3.46) [or, more accurately, from the spectrum of the propagator of equations (3.42)] are fundamentally linked to an interplay between the drive and the interactions in the BEC. The replication, or Brillouin zone indeterminacy, of the Floquet bands (separated by $\hbar\omega$) becomes relevant when clarifying the origin of these unstable modes, with the latter being graphically interpreted as resonant conditions between the replicated bands. This last point is illustrated in the examples presented later in the section 3.3.3.1.

The BdG equations (3.42) describing the perturbations of a condensate in a periodically driven lattice in the single-band approximation can be mapped onto the equations describing the modes of a parametric oscillator. (This similarity was formally derived in Refs. [78, 80] for off-resonance shaken lattices using a single-band tight-binding description.) Due to this analogy,

which is further examined in the section 3.3.3.2, the instabilities in modulated lattices obeying Eqs. (3.42) have been described as *parametric instabilties*. A few properties of these instabilities in the case of off-resonance shaken lattices are presented in the section 3.3.3.3.

3.3.3.1 Graphical examples of parametric instabilities

Figure 3.8(a) shows the spectrum of Lyapunov exponents γ_{k_x} and excitation energies of a condensate in a shaken 1D lattice, calculated numerically using the propagator of Eqs. (3.42). Blue and red lines in the bottom panel correspond to phonon and anti-phonon modes, with the dashed purple lines indicating the resonance condition betwen the two replicated Floquet bands (in blue) highlighted with a higher opacity. The red anti-phonon curves, resulting from simultaneous reflections of the blue phonon curves across the k_x and k_y axes, aid in the identification of the resonance conditions. The approximate characteristic polynomials $\mathcal{P}(\eta; k_x)$ [Eq. (3.46)], for the quasimomenta indicated by the circle ($k_x = 0.38\ k_R$) and square ($k_x = 0.65\ k_R$) markers in Fig. 3.8(a), are plotted along the real axis of η in Fig. 3.8(b).

Figure 3.9 compares calculated spectra for a driven and undriven lattice, similar to the one shown in Fig. 3.8(a) but with a drive frequency $\omega_s = 0.085\ E_R/\hbar$ (half of the one in Fig. 3.8). No unstable modes are present in the undriven case. The dashed arrow lines in Fig. 3.9(a) indicate resonances between the Floquet bands that result in unstable modes caused by the even order oscillating terms in the BdG equations. The dot-dashed arrow lines point to a resonance that leads to no instabilities since odd order oscillating terms are not present in the BdG equations, as will be explained in the subsubsection 3.3.3.3.

Figure 3.10 shows the Bogoliubov spectrum as a function of k_x (along $k_y = 0$) for a

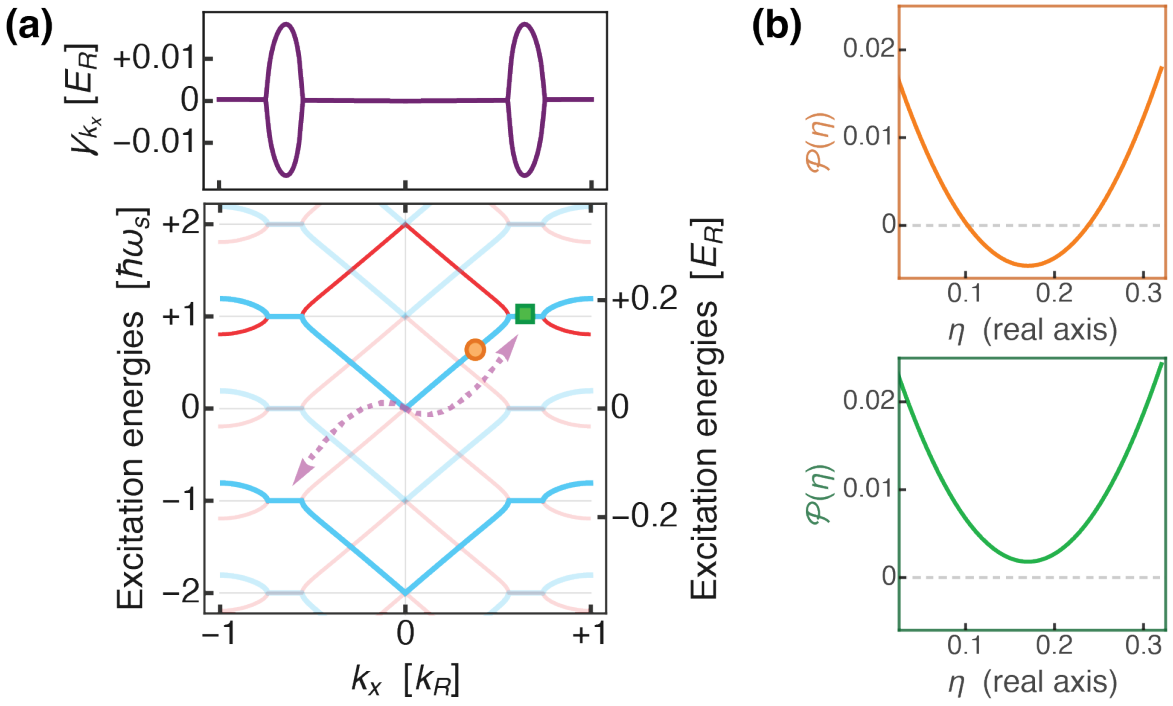

Figure 3.8: Calculated Bogoliubov excitation spectrum for a condensate with momentum $q_{c,x} = 0$ and interaction coupling $g\bar{n} = 0.1\ E_R$ in a shaken 7 E_R deep 1D optical lattice. Modulation parameters are $K_0 = 1.3, \omega_s = 0.17\ E_R/\hbar$. (a) Upper and lower panels show, respectively, the numerically calculated imaginary (Lyapunov exponents γ_{k_x}) and real (excitation energies μ_{k_x}) parts of the Floquet exponents λ_{k_x}. In the lower panel, energies of the phonon (anti-phonon) modes are indicated in blue (red). (b) Characteristic polynomial $\mathcal{P}(\eta; k_x)$ plotted versus real values of η for $k_x = 0.38\ k_R$ (top) and $k_x = 0.65\ k_R$ (bottom), corresponding to the circle and square markers in (a).

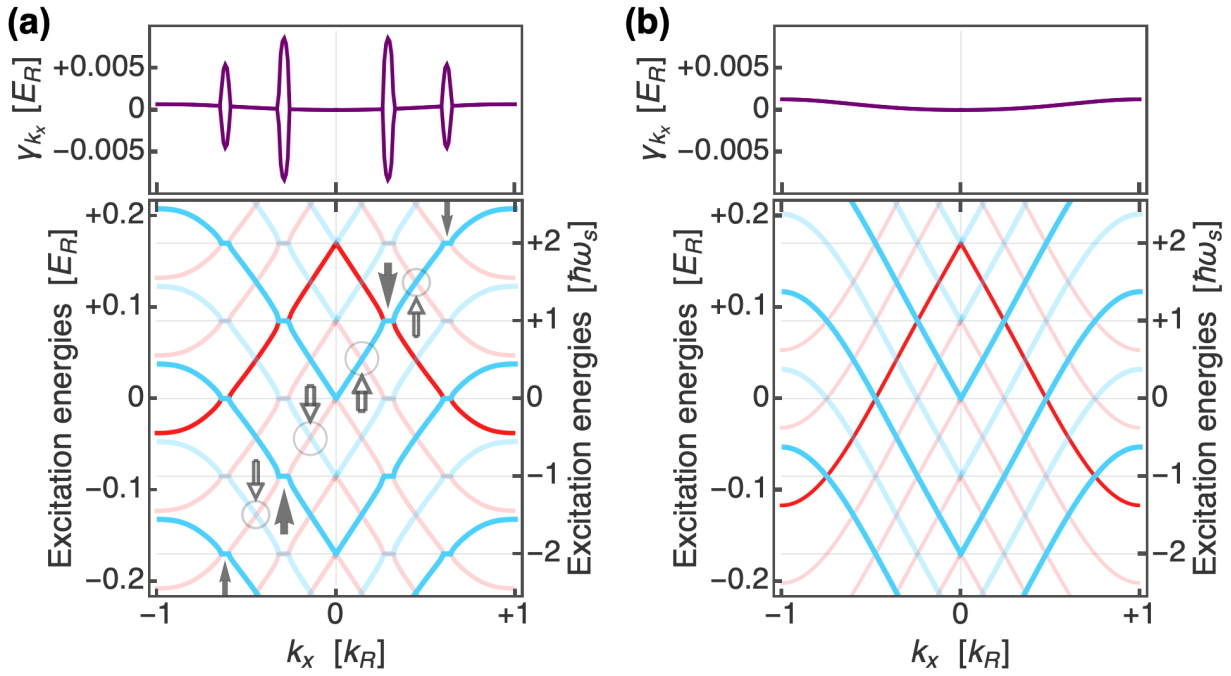

Figure 3.9: Comparison of (a) the driven and (b) the undriven Bogoliubov excitation spectra for a condensate with momentum $q_{c,x} = 0$ in a shaken 1D optical lattice. The shaking strengths are (a) $K_0 = 1.3$ and (b) $K_0 = 0$. Top and bottom panels show, respectively, the Lyapunov exponents γ_{k_x} and the excitation energies. The lattice depth is 7 E_R and the interaction coupling is $g\bar{n} = 0.1\ E_R$. Modulation frequency is $\omega_s = 0.085\ E_R/\hbar$. The width of the band is lower in the driven case (a) due to the tunneling renormalization. Filled (solid) arrows in (a) indicate resonances leading to unstable modes due to the $\pm 2\omega_s$ and $\pm 4\omega_s$ oscillating terms. Empty arrows in (a) point to the resonances (surrounded by faint circles) that do not induce instabilities since odd order oscillating terms ($\pm 1\omega_s$, $\pm 3\omega_s$, ...) are absent from the dynamical equations.

condensate with crystal momentum $\boldsymbol{q}_c = 0$ in an amplitude modulated 2D checkerboard optical lattice. In this case, all resonances (caused by oscillating terms of even and odd orders) yield unstable modes.

3.3.3.2 Relation to the parametric oscillator equation

To elaboratore more on the similarity between the FBdG equations and a simple parametric oscillator, let's recall that the latter obeys the equation

$$\frac{d^2x}{dt^2} + \omega_n^2[1 + \alpha_p \sin(\omega_p t)]x = 0, \tag{3.49}$$

where α_p and ω_p denote, respectively, the amplitude and frequency of the pump drive, and ω_n is the natural frequency of the oscillator. The presence of unstable modes in the parametric oscillator and their corresponding growth rates are determined by the discriminant $\sqrt{(\omega_p - 2\omega_n)^2 - (\alpha_p\omega_n/2)^2}$, whose imaginary values correspond to unstable modes. Similar to the condition for roots of $\mathcal{P}$ with nonzero imaginary parts, unstable parametric oscillator modes appear when two energies (ω_p and ω_n) are close to each other, and the width of this resonance is set by the strength α_p of the pump. The analogy between the instabilities in the parametric oscillators and the ones resulting from Eq. (3.42) is made clear by noting that the natural frequency of the oscillator corresponds to the separation $\Delta\mu$ between the replicated Floquet bands at the quasimomenta $\boldsymbol{q}_c \pm \boldsymbol{k}$, the pump frequency is $\nu\omega$, and the pump drive strength is set by the dominating Fourier coefficient $B_{\nu\omega}$:

$$\omega_n \leftrightarrow \Delta\mu, \quad \omega_p \leftrightarrow \nu\omega, \quad \alpha_p \leftrightarrow B_{\nu\omega}. \tag{3.50}$$

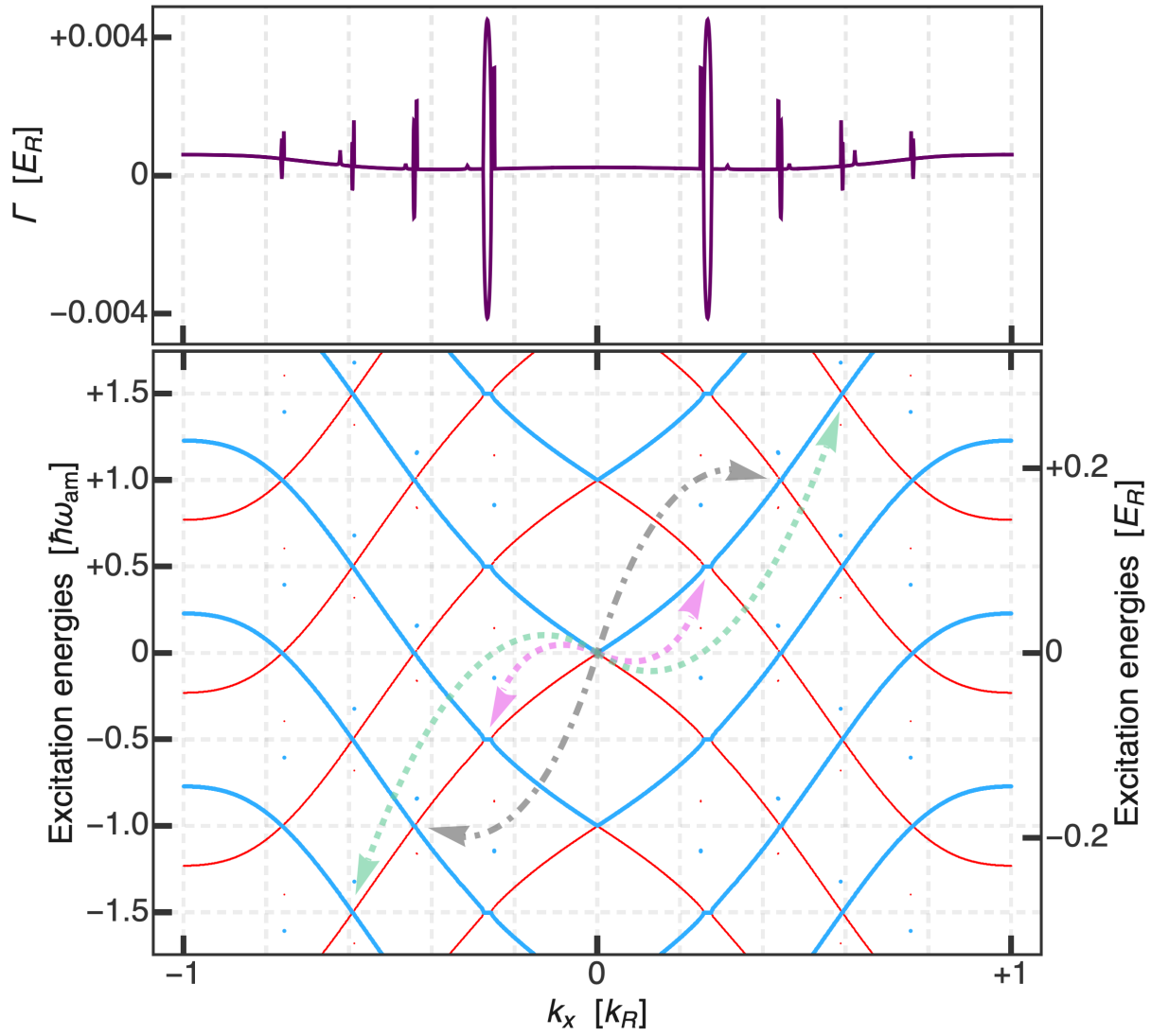

Figure 3.10: Calculated parametric instabilities along k_x for a $\boldsymbol{q}_c = 0$ condensate in an amplitude modulated checkerboard optical lattice with depth $5.9\ E_R$ and tilt $0.44\ E_R$. Frequency of the drive is $\omega_{\text{am}} = 0.19\ E_R/\hbar$. Dashed (dot-dashed) arrow lines indicate resonances associated with oscillating terms of odd (even) order. All resonances (not only those of even order) lead to unstable modes.

The resonance occurs when $n'\omega$ approaches $\Delta\mu$ and the width is set by $|B_{n'\omega}|$.

3.3.3.3 Parametric instabilities in off-resonance shaken 1D lattices

In the case of off-resonance shaken 1D lattices (discussed in a single-particle context in Section 3.1.3), further insight into the form of the off-diagonal coupling term $B(t; q_{c,x}, k_x)$ and, hence, the dynamical instabilities obtained from the spectrum of Eq. (3.46), can be gained by using Eqs. (3.24) and (3.25) as approximations to the Floquet modes u_c at $q_{c,x} = 0$ and χ at $0 \pm k_x$ [see expression Eq. (3.45) for $B(t; q_{c,x}, k_x)$]. First, since the coefficient of the $\sin(\omega_s t)$ term in Eq. (3.25) possesses opposite signs for the conjugate momenta $\pm k_x$, the first order Fourier terms (i.e., the $\pm 1\omega_s$ terms) will vanish in the expression (3.45) for $B(t)$. The dominating time oscillating terms are thus the second order Fourier components $B_{2\omega_s}$ of the term $B(t; q_{c,x} = 0, k_x)$. This explains the absence of first order resonances in the Bogoliubov spectra displayed in Figs. 3.8 and 3.9.

Collecting all the terms varying with the frequency $2\omega_s$, one gets

$$B_{2\omega_s}(q_{c,x} = 0, k_x) \sim g\bar{n} \times i\frac{2J}{\hbar\omega_s}\mathcal{J}_2(K_0)\left[1 - \cos(k_x a_\ell)\right]. \tag{3.51}$$

Using the following approximation for the effective Bogoliubov (or *acoustic*) energy spectrum

$$\mu_{0+k_x} - \mu_c = \mu_{0-k_x} - \mu_c \approx \sqrt{2J_{\text{eff}}\left(1 - \cos(k_x a_\ell)\right)\left[2J_{\text{eff}}\left(1 - \cos(k_x a_\ell)\right) + 2g\bar{n}\right]},$$

where $J_{\text{eff}} = J\mathcal{J}_0(K_0)$, the resonant quasimomentum $0 + k_{x,\text{res}}$ [defined by the resonance condi-

tion $\mu_{0+k_{x,\mathrm{res}}} - \mu_c = -(\mu_{0-k_{x,\mathrm{res}}} - \mu_c) + 2\hbar\omega_s$] has the following dependence on ω_s and $g\bar{n}$

$$1 - \cos(k_{x,\mathrm{res}} a_\ell) = \frac{1}{2J\mathcal{J}_0(K_0)} \left(\sqrt{(g\bar{n})^2 + (\hbar\omega_s)^2} - g\bar{n} \right). \tag{3.52}$$

(A requirement for this resonance condition to exist is $\sqrt{(g\bar{n})^2 + (\hbar\omega_s)^2} - g\bar{n} < 4J\mathcal{J}_0(K_0)$.) Since the maximum growth rate Γ_{M} among all the unstable modes occurs near the resonant quasimomentum [see the comments following Eq. (3.47)], one gets after inserting the expression (3.52) into Eq. (3.51)

$$\Gamma_{\mathrm{M}} = |B_{2\omega_s}(q_{c,x} = 0, k_{x,\mathrm{res}})| \sim \frac{|\mathcal{J}_2(K_0)|}{|\mathcal{J}_0(K_0)|} \left(\sqrt{(g\bar{n})^2 + (\hbar\omega_s)^2} - g\bar{n} \right) \frac{g\bar{n}}{\hbar\omega_s}, \tag{3.53}$$

which implies that Γ_M is linear in $g\bar{n}|\mathcal{J}_2(K_0)|/|\mathcal{J}_0(K_0)|$ and grows with the frequency ω_s (vanishing at $\omega_s = 0$).

The preceding analysis assumes that ω_s is small enough (or J_{eff} is large enough) to allow for the resonance condition to be met for some quasimomentum $k_{x,\mathrm{res}}$; explicitly, no unstable modes should appear when $\hbar\omega_s > \frac{1}{2}(\mu_{0+k_R} + \mu_{0-k_R} - 2\mu_c) = \sqrt{4J_{\mathrm{eff}}(4J_{\mathrm{eff}} + 2g\bar{n})}$ [see Fig. 3.11(a)]. In a more realistic description, where transverse free degrees of freedom are included, the resonance condition is always attainable by exciting modes along the tubes, as illustrated in Fig. 3.11(b). Since the shaken degree of freedom x and the unmodulated free-particle degree of freedom (denoted as $\boldsymbol{r}_\perp$) are separable, the growth rate of the unstable mode with conjugate quasimomenta $\pm\boldsymbol{k} = \pm(\boldsymbol{k}_\perp + k_x\hat{e}_x)$ is determined by the Fourier component $|B_{2\omega_s}(q_{c,x} = 0, k_x)|$ in Eq. (3.51) alone and does not depend on the projection $\boldsymbol{k}_\perp$ of $\boldsymbol{k}$ on the free degree of freedom. At a fixed frequency ω_s, $|B_{2\omega_s}(q_{c,x} = 0, k_x)|$ grows monotonically with k_x,

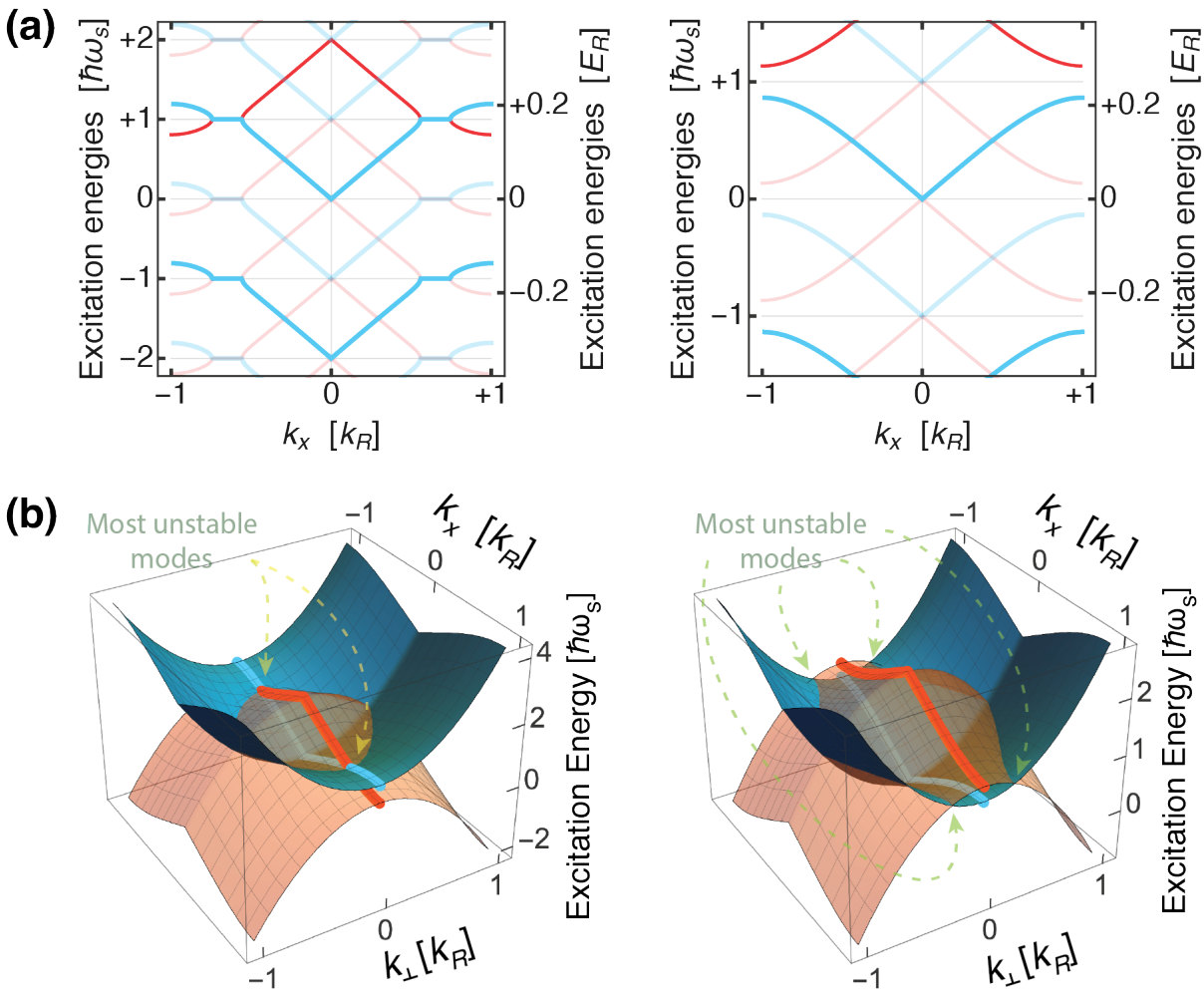

Figure 3.11: (a) One-dimensional Bogoliubov excitation energies in a shaken lattice. Left panel is the same as Fig. 3.8(a). Right panel, where no instabilities are observed, is obtained with the same parameters as the ones used for the left panel, except for the drive frequency which is increased to $\omega_s = 0.25\ E_R/\hbar$ (above the height of the effective excitation spectrum). (b) If transverse free degree of freedoms $k_\perp$ are considered, the resonance condition is always attained regardless of the value of ω_s. If $\omega_s < \sqrt{4J_{\text{eff}}(4J_{\text{eff}} + 2g\bar{n})}$ (left panel), resonant momenta with values of k_x only up to $k_{x,\text{res}}$ are possible and the fastest growing modes (indicated by the dashed arrows) are located along $k_\perp = 0$. If $\omega_s > \sqrt{4J_{\text{eff}}(4J_{\text{eff}} + 2g\bar{n})}$ (right panel), resonant momenta with all possible values of k_x within the first Brillouin zone $[-k_R, +k_R]$ are obtained. In this case, the most unstable modes are located on the edge of the Brillouin zone ($k_x = \pm k_R$).

and the fastest growing mode thus occurs at the largest value k_x where a resonant condition takes place. Hence, we have the following two regimes:

- If ω_s does not exceed the height of the effective Bogoliubov spectra [left panel in Fig. 3.11(b)], the fastest growing mode has conjugate quasimomenta with $\boldsymbol{k}_{\perp,\text{res}} = 0$ and the previous discussion ignoring transverse degrees of freedom holds. In particular, the expression (3.53) for Γ_M remains valid.

- If, on the other hand, ω_s does exceed the threshold $\sqrt{4J_{\text{eff}}(4J_{\text{eff}} + 2g\bar{n})}$ [right panel in Fig. 3.11(b)], the quasimomenta of the most unstable mode will lie on the edge of the Brillouin zone (with the largest value of k_x), namely, $\pm\boldsymbol{k}_{\text{res}} = \pm(\boldsymbol{k}_{\perp,\text{res}} \pm k_R\hat{e}_x)$. Using Eq. (3.51), the maximum growth rate is now

$$\Gamma_M = |B_{2\omega_s}(q_{c,x} = 0, k_x = \pm k_R)| = 4J\mathcal{J}_2(K_0)\frac{g\bar{n}}{\hbar\omega_s}, \tag{3.54}$$

  where $\cos(\pm k_R a_\ell) = -1$ has been used.

3.3.3.4 Parameric instabilities in an off-resonance shaken 2D square lattice

Our experimental study of parametric instabilities in shaken lattices, to be discussed in the next chapter, were carried out using a separable square lattice. In this lattice, the two-dimensional Floquet modes u_c and χ have the form

$$u_c(x, y, t; \boldsymbol{q}_c) = u_{c,X}(x, t; q_{c,x}) \times u_{c,Y}(y, t; q_{c,y}), \tag{3.55}$$

$$\chi(x, y, t; \boldsymbol{\kappa}) = \chi_X(x, t; \kappa_x) \times \chi_Y(y, t; \kappa_y), \tag{3.56}$$

with $u_{c,X}$, $u_{c,Y}$, χ_X and χ_Y representing the Floquet modes of the one-dimentional problems (discussed above in section 3.3.3.3) along x and y, respectively. The form of the B term (3.44) in this 2D separable lattice is

$$\begin{aligned} B(t;\boldsymbol{q}_c,\boldsymbol{k}) &= g\bar{n}\times\left[\frac{1}{g\bar{n}}B_X(t;q_{c,x},k_x)\right]\times\left[\frac{1}{g\bar{n}}B_Y(t;q_{c,y},k_y)\right]= \\ &= g\bar{n}\int dx\chi_X^*(x,t;q_{c,x}+k_x)u_{c,X}^2(x,t)\chi_X^*(x,t;q_{c,x}-k_x)\times \\ &\quad\times\int dy\,\chi_Y^*(y,t;q_{c,y}+k_y)u_{c,Y}^2(y,t)\chi_Y^*(y,t;q_{c,y}-k_y), \end{aligned} \tag{3.57}$$

where B_X and B_Y denote the off-diagonal terms along the separable degrees of freedom X or Y, respectively. The term B_X (B_Y) is time-independent if the lattice is static along X (Y) and would thus contribute nothing to the time oscillating terms of $B(t)$. The problem then reduces to the one-dimensional one and the equations derived in section 3.3.3.3 remain valid.

For a diagonal shake, both the spatial motion and the independent terms $B_X(t)$ and $B_Y(t)$ (whose dominant time-oscillating coefficients possess a frequency $\pm2\omega_s$) oscillate in phase and their product [and hence $B(t)$] interferes constructively. For a circular shake, the spatial motion along x and y are out of phase by $\pi/2$ causing $B_X(t)$ and $B_Y(t)$ to oscillate out of phase (i.e., with a phase difference of π). Hence, $B(t)$ in Eq. (3.57) displays a weak dependence of time when the lattice is shaken circular. The 2ω Fourier component for $B(t)$ will be

$$B_{2\omega}\approx B_{0,X}B_{Y,2\omega}+e^{i2\phi}B_{0,Y}B_{X,2\omega}, \tag{3.58}$$

where the phase ϕ captures the relative phase between the oscillations for X and Y. This implies that the most unstable modes for diagonal occurs at the points $\pm(k_R,k_R)$ and $\pm(k_R,-k_R)$ in

reciprocal space, with a growth rate given by $2|B_{2\omega,Y}|$. The dominating unstable modes for circular occurs at the points $\pm(k_R, 0)$ and $\pm(0, -k_R)$ with a rate given by $|B_{2\omega,Y}|$.

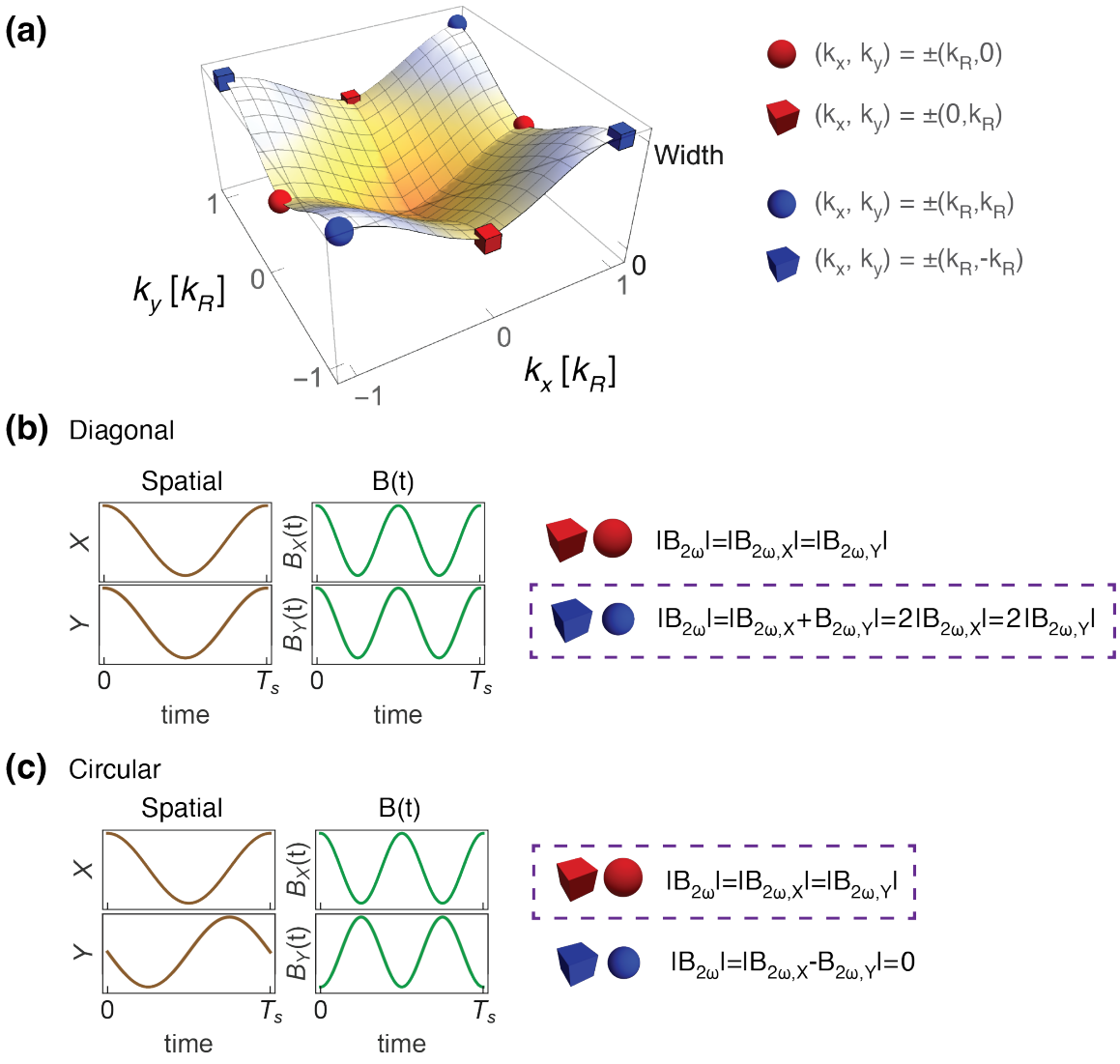

Figure 3.12: (a) Due to constructive interference, the dominating unstable modes for a diagonally shaken square lattice occur at $\pm(k_R, k_R)$ and $\pm(k_R, -k_R)$ (blue markers). Due to destructive interference, the dominating unstable modes for circularly shaken square lattice occur at $\pm(k_R, 0)$ and $\pm(0, k_R)$ (red markers). (b) For diagonal shaking, the growth rate of most unstable modes (due to constructive interference) is $2|B_{2\omega,Y}|$ at the points $\pm(k_R, k_R)$ and $\pm(k_R, -k_R)$. (c) For circular shaking, the growth rate of most unstable modes (due to destructive interference) is only $|B_{2\omega,Y}|$ (half the one for the diagonal shaking) at the points $\pm(k_R, 0)$ and $\pm(0, k_R)$.

Chapter 4: Parametric heating in a periodically shaken bosonic lattice

This chapter describes the experimental study of heating that our group carried out in a periodically shaken BEC held in a 2D lattice and prepared under conditions where parametric instabilities described by the Floquet Bogoliubov-deGennes (FBdG) equations (discussed in Chapter 3) should heavily affect the evolution of the BEC depletion. The observed dependence of the heating on the parameters of our 2D lattice were contrasted with the predictions from a model along the lines of Ref. [80], which contains a thorough analytical and numerical study of parametric instabilities in 1D lattices with a transverse free degree of freedom.

The predicted emergence of parametric instabilities in the context of driven optical lattices represents an example of the parametric amplification of field modes, an ubiquitous phenomenon in systems that obey nonlinear equations. Optical effects such as harmonic generation and down conversion (that have been employed, for example, to produce entangled photons and squeezed light) originate from the interaction between light fields in a nonlinear dielectric material, and are described by the Manley-Rowe equations for parametric amplifiers [189]. In a different range of the electromagnetic spectrum, the nonlinear capacitance of varactor diodes has been used to amplify weak microwave signals in low noise radio receivers. Another example is the parametric oscillation instability that occurs when the radiation pressure couples the mechanical eigenmodes of a Fabry-Perot cavity to its optical modes [190]; these instabilities are considered detrimental

in the context of gravitational waves interferometers, where they were first predicted [191]. In the context of bosonic gases, BECs obey a nonlinear Schrödinger equation [Eq. (3.30)] and it is thus not surprising that an external periodic drive can induce the parametric growth of bosonic modes.

The present chapter is organized as follows: Section 4.1 provides a link between some of the predicted attributes of parametric instabilities (discussed in the previous chapter) and the expected heating rates of the physical observable we measured in our experiments, with section 4.1.1 listing some of the shortcomings in the FBdG model used to calculate these rates and section 4.1.2 commenting on the differences between the FBdG theory and the alternative FFGR approach. Section 4.2 goes over some of the regular calibrations we performed on our lattice setup before the systematic measurement of heating rates. Some of these undertakings were the minimization of the optical lattice imbalance (section 4.2.1) and the experimental corroboration of the tunneling renormalization in shaken lattices (section 4.2.2). Section 4.3 begins by explaining our choice of lattice and shaking parameters. It then describes the experiments and results on the shake-induced decay of the atomic condensate fraction. Section 4.4 concludes this chapter by commenting on the agreement between our observations and the FBdG model.

4.1 Expected properties of the observables related to parametric instabilities

A few theoretically calculated properties of parametric instabilities in off-resonance shaken lattices were motivated in Chapter 3 using a slightly different approach from the formal derivations included in Refs. [80, 86], where a tight-binding approximation was employed. In terms of the drive parameters K_0 and ω_s, the tunneling matrix element J and the interaction coupling den-

sity $g\bar{n}$, the features of these instabilities that will be more relevant in the experiments described below are:

- The growth rate $\gamma_{\boldsymbol{\kappa}}$ of the unstable mode with a momentum $\boldsymbol{\kappa}$ (including the maximally unstable one) is predicted to possess a linear dependence on $g\bar{n}$.

- $\gamma_{\boldsymbol{\kappa}}$ is expected to vary with K_0 as $\gamma_{\boldsymbol{\kappa}} \propto |\mathcal{J}_2(K_0)|$.

- The dependence of the dominating growth rate $\Gamma_{\rm M}$ on the frequency ω_s exhibits two regimes separated by a threshold frequency $\omega_{\rm th}$ (whose value depends on the type of shaking). The two scalings are

$$\Gamma_{\rm M} \propto \begin{cases} \dfrac{|\mathcal{J}_2(K_0)|}{|\mathcal{J}_0(K_0)|}\left(\sqrt{(g\bar{n})^2+(\hbar\omega_s)^2}-g\bar{n}\right)\dfrac{g\bar{n}}{\hbar\omega_s}, & \text{if } \omega_s \leq \omega_{\rm th}, \\ 4|\mathcal{J}_2(K_0)|J\,\dfrac{g\bar{n}}{\hbar\omega_s}, & \text{if } \omega_s \geq \omega_{\rm th}. \end{cases} \tag{4.1}$$

Although calculations yield a continuum of unstable modes having a broad range of growth rates $\gamma_{\boldsymbol{\kappa}}$, it was argued in Ref. [80] that the rate with which the experimental observables O connected with parametric instabilities (such as the noncondensed fraction of the atomic cloud or the energy density of the excitations) are expected to grow exponentially is $2 \times \Gamma_{\rm M} = 2 \times \max_{\boldsymbol{\kappa}}\gamma_{\boldsymbol{\kappa}}$. This expectation relies on (a) the observables O typically being quadratic functionals of the Bogoliubov modes and (b) the most unstable mode dominating the late growth of these quantities. Further discussion of this hypothesis can be found in Ref. [80], where a full time evolution of some physical observables validates the behavior $O(t) \propto e^{(2\times\Gamma_{\rm M})t}$ for sufficiently long times t. (It is worth commenting that different scalings are anticipated during the early stages of the instabilities growth with the initial populations of the modes being more consequential;

this timescale is, however, believed to be hardly accessible in our experiments.) This predicted scaling remains valid if multiple independent modes share the maximum growth rate Γ_{M} because the total depletion would remain proportional to the exponential $e^{+(2\times\Gamma_{\mathrm{M}})t}$. The assumption that the maximally unstable mode dictates the time dependence of experimental quantities was also employed in the first reported observations of dynamical instabilities in static lattices [182].

To obtain the expected exponential growth rate Γ_{FBdG} of physical quantities resulting from the parametric instabilities in the case of a shaken 2D square lattice, one needs to consider the dependence of Γ_{M} on the type of shaking, e.g., circular or diagonal, as was discussed in Section 3.3.3.4. The values of Γ_{FBdG} for the three types of shaking considered in our experiments, in the respective regimes $\omega_s > \omega_{\mathrm{th}}$, are

$$\Gamma_{\mathrm{FBdG}}^{x\text{-only}} = 2 \times \Gamma_{\mathrm{M}}^{x\text{-only}} = 1 \times 2 \times \Gamma_{\mathrm{M}}^{\mathrm{1D}} \qquad (\omega_s > \omega_{\mathrm{th}}^{x\text{-only}} = 1 \times \omega_{\mathrm{th}}^{\mathrm{1D}}) \tag{4.2}$$

$$\Gamma_{\mathrm{FBdG}}^{\mathrm{diagonal}} = 2 \times \Gamma_{\mathrm{M}}^{\mathrm{diagonal}} = 4 \times 2 \times \Gamma_{\mathrm{M}}^{\mathrm{1D}} \qquad (\omega_s > \omega_{\mathrm{th}}^{\mathrm{diagonal}} = 2 \times \omega_{\mathrm{th}}^{\mathrm{1D}}) \tag{4.3}$$

$$\Gamma_{\mathrm{FBdG}}^{\mathrm{circular}} = 2 \times \Gamma_{\mathrm{M}}^{\mathrm{circular}} = 2 \times 2 \times \Gamma_{\mathrm{M}}^{\mathrm{1D}} \qquad (\omega_s > \omega_{\mathrm{th}}^{\mathrm{circular}} = 1 \times \omega_{\mathrm{th}}^{\mathrm{1D}}), \tag{4.4}$$

where $\Gamma_{\mathrm{M}}^{\mathrm{1D}}$ is the dominating growth rate of the 1D problem along any of the shaken directions (i.e., ignoring the other two degrees of freedom).

The physical quantity we measured in our experimental studies of parametric heating of driven condensates was the condensed fraction (CF), i.e., the population of atoms that remained in the BEC relative to the total number of both condensed and noncondensed atoms. We chose this observable because it was was argued in Ref. [80] that its complement, namely, the noncondensed fraction, obeyed the type of exponential growth discussed above. An alternative measurable

quantity considered in that same reference, and whose detection proved to be ambiguous in our setup, is the momentum distribution of quasiparticle modes. This proposed momentum-resolved measurement of the parametric instabilities in shaken bosonic 1D lattices was successfully carried out in a similar experimental work reported in Ref. [87], where it was claimed that the tuning of the scattering length via a Feshbach resonance (which is essentially unavailable for rubidium-87) was vital to attain the parameter regimes where the unstable modes were recognizable in TOF images.

4.1.1 Limitations of the FBdG framework

As some of them will arise in the interpretation of our experimental results, a list of relevant deficiencies in the FBdG model accompanying our experimental work is the following:

- It disregards the fact that the interactions make the problem non-separable in the x and y coordinates.

- The validity of the FBdG-calculated excitation growth rates Γ_{FBdG} is anticipated to be limited to a very specific time window since (a) at early times, and as commented earlier, the instabilities evolution may exhibit behaviors that differ from the exponential growth, while (b) at late times, saturation effects that effectively reduce the observed rate are likely to occur. The saturation stems from the interaction between both the excitations and the condensate, as well as among the excitations themselves.

- The model only includes the lowest order terms in the high-frequency expansion.

- It assumes a bosonic superfluid, and will fail as the effective tunneling amplitude becomes

small and a transition to a correlated Mott insulator takes place [192].

- The effects of a finite duration of the initial modulation ramp in the preparation protocol are not considered in the calculations.

4.1.2 Contrast with the Floquet Fermi's golden rule

An alternative and well-studied perturbative approach to describe the observed heating in periodically driven lattices similar to the one treated in our work is based on the Floquet Fermi's golden rule (FFGR) [84, 90, 193]. In this framework, the scattering rate dN/dt between the BEC state $|\Psi_i^{\text{FGR}}\rangle$ and a excited state $|\Psi_f^{\text{FGR}}\rangle$ possessing two excitations outside the condensate is calculated using the golden rule

$$\frac{dN}{dt} = \frac{2\pi}{\hbar} \sum_n |\langle \Psi_f^{\text{FGR}}| H_{\text{int}} |\Psi_i^{\text{FGR}}\rangle|^2 \delta(\varepsilon_f - \varepsilon_i) \tag{4.5}$$

where the interaction term H_{int} (proportional to the coupling density $g\bar{n}$) is considered a perturbation to the effective Hamiltonian, and $\varepsilon_f - \varepsilon_i$ is the difference between the total quasienergy of the final state $|\Psi_f^{\text{FGR}}\rangle$ (which includes fluctuations) and the total quasienergy of the macroscopically occupied state $|\Psi_i^{\text{FGR}}\rangle$. In the case of off-resonance shaken lattices, the rate (4.5) has the following expression

$$\frac{dN}{dt} = \mathcal{C}_m \times \left[g\bar{n} \frac{J\mathcal{J}_m(K_0)}{\omega_s} \right]^2, \tag{4.6}$$

where $\mathcal{C}_m$ is a coefficient that depends on the order m of the resonance, i.e., the order of the time Fourier component that induces the resonant scattering (see Ref. [84]). In contrast to the FBdG

rates [Eqs. (4.1) and (4.2)], the FFGR rates are quadratic in $g\bar{n}J$.

4.2 Lattice characterization

This section describes some regular calibrations that eliminate dissipative effects not related to the parametric instabilities we are studying, as well as the experimental corroboration of a renormalized effective tunneling in our shaken optical lattice (discussed in Section 3.1.3 and illustrated in Fig. 3.2).

4.2.1 Cancelation of lattice site-imbalance

Imperfections caused by a residual vector light shift [103] in the folded, retroreflected lattice used in our experiments, gave rise to an unintended double-well checkerboard potential, whose tilt between adjacent sites could enable undesired resonant transfers in the shaken lattice, something that could interfere with the measurement of parametric heating. This lattice imbalance was routinely assessed by measuring the relative populations in the lattice A and B sites using microwave spectroscopy of an alternating lattice site-dependent transition. In this technique [101], an adiabatic loading of the cloud in the nearly balanced checkerboard lattice produced an atomic wavefunction ψ_1, illustrated in Fig. 4.1(a), whose relative populations on sites A and B is set by the accidental tilt. The lattice amplitude and the tilt were then ramped up to "freeze in" the local A/B populations, and to induce a substantial separation between the measured center frequencies of the microwave transition $|F = 1, m_F = -1\rangle \rightarrow |F = 2, m_F = -2\rangle$ on sites A and B [see Fig. 4.1(b)]. As shown in Fig. 4.1(c), the difference in height between the two resonances in the microwave spectra (revealing the population imbalance between A and B

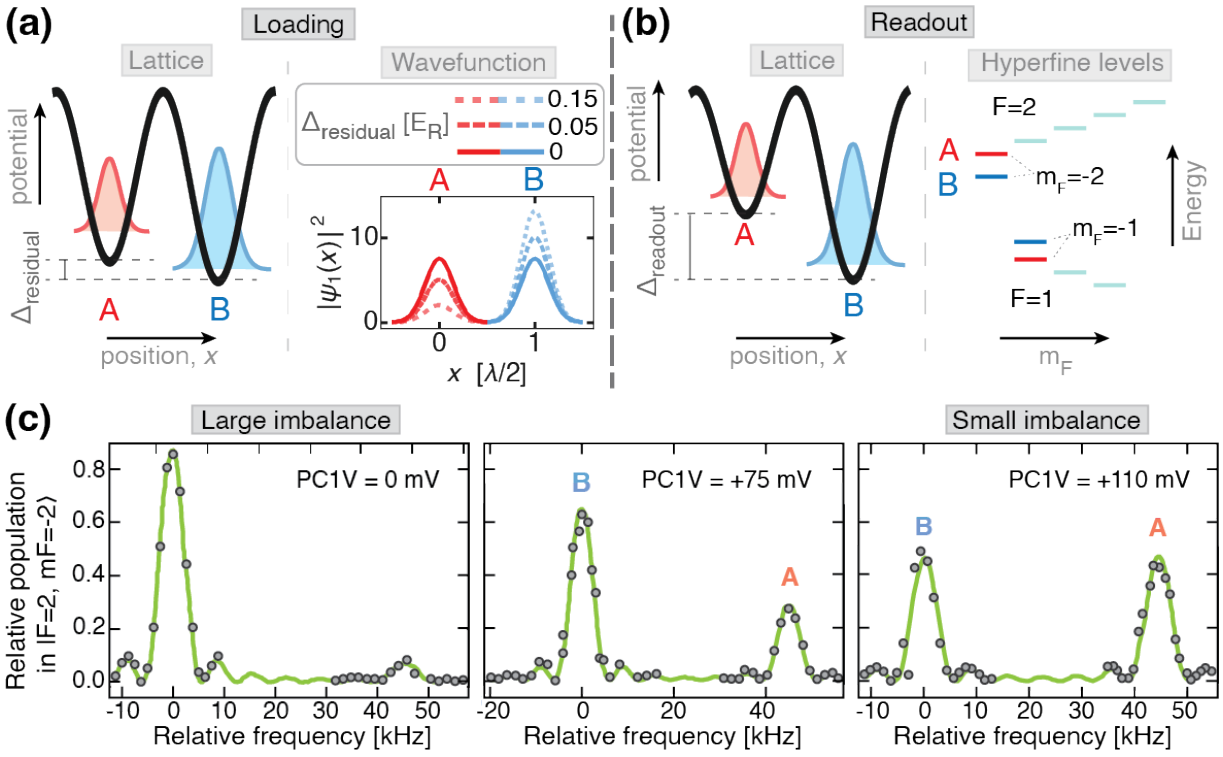

Figure 4.1: Reduction of the lattice site imbalance using microwave spectroscopy of a site-dependent microwave transition. (a) Atoms were initially loaded in a lattice with a residual tilt Δ_{residual}. Left figure shows the calculated, imbalanced square modulus of wavefunction ψ_1 in a checkerboard lattice with depth 22 E_R and residual tilts 0, 0.05 and 0.15 E_R. (b) The tilt between the A and B sites was then increased to a large value Δ_{readout} that produced a significant difference between the frequencies of the hyperfine transition $|F = 1, m_F = -1\rangle \rightarrow |F = 2, m_F = -2\rangle$ for the A and B sites. (c) Microwave spectra obtained with the tilt Δ_{readout}. Measured relative population in the hyperfine state $|F = 2, m_F = -2\rangle$, as a function of the relative frequency of the microwave radiation addressing the $|F = 1, m_F = -1\rangle \rightarrow |F = 2, m_F = -2\rangle$ transition, is shown here for three different values of the voltage PC1V applied on the input Pockels cell PC1. These spectra displayed two separate resonances corresponding to sites A and B. The energy imbalance between adjacent sites, inferred from the height difference between the two separate profiles, was corrected by tuning PC1V.

sites) was corrected by slightly adjusting the input polarization of the lattice beam using the input Pockels cell PC1.

An alternative calibration technique, described in Ref. [103], that directly measures the energy offset between the A and B sites consisted in measuring the frequency of the oscillations in the observed ground band diffraction pattern [see Fig. 4.2(a)] after rapidly loading the BEC in the tilted lattice and varying the time t_{h} the cloud is held in this potential [see Fig. 4.2(c)]. The loading was carried out faster than the tunneling amplitude J to avoid having the BEC prepared in the ground state, wherein the A sites have a small population for non-negligible offsets. The oscillations in the diffraction TOF images were induced by the different phases acquired by the atoms in the A and B sites due to the energy tilt. This method was, unfortunately, not always suitable for direct measurements of small tilts (which produce slow variations of the diffraction patterns) because, as exemplified in Fig. 4.2(c), the oscillations typically dwindled significantly after ~ 1 ms, preventing an accurate extraction of frequencies below 1 kHz. (We attribute the observed dephasing to an inhomogeneous spread in the on-site interaction energies produced by a nonuniform population among the sites of the quickly loaded lattice.) In spite of these complications, the small tilts could still be inferred from extrapolating the dependence of large tilts with the PC1V voltage [Fig. 4.2(d)].

4.2.2 Tunneling renormalization

We took advantage of the intrinsic sensitivity of the microwave transitions to the sites A and B in our double-well lattice, along with the ability to resolve different hyperfine states, to measure the effective tunneling J_{eff} in our shaken square lattice. The main stages of the measurement

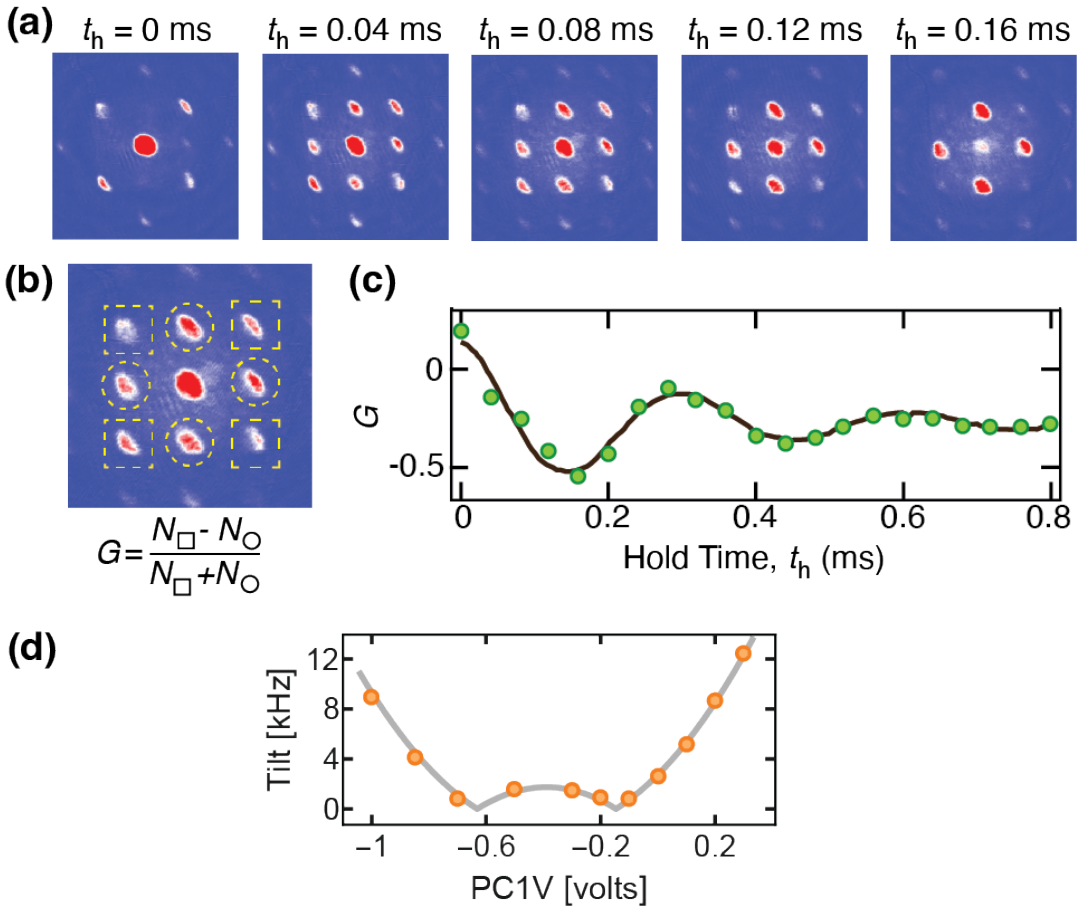

Figure 4.2: Measurement of the the lattice tilt using the oscillations of the diffraction pattern. (a) Example of observed oscillations in the ground band diffraction pattern for a lattice with depth 33 E_R. (b) The patterns were characterized by the quantity G, defined as the normalized difference between the population in the diffraction peaks surrounded by squares and the population in the peaks surrounded by circles. (c) The frequency of these pattern variations [corresponding to the images in (a)], which is about ~ 3.3 kHz in this example, was a measurement of the effective energy offset between adjacent sites. The oscillations were typically not sustained for more than ~ 1 ms. (d) By varying the voltage PC1V applied on the input Pockels cell, we could measure larger tilts (i.e., higher frequencies in the oscillations), from which smaller tilts were inferred with a higher accuracy by fitting a "rectified" parabola.

protocol are illustrated in Fig. 4.3(a). In this procedure, a relatively large tilt between sites was employed to prepare an antiferromagnetic-ordered state (stage II), in which the A sites were only occupied by atoms in the hyperfine $|h_1\rangle$ state, while B sites were exclusively occupied by atoms in a different state $|h_2\rangle$. The tilt (and lattice depth) were then rapidly ramped down before the beginning of the modulation. After the lattice was shaken for a time t_e (stage III), the particles were redistributed among the lattice sites at a rate predominantly set by J_{eff}. In the resulting new arrangement of the atoms in the lattice, the ones that started at the A sites were differentiated from those that did it at the B sites via the hyperfine state. To image the relative population of the atoms that switched from A sites to B sites (or viceversa) in a Stern-Gerlach detection, these particles were transferred to new hyperfine states $|h_3\rangle$ and $|h_4\rangle$ differing from $|h_{1,2}\rangle$ (stage IV); the atoms that did not switch sites remained in their original hyperfine states $|h_{1,2}\rangle$. J_{eff} was deduced from the decay rate of the initial ordered state quantified by the magnetization M_s. We measured a reduced J_{eff} as K_0 grew from 0 to $K_0 \sim 2.4$, and an increase in J_{eff} with K_0 in the range $2.4 \lesssim K_0 \lesssim 3.3$, as expected from the relation $J_{\text{eff}} = \mathcal{J}(K_0)$ [see Eq. (3.20)].

4.3 Experiments on parametric heating

In our experiments, we extracted the BEC condensate fractions (CF) following the shaking of the optical lattice holding the cloud. The CF decay rates were measured under different conditions that would allow us to evaluate the validity of our theoretical model. This section presents the results of these explorations. Section 4.3.1 goes over some details in the selection of the experimental lattice and shaking parameters. A brief discussion of the observed CF decay with the modulation time, as well as the dependence of the extracted condensate loss rate on different

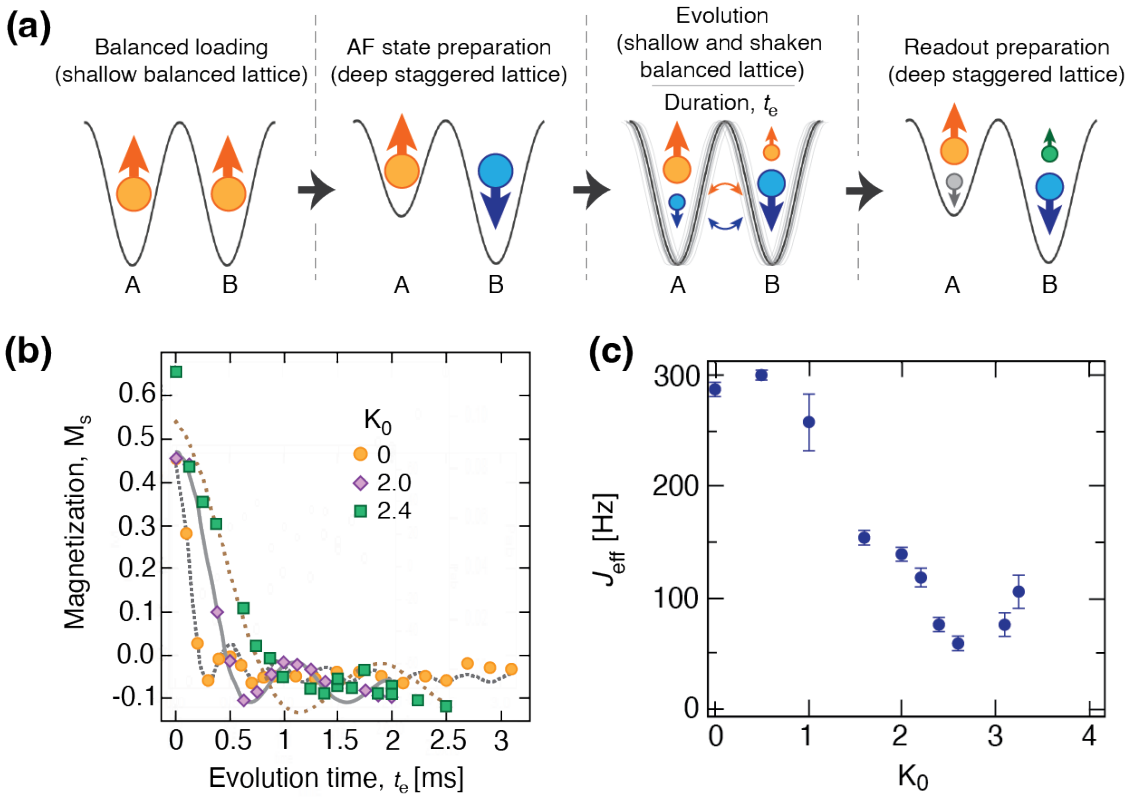

Figure 4.3: Observing tunneling renormalization in a shaken lattice. (a) Outline of the protocol used to measure the effective tunneling J_{eff}: I. The atomic cloud was first loaded in a balanced square optical lattice with equal populations in A and B sites, and all atoms in the $|h_1\rangle = |F = 1, m_F = -1\rangle$ hyperfine state (indicated with orange). II. Next, the lattice depth and the tilt were increased to induce a site dependence on the microwave transition between $|h_1\rangle$ and a different hyperfine state $|h_2\rangle$ (blue). This transition was used to prepare an antiferromagnetic- (AF-) ordered state, in which all atoms in the B sites were transferred to $|h_2\rangle$, while those in A remained in $|h_1\rangle$. III. The lattice potential was set to a configuration where the effective tunneling J_{eff} was to be measured (via the redistribution of atoms in $|h_{1,2}\rangle$ among the A and B sites). In our case, this was a shaken and shallower square lattice. IV. Lattice depth and the tilt were quenched to higher values (as in step III) so that the atoms in the $|h_2\rangle$ state occupying the A sites, as well as those in the $|h_1\rangle$ occupying the B sites, were, respectively, transfered to different hyperfine states $|h_3\rangle$ (gray) and $|h_4\rangle$ (green). (States $|h_{1,2,3,4}\rangle$ were all different and resolvable via Stern-Gerlach imaging.) (b) Observed decay of the magnetization M_s for different shaking strengths K_0. The effective tunneling is inferred from the speed of the decay. (c) Obtained effective (renormalized) tunneling J_{eff} for different values of K_0.

parameters of our system is included in section 4.3.2.

4.3.1 Parameter regimes and other considerations

The drive frequencies ω_s we used in the experiments did not exceed $2\pi \times 4$ kHz, an upper bound lying below the lowest value ($\sim 2\pi \times 6.2$ kHz) at which appreciable (and intrusive) multiphoton transitions [83, 194] between the ground and excited energy bands were detected by vibrational heating spectroscopy. Additionally, ω_s was also picked to be larger than the range of values for the bare tunneling amplitude J and the interaction density $g\bar{n}$, so that the high-frequency approximation mentioned in the subsubsection 3.1.3 is valid and the tunneling matrix elements along both spatial directions can be replaced with the effective tunneling amplitude $J_{\text{eff}} = J\,\mathcal{J}_0(K_0)$ [75, 192]. As for the drive strengths, we explored K_0 between 0 and 4. However, the following discussion focuses on the range $0 \leq K_0 < 2.4$, where J_{eff} remains positive, as these are the conditions where the parametric nature of the instabilities should dominate over the dynamical instabilities caused by a negative curvature of the band.

The initial and final ramps of the modulation profile also required some consideration. The drive amplitude was ramped smoothly (at a fixed frequency) because a rapid turn-on or turn-off in the modulation profile caused undesired higher-band excitations, whose thermalization with the condensate led to a detrimental decrease of the condensed fraction on a timescale of 2 ms (see Appendix A of Ref. [86]). On the other hand, the ramps were as fast as they could be in order to avoid these excitations while having no significant CF decay at the end of the initial turn-on ramp. To avoid complications associated with micromotion on the measured CF, each experiment concludes after an integer number of modulation periods including the initial smooth turn-on of

the drive and the ending ramp-down.

As an additional consideration, we verified that the observed heating could be largely attributed to a Floquet-induced mechanism rather than to the emergence of a Mott insulator phase induced by the suppressed tunneling matrix element. This was done by checking that the BEC lifetime in a static lattice possessing a small (bare) tunneling J_{test} was substantially longer than the lifetime obtained with a shaken (and shallower) lattice with bare tunneling J_2, and whose effective tunneling $J_{\text{eff}} = J_2\mathcal{J}(K_0)$ nearly matched J_{test}.

4.3.2 Observed behavior of the condensed fraction decay rate

The condensate fraction (CF) was extracted from TOF absorption images resolving the 2D lattice Brillouin zones (captured by the PI PIXIS camera in Fig. 2.2), and obtained after a 300 μs band map immediately following the turn-off modulation ramp. As shown in Fig. 4.4, the observed dependence of the CF with the shaking time agreed with an exponential fit $Ce^{-\Gamma_{\text{CF}}t}$, from which we extract the decay rate Γ_{CF}. Although a decelerated condensate loss rate was inevitable for long modulation times due to the finite size of the BEC, it is worth noting that the measured scaling of the CF with the shaking time was never consistent with the FBdG theory because the exponential growth of the parametric excitations predicted by this model implies an accelerated loss of CF. A potential justification for this discrepancy is the short duration of the undamped FBdG regime compared to the BEC lifetime owing to eventual saturation effects of the condensate depletion rate caused by interactions (not accounted for by the FBdG model) between the collective unstable modes and the remaining condensate. In our experiments, we measured Γ_{CF} for different values of the tunneling amplitude J and the interaction coupling density $g\bar{n}$,

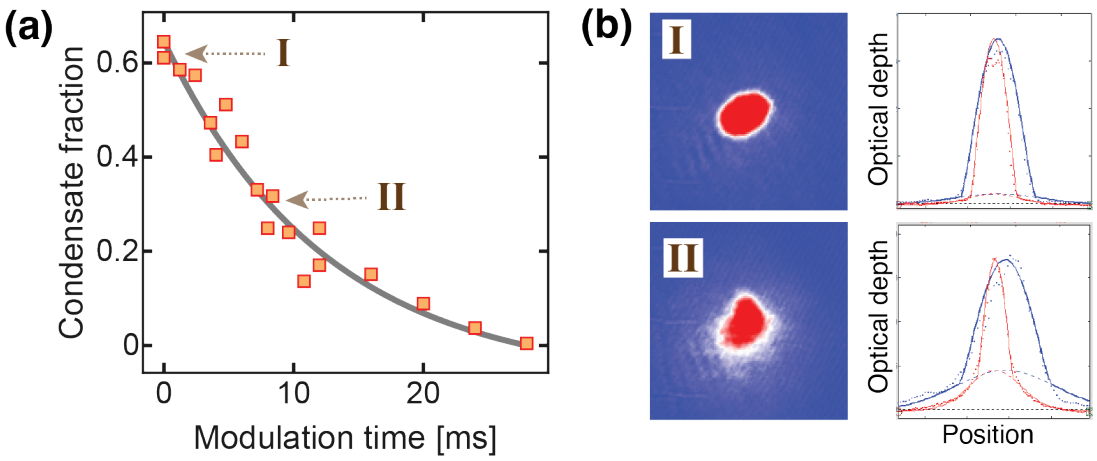

Figure 4.4: (a) Example of the observed decay of the condensate fraction CF as a function of the modulation time in a shaken lattice. Data corresponds to a 22 E_R deep lattice, shaken diagonally with a strength K_0 =2.2 and a frequency $\omega_s = 2\pi \times 2.5$ kHz. The gray solid line is an exponential fit of the form $Ce^{-\Gamma_{\rm CF}t}$, from which the decay rate $\Gamma_{\rm CF}$ is determined. The values of the condensate fraction were extracted from TOF images by fitting the optical depth distribution with a two-dimensional Thomas-Fermi profile on top of a Gaussian one. This is illustrated in (b) for the pair of points labeled I and II in (a). In (b), the left panels show the captured TOF images, and the right panels display two transversal cuts of the corresponding two-dimensional fits.

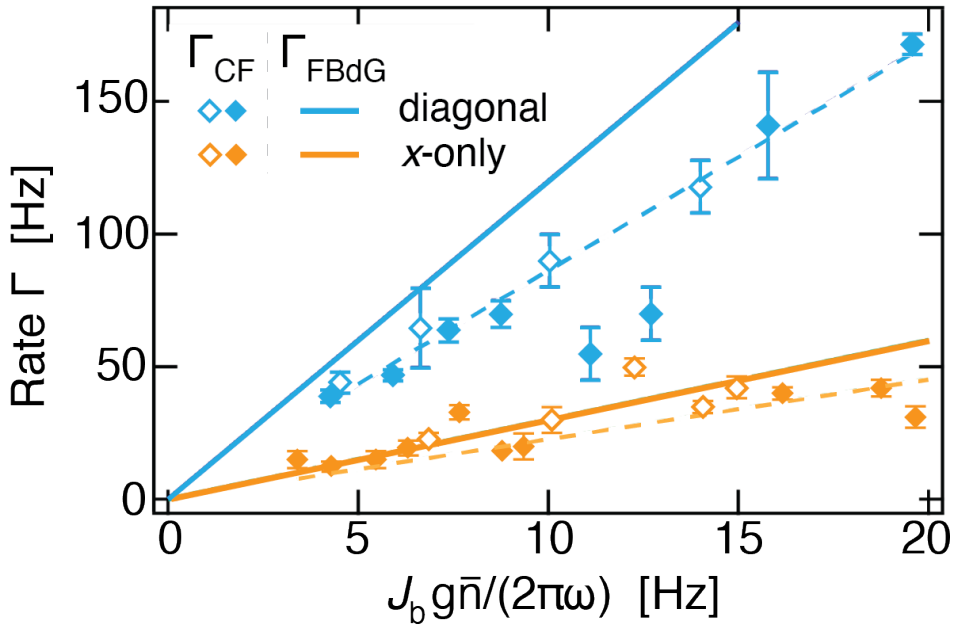

Figure 4.5: Linear scaling of decay rates Γ with $Jg\bar{n}$. For the experimental data shown here, J and $g\bar{n}$ were (not independently) tuned using the lattice depth, and were taken with a drive strength $K_0 = 2.1$, and the modulation frequencies $\omega_s = 2\pi \times 4$ kHz (filled markers) and $\omega_s = 2\pi \times 2.5$ kHz (empty markers). Solid lines correspond to FBdG theory, which predicts Γ_{M} scales linearly with Jg/ω_s. Dashed lines are linear fits to the data.

as well as for different values of the modulation parameters ω_s and K_0 that define the x-only, diagonal and circular shakings.

Figure 4.5 displays the measured decay rate Γ_{CF} as a function of $J\,g\bar{n}/\omega_s$ using $K_0 = 2.1$ and a couple of modulation frequencies ($\omega_s = 2\pi \times 2.5$ kHz and $\omega_s = 2\pi \times 4$ kHz). J, $g\bar{n}$, and their product $J\,g\bar{n}$, were tuned by changing the depth V_0 of the optical lattice, and their values were calculated from the calibrated lattice depth, the atom number and the frequencies of our harmonic trap. Lowest depth V_0 in Fig. 4.5, corresponding to the largest value of $Jg\bar{n}$, was 7.3 E_R. The predicted rates Γ_{FBdG} are displayed as solid lines. The observed magnitude of Γ_{CF} along with its predominantly linear scaling with $Jg\bar{n}$ match the expectation [see Eq. (4.1)] for

heating mechanisms largely induced by parametric instabilities, and is in marked contrast to the quadratic power law predicted in a Floquet FGR approximation. It is worth mentioning that the rates predicted for the diagonal and circular trajectories are, respectively, four times and twice the ones expected for x-only trajectories, as explained in Chapter 4.

The dependence of Γ_{CF} on K_0 is presented in Fig. 4.6 for a 22 E_R deep lattice modulated at 2.5 kHz. This behavior follows approximately the scaling $\mathcal{J}_2(K_0)$ predicted from the FBdG calculations (solid lines). For the x-only drive, in particular, the magnitude of Γ_{CF} nearly matches the theoretical values (orange solid line) and, although the scaling $(\mathcal{J}_2(K_0))^2$ in the FGR theory is not clearly ruled out by our data, it differs by a factor of about 30 from the magnitude obtained with a FGR approach (red dashed line). The sudden increase of Γ_{CF} shown in Fig. 4.6 for the circular and diagonal modulations as K_0 approaches 2.4 from below (where the tunnelings in the x and y directions are both expected to nearly vanish) strongly suggests a breakdown of the FBdG theory, and is further examined in Ref. [86].

Experimental evidence of the two different regimes in the scaling of Γ_{CF} with ω_s (discussed in sections 3.3.3.4 and 3.3.3.3) separated by the respective threshold frequencies ω_{th}^{x}, $\omega_{\text{th}}^{\text{diag}}$ and $\omega_{\text{th}}^{\text{circ}}$ is shown in Fig. 4.7. This behavior is closely related to the role of transverse degrees of freedom in the resonance condition for the instabilities and, for this reason, constitutes strong evidence of the parametric nature of this heating. The relatively poorer agreement between the measured and predicted rates at frequencies below 1 kHz was ascribed to a potential failure of the employed high-frequency approximations in the theory and the need to include corrections on the order of ω_s^{-1}.

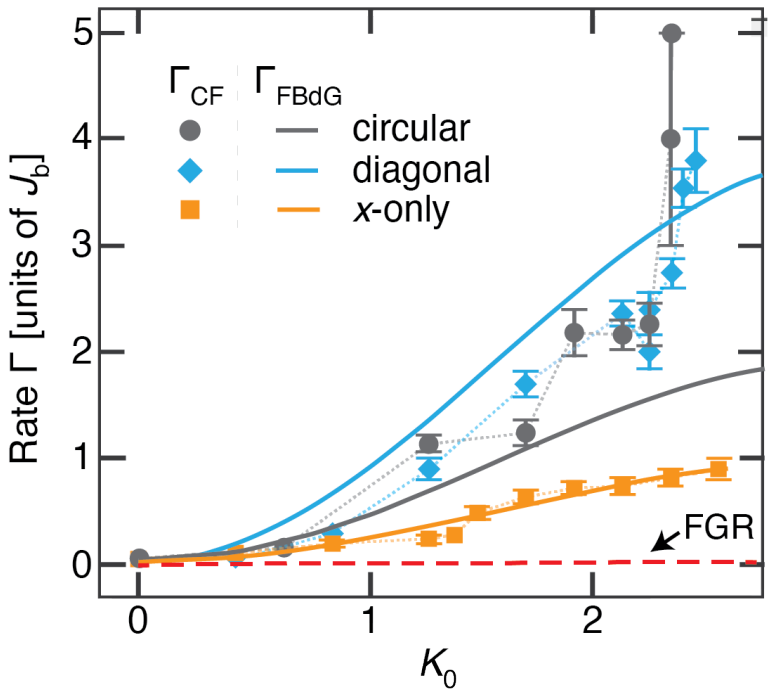

Figure 4.6: Decay rates Γ as a function of K_0 for a drive frequency of 2.5 kHz. Lattice depth is $22\ E_R$, at which J and $g\bar{n}$ are $2\pi \times 50$ Hz and $2\pi \times 700$ Hz, respectively. Solid lines indicate the respective rates predicted by a FBdG analysis. The expected rates using the FGR theory for the x-only drive are shown as a dashed red line.

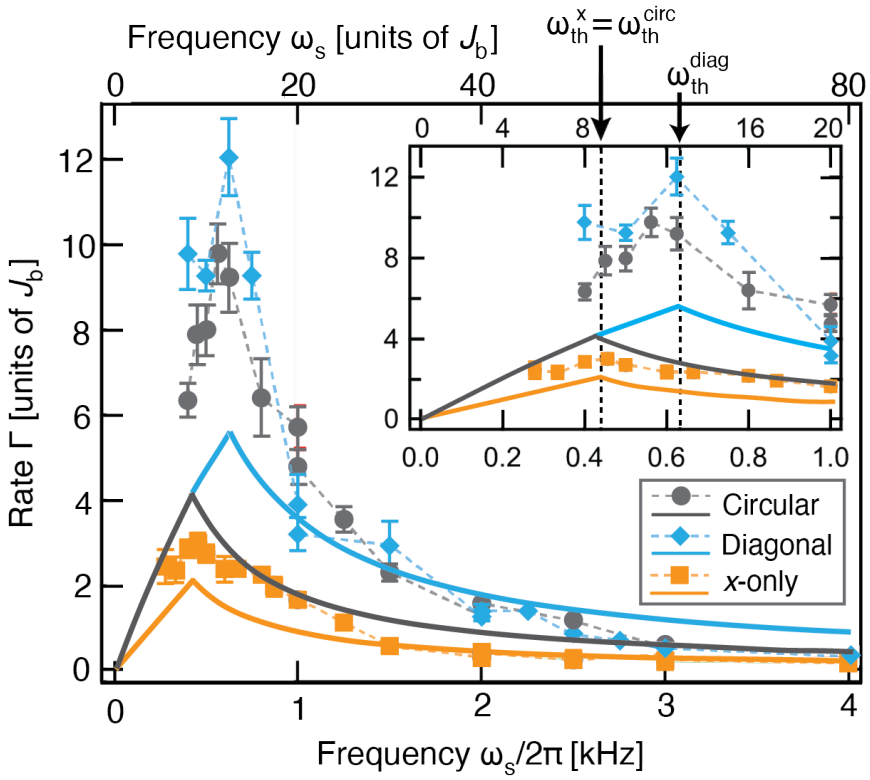

Figure 4.7: Γ vs ω_s for a 11 E_R deep lattice and a drive amplitude of $K_0 = 1.25$. Respective values of the calculated Γ_{FBdG} are displayed as solid lines. The inset zooms into the region 0 kHz $\leq \omega_s/2\pi \leq$ 1 kHz with the position of the threshold frequencies ω_{th} indicated by the down-pointing arrows.

4.4 Conclusions and outlook

We measured BEC decay rates in a periodically shaken square lattice under conditions where parametric instabilities were expected to represent a major dissipative mechanism. A goal of this experiment was to corroborate the suitability of the theory originally proposed in Refs. [78,80], and later adapted to 2D shaking in Ref. [86], to account for the interaction-induced heating in our modulated lattice. Motivated by a calculated nontrivial dependence of Γ_{CF} on the drive geometry, we explored different shaking trajectories.

Although we did not obtain direct evidence of parametric instabilities by resolving the exponential growth of collective modes, the observed heating possessed some robust signatures of a dissipative mechanism heavily influenced by parametrically amplified excitations. One of our experimental results supporting this last claim is the linear scaling of Γ_{CF} with $Jg\bar{n}$ (shown in Fig. 4.5), which in theory follows from the form of the off-diagonal terms in the Bogoliubov coupling matrix [Eq. (3.46)]. The presence of the threshold frequencies ω_{th} in the profiles of Γ_{CF} vs ω_s, along with their fair agreement with the expected values (see Fig. 4.7), represents additional experimental evidence since the predicted values of ω_{th} are determined by (i) the effect that the finite bandwidth along the lattice directions has on the parametric resonance condition (see Fig. 3.11) and (ii) the order of the Fourier components dominating the parametric coupling.

The weak agreement between the measured Γ_{CF} and the calculated Γ_{FBdG} that we observed in other features of our data prodded us to think about the relevance of the limitations in our FBdG model (some of them listed in Section 4.1.1). For instance, the difference between the values of Γ_{CF} and Γ_{FBdG} was more noticeable for the diagonal and circular trajectories than it was for x-only modulation, suggesting a breakdown of the separability along the x and y coordinates that

was assumed in our calculations. In addition, the absence of an accelerated condensate loss rate in the measured dependence of the fraction CF with the modulation time (subsection 4.3.2 and Fig. 4.4) was potentially caused by a significant initial buildup of the excited population (acting as seed populations for the instabilities) that hampered the detection of the exponential growth scaling predicted by the FBdG model. This would suggest that the later regime with decelerated (saturated) growth rates is more prevalent in realistic scenarios.

Possible avenues to mitigate the the parametric growth of excitations that we describe here include the reduction of the initial population of unstable modes and the minimization of the off-diagonal coupling terms in the FBdG equations. The latter could be attained by combining different modulation schemes whose coupling terms cancel out. Although seemingly far-fetched, this idea has been employed to suppress dissipative coupling in the two-path interference scheme described in Ref. [88]. However, the feasibility of these mitigation techniques relies on the validity of the FBdG model, which was partially successful at explaining our data, and prompts a further refinement of the theory. In addition, one of the main interests in Floquet systems is in the production of and study of highly correlated states, which will have different heating mechanisms than the weakly interacting condensate.

Chapter 5: Floquet-engineered moat band for ultracold atoms

This chapter covers the realization of a Mexican-hat band, whose importance was discussed in Chapter 1. To accomplish this energy spectrum we employed a Floquet approach by modulating the amplitude of a checkerboard optical lattice.

Section 5.1 mentions some of the ideal characteristics that a cold-atom approach that produces a Mexican-hat band (MHB) should possess. Next, Section 5.2 provides an account of some preliminary theoretical and experimental considerations of the Floquet protocol we planned to implement in our experimental setup. The theory employed in this section recovers the notions presented in Section 3.1.3 within the context of near-resonance shaken lattices [see equations (3.26) and (3.27)], departing (to some degree) from the terminology used in the previous chapter. In particular, the effective coupling term $\Omega_{1,2}$ between the lowest-lying bands and the detuning δ of the drive frequency with respect to the band spacing were both instrumental to infer the shape of the hybridized bands. Section 5.2 also reviews the incipient signatures (e.g., Fig. 5.5) of a ring-shape band when we modulated the depth of a checkerboard lattice. Section 5.3 then presents a set of systematic measurements that constitute a more unambiguous evidence of a moatlike band [Figs. 5.15, 5.16(c), 5.19(c), 5.22]. This section demonstrates that the BEC can be prepared in a Floquet state associated with the effective Mexican-hat band. Section 5.4 contains our observations on the stability of a BEC in the effective MHB [Fig. 5.23], which we analyzed numerically

in light of the FBdG formalism discussed in Section 3.3. The FBdG equations [Eqs. (3.38), (3.39), (3.40)] that were used throughout Chapter 4 to discuss parametric instabilities under a single-band approximation, were here adapted to include both the ground and the first-excited band, and were applied to model the stability of mean-field Floquet states associated with the hybridized moat band. Finally, a possible optimization in our Floquet protocol is described in Section 5.5.

A peer-reviewed, more succinct report of some of the results presented in this chapter can be found in Ref. [107].

5.1 Requirements for a moatlike band

A cold-atom approach to generate well defined moatlike bands should have several properties: (i) it should have a clear maximum near $\boldsymbol{q} = 0$ so that a continuum of minima can exist along a ring of $\boldsymbol{q}$, (ii) the variation in the minimum energy along the ring of minima should be smaller than all other energy scales in the problem, (iii) the drive-induced heating should not be too strong, and (iv) it should be generally applicable to many atomic species, both bosons and fermions.

Proposed approaches to produce moatlike energy dispersions include inducing Rashba spin-orbit coupling (SOC) [195] and Floquet engineering the desired band in a driven optical lattice [41]. In both cases, the modified dispersion results from hybridizing different motional states. Experimentally, approximate moatlike dispersions have been realized with ultracold atoms using SOC [195–198]. The resulting dispersions retain the discrete rotational symmetry of the spin-orbit coupling beams, and the moat minimum consists of 3 or 4 distinct minima instead

of a completely degenerate ring [199]. In addition, the SOC approach relies on particular spin structures, and is not generally amenable to any atomic species.

We considered several Floquet approaches to generate and hybridize bands to meet the criteria (i)-(iv) listed above, some of which are discussed in detail in the next section.

5.2 Experimental design considerations

5.2.1 Floquet dressed bands

The proposal for the Floquet approach in Ref. [41] to engineer an effective band with a moat shape was inspired by the Floquet engineered double-well band reported in Ref. [43]. As discussed in Section 3.1.3, this double-well effective dispersion is produced by a shaking-induced coupling between the two lowest bands of a 1D sinusoidal lattice, where the $|\Omega_{1,2}(\boldsymbol{q})|$ profile of the shake-induced band coupling featured a bump around the center of the BZ [see Figs. 3.5(c)]. This local maximum plays an important role in generating the double-well dispersion, as the two bands are more strongly repelled near the center of the BZ. It is then reasonable to conclude that, for a 2D optical lattice, it would be beneficial to have a symmetric "bump" in the band coupling near $\boldsymbol{q} = 0$.

5.2.2 Ruling out separable square lattices

It is tempting to try and apply the 1D shaking approach to our square separable lattice $V_{\text{ip}}(x, y) \propto \cos(2k_R x) + \cos(2k_R y)$ [see Eq. (2.1) and Fig. 2.4(a)]. However, $V_{\text{ip}}(x, y)$ is not appropriate to produce an effective moat dispersion. An amplitude- or phase- modulated square lattice system would remain separable in the x and y coordinates since the unitary evolu-

tion operator is the product of an operator dependending exclusively on x and another depending exclusively on y. The resulting two-dimensional quasienergy spectra would have the form $\varepsilon(q_x, q_y) = \varepsilon_X(q_x) + \varepsilon_Y(q_y)$, for which it would be impossible to get a flat minimum. To see this, note that if ε_X and ε_Y each had a similar double-well minima at $\pm q_{x,\text{min}}$ and $\pm q_{y,\text{min}}$, respectively, the energy at $\boldsymbol{q} = (0, q_{y,\text{min}})$ would be halfway between the energy at $\boldsymbol{q} = 0$ and $\boldsymbol{q} = (q_{x,\text{min}}, q_{y,\text{min}})$.A further complication is that for a square lattice, the first excited states consist of two bands (one for the x-direction and one for the y-direction). This three-band problem is more complicated to "dress" than a simpler two-band model of two isolated bands. It is worth mentioning that the failure of a separable square lattice to yield ring-shape band was already pointed out in Ref. [41]. For the reasons just mentioned, one needs to employ lattices with more complicated geometries.

Figure 5.1 presents the observed behavior of a BEC when it was loaded in the double- and quadruple- well dispersions produced by near-resonance shaking a separable square lattice. In agreement with results in Ref. [43], the time-of-flight images showed atoms condensing predominantly in only one of the wells, whose selection among the multiple degenerate minima was controlled by inducing a small velocity on the cloud before turning on the modulation. These observations confirmed experimentally the discrete nature of the degeneracy in these bands, as opposed to the continuous degeneracy in a MHB. The lifetime of the condensate was on the order of several tens of miliseconds, $\sim$ 80 ms - 120 ms, when shaking with a frequency above (but not too close to) the gap separating the lowest two bands. (A frequency too far from the gap reduced the effectiveness of the coupling, requiring a larger modulation strength, which was accompanied by undesired transfer to higher bands.)

The following subsections discuss the suitability of some modulated lattices available in

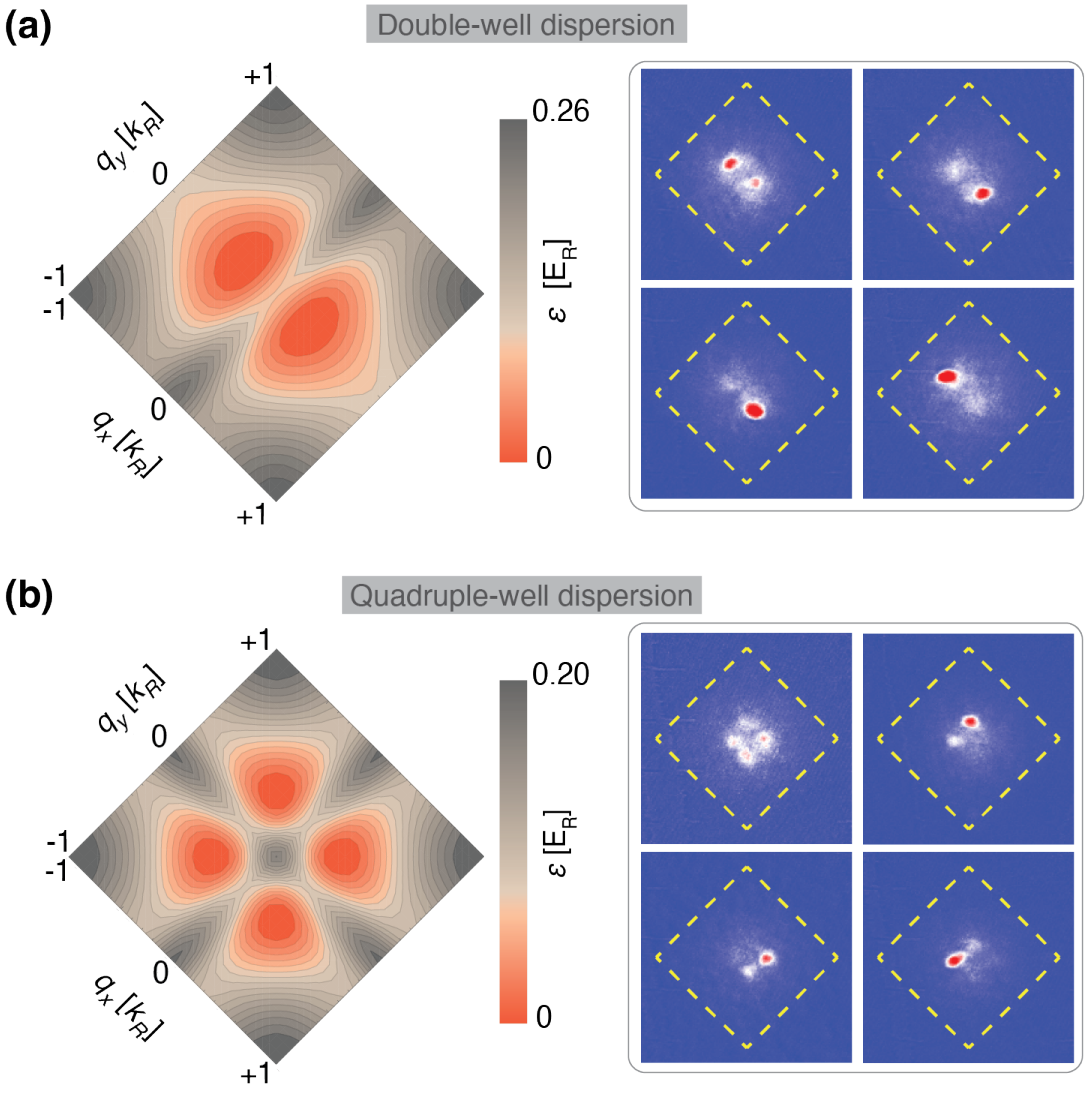

Figure 5.1: Effective bands generated by near-resonance shaking the separable square lattice V_{ip}. Left panels show contour plots over the first Brillouin zone of the calculated double- and quadruple- well effective dispersions produced by shaking (a) only along x and (b) along both x and y. Right panels display TOF images after adiabatically loading a BEC in the respective double- and quadruple- well bands. Each TOF image correspond to a slightly different velocity of the BEC (induced by kicking the cloud).

our experimental setup, other than the square lattice V_{ip}, to produce a MHB.

5.2.3 Floquet coupling approaches

Due to this non-separability constraint, a moat band generated using a Floquet approach requires a lattice with a non-trivial unit cell. A non-separable unit cell, however, does not guarantee favorable conditions for forming a Mexican-hat shape.

5.2.3.1 Shaking square and checkerboard lattices

Any shaking-induced coupling $\Omega_{1,2}(\boldsymbol{q})$ between the two lowest Bloch bands of a checkerboard lattice should vanish at $\boldsymbol{q} = 0$, as illustrated both theoretically and experimentally in Fig. 5.2 for x-, diagonal and circular shaking, respectively. To see why $\Omega_{1,2}$ is expected to be 0 at the center of the BZ let's begin by noting that the ground and first-excited Bloch waves at $\boldsymbol{q} = \mathbf{0}$ in the checkerboard potential have even parity around the center of the lattice sites [see, for example, Figs. 2.6(b) and 4.1(a)]. Since the coupling operator $\hat{H}'$ associated with shaking is a linear combination of the operators $\hat{p}_x \propto \partial_x$ and $\hat{p}_y \propto \partial_y$ [see Eq. (3.6)], the term $\Omega_{1,2}$ is the inner product of two functions with opposite parity and thus vanishes. An experimental confirmation of the coupling's profile can be obtained by performing Landau-Zener (LZ) sweeps centered around the $\boldsymbol{q} = 0$ resonant frequency between the two lowest bands. This procedure starts by heating the cloud within the lowest Bloch band to induce a significant spread of atoms in reciprocal space, after which the lattice potential is shaken with a time-dependent detuning crossing the resonance value. Atoms are transferred from the ground band to the first excited band with a probability dependent on $|\Omega_{1,2}(\boldsymbol{q})|$ according to the Landau-Zener formula

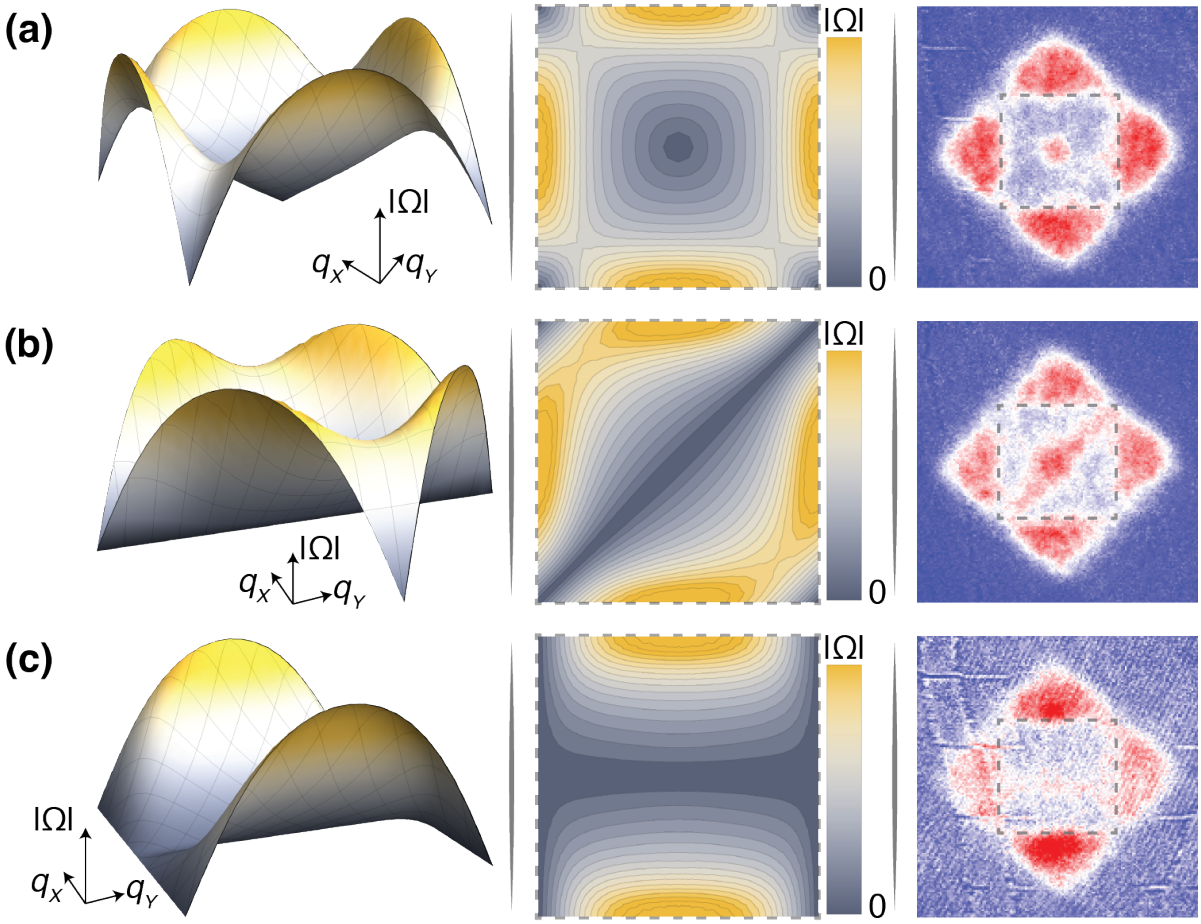

Figure 5.2: Three-dimensional plots (left) and contour plots (middle) of the coupling term $|\Omega_{1,2}|$, along with the experimentally observed profiles (right) obtained from single-shot TOF images following Landau-Zener sweeps for (a) circular, (b) x-, and (c) diagonal shaking.

$P_{\mathrm{LZ}}(\boldsymbol{q}) = 1 - \exp\left(-\kappa_{\mathrm{LZ}}|\Omega_{1,2}(\boldsymbol{q})|^2\right)$, where κ_{LZ} depends on the sweep rate; the atoms in states where the coupling vanishes have a lower probability to be transferred to the excited band than those in states where coupling is maximum. Figure 5.2 shows TOF images obtained using the bandmapping technique after performing LZ sweeps. In these images, the central square (mostly depleted due to the LZ transfer) corresponds to atoms remaining in the ground band after the sweep, and the outer triangles correspond to atoms transferred to the first excited band [see Brillouin zone illustration in Fig. 2.5(a)].

A consequence of a zero $\Omega_{1,2}$ at the center of the BZ is that periodic shaking of a checkerboard lattice will not give rise to an effective moat band when its frequency is above (blue-detuned with respect to) the energy gap at $\boldsymbol{q} = 0$ as, regardless of the modulation strength, the energy of the upper dressed band is always a local minimum. This type of coupling does, however, still allow for an effective Mexican-hat dispersion if the frequency is red-detuned and if the coupling possesses an appropriate rotational symmetry around $\boldsymbol{q} = 0$. In this "avoided crossing" regime, the local maximum at $\boldsymbol{q} = 0$ arises from the curvatures of the two bare bands, not from the $\boldsymbol{q}$-dependence of the coupling strength. Unlike the blue-detuned case, preparing atoms in the red-detuned effective bands is expected to require a frequency sweep starting far from $\Delta_{\boldsymbol{q}=\boldsymbol{0}}$ and will also be sensitive to the initial modulation frequency; this consideration will be illustrated later when discussing the effective bands obtained by modulating the lattice depth (section 5.2.3.4 and Fig. 5.7). Unfortunately, a vanishing $\Omega_{1,2}(\boldsymbol{q} = 0)$ can be anticipated to complicate an adiabatic preparation into the target ring-shape band with a cloud at rest.

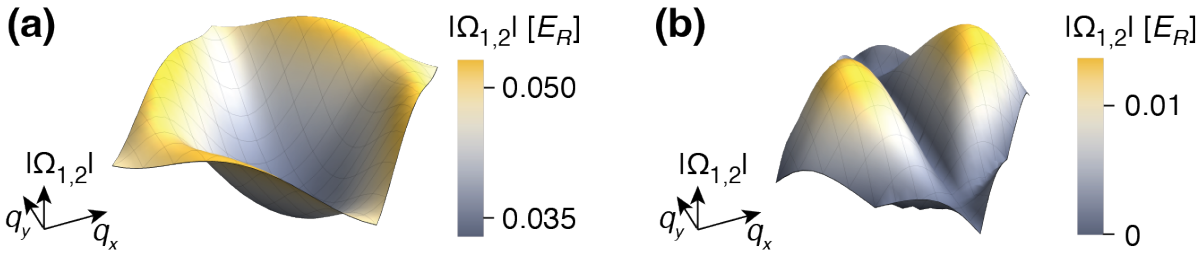

Figure 5.3: Form of the coupling term $|\Omega_{1,2}|(\boldsymbol{q})$ profiles for a (a) x-shaken (with drive amplitude of 32 nm) and an (b) amplitude modulated dimer lattice with $\alpha_m = 0.12$. For the example shown here, the lattice has a depth of $5.89\ E_R$ and a tilt of $0.44\ E_R$.

5.2.3.2 Shaking a dimer lattice

In order to have a non-zero band coupling at $\boldsymbol{q} = 0$, one needs to break the symmetry of the unit cell. The proposal in Ref. [41] used a shaken, non-separable dimer lattice to generate moat bands. The electro-optic modulator PC2 in our lattice setup [Fig. 2.3] allows to implement a double-well optical lattice with a dimer configuration [Fig. 2.4(d)]. The ground and first-excited Bloch waves at $\boldsymbol{q} = 0$ possess opposite parity around the center of the dimer lattice sites: it is even for the ground wave and odd for the excited one [see Fig. 2.6(c)]. Both amplitude and PC1 modulation preserve the wavefunction parity and will not be effective in coupling the lowest two bands [see Fig. 5.3(b) for the coupling profile of an amplitude modulated dimer lattice]. Shaking, on the other hand, shifts the wavefunction parity and thus provides a significant coupling between the lowest bands, including the $\boldsymbol{q} = 0$ states. However, our calculations indicate that, for all types of shaking, the coupling $|\Omega_{1,2}(\boldsymbol{q})|$ is a (weakly) concave up function of $\boldsymbol{q}$ [Fig. 5.3(a)]; for this reason, a moat dispersion can not be obtained with blue detuning. The moat band can still be realized using the band curvature and operating at red detuning.

5.2.3.3 Tilt modulation in a checkerboard lattice

Amplitude modulation of the checkerboard potential varies the depth of all lattice sites in the same proportion and with equal phase. An alternative mechanism to change the sites depths is to tune the voltage applied on PC1 (Fig. 2.3). This modulation the polarization of the field inducing the lattice potential. Unlike amplitude modulation, the depth variation in adjacent sites occurs with opposite phase; if the depth of the shallow wells grows, it decreases for the deep wells, and vice versa. The explicit expression for the time dependence of the potential is

$$V_{\text{LATT}}^{(\text{PC1M})}(x,y,t) = [1+\alpha\sin(\omega t)]V_{\text{ip}}(x,y) + [1-\alpha\sin(\omega t)]V_{\text{op}}(x,y). \tag{5.1}$$

The combination of amplitude and PC1 modulation produces the driven potential

$$V_{\text{LATT}}^{(\text{PC1M + AM})}(x,y,t) = [1+\alpha\sin(\omega t)]V_{\text{ip}}(x,y) + [1+\alpha\sin(\omega t+\delta_m)]V_{\text{op}}(x,y). \tag{5.2}$$

The coupling profile derived from this type of driving is very similar to the one obtained with amplitude modulation. While it would still allow to obtain the Rashba-like dispersion, it turns out that the coupling is not as effective as when the sites depths vary in phase; for the same value of α, $|\Omega_{1,2}|$ is larger when $\delta_m = 0$.

5.2.3.4 Amplitude modulation in checkerboard lattice

Given the limitations of the shaken dimer lattice for the blue-detuned driving, we also considered coupling the two lowest bands by periodically varying the overall depth of the potential.

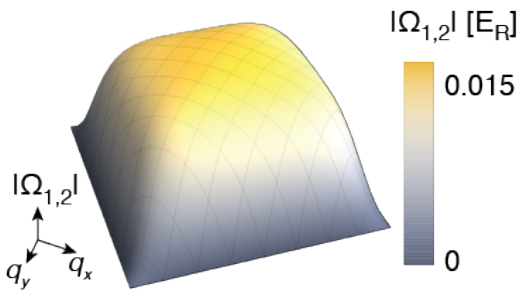

Figure 5.4: Form of the coupling term $|\Omega_{1,2}|(\boldsymbol{q})$ profiles for an amplitude modulated checkerboard lattice with $\alpha_m = 0.12$. For the example shown here, the lattice has a depth of $5.89\ E_R$ and a tilt of $0.44\ E_R$.

Explicitly, the time dependence is given by

$$V_{\text{LATT}}^{(\text{AM})}(x,y,t) = [1+\alpha_m \sin(\omega t)] V_{\text{LATT}}(x,y) = [1+\alpha_m \sin(\omega t)]\left[V_{\text{ip}}(x,y) + V_{\text{op}}(x,y)\right], \quad (5.3)$$

where $|\alpha_m| < 1$ sets the driving strength and $V_{\text{LATT}}(x,y)$ is the static potential. In our setup, this periodic variation of the lattice depth is accomplished by controlling the RF power feeding an AOM whose first diffraction order is used as the lattice beam.

As opposed to shaking, the coupling operator $\alpha_m \hat{V}_{\text{LATT}}(x,y)$ for amplitude modulation preserves the parity of Bloch waves around the center of the lattice sites and the effective coupling term $\Omega_{1,2} = \frac{1}{2}\langle 1|\, \alpha_m \hat{V}_{\text{LATT}}(x,y)\, |2\rangle$ will not vanish at the center of the Brillouin zone. Not only is the coupling at $\boldsymbol{q} = \mathbf{0}$ nonzero at the center of the BZ but this value is the largest one over the entire Brillouin zone, as shown in Fig. 5.4. While $\Omega|_{\boldsymbol{q}=\mathbf{0}}$ being a maximum is a favorable feature to obtain an effective moat band, the curvature at the center is not large; this reduces the range of blue-detuned frequencies that yield the desired band shape.

In the first implementations of AM hybridization in the chekerboard lattice, care was taken

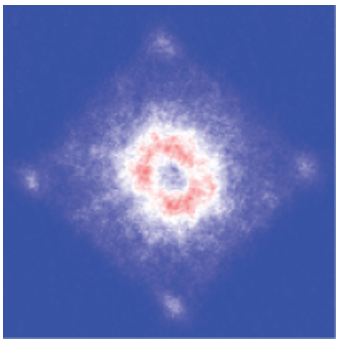

Figure 5.5: Initial TOF images in a motalike effective band (prepared with a frequency sweep in an amplitude modulated checkerboard lattice) displayed a ring-like feature, which contrasts with the discrete condensation shown in Fig. 5.1.

to sweep the frequency starting blue-detuned and ending red-detuned to make sure atoms were prepared in the dressed band having the Mexican hat shape and not in the other hybridized band; turning on the shaking at a single fixed red-detuned frequency was expected to induce uncontrolled transfer between the dressed bands. Initial evidence that bosons had been loaded in a moat-like band was obtained from time of flight images where atoms were distributed along a ring inside the first Brillouin zone and population at the center was relatively more depleted [see Fig. 5.5(a)].

One straightforward test on the moatlike band was to load the lattice in the far blue detuned limit and sweeping the detuning adiabatically to different final detunings. Lower final detuning increased the radius of the ring-shaped feature observed in TOF images [see Fig. 5.6], as one would expect from the dressed picture describing the hybridization.

Another aspect of our understanding on how a Mexican-hat band arises is illustrated in Fig. 5.7(a). If the frequency sweep to hybridize bands starts red-detuned with respect to the band gap at $\boldsymbol{q} = 0$, then the atoms will not be prepared in the band with a moat shape [upper sequence

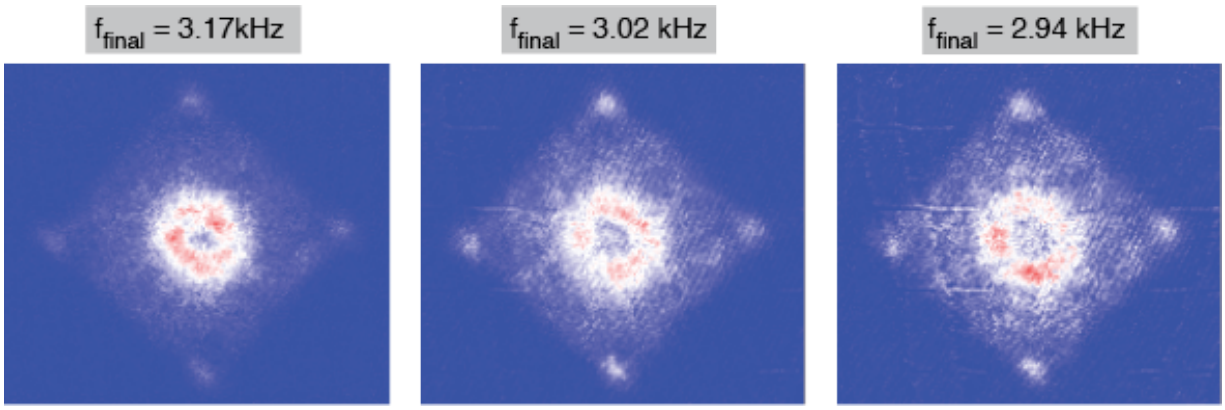

Figure 5.6: Growth of moat radius by lowering the value of the final drive frequencies f_{final} in the amplitude modulation sweep (larger red detunings).

in Fig. 5.7(a)]. To load the cloud into the moatlike band the sweep should start blue-detuned [lower sequence in Fig. 5.7(a)]. This hypothesis was tested, as shown in Figs. 5.7(b), 5.7(c) and 5.7(d). The obtained images showed a clear difference between the sweep direction; sweeps with an increasing frequency favored atoms condensing at the center of the Brillouin zone, while those with a decreasing frequency had stronger signatures of the "filled" ring.

Originally, we thought the procedures to prepare the cloud in the Rashba-like band should start with a condensate at $\boldsymbol{q} = 0$; this was the case in the initial implementations. As shown in Fig. 5.5, bosons did not condense into a single quasimomentum state but rather showed a broad distribution along a ring inside BZ1. It was later noticed through experiments that the cloud quasimomentum during preparation was a very important parameter. When atoms were kicked by a sudden shift of the trap position the cloud oscillates, allowing the hybridized band production to be accomplished with different BEC crystal momentum. Adiabatic loading of the BEC into the moat band at different times, and therefore different quasimomenta, during this oscillation led to contrasting results. If the hybridization was achieved when atoms were close to $\boldsymbol{q} = 0$, the

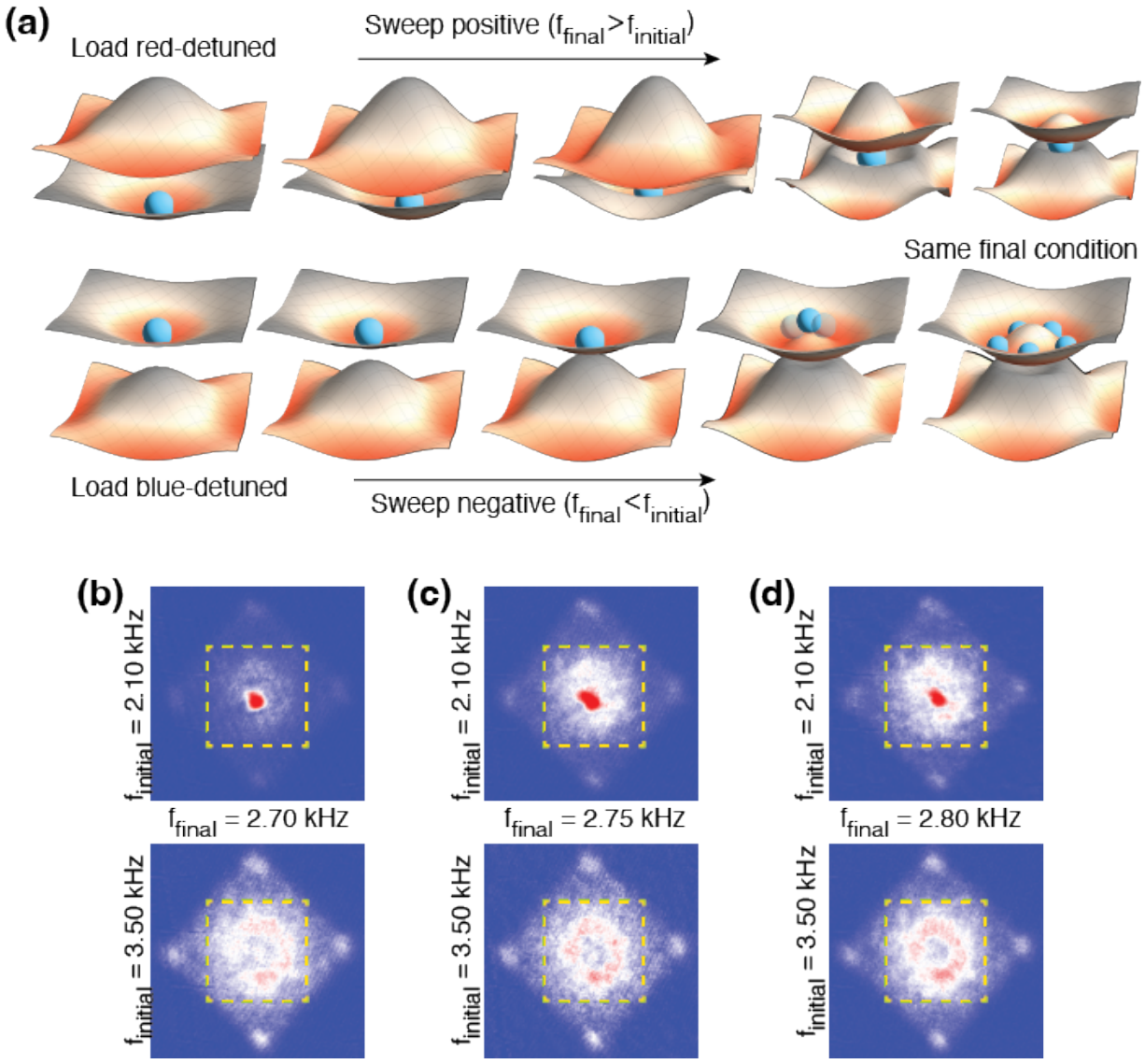

Figure 5.7: (a) Upper panel: to load the cloud into the hybrid band that does not have a moat shape, the sweep should start red-detuned and end close to resonance. Lower panel: to load the cloud into the moatlike band, the modulation should start blue-detuned and end close to resonance. (b) TOF images following amplitude modulation sweeps that have the same final frequencies f_{final} (at which an effective moat band is formed) but different initial frequencies f_{initial} (and hence different sweep signs). Lower (upper) panels correspond to $f_{\text{initial}} = 3.50$ kHz $(2.10$ kHz$)$.

condensate is rapidly destroyed and atoms show a broad distribution along a ring. On the other hand, preparing the hybrid bands when the cloud lay close to the moat minimum and far from the Brillouin zone center favors condensation at a single quasimomentum. An additional observation is that the non-condensed fraction of the condensate obtained along the moat increases with the atom number in the cloud, as will be illustrated later in Fig. 5.17(a) in Section 5.3.4. All in all, the stability of the bosonic condensate seemed strongly dependent on the quasimomentum of the cloud and on its density. Ultimately, we found that the amplitude modulated checkerboard lattice was the most favorable approach to engineer a moat band, and we used it in the detailed experiments that follow.

5.2.4 Mexican-hat band from amplitude modulating a checkerboard lattice

After considering various other options, we chose to Floquet engineer a moatlike band for ultracold atoms using an optical lattice consisting of a two-dimensional checkerboard array of one-dimensional tubes, hybridizing [43] its two lowest energy bands [Fig. 5.8(a)] by modulating the lattice depth. The form of the resulting dressed bands $\varepsilon_i(\boldsymbol{q})$ depends on the frequency f_m and fractional amplitude α_m of the modulation [Fig. 5.8(c)]. For drive frequencies f_m close to the bare band spacing at $\boldsymbol{q} = 0$, one of the hybrid bands (which we denote the "upper" band) has a nearly circular minimum at nonzero radius q_{min} [Fig. 5.8(b)].

The rotational symmetry of the resulting effective Mexican-hat dispersion relies on the intrinsic symmetry of the unmodulated coupled bands and of the coupling $\Omega_{1,2}$ associated with the periodic drive. If the latter are symmetric enough, the generated ring-shaped band is expected to exhibit a high intrinsic rotational symmetry, allowing for smaller absolute energy variation

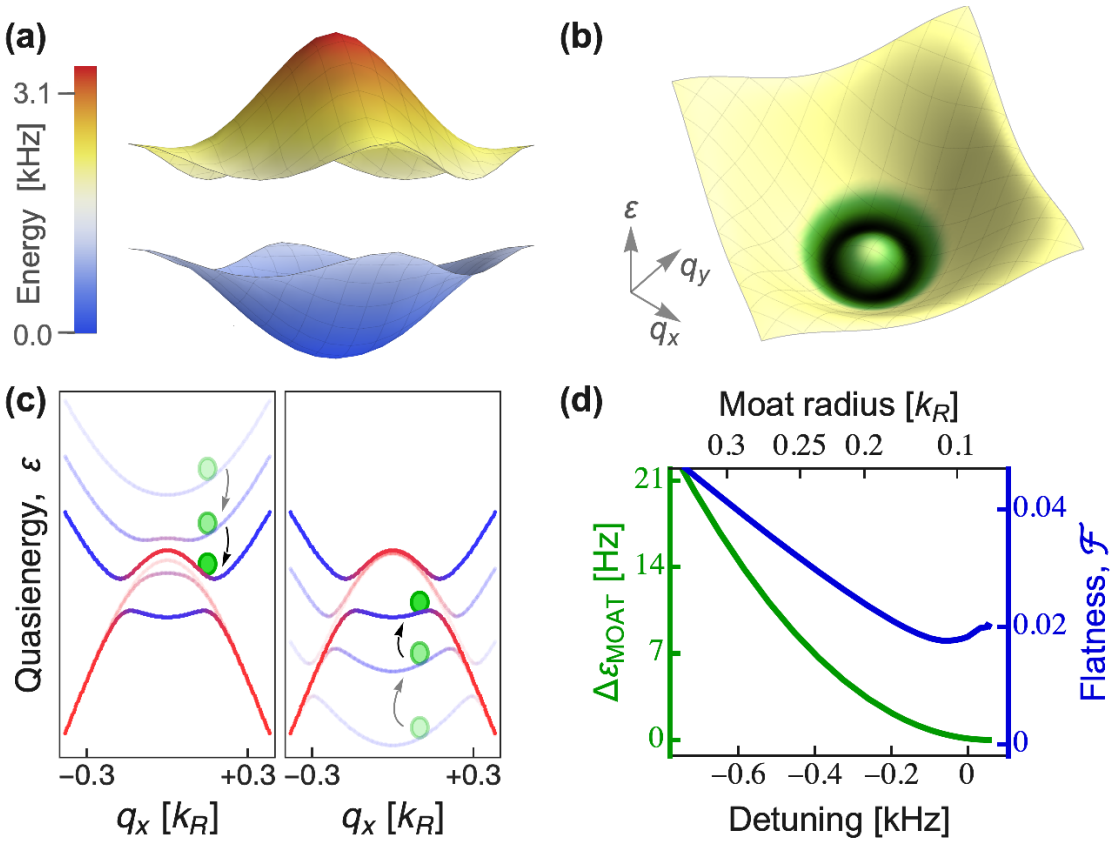

Figure 5.8: Production of a Mexican-hat band via amplitude modulation. (a) Lowest bare energy bands of the checkerboard lattice, plotted versus crystal momentum $\boldsymbol{q} = (q_x, q_y)$ over the first Brillouin zone. (b) Calculated Floquet-Bloch energy band with nearly degenerate moatlike minima, resulting from the hybridization of the bands shown in (a). (c) Cross section along q_x (with $q_y = 0$) of the quasienergy spectrum $\varepsilon(\boldsymbol{q})$ showing both dressed bands $\varepsilon_{1,2}$. Left panel: adiabatic preparation of a condensate, initially occupying the bare ground band, into the upper band by sweeping the drive frequency down, starting above resonance. Right panel: preparation into the lower band by sweeping the frequency up, starting below resonance. (d) Peak-to-peak variation of the Floquet energy ε along the bottom of the Mexican-hat dispersion, $\Delta\varepsilon_{\mathrm{MOAT}}$, and moat flatness $\mathcal{F}$ versus detuning of the drive. The moat radii are indicated in the upper axis.

along the Mexican-hat minimum than typical Raman SOC schemes [195–198]. Figure 5.8(d) presents two indicators of the MH band degeneracy calculated as a function of the detuning of the drive frequency f_m relative to the static (bare) band spacing at $\boldsymbol{q} = 0$. The magnitude of the peak-to-peak amplitude of ε along the ring-shaped minima, $\Delta\varepsilon_{\mathrm{MOAT}}$, is less than 21 Hz over the entire range. The calculated flatness $\mathcal{F}$, defined as the ratio of $\Delta\varepsilon_{\mathrm{MOAT}}$ relative to the local maximum of the band at $\boldsymbol{q} = 0$, is similar to the $\mathcal{F}$ determined in Ref. [41].

5.3 Experimental demonstration of an effective moat band

This section discusses the measurements and numerical analysis we carried out to confirm we had generated an effective ring-shaped band. All the experiments described in this section began with a BEC held in a hybrid trap, consisting of a crossed optical dipole trap and a vertically offset magnetic quadrupole trap. A 2D checkerboard lattice, discussed previously in Chapter 2 and depicted in real space in Figs. 2.4(c) and 2.5(b), was then adiabatically loaded in 200 ms to a depth V_0, with a staggered offset ΔV between neighboring sites. The explicit form of this checkerboard periodic potential is given by

$$V_{\mathrm{latt}}^{[\mathrm{S}]}(x,y) = -V_0 \times \frac{1}{4}\left[\cos(k_R x) + \cos(k_R y)\right] - \Delta V \times \left[\cos\left(\frac{k_R}{2}(x+y)\right)\right]^2 \left[\cos\left(\frac{k_R}{2}(x-y)\right)\right]^2, \tag{5.4}$$

where $k_R = 2\pi/\lambda$ (λ being the wavelength of the laser beam generating the lattice), V_0 is the amplitude of a square lattice with spacing $\lambda/2$ (referred to as the '$\lambda/2$ lattice'), and ΔV is the amplitude of a square lattice with spacing $\lambda/\sqrt{2}$ (referred to as the 'λ lattice'). The 'λ lattice' induces an energy offset ΔV between the (otherwise balanced) $\lambda/2$ lattice sites [labeled A and B in

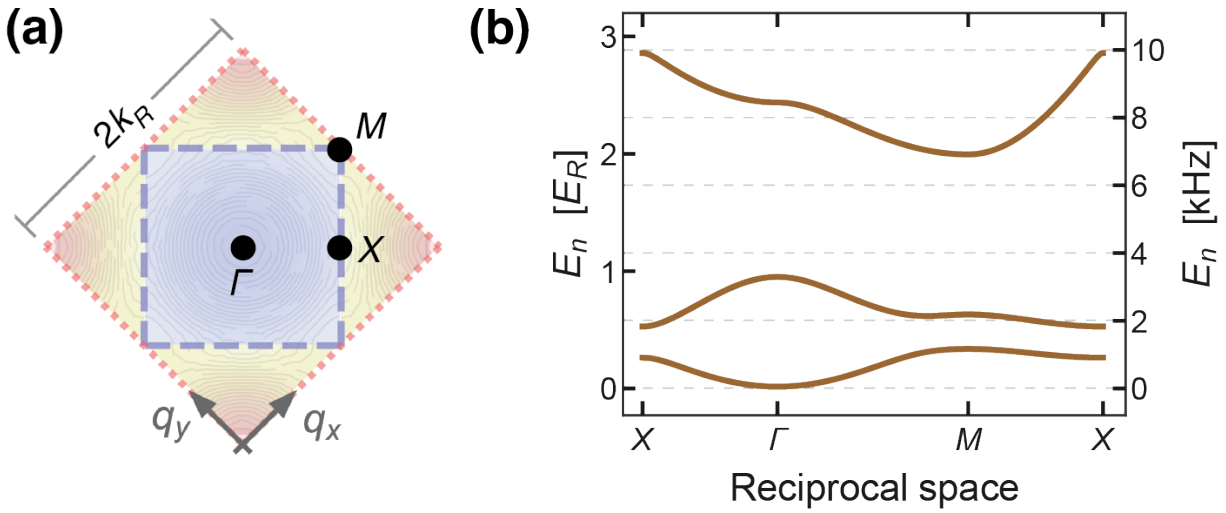

Figure 5.9: Brillouin zones and band structure for a checkerboard lattice with a depth $V_0 = 5.9(1)\,E_R$ and a tilt $0.44(1)\,E_R$. (a) Associated Brillouin zones. The first Brillouin zone BZ1 is enclosed by the dashed blue square, while the second Brillouin zone BZ2 is region bordered by the dotted red square and outside of BZ1. Contour profiles, corresponding to the three-dimensional plots of the ground and first excited bands displayed in Fig. 5.8(a), are here plotted (in an extended Brillouin zone scheme) over BZ1 and BZ2, respectively. (b) Band structure plotted along the segments $X - \Gamma - M - X$. The two lowest bands are both separated from the second-excited band by at least $h \times 5.2$ kHz.

Fig. 2.5(b)]. The first two Brillouin zones of the periodic two-dimensional potential $V_{\text{latt}}^{[\text{S}]}(x, y)$ are shown in Fig. 5.9(b). In this set of experiments, the parameters defining the lattice potential typically take the values $V_0 = 5.9(1)\,E_R = h \times 20.4(3)$ kHz, $\Delta V = 0.44(1)\,E_R = h \times 1.52(3)$ kHz and $\lambda = 813$ nm. (For rubidium-87 the single-photon recoil energy is $E_R = \hbar^2 k_R^2/2m = h \times 3.5$ kHz, where $k_R = 2\pi/\lambda$ is the single-photon wave-vector.) This resulted in the two lowest bare bands having a spacing at $\boldsymbol{q} = 0$ of $h\Delta_0 = h \times 3.2$ kHz, both separated from the next adjacent (weakly-coupled) excited band by no less than $h \times 5.2$ kHz [see Fig. 5.9(b)]. In the presence of the optical lattice, the trap frequencies were $\omega_\perp/2\pi = 11(1)$ Hz, $\omega_z/2\pi = 50(2)$ Hz, and the atomic cloud (containing approximately 10^4 atoms) possessed an average mean-field interaction

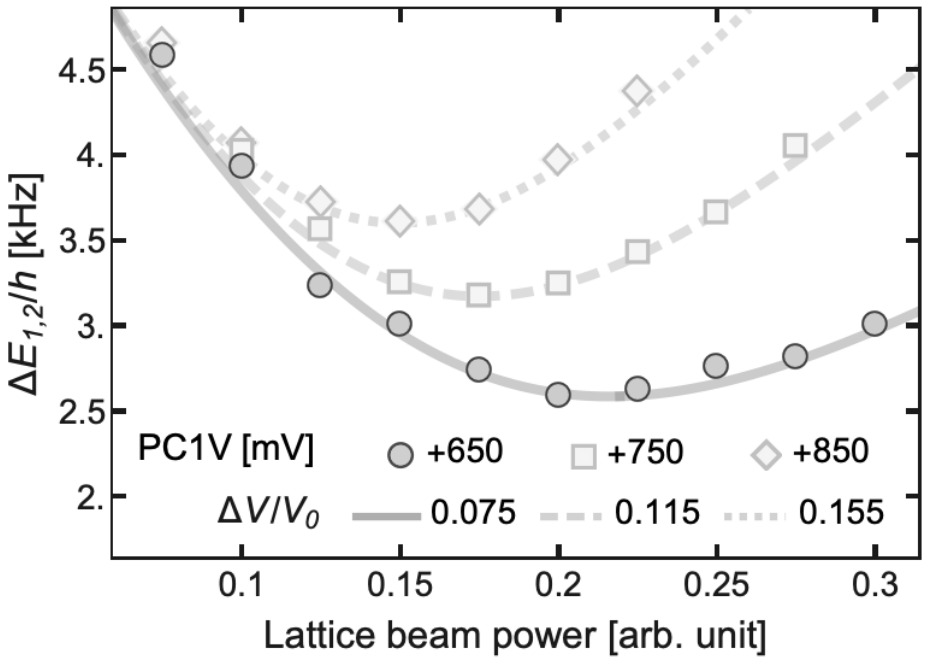

Figure 5.10: Calibration of $\Delta V/V_0$ from the energy difference $\Delta E_{1,2}$ between the lowest bare bands at $\boldsymbol{q} = 0$. The tilt-to-depth ratio $\Delta V/V_0$ is deduced from the minimum value of $\Delta E_{1,2}$ for different values of the lattice beam power at fixed PC1V. Points in this figure correspond to the center frequencies resulting from fitting parametric heating spectra.

energy of approximately $h \times 125$ Hz, which dropped to $h \times 70$ Hz when the lattice was absent.

The ratio between the depths of the λ and $\lambda/2$ lattices, $\Delta V/V_0$, is determined by the voltage PC1V applied to the high-voltage input Pockels cell PC1 (see Fig. 2.3). To calibrate this ratio, we measured, using vibrational heating spectroscopy of a BEC loaded into the lattice, the energy difference $\Delta E_{1,2}$ between the lowest bare bands at $\boldsymbol{q} = 0$, for different values of the lattice beam power, see Fig. 5.10. The value of $\Delta V/V_0$ is inferred from the minimum value of $\Delta E_{1,2}$, at a fixed PC1V. The values of V_0 and ΔV, that fully characterize $V_{\text{latt}}^{[\text{S}]}(x, y)$, are then determined from $\Delta E_{1,2}$ and the measured $\Delta V/V_0$.

We chose this calibration approach because both our lattice depth V_0 and its tilt ΔV are

relatively small. Alternative calibration techniques, such as Kapitza-Dirac diffraction or the tilt ("G"-) measurement illustrated in Fig. 4.2, are typically reliable only when using larger values of V_0 and ΔV, with the parameters of shallower lattices being measured only indirectly. Since the results presented in this chapter are related to a near-resonance modulation protocol, and their interpretation depends heavily on having an accurate value of the spacing between the lowest bare energy bands, we preferred a calibration method that allowed for a direct measure of the parameters V_0 and ΔV.

5.3.1 Functional form of the lattice modulation

We modulated the amplitude of our optical lattice by varying the intensity of the beams through the RF power applied on an AOM placed along the path of the lattice light. A feedback loop, whose error signal was constructed from a beam sample acquired near the main science chamber, actively stabilized the light intensity to a dynamically varying setpoint defining the modulation profile.

The amplitude modulation we used to hybridize the energy bands of the static lattice $V_{\text{latt}}^{[\text{S}]}$ [Eq. (5.4)] has the explicit form

$$V_{\text{latt}}(x, y, t) = \left[1 + \alpha_m \cos\left(\frac{2\pi}{T} t\right)\right] V_{\text{latt}}^{[\text{S}]}(x, y), \tag{5.5}$$

with α_m and T denoting, respectively, the strength and the period of the drive. (Unless otherwise noted, $\alpha_m = 0.12$ in all experiments described later in this chapter.)

For some of the measurements that will be described later, we required a smooth turn-on of the modulation strength, which was accompanied by a simultaneous frequency ramp. In those

cases, the complete functional form of the drive was given by

$$\mathcal{V}_{\text{latt}}(x, y, t) = [1 + \alpha_m \mathcal{P}(t)]\, V_{\text{latt}}^{[\text{S}]}(x, y), \tag{5.6}$$

where

$$\mathcal{P}(t) = \begin{cases} \mathcal{E}(t) \cos\left(2\pi \left(f_{\text{i}} + \frac{1}{2}\Delta f \, \frac{t}{\tau_1}\right) t\right) & t \leq \tau_1 \\ \cos\left(2\pi f_{\text{f}}\, t + \theta_m\right) & t > \tau_1 \end{cases}. \tag{5.7}$$

Here, $\mathcal{E}(t)$ is the envelope characterizing the gradual turn-on of the modulation strength, f_{i} and f_{f} are the initial and final frequencies, Δf is the difference between the frequencies ($\Delta f = f_{\text{f}} - f_{\text{i}}$), τ_1 is the sweep time (taken to be 12 ms throughout these experiments), and θ_m is a phase that ensures $\mathcal{P}$ has no discontinuities at time τ_1. As shown in Fig. 5.11, we smoothly ramped on the modulation, starting off-resonantly, with the exponential envelope $\mathcal{E}(t)$ while ramping the frequency to its final value in τ_1 ms.

5.3.2 Calculation of noninteracting Floquet-Bloch bands

The unmodulated energy spectrum $E_n(\boldsymbol{q})$ and the Bloch states

$$\psi_{\text{B},n} = e^{i\boldsymbol{q}\cdot\boldsymbol{r}} e^{-iE_n t/\hbar} \chi_n(\boldsymbol{r}; \boldsymbol{q}) \tag{5.8}$$

are calculated using an 81×81 matrix representation [see Eq. (2.8)] of the static lattice Hamiltonian in a plane wave basis. To determine the single-particle quasienergy spectrum $\varepsilon_n(\boldsymbol{q})$ of the

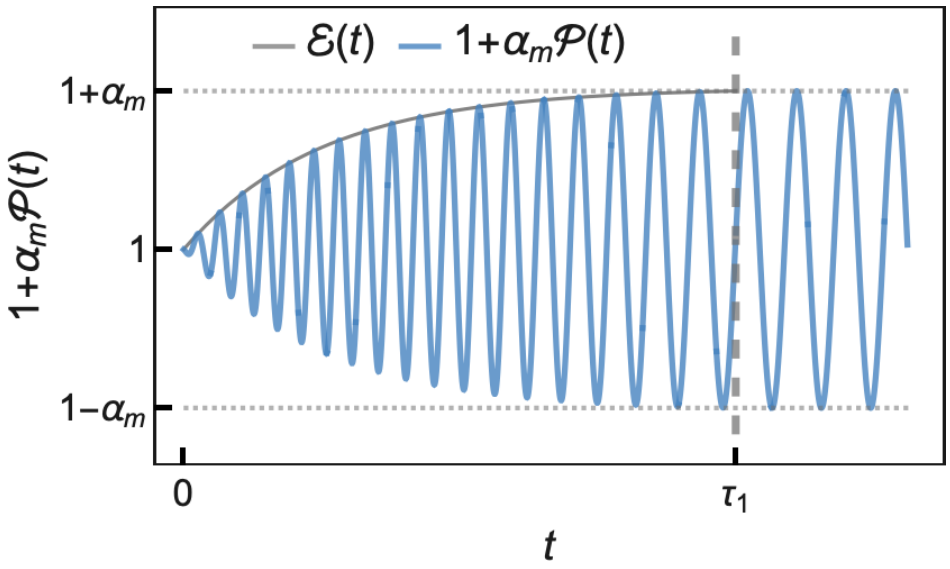

Figure 5.11: Example of gradual turn-on of amplitude modulation as described by Eq. (5.6). The modulation strength is smoothly ramped on during $\tau_1 = 12$ ms (indicated by vertical dashed line) while the frequency is simultaneously swept from its initial value to its final value. After the sweep, the modulation occurs for a variable time at the final frequency.

driven Hamiltonian and the corresponding Floquet-Bloch states

$$\phi_n = e^{i\boldsymbol{q}\cdot\boldsymbol{r}} e^{-i\varepsilon_n t/\hbar} u_n(\boldsymbol{r}, t; \boldsymbol{q}), \tag{5.9}$$

with time- and space- periodic Floquet mode u_n, we solve the Schrödinger equation

$$i\hbar \frac{\partial \phi_n}{\partial t} = \left[-\frac{\hbar^2}{2m} \nabla_{\boldsymbol{r}}^2 + V_{\text{latt}}(\boldsymbol{r}, t) \right] \phi_n, \tag{5.10}$$

with V_{latt} given by Eq. (5.5), by calculating the associated unitary time-evolution operator $U(\boldsymbol{q}, T)$ over a single period T of the drive [144, 148] [see Eq. (3.4)]. The operator U is computed using the Suzuki-Trotter product decomposition [see Eq. (3.9)] with > 600 steps, where all factors are represented either in a subset of the plane wave basis (81×81 matrices) or in a subset of the Bloch basis (2×2 matrices). A representative spectrum ε is shown in Fig. 5.12 for the following parameters: $V_0 = 5.9\, E_R$, $\Delta V = 0.44\, E_R$, $\alpha_m = 0.12$ and $T = 1.17\, h \cdot E_R^{-1} = 339\ \mu$s. The Floquet bands ε_1 and ε_2 (figure 5.12, thick lines), corresponding to the lowest bands of the unmodulated lattice, are well isolated from the other Floquet bands, with only small avoided crossing couplings to higher bands (not visible in Fig. 5.12). We found that a two-band model provides an accurate description of the system.

The rotational symmetry of the moat band minima (flatness and radial position of the minima) depends on the respective symmetries of the coupled bare bands and the $\boldsymbol{q}$-dependent coupling matrix element between the bands, both of which contribute to the shape of the hybridized bands. Fig. 5.13(a) shows the quasienergy ε_M and position of the moat band minima for two different detunings, with all other conditions the same as in Fig. 5.8(d). The variation of ε_M has

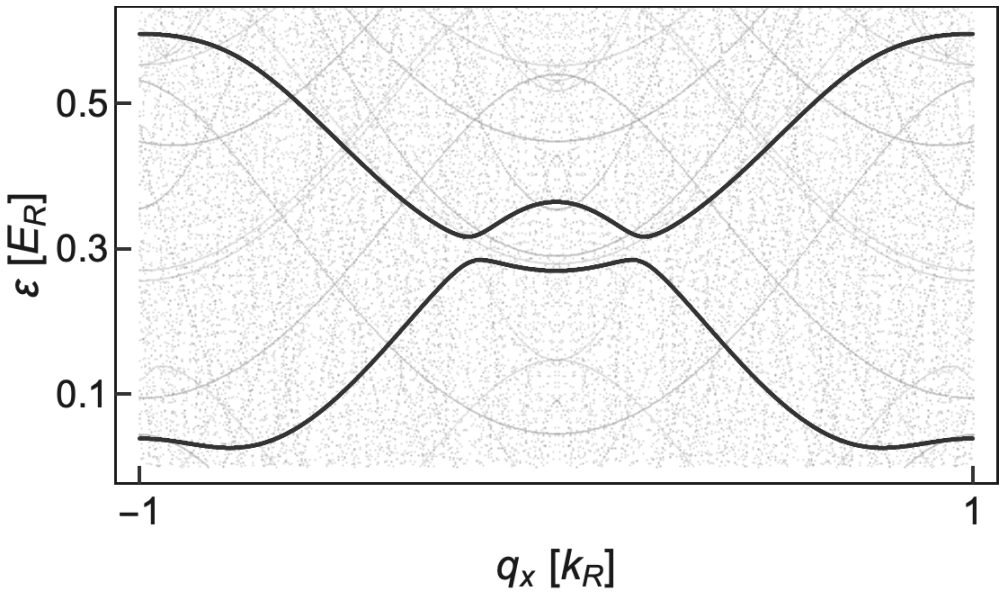

Figure 5.12: Floquet quasienergy spectrum (small dots) obtained using the Trotter decomposition of U in a plane wave basis consisting of 81 momentum states. Thick lines indicate the quasienergies of the dressed states possessing the largest overlap with the lowest bare Bloch bands. On the scale of this figure, the two-state Bloch basis calculation is indistinguishable from the 81 plane waves calculation.

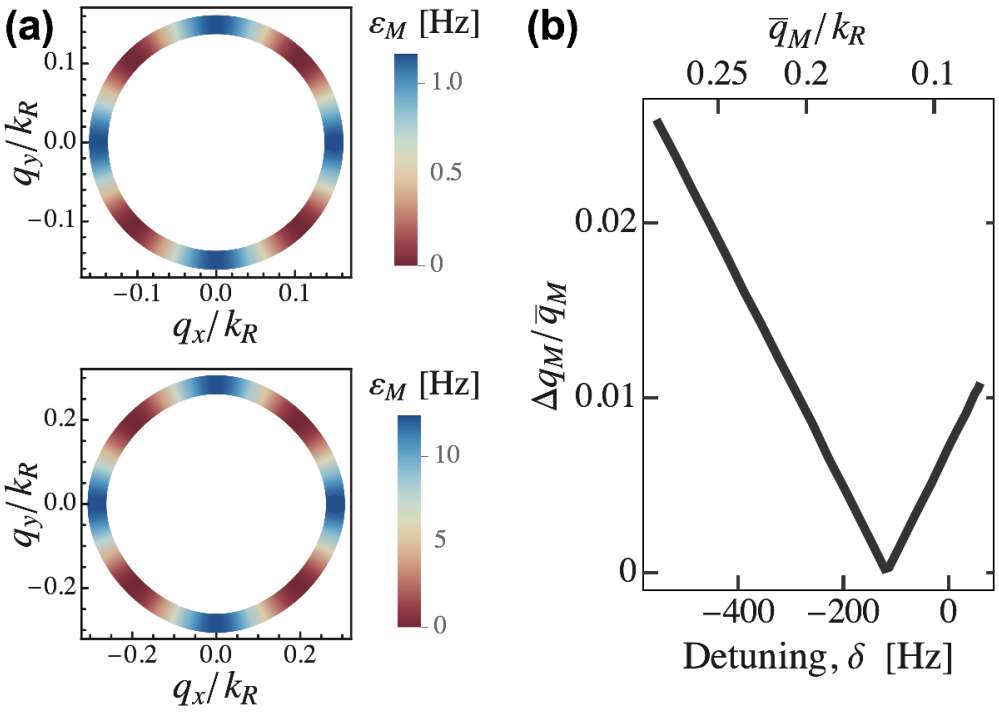

Figure 5.13: (a) Examples of moat minima for different values of the modulation detuning δ. Upper (lower) panel corresponds to $\delta = -130$ Hz ($\delta = -550$ Hz), which yields a mean value $\bar{q}_M$ of the radial position of $\bar{q}_M = 0.15\, k_R$ ($\bar{q}_M = 0.28\, k_R$). (b) Variation with δ of the difference Δq_M between the largest and smalles values of the radial position relative to the mean value $\bar{q}_M$.

the four-fold symmetry of the Brillouin zone. For the larger detuning, slight deviations from a circle can be seen, where the moat minima resembles a bit more a rounded square (*squircle*). The fractional variation $\Delta q_M/\bar{q}_M$ of the radial positions q_M of the minima is plotted in Fig. 5.13(b) as function of detuning δ, which indicates less than 2.5% variation in moat radius over the range shown. Due to the interplay of the bare band shape and the band coupling shape, at $\delta \approx -130$ Hz, the moat is a circle with constant radial positions of the minima.

5.3.3 Quench spectroscopy

We first corroborated the effectiveness of amplitude modulation to hybridize (i.e., induce avoided crossings between) the lowest bare bands by measuring the spacing $\Delta\varepsilon(\boldsymbol{q})$ between the dressed bands for two different detunings, $\delta = f_m - \Delta_0$. To extract the values of $\Delta\varepsilon$ we observed the bare band population dynamics after a sudden quench into the dressed bands [see Fig. 5.14(b) for an example of the oscillations in the band population]. Similar spectroscopic techniques are reported in Refs. [200, 201]. This quench protocol, sketched in Fig. 5.14(a), began with the atoms loaded in the lowest band E_1 of the static lattice, followed by a sudden turn-on of the modulation. While the lattice was driven, the condensate wave function was approximately described by $s_{\text{quench}}(t) = c_1\phi_1(t) + c_2\phi_2(t)$, where $\phi_{1,2}(t)$ are the Floquet states corresponding to the bands $\varepsilon_{1,2}$ [given by Eq. (5.9)], and $c_{1,2}$ are constants whose values are set by the initial condition $s_{\text{quench}}(t = 0) = \psi_{\text{B},1}$, the Bloch state associated with the ground band [equation (5.8)]. After a variable time t_{aq}, we measured the relative population in the static ground band, $|\langle\chi_1|s_{\text{quench}}(t)\rangle|^2$ using a band map [202], where the lattice was ramped off in $800\ \mu$s. This relative population $|\langle\chi_1|s_{\text{quench}}(t)\rangle|^2$ oscillated at frequencies dominated by the Floquet quasienergy difference $|\varepsilon_2(\boldsymbol{q}) - \varepsilon_1(\boldsymbol{q})|$. Examples of the measured time evolution along with fits to exponentially damped sinusoids are shown in Fig. 5.14(b).

Figure 5.15 shows the measured band spacing $\Delta\varepsilon$ at different quasimomenta q. For measurements at nonzero quasimomenta, a kick is imparted to the condensate before the modulation starts, by suddenly translating the magnetic quadrupole field. This induces oscillatory motion of the cloud along a line passing through the center of the trap in the unmodulated lattice. For detuning $\delta = -550$ Hz, the measured dressed band spacing has a minimum $\simeq 200$ Hz ($0.06\ E_R/h$)

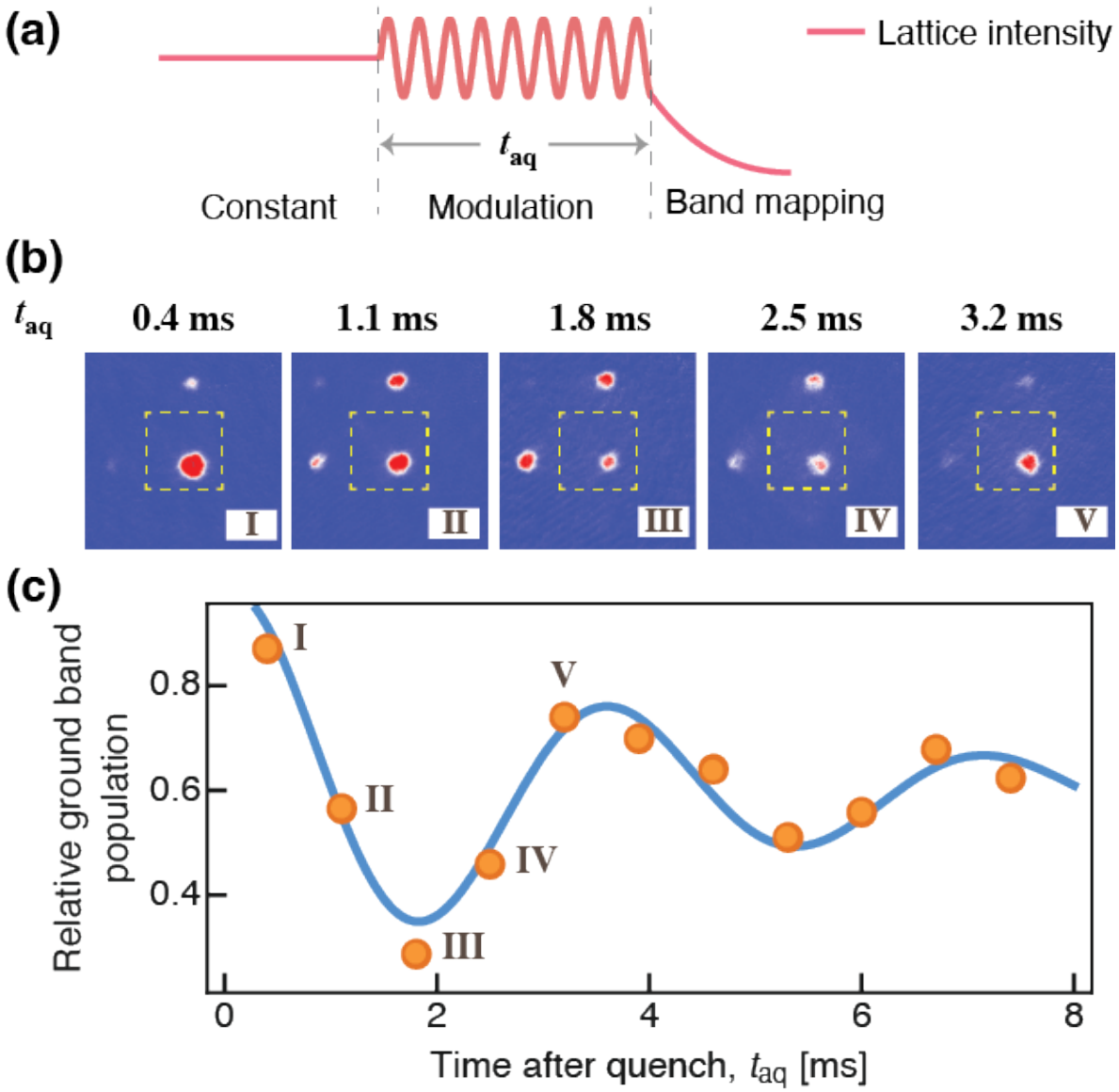

Figure 5.14: Dynamics of the bare band population after a quench into the modulated Hamiltonian. (a) Quench protocol began with an unmodulated lattice, followed by a sudden turn-on of the modulation whose duration was t_{aq}. (b) Example of observed variation in the relative band populations as a function of the time t_{aq} the cloud was held in the driven lattice following the quench. The amplitude modulation was suddenly turned on with a strength $\alpha_m = 0.18$. Starting in the ground band, the population oscillates between the ground and excited bands. (c) The relative ground band population is fitted to a damped sinusoid (dotted and dashed lines). For the example shown here, the measured frequency of the oscillation (corresponding to the effective band spacing) was $\Delta\varepsilon = 280$ Hz.

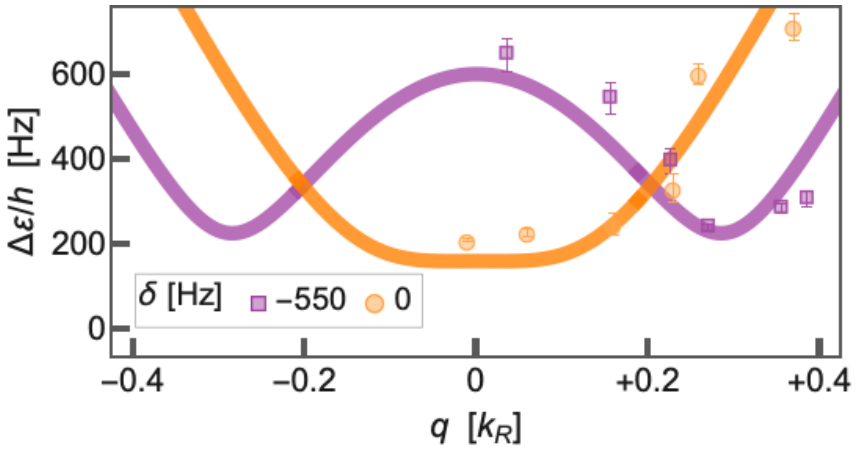

Figure 5.15: Dressed band spacing $\Delta\varepsilon$ between the Floquet bands as a function of crystal momentum q, measured along a line passing through the center of BZ1. The circle and square markers correspond to detunings $\delta = 0$ Hz and $\delta = -550$ Hz. Experimental values of $\Delta\varepsilon$ were obtained from quench spectroscopy, as illustrated in Fig. 5.14. Solid lines indicate calculated spacings. (For $\delta = -550$ Hz only, $\alpha_m = 0.18$.)

at $q \simeq 0.3\ k_R$, as expected from calculations.

5.3.4 Bare band admixture of the Floquet states

In order to adiabatically prepare the condensate in a single dressed band, the amplitude modulation coupling the two bands was slowly turned on, starting off-resonance, using the modulation profile described by Eq. (5.6) and illustrated in Fig. 5.11. The magnitude and frequency of the coupling were simultaneously ramped to their final values in 12 ms starting at a detuning $|\delta| > 600$ Hz. The direction of the frequency sweep determined which dressed band the BEC was loaded into: a sweep starting blue (red) detuned and ending close to resonance prepared atoms in the upper (lower) dressed band [see Fig. 5.8(c)].

We measured the bare band admixture of the experimentally prepared state immediately

after the 12 ms ramp [see Fig. 5.16(a)] as a function of q and compared it to the expected bare state populations [see Fig. 5.16(c)]. The theoretical profiles from a non-interacting Floquet calculation [Fig. 5.16(c), dashed lines] captured the magnitude of the admixture, particularly near the center of the band. A nonlinear mean-field calculation based on the time-dependent GP equation improved the overall agreement with the data [Fig. 5.16(c), solid lines].

We complemented the admixture profile along a single direction within BZ1, shown in Fig. 5.16(c), with the 2D bare band admixture extracted from single-shot TOF images of a heated cloud having a significant spread around the center of the first Brillouin zone (BZ1), showing the 2D nature of the moat band. To clarify how these TOF images were produced, Fig. 5.17(a) shows the TOF images of BECs with different atom number loaded into the dressed lattice band, with all other conditions the same. Instability heating occurred during the loading process, and the final condensate fraction depended on the initial number of BEC atoms, as expected for an interaction driven instability. In Fig. 5.17(b) we show single-shot measurements of the excited band admixture (lower row) extracted from the TOF images (upper row) under conditions similar to those in the right-most panel of Fig. 5.17(a). The inability to adiabatically preserve band populations near the band edge while "band mapping" [203] leads to discrepancies with the expected admixture near the band edge. The admixture is more azimuthally homogeneous than the raw populations [Fig. 5.17(c)], whose distribution was affected by both stochastic and systematic fluctuations of the initial momentum of the BEC.

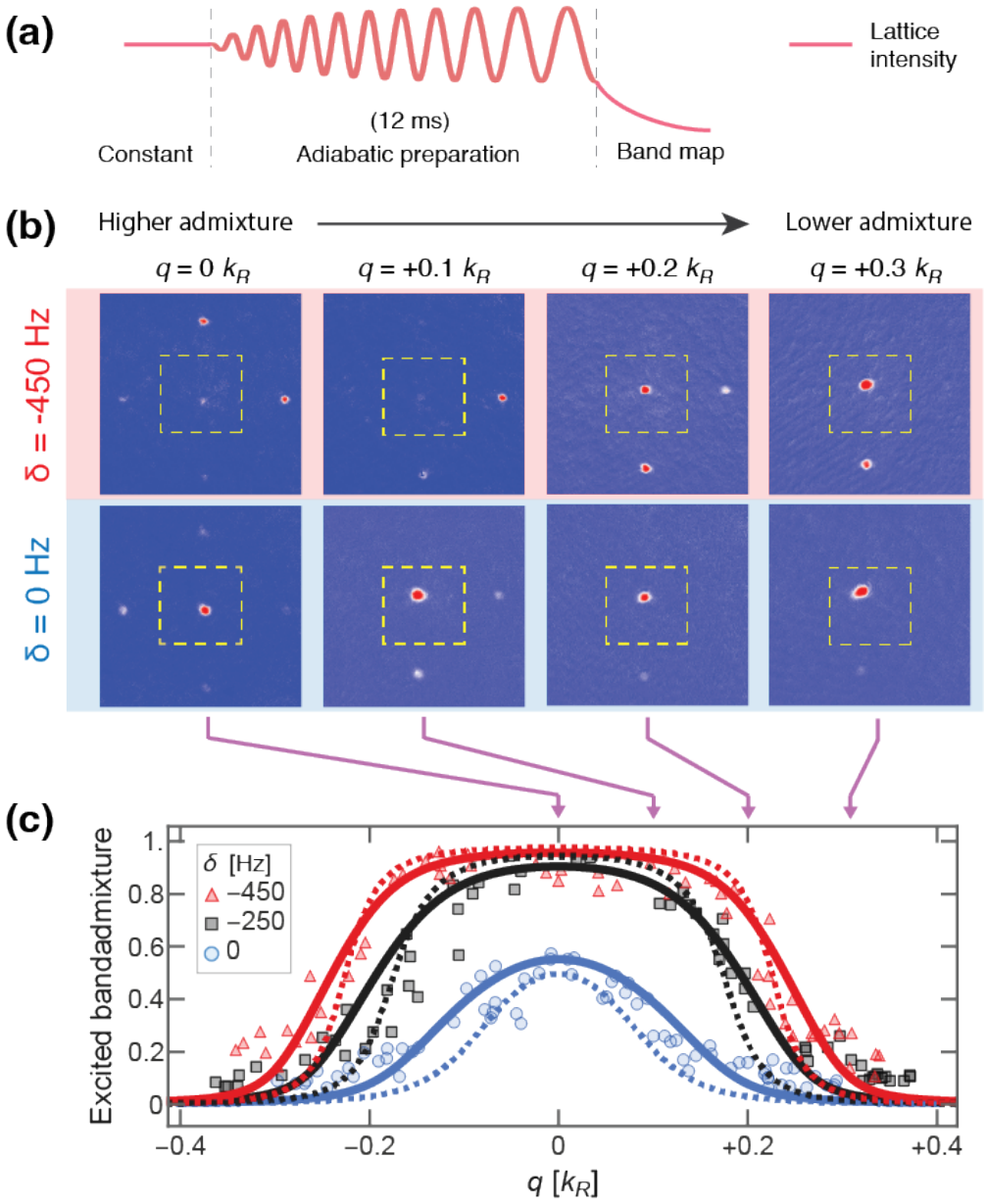

Figure 5.16: Bare band admixture in the Floquet bands as a function of crystal momentum q, measured along a line passing through the center of BZ1. (a) The admixture is obtained by band mapping an adiabatically prepared Floquet state in the moat band, obtained after a 12 ms modulation ramp. (b) TOF images after band mapping for moat bands with $\delta = 0$ and $\delta = -450$ Hz, and different condensate q. (b) Measured bare excited band admixture for Floquet states in the moat band. The solid (dashed) lines are the admixture calculated with (without) mean-field interactions. Marker shapes correspond to different modulation detunings.

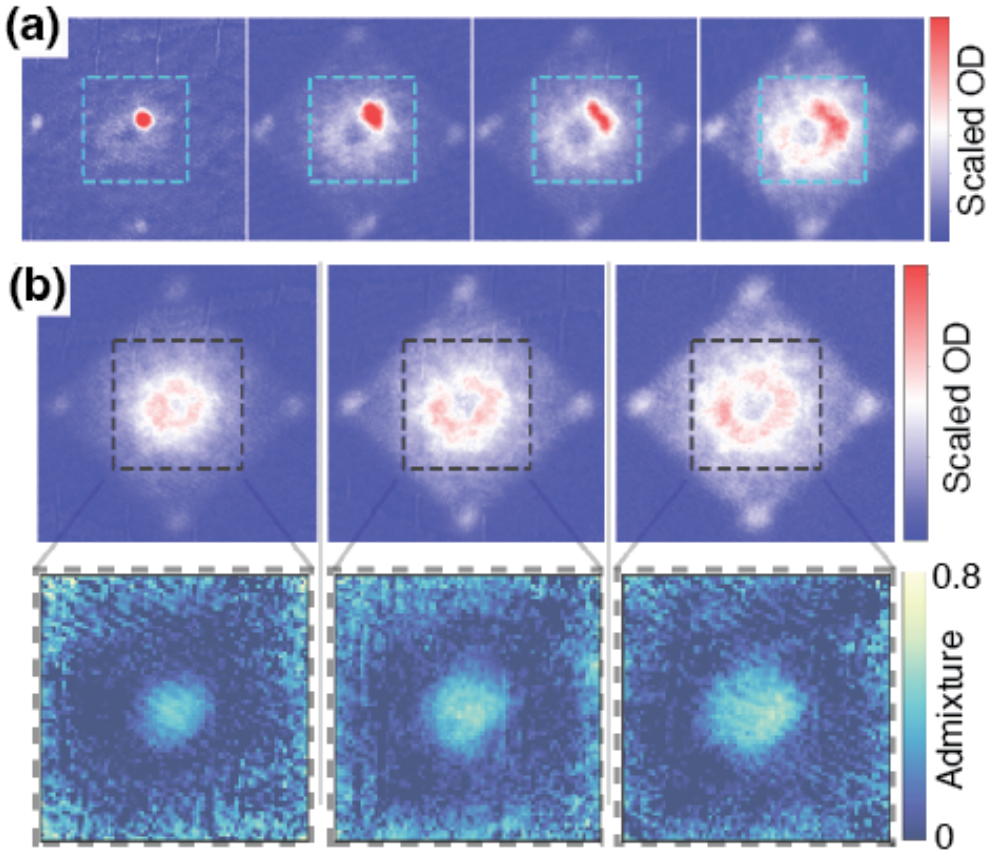

Figure 5.17: (a) TOF images of BECs adiabatically prepared in a dressed ring-shaped band for different number N_a (and, hence, density) of atoms in the condensate, with all other experimental conditions being the same. From left to right, the values of N_a are approximately 2×10^3, 20×10^3, 40×10^3 and 80×10^3. Red regions correspond to higher optical depth (OD). Dashed lines outline the edges of the first Brillouin zone (BZ1). Color scale has been adjusted for each figure for visualization purposes. Images were obtained after a 800 μs bandmap. (b) Upper row: TOF images obtained under similar conditions to those in the right-most panel of (a) with a high N_a and the crystal momentum of the initial condensate (before the start of the modulation) lying close to the center of BZ1. The three images correspond to different values of the modulation detuning δ, with all other parameters being the same. From left to right the values of δ are -200 Hz, -300 Hz and -400 Hz. Lower row: Corresponding excited band admixture profiles plotted over BZ1. Lighter colors indicate higher values of the excited band admixture.

Determination of quasimomentum from time-of-flight images

To extract an accurate value of the crystal momentum q from TOF images, we required a model of the dynamics of the cloud in the trap. This point will be explained below, along with an illustration of how an improper determination of q significantly distorts the profiles presented in Fig. 5.16(c).

Time-of-flight (TOF) absorption images are captured 30 ms after release from the trap. When measuring the plane wave composition, the lattice and trapping potential are abruptly turned off at the same time in order to project the state onto nearly free-particle states. When measuring the population in the bare bands, we 'band map' the state by turning off the lattice in 800 μs, which was chosen to be adiabatic with respect to band excitation but fast with respect to interaction and trap time scales.

We calibrate the dimensions of the first Brillouin zone BZ1 in TOF images using the spacing between lattice diffraction peaks. Since the condensate position after time of flight $\boldsymbol{r}_{\text{TOF}}$ is determined not only by its quasimomentum $\boldsymbol{q}$, but also by its initial position within the trap $\boldsymbol{r}_{\text{trap}}$, namely,

$$\boldsymbol{r}_{\text{TOF}} = \frac{\hbar}{m}\boldsymbol{q}\, t_{\text{TOF}} + \boldsymbol{r}_{\text{trap}}, \tag{5.11}$$

where t_{TOF} ($= 30$ ms) is the time of flight, a simple linear scaling of $\boldsymbol{r}_{\text{TOF}}$ by the size of BZ1 is not enough to determine an accurate estimate of $\boldsymbol{q}$.

To properly account for the value of $\boldsymbol{r}_{\text{trap}}$ from the position after time of flight, we model

the oscillatory evolution of $\boldsymbol{r}_{\text{trap}}$ and $\boldsymbol{q}$ using semiclassical equations of motion

$$\frac{d\boldsymbol{q}}{dt} = \frac{1}{\hbar}\boldsymbol{f}_{\text{trap}}(\boldsymbol{r}_{\text{trap}}), \quad \frac{d\boldsymbol{r}_{\text{trap}}}{dt} = \nabla_{\boldsymbol{q}} E, \tag{5.12}$$

where $\boldsymbol{f}_{\text{trap}}$ is the force due to the harmonic confinement, and E is the dispersion associated with the unmodulated lattice.

Figure 5.18(a) compares the displacement of the condensate after time of flight, d_{TOF}, relative to its equilibrium position and its associated quasimomentum contribution $\hbar q t_{\text{TOF}}$ for motion along a straight line and conditions matching those in our experiment. The contribution of $\boldsymbol{r}_{\text{trap}}$ to the displacement d_{TOF} is sensitive to the dispersion E. In Fig. 5.18 we show the values of q calculated assuming either a free-particle (dashed line) or a bare lattice (dotted line) dispersion. To indicate the impact of the dispersion used to calculate q from $\boldsymbol{r}_{\text{TOF}}$, we show in Fig. 5.18(b) the red points presented in Fig. 5.16(c), plotted against the different quantities depicted in Fig. 5.18(a). Due to the fact that $\boldsymbol{r}_{\text{trap}}$ is out of phase with $\hbar q t_{\text{TOF}}$, the admixture has a non-single valued dependence on the directly measured d_{TOF} (left panel). This effect is decreased when plotting versus q determined using the free particle dispersion (middle panel), and is almost entirely removed when plotting the admixture against the q determined using the bare lattice dispersion (right panel).

5.3.5 Group velocity of the Floquet states

The dispersion $\varepsilon(\boldsymbol{q})$ determines the condensate's center of mass velocity v_g, which is related to the gradient of the Floquet band according to the equation

$$\nabla_{\boldsymbol{q}}\varepsilon = \hbar\langle v_g\rangle_T, \tag{5.13}$$

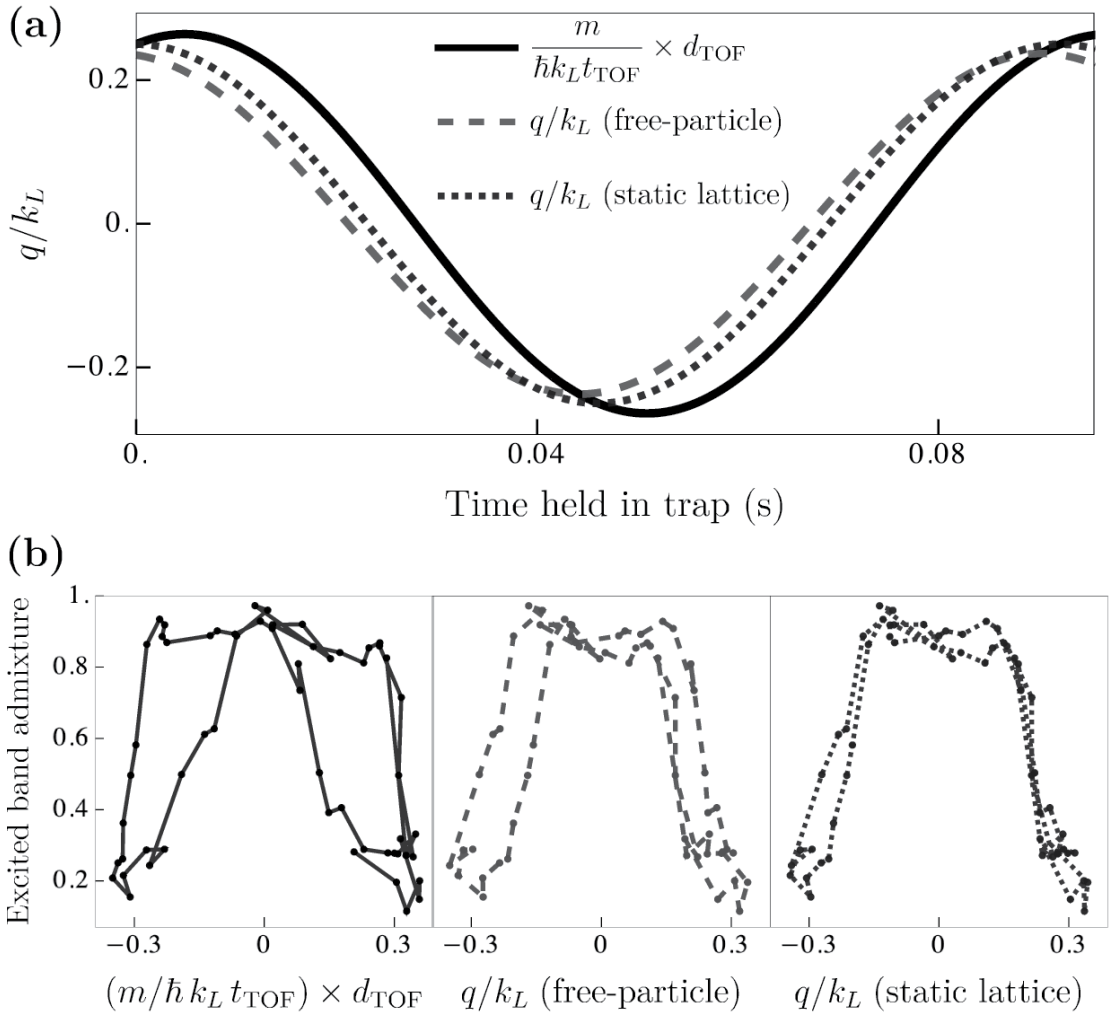

Figure 5.18: Determination of crystal momentum from TOF images. (a) Displacement d_{TOF} after time of flight (scaled by the factor $m/\hbar k_R t_{\mathrm{TOF}}$) for motion along a straight line as a function of the time held in the trap (black thick curve). Expected quasimomentum contribution to d_{TOF} (accounting for the motion in the trap), when E is the free-particle dispersion (dashed curve) and when E is the dispersion associated with a static lattice (dotted curve). (b) Excited band admixture data, corresponding to the red points in Fig. 5.16(c), when plotted against the (scaled) raw TOF position d_{TOF} (left panel), q calculated according to a free-particle dispersion (middle panel), and q calculated according to the static lattice dispersion (right panel).

where the symbol $\langle \ldots \rangle_T$ indicates time-average over a single period $T = 1/f_m$ of the modulation. The validity of Eq. (5.13) is not obvious as the time average of an observable over micromotion does not in general equal the Floquet effective quantity. This relation can be found, for example, in Ref. [204], where it was discussed within the context of a particle in a periodic potential subject to a uniform time-periodic force, and was motivated by invoking the Hellmann-Feynman theorem. The derivation of Eq. (5.13) for a periodically modulated lattice is outlined in Appendix B, where the explicit form of the micromotion term for v_g is also presented. A generalization of this equation to a nonlinear mean-field context, where the wave function of the condensate is described by the time-dependent GP equation, is also included in Appendix B.

We measured v_g under the same conditions used for the admixture profile [Fig. 5.16(c)], except that the bare band population detection was replaced by a diabatic snap-off of the lattice [see Fig. 5.19(a)], which projects the condensate onto its plane-wave components. Micromotion during the drive period gave rise to periodic instantaneous v_g, which we accounted for by averaging over different snap-off times relative to T. The values of v_g were extracted from time-of-flight (TOF) images, as the one shown in Fig. 5.19(b), by computing the mean velocity of the momentum peaks, weighted by their populations. TOF images resulting from a diabatic turn-off of the lattice reveal a time-periodic micromotion (characteristic of Floquet states [148]) set by the phase Θ of the drive at which the lattice is snapped off (maximum and minimum lattice depths during the modulation correspond, respectively, to $\Theta = 0$ and $\Theta = \pi$). Fig. 5.20 illustrates the micromotion-related effects on the population measurements used in the measurements of v_g. The measured $\langle v_g \rangle_T$ profile, presented in Fig. 5.19(c), is the result of averaging v_g at modulation phases 0, $\pi/2$ and π, corresponding to maximum, average and minimum lattice intensities. A vanishing group velocity for nonzero $\boldsymbol{q}$, a feature easily recognized in the black and red data, is a

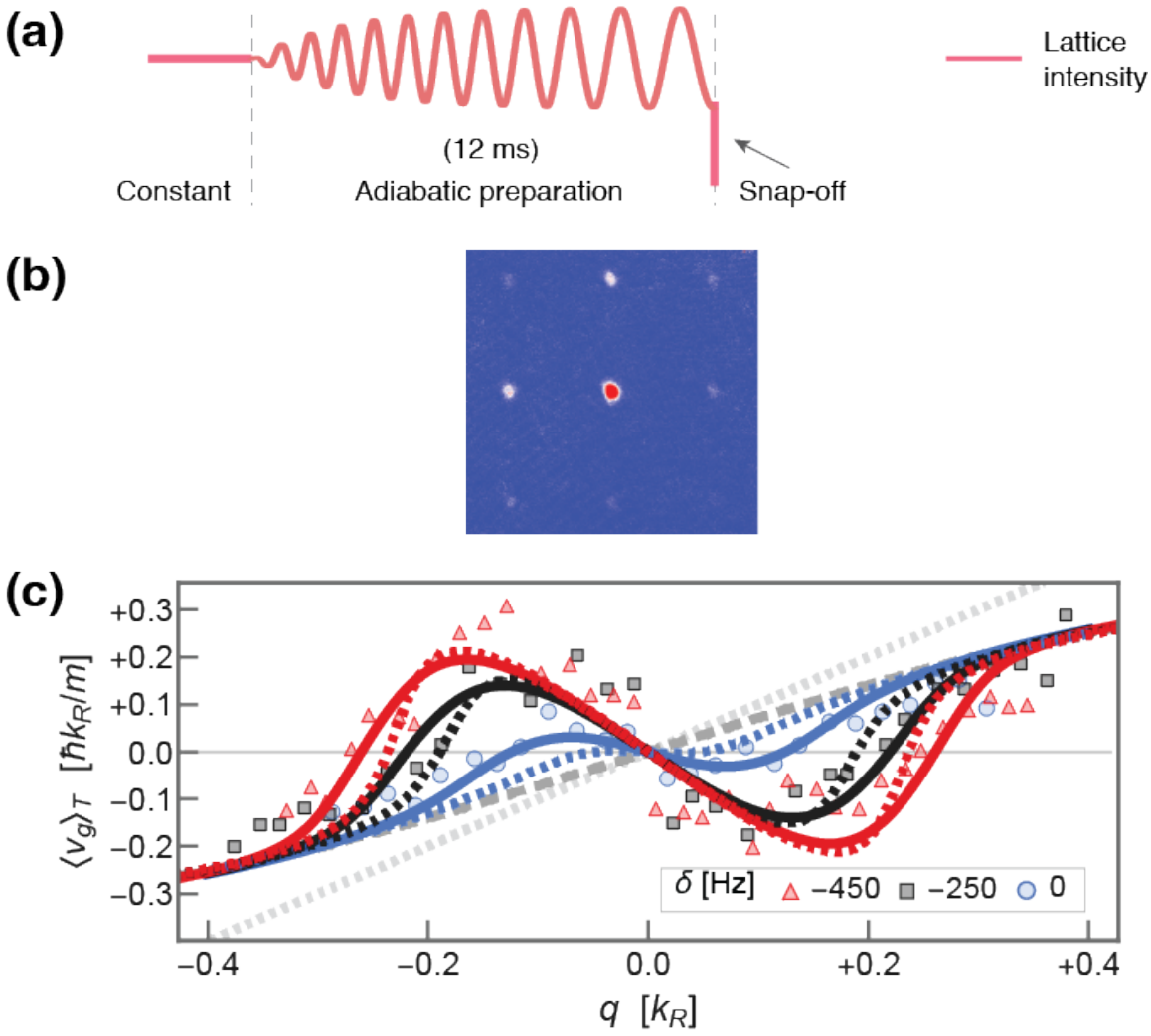

Figure 5.19: Group velocity profiles of the Floquet states as a function of crystal momentum q, measured along a line passing through the center of BZ1. (a) The group velocity is obtained by snapping off an adiabatically prepared Floquet state in the moat band, obtained after a 12 ms modulation ramp. (b) Example of a time-of-flight (TOF) images from which v_g was extracted by computing the mean velocity of the momentum peaks, weighted by their populations. (c) Time-averaged group velocity $\langle v_g \rangle_T$ for Floquet states in the moat band. The solid and dashed colored lines are calculated numerically assuming interacting and noninteracting particles, respectively. The dashed (dotted) gray lines indicates the group velocity associated with the bare lattice (free-particle) dispersion.

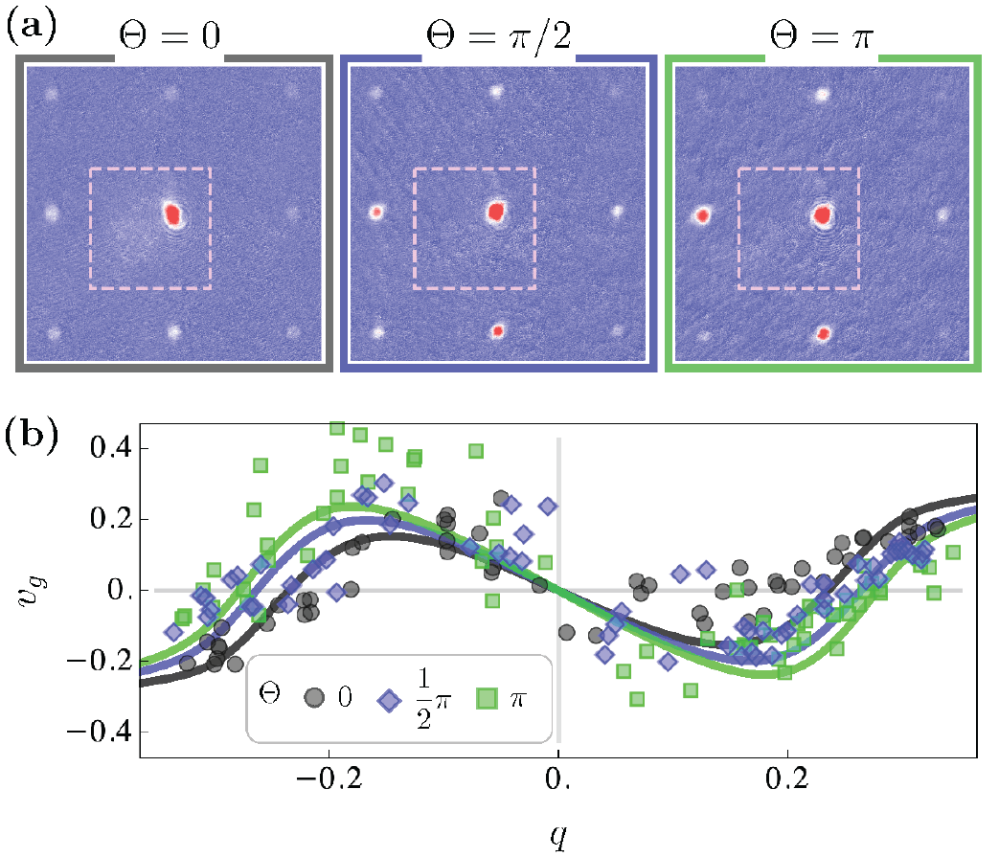

Figure 5.20: (a) Observed micromotion in TOF absorption images following snap-off of the lattice with $\Theta = 0$ (left), $\Theta = \pi/2$ (middle), and $\Theta = \pi$ (right). The Floquet state (and, hence, the quasimomenta) is the same for all TOF images shown here. Red regions indicate higher optical depth (OD). Dashed lines delineate the border of the first Brillouin zone. (b) Group velocity v_g as a function of the crystal momentum q for snap-off phases $\Theta = 0$ (circles), $\Theta = \pi/2$ (diamond) and $\Theta = \pi$ (square). These values of v_g correspond to the average $\langle v_g \rangle_T$ shown in Fig. 5.19(c) for $\delta = -450$ Hz (red triangles). Solid lines indicate predicted values from the Floquet-Bloch solutions to the GP equation.

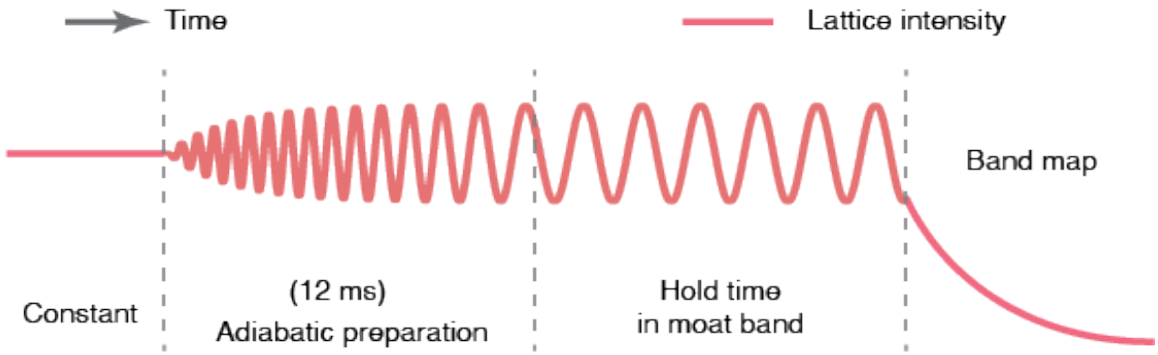

Figure 5.21: To measure the evolution of the crystal momentum of the BEC, we held the atoms in the Mexican-hat band for a variable time. The effective dispersion was adiabatically generated with a 12 ms modulation ramp.

clear signature of a band with a moat-like shape.

5.3.6 Effect of modified dispersion on the motional dynamics of the BEC

Spectroscopic measurements like those in Figs. 5.15, 5.16(c) and 5.19(c) provide information about dressed energies, but do not capture the modified dressed state behavior. While the data in Fig. 5.19(c) directly show the velocity, it is an instantaneous measurement. The modification of v_g should impact the motional dynamics of the BEC in the trap, if the heating of the BEC is sufficiently small relative to the timescale of the trap.

We employed the protocol sketched in Fig. 5.21 to observe the motional dynamics of the BEC in the trap after adiabatic preparation in the upper dressed state. Figure 5.22 shows the expected and observed evolution of crystal momentum $\boldsymbol{q}$ with an initial value away from zero, for bands with different moat radii. Theoretical calculations of the time evolution of the crystal momentum $\boldsymbol{q}$, superimposed on the corresponding dispersion, are displayed in Fig. 5.22(a). These

trajectories were computed using the quasiclassical equations of motion [205]

$$d\boldsymbol{q}/dt = \hbar^{-1}\boldsymbol{f}_{\text{trap}}(\boldsymbol{r}_c), \quad d\boldsymbol{r}_c/dt = \hbar^{-1}\nabla_{\boldsymbol{q}}\varepsilon, \tag{5.14}$$

where $\boldsymbol{f}_{\text{trap}}$ is the force exerted by the harmonic trap, $\boldsymbol{r}_c$ is the position of the condensate, and ε is the quasienergy spectrum inferred from the calibration of lattice parameters. Initial conditions $(\boldsymbol{q}_0, \boldsymbol{r}_{c0})$ were the same for all curves, and were chosen so that the trajectories have a significant dependence on the moat position. For the unmodulated case, the trajectory was a standard ellipse associated with the isotropic harmonic trap. For the modulated case, the change in effective mass significantly modified the atoms' response to the restoring force of the trap.

We experimentally verified the effect of the dressed band dispersion on the dynamics of a condensate. Using parameters that produced the effective bands in Fig. 5.22(a), we measured the position after time-of-flight as a function of the time held in the Mexican-hat band [see Fig. 5.22(b)], using a two-kick sequence that resulted in elliptical motion for the unmodulated case. (The scaled time-of-flight position is approximately equal to $\boldsymbol{q}/k_R$, with a small additional contribution from the position $\boldsymbol{r}_c$, as explained above in Section 5.3.4.) Although heating effects limited the longest hold time in the dressed band to 26 ms (black curve) and 21 ms (red curve), the effect of the modification of the dispersion on the motion in the trap is evident.

5.4 BEC stability in the Floquet generated Mexican-hat band

An important requirement for effective Floquet systems is that they are stable against heating. We also present our observations regarding the stability of condensed dressed states in both Floquet bands. We found that the observed instability rates are dominated by frequently over-

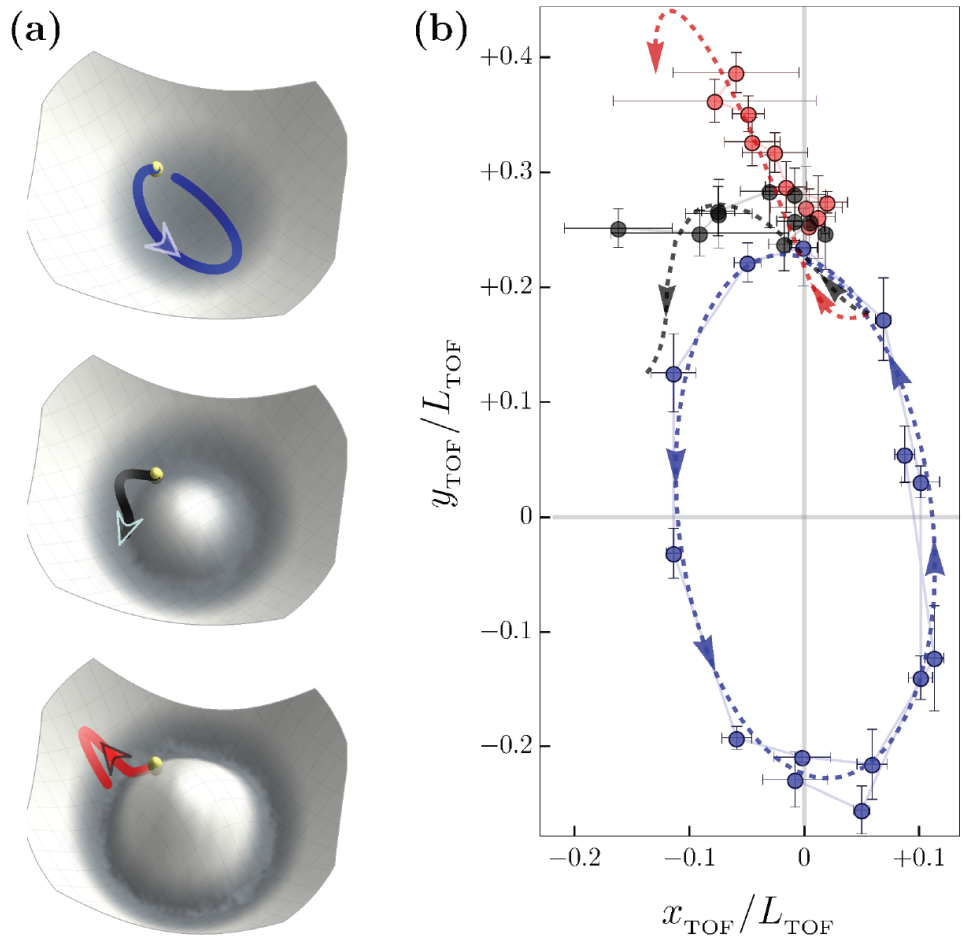

Figure 5.22: Time evolution of quasimomentum in different moat bands for the same initial conditions. (a) Predicted quasimomentum trajectories, plotted on top of the respective quasienergy spectrum. The yellow dots indicate the initial value $\boldsymbol{q}_0$ of the crystal momentum. Blue, black and red curves correspond to moats with radii 0 k_R (no modulation), 0.23 k_R, and 0.30 k_R. (b) Position after time of flight, $(x_{\mathrm{TOF}}, y_{\mathrm{TOF}})$, scaled by $L_{\mathrm{TOF}} = \hbar k_R / m T_{\mathrm{TOF}}$, for different times held in the effective moat band. Experimental data taken under conditions that yield dressed bands similar to those shown in (a). Blue points were obtained in the absence of modulation. Modulation frequencies for the black and red points are $f_m = 2.90$ and $f_m = 2.65$ kHz, respectively. Time elapsed for blue, black, and red points is 130, 26, and 21 ms, respectively. Dashed lines are the predicted position after time of flight for condensates held in the bands shown in (a).

looked dynamical instabilities inherent to the effective ring-shaped dispersion.

Figure 5.23(a) shows the measured condensate fraction decay rates for BECs loaded into the upper and lower hybridized band as a function of the detuning δ, which changes the moat radius q_{min} of the upper band. Rates were measured for condensates prepared at $|\boldsymbol{q}| = 0\ k_R$ and $|\boldsymbol{q}| \simeq 0.20\ k_R$. To keep an approximately constant value of $|\boldsymbol{q}|$ during the decay measurement, we carefully prepare the initial condition so that the resulting trajectory is circular. We find that the decay rates in the upper band increase dramatically when $|\boldsymbol{q}|$ approaches q_{min}, becoming difficult to measure for $|\boldsymbol{q}| < q_{\text{min}}$.

To understand the condensate decay, we modeled the system with a periodically driven GP equation and calculated condensate depletion rates using a linear stability analysis, as outlined in Section 3.3.2 [see Eqs. (3.39) and (3.40)]. The calculations were carried out using: (i) a 2-band approximation of the FBdG model, where Bogoliubov excitations may arise in any of the Floquet upper and lower bands (ignoring the higher-excited bare bands), and (ii) a 1-band approximation, where excitations are restricted to the macroscopically occupied Floquet band (ignoring the "complementary" dressed band). Examples of calculated growth rates $\gamma_{\boldsymbol{k}}$ (Lyapunov exponents) of Bogoliubov excitations with momenta $\boldsymbol{k}$, plotted over the first Brillouin zone, are displayed in Figs. 5.24 and 5.25 under the 2-band and 1-band approximations using the same modulation parameters.

In Fig. 5.23(b) we present the theoretical condensate depletion rates, which are calculated as the largest growth rate of the unstable modes, for the frequency range used for the experimental data in Fig. 5.23(a). The frequencies at which the condensate in the upper and lower bands are most unstable differ substantially, due to the opposite band curvatures [185]. We find that there are two contributions to the decay: intra-band scattering processes within the dressed band and

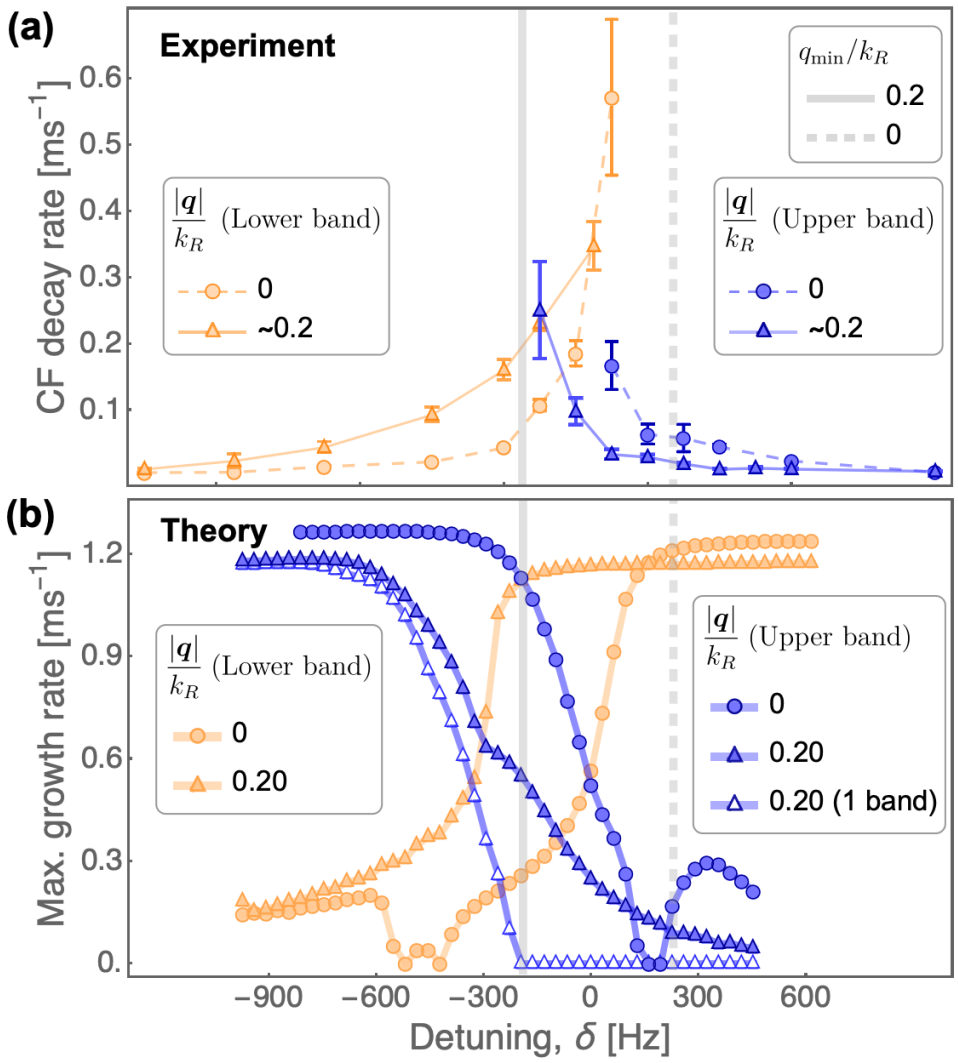

Figure 5.23: Instabilities of a condensate in the dressed bands. (a) Observed condensate fraction decay rates for BECs in lower and upper bands. For each band, we measured rates for $|\boldsymbol{q}| = 0\ k_R$ and $|\boldsymbol{q}| = 0.2\ k_R$. The solid (dashed) vertical gray line indicates the frequency at which the moat radius $q_{\min}$ is $0.2\ k_R$ ($0\ k_R$). (b) Calculation of the growth rate of the most unstable mode, based on a Floquet-Bogoliubov linear stability analysis for conditions similar to those in (a). The instability rates calculated for $|\boldsymbol{q}| = 0.2\ k_R$ including only contributions from the single BEC-occupied band are shown with open symbols. The unoccupied band induces increased decay for $|\boldsymbol{q}|$ near resonance.

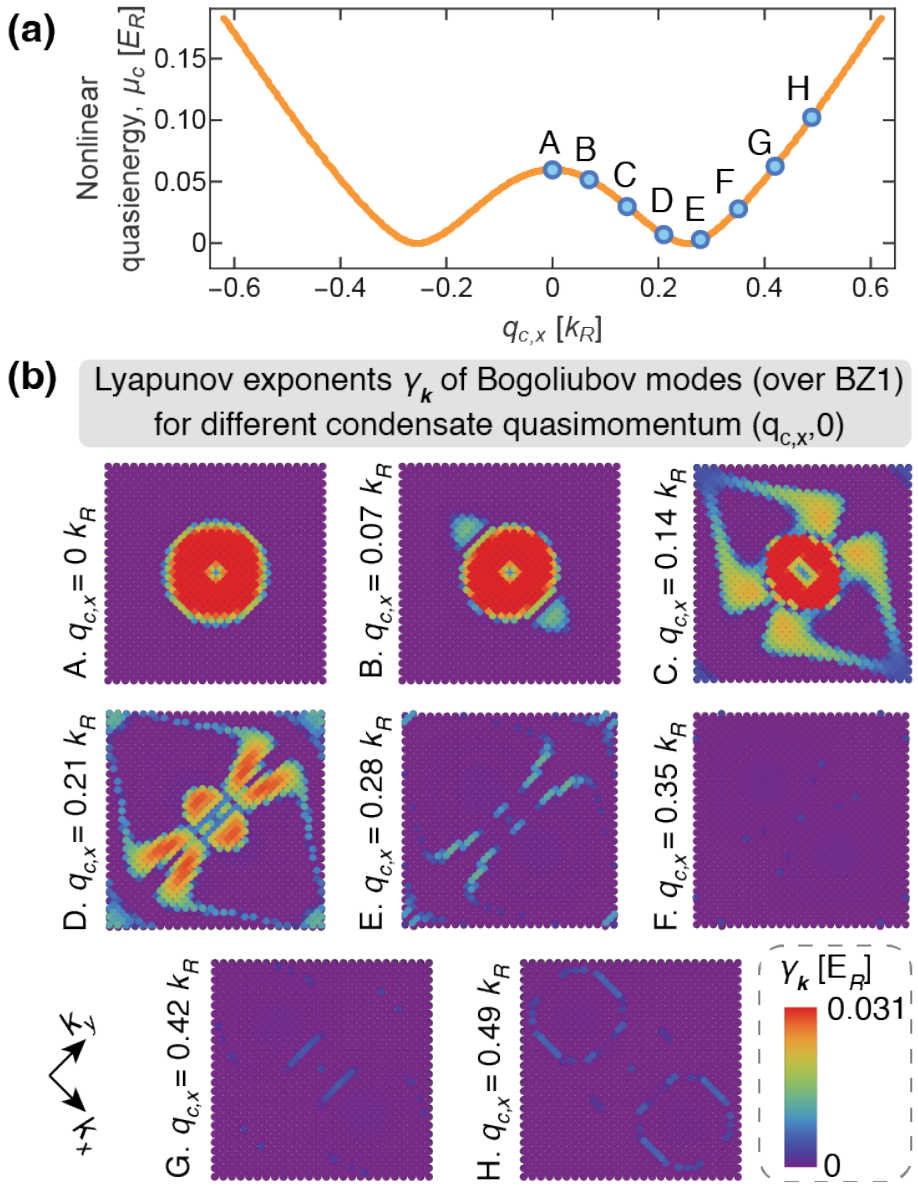

Figure 5.24: (a) Nonlinear moatlike band μ_c with an approximate radius of $q_{\text{min}} = 0.25\ k_R$, corresponding to a detuning $\delta \approx -300$ Hz (modulation frequency $f_m = 2.92$ kHz). This was calculated for a condensate with $g\bar{\rho} = 0.02\ E_R$. Blue circles indicate points with condensate crystal momenta $q_{c,x} = 0,\ 0.07,\ 0.14,\ 0.21,\ \ldots,\ 0.49\ k_R$ (with $q_{c,y} = 0\ k_R$). (b) Lyapunov exponents $\gamma_{\boldsymbol{k}}$ of Bogoliubov excitations with momenta $\boldsymbol{k} = (k_x, k_y)$, plotted over the first Brillouin zone BZ1 for different BEC quasimomenta $q_{c,x}$ [labeled A, B, C, ..., H in (a)]. The $\gamma_{\boldsymbol{k}}$ shown here were calculated using a 2-band approximation of the FBdG model, where excitations are restricted to the effective bands resulting from hybridizing the two lowest bare bands.

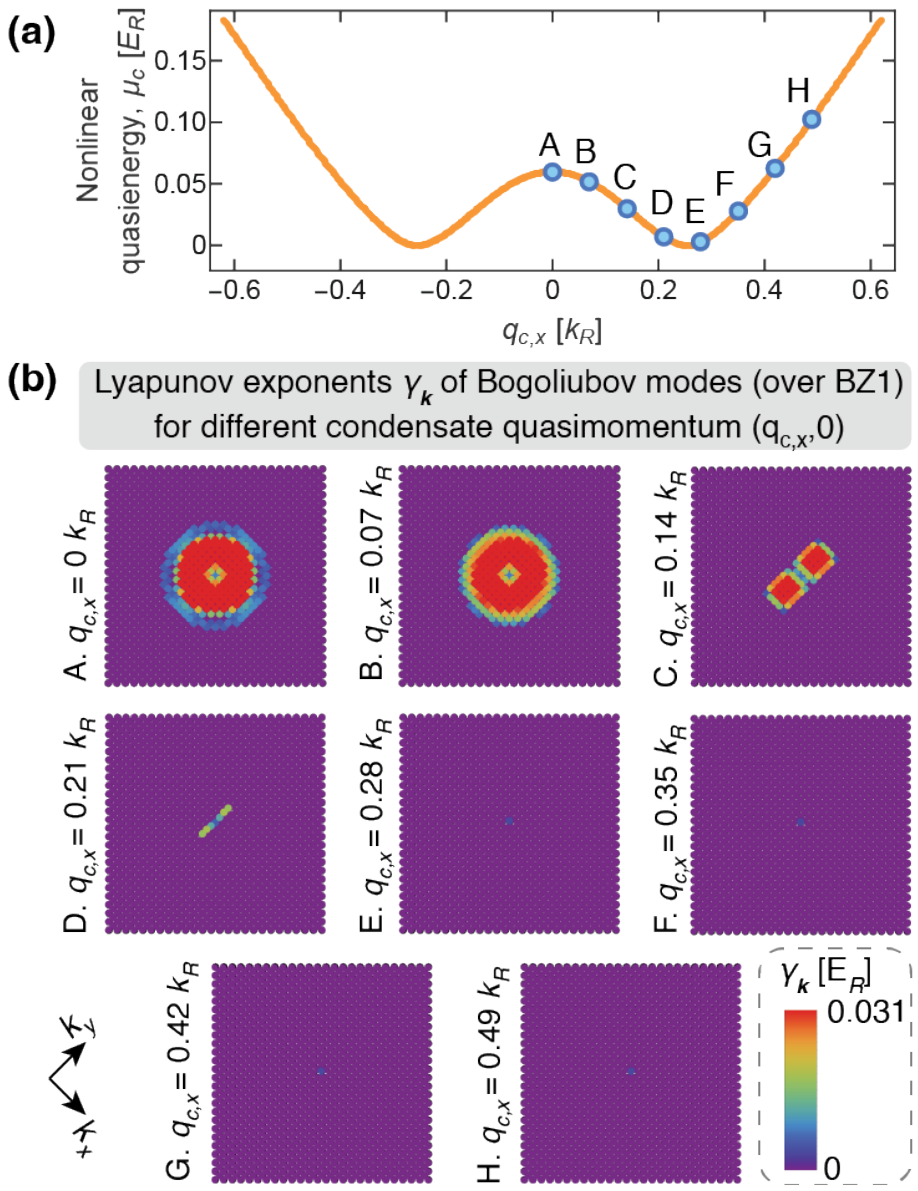

Figure 5.25: (a) Nonlinear moatlike band μ_c with an approximate radius of $q_{\text{min}} = 0.25\ k_R$, corresponding to a detuning $\delta \approx -300$ Hz (modulation frequency $f_m = 2.92$ kHz). This was calculated for a condensate with $g\bar{\rho} = 0.02\ E_R$. Blue circles indicate points with condensate crystal momenta $q_{c,x} = 0,\ 0.07,\ 0.14,\ 0.21,\ \ldots,\ 0.49\ k_R$ (with $q_{c,y} = 0\ k_R$). (b) Lyapunov exponents $\gamma_{\boldsymbol{k}}$ of Bogoliubov excitations with momenta $\boldsymbol{k} = (k_x, k_y)$, plotted over the first Brillouin zone BZ1 for different BEC quasimomenta $q_{c,x}$ [labeled A, B, C, ..., H in (a)]. The $\gamma_{\boldsymbol{k}}$ shown here were calculated using a 1-band approximation of the FBdG model, where the excitations are restricted to the macroscopically occupied moat band.

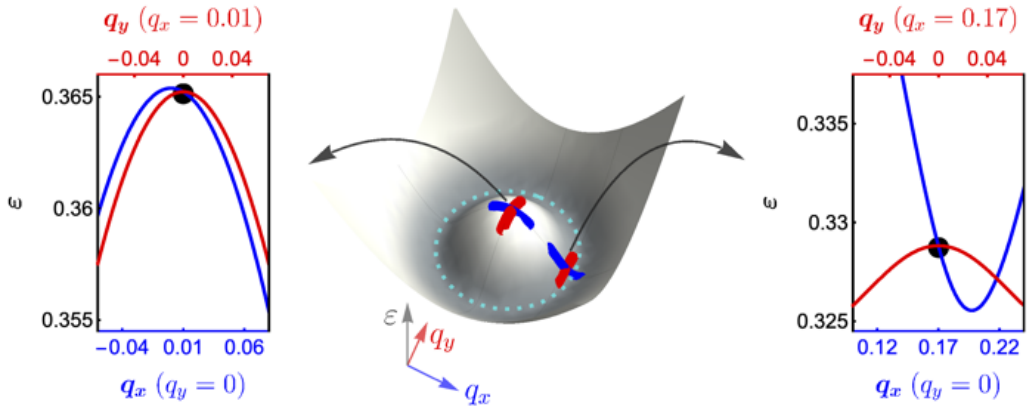

Figure 5.26: Transverse cuts of a numerically calculated Mexican-hat band along $q_x = 0$ and $q_y = 0$, crossing the points with crystal momentum $(q_x, q_y) = (0, 0.01)\ k_R$ and $(q_x, q_y) = (0, 0.17)\ k_R$. The minima of the dispersion in this example possesses a radius of approximately $0.2\ k_R$, and is indicated by the dotted light blue line in the center figure.

inter-band scattering between the bands. The intra-band processes are fundamentally related to the shape of the band, and dynamical instabilities [181, 182] for a moat-like dispersion generally arise for $|\boldsymbol{q}| < q_{\text{min}}$, where the band curvature becomes negative along the direction perpendicular to $\boldsymbol{q}$ (see Fig. 5.26). On the other hand, the inter-band processes are not restricted to $|\boldsymbol{q}| \gtrsim q_{\text{min}}$. Figure 5.23(b) (open triangles) shows the stability analysis restricted to the single moat band, and it shows no decay until the sudden turn on of loss at $|\boldsymbol{q}| = q_{\text{min}}$. Despite the fact that the mode stability analysis is only applicable to the initial exponential dynamics that are dominated by decay into a single mode, the model captures the overall scale of the condensate decay rate and its dependence on detuning.

Previous theoretical work [63, 64] in the Rashba SOC system with similar moat-like dispersion indicates that a single-momentum condensate is stable exactly at $|\boldsymbol{q}| = q_{\text{min}}$. This is consistent with the absence of inter-band processes contributing to the decay for $|\boldsymbol{q}| \geq q_{\text{min}}$ for the

Rashba case. However, while the stability analysis shows that the condensate is stable at the moat minima, we note that, as with our case, the Rashba SOC system is also unstable for $|\boldsymbol{q}| < q_{\text{min}}$, and therefore sits at a critical point in momentum space (see Fig. A.1(b) in Appendix A and Ref. [206]). The $|\boldsymbol{q}| < q_{\text{min}}$ instability is related to the curvature of the moat band, and is generally present, regardless of the underlying mechanism for generating the moat. It is indicative of the fact that the BEC is not a many-body eigenstate of the static effective Halmiltonian. The fact that the moat minima coincide with the boundary of the instability region likely has implications for the ground state of the system, even in the weakly-interacting limit. The $|\boldsymbol{q}| \gtrsim q_{\text{min}}$ instability is due to resonant coupling to the second band and depends on the specific lattice configuration used. It can be avoided under configurations lacking resonant dispersion conditions.

The instability at $|\boldsymbol{q}| < q_{\text{min}}$ can be seen in Figure 5.23(b) where we show the single-band linear stability analysis calculation (open triangles). The decay rate increases sharply from near-zero at $|\boldsymbol{q}| = q_{\text{min}}$, as illustrated in Fig. 5.25 where a 1-band approximaton of the FBdG model shows all Bogoliubov modes become stable as soon as the crystal momentum exceeds q_{min}. The contribution from the lower band induces more loss in the region $|\boldsymbol{q}| \gtrsim q_{\text{min}}$, as shown by the two-band calculation (blue filled triangles) and illustrated by the $\gamma_{\boldsymbol{k}}$ in Fig. 5.24 where a 2-band approximation (which includes the lower band) was employed.

5.5 Optimized Floquet engineering of a Mexican-hat band

This section presents some potential improvements to the modulation coupling that produces a ring-shaped band. Section 5.5.1 discusses again some numerical results for near-resonance shaken 1D lattices, like the ones presented in Section 3.1.3, and attempts to explain

the presence and the relative size of the "bump" at the center of the effective coupling term $|\Omega_{1,2}|$ profile [see Fig. 3.5(c)]. The insight obtained from this brief review of shaken 1D lattice is then applied in section 5.5.2 to an amplitude modulated 2D honeycomb lattice whose $|\Omega_{1,2}|$ displays a bump at $\boldsymbol{q} = 0$ (similar to the 1D case), that can be enhanced by a mechanism analogous to the one illustrated in section 5.5.1. Section 5.5.2 also includes a stability analysis, using the FBdG model, for a BEC in the moat band obtained with the driven honeycomb lattice.

5.5.1 Revisiting the 1D shaken lattice

Figure 5.27(a) shows the three lowest energy bands $E_{1,2,3}$ and the effective coupling $|\Omega_{1,2}|$ for shaken 1D lattices with depths 5, 7 and 9 E_R. [The band structure E_n and its $|\Omega_{1,2}|$ for the 7 E_R case (green lines) were already shown, respectively, in Figs. 3.1 and 3.5(c).] As observed in this figure, the bump is more pronounced for the shallowest lattice (blue dashed lines), which also happens to possess the smallest spacing between the first- and second- excited bands at $q_x = 0$.

The proximity between the bands E_2 and E_3 is connected to a substantially different form of the first-excited wavefunction ψ_2 near $q_x = 0$, as illustrated in Fig. 5.27(b) [compare the dark solid blue line ($q_x = 0$ k_R) with the dark dashed line ($q_x = 0.08$ k_R)]. The first-excited wavefunction ψ_2 for the 9 E_R potential, which exhibits a larger spacing between E_2 and E_3, is shown in Fig. 5.27(c) for different crystal momenta. For the 9 E_R lattice [Fig. 5.27(c)], the form of ψ_2 near $q_x = 0$ does not differ from the form of ψ_2 at q_x far from 0 as much as it does in the 5 E_R case [Fig. 5.27(b)]. Since the effective coupling term is given by $\Omega_{1,2} = \frac{1}{2} \langle \psi_2 | \hat{H}_{\text{modulation}} | \psi_1 \rangle$, it is reasonable to conclude that the bump in $|\Omega_{1,2}|$ is caused by the pronounced change in the shape of ψ_2 near the center of the Brillouin zone, which is in turn related to the proximity between the

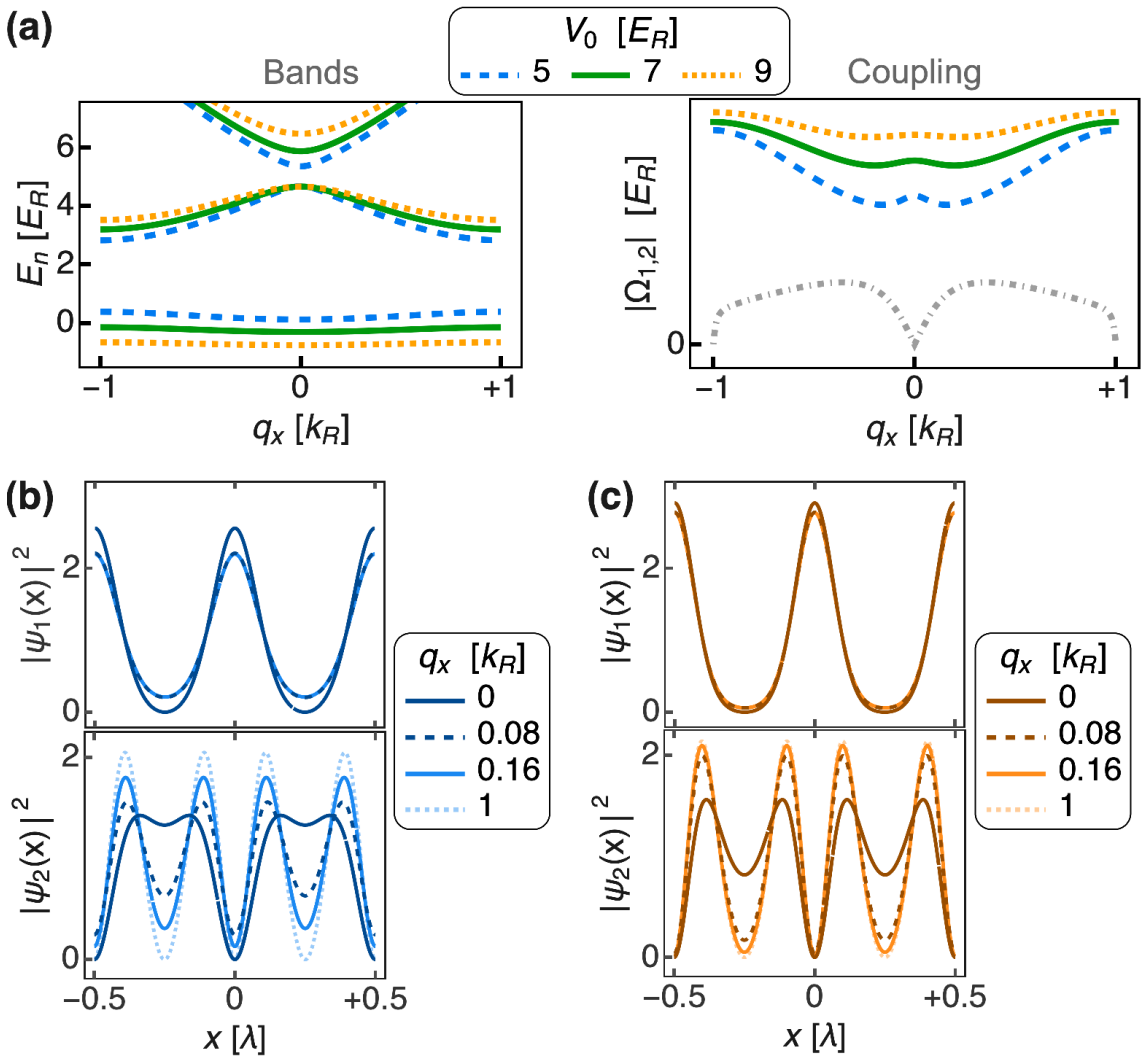

Figure 5.27: Revisiting the problem of a near-resonance shaken 1D lattice to illustrate a potential relation between an enhanced bump in $|\Omega_{1,2}(q_x)|$ at $q_x = 0$ and the reduced band spacing between the second and third bands. (a) Left panel: Three lowest energy bands E_1, E_2 and E_3 (left) for 1D static lattices with depths 5, 7, 9 E_R. Right panel: Effective coupling $|\Omega_{1,2}(q_x)|$ for 1D shaken lattices with depths 5, 7, 9 E_R. (The gray dash-dotted line in the right panel indicates the coupling $\Omega_{1,3}$ between the first and third band for the 7 E_R lattice.) The shallowest potential (5 E_R) exhibits the smallest separation between E_2 and E_3, along with a more protruding bump in the $|\Omega_{1,2}|$ profile. (b) Modulus of ground and first-excited wavefunctions ψ_1 and ψ_2 for the 5 E_R lattice. (c) Modulus of ground and first-excited wavefunctions ψ_1 and ψ_2 for the 9 E_R lattice. The shape of $|\psi_2(x)|^2$ for the shallowest potential displays a higher sensitivity with q_x near the center of the Brillouin zone, which we believe induces the more pronounced bump in $|\Omega_{1,2}|$.

bands E_2 and E_3 at $q_x = 0$.

5.5.2 Near-resonance modulation in a hexagonal lattice

We now present an example of an amplitude modulated lattice $V_{\text{HC}}(\boldsymbol{r}, t)$ that yields a moat-like Floquet band which, according to our FBdG model, should avoid instabilities arising from the proximity of the lower dressed band for $|\boldsymbol{q}|$ near q_{min}. This would offer an advantage over the protocol we employed [Eq. (5.5)] in our experiment. It should be noted, however, that the instabilities for $|\boldsymbol{q}| < q_{\text{min}}$ inherent to the curvature of the moat band persist in the modulated lattice we briefly discuss here.

The potential $V_{\text{HC}}(\boldsymbol{r}, t)$ is driven with the same amplitude modulation as Eq. (5.5),

$$V_{\text{HC}}(\boldsymbol{r}, t) = \left[1 + \alpha_m \cos\left(\frac{2\pi}{T} t\right)\right] V_{\text{HC}}^{[\text{S}]}(x, y), \tag{5.15}$$

but the static potential $V_{\text{latt}}^{[\text{S}]}$ is replaced with a honeycomb lattice $V_{\text{HC}}^{[\text{S}]}(\boldsymbol{r})$ given by

$$\begin{aligned} V_{\text{HC}}^{[\text{S}]}(\boldsymbol{r}) =& V_{1,\text{HC}} \left[\cos\left(\boldsymbol{b}_1 \cdot \boldsymbol{r}\right) + \cos\left(\boldsymbol{b}_2 \cdot \boldsymbol{r}\right) + \cos\left((\boldsymbol{b}_1 + \boldsymbol{b}_2) \cdot \boldsymbol{r}\right)\right] + \\ & V_{2,\text{HC}} \left[\cos\left(\boldsymbol{b}_1 \cdot (\boldsymbol{r} + \boldsymbol{d}_s)\right) + \cos\left(\boldsymbol{b}_2 \cdot (\boldsymbol{r} + \boldsymbol{d}_s)\right) + \cos\left((\boldsymbol{b}_1 + \boldsymbol{b}_2) \cdot (\boldsymbol{r} + \boldsymbol{d}_s)\right)\right], \end{aligned} \tag{5.16}$$

with $\boldsymbol{b}_1 = \frac{1}{2}(\sqrt{3}, 3)\ \tilde{k}_R$, $\boldsymbol{b}_2 = (-\sqrt{3}, 0)\ \tilde{k}_R$ and $\boldsymbol{d}_s = 4\pi\times\ (1/\sqrt{27}, 0)\ \tilde{k}_R^{-1}$. In the following example, the amplitudes are chosen to be $V_{1,\text{HC}} = 3.0\ \tilde{E}_R$, $V_{2,\text{HC}} = 0.84\ \tilde{E}_R$ ($\tilde{E}_R$ is defined here as $\hbar^2 \tilde{k}_R^2 / 2m$). The lattice $V_{\text{HC}}^{[\text{S}]}$ is illustrated in Fig. 5.28(a). The interband coupling $|\Omega_{1,2}|$ for the amplitude modulated honeycomb lattice [Eq. 5.15] is shown in Fig. 5.28(b), along with the corresponding band structure. The dashed lines indicate a deper lattice where the larger

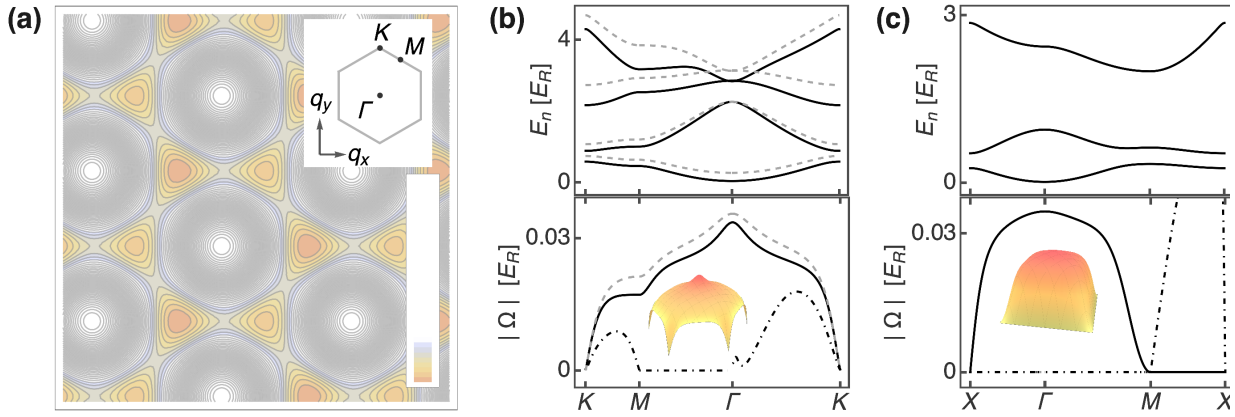

Figure 5.28: (a) Contour plot of honeycomb lattice $V_{\rm HC}^{[\rm S]}$ [Eq. (5.16)]. Inset shows the corresponding first Brillouin zone. (b) Coupling $|\Omega_{1,2}|$ and band structure E_n for an amplitude modulated potential $V_{\rm HC}(\boldsymbol{r}, t)$ with $\alpha_m = 0.12$. Dashed lines correspond to a honeycomb lattice with different depth and tilt, that produce a larger band spacing between E_2 and E_3. (c) Coupling $|\Omega_{1,2}|$ and band structure E_n for the amplitude modulated potential we used in our experiments ($\alpha_m = 0.12$). In both (b) and (c) the dash dotted line indicates the coupling $\Omega_{1,3}$ between the ground band and the second-excited band.

separation between the band E_2 and the higher bands reduce the protruding aspect of the bump at the Γ point ($\boldsymbol{q} = 0$), as discussed in section 5.5.1 for the shaken 1D lattice [see Fig. 5.27(b)]. (Dash dotted line indicates the coupling $\Omega_{1,3}$ between the ground band and the second-excited band.) The profile $|\Omega_{1,2}|$ for the amplitude modulated checkerboard potential employed in our experiments is included in Fig. 5.28(c) for comparison.

Figure 5.29(a) shows the growth rate $\Gamma_{\rm M}$ of the most unstable mode as a function of quasi-momentum for condensates occupying the moatlike band generated using the driven square checkerboard lattice in Eq. (5.5) (blue points) and a moatlike band produced using the driven lattice $V_{\rm HC}$ in Eq. (5.15) (orange points). The amplitude modulation strength in both cases was $\alpha_m = 0.14$, and the modulation frequencies were chosen to yield same band moat radii $q_{\rm min} \approx 0.17\ k_R$ [indicated by the gray vertical line in Fig. 5.29(a)]. The rates $\Gamma_{\rm m}$ in Fig. 5.29(a)

were calculated using the same two-band linear stability analysis used to compute the filled triangles in Fig. 5.23. Unlike $\Gamma_{\rm m}$ corresponding to $V_{\rm latt}$, the $\Gamma_{\rm m}$ profile associated with $V_{\rm HC}$ nearly vanishes for $|\boldsymbol{q}|$ near and larger than $q_{\rm min}$.

The stability of the honeycomb lattice for $|\boldsymbol{q}| \gtrsim q_{\rm min}$ is due to the absence of inter-band scattering processes. To see this, we show in Figs. 5.29(b) and 5.29(c) the Bogoliubov spectra of condensates sitting at $(q_x, q_y) = (q_{\rm min}, 0)$ for the checkerboard and honeycomb Floquet bands used in Fig. 5.29(a). Unlike the checkerboard spectrum, the honeycomb spectrum lacks inter-band scattering processes at similar lattice depths and modulation amplitudes, due to the smaller width of the dressed band and the larger gap separating the bands.

5.6 Conclusions and outlook

In conclusion, we synthesized a ring-shaped energy band for ultracold atoms in a double-well optical lattice, and corroborated the dispersion by measuring the dynamics of a BEC in the modulated lattice. We also measured condensate lifetimes under different moat conditions. In addition to the condensate decay inherent to the shape of the Mexican-hat band, our model indicates that interactions coupling to the other dressed band may be important and warrant consideration in protocols involving near-resonance hybridization. For the most part, our observations are in fair agreement with the theoretical prediction that a BEC at the minimum of a moat dispersion sits at the edge of an instability region and should hence be unstable in realistic scenarios, which likely has implications for the ground state of the system (even in the weakly-interacting limit).

The many-body ground state of interacting bosons in the low density, strongly correlated limit in such a moat remains an open question [41, 56–61]. It has been argued [41, 59–61] that

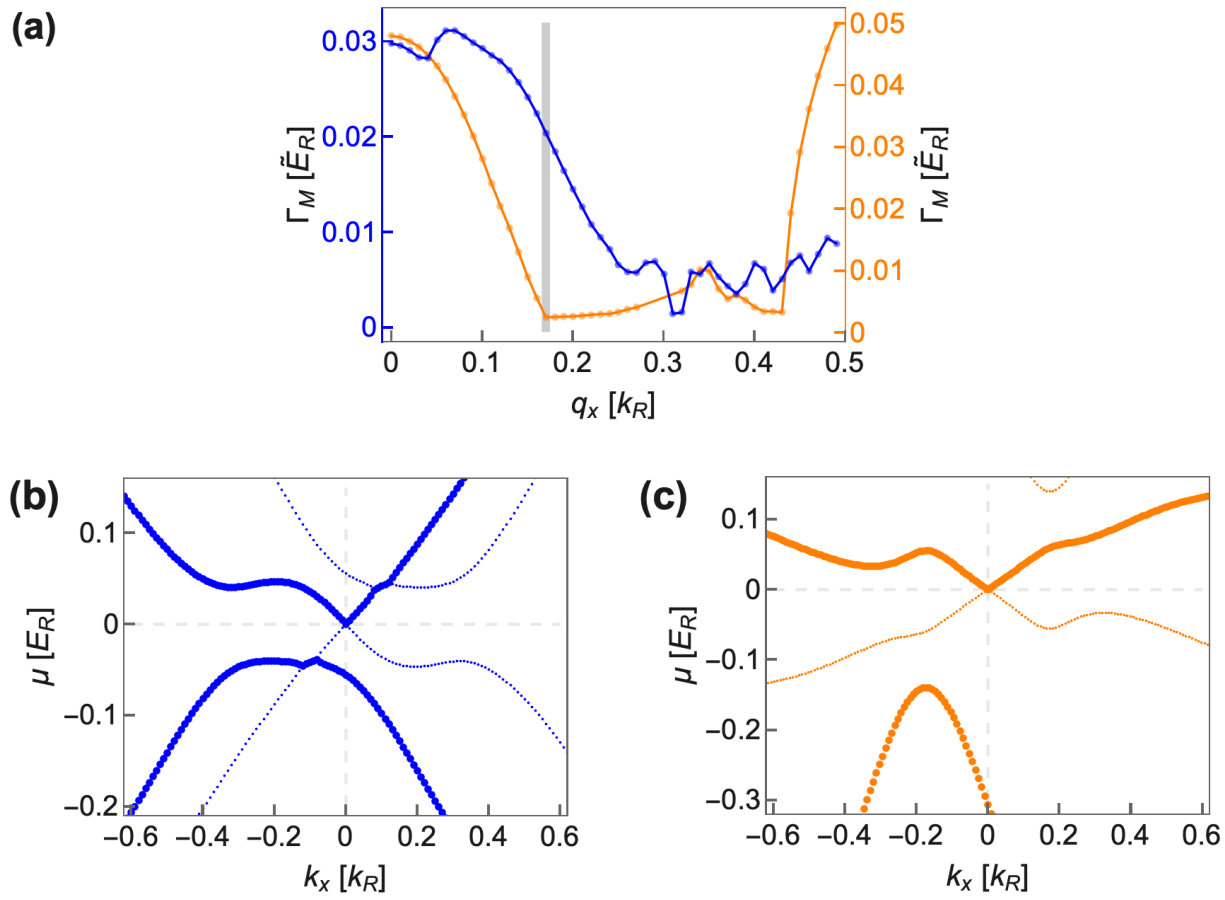

Figure 5.29: (a) Growth rate of most unstable Bogoliubov mode Γ_{M} as a function of q_x (with $q_y = 0$) for condensates occupying moatlike Floquet bands generated using the driven lattices V_{latt} in Eq. (5.5) (blue points) and V_{HC} in Eq. (5.15) (orange points). Both bands have a moat radius $q_{\mathrm{min}} \sim 0.17\ k_R$ (indicated by vertical gray line). (b), (c) Bogoliubov spectra $\mu(\boldsymbol{k}) = \mathrm{Re}[\lambda_{\boldsymbol{k}}]$ along $k_y = 0$ for condensates at $(q_x, q_y) = (q_{\mathrm{min}}, 0)$ for the checkerboard and honeycomb lattices in (a). The thick lines show $\mu(\boldsymbol{k})$, and the thin lines show $-\mu(-\boldsymbol{k})$. Energy and momentum conserving scattering occurs at crossings of the two curves. Interband scattering is absent for the honeycomb lattice.

the low density ground state in a moat-like dispersion is a composite-fermion-like state leading to a chiral spin liquid, and it will be interesting to explore this limit experimentally. Reaching the highly correlated regime requires confinement in the transverse direction (attainable with the addition of an out-of-plane optical lattice) to ensure the system is fully 2D. Additionally, the density would need to be much lower; for example, with $q_{\min} \lesssim 0.3\ k_R$, the density should not exceed one atom per ten lattice sites [41]. It remains an outstanding experimental and theoretical question as to how to prepare a low energy state in such a system, as well as how and how quickly the correlated system heats.

Appendix A: Rashba SOC stability analysis

The Bogoliubov spectrum of isotropically interacting bosons with ideal Rashba spin-orbit coupling (SOC) has been discussed previously, for example in Refs. [63, 64, 206], for a single-momentum condensate at one of the circularly degenerate lowest-energy states, $|\boldsymbol{q}| = Q$. Here we review the equations governing the linear stability analysis of the corresponding single-momentum condensates with arbitrary momenta $\boldsymbol{q}$. This analysis is very similar to the one outlined in Section 3.3 to study the BEC stability in periodically modulated optical lattices. However, the absence of time dependence in the noninteracting Rashba Hamiltonian and the simplicity of its resulting mean-field states make it possible to write the Bogoliubov equations in a compact analytical form, which was not feasible in the model for driven lattices. We show that the condensate is unstable whenever the magnitude of its momentum is less than that of the degenerate minima, $|\boldsymbol{q}| < Q$. This is the same behavior as that calculated in the single-band approximation for our Floquet-engineered moat band.

Analogous to Eq. (3.30), the Gross-Pitaevskii equation describing the Rashba SOC system is [207]

$$i\hbar\frac{\partial}{\partial t}\Psi = \left[-\frac{\hbar^2}{2m}\nabla_{\boldsymbol{r}}^2 + i\frac{\hbar^2 Q}{m}\boldsymbol{\sigma}_\perp \cdot \nabla_{\boldsymbol{r}} + g\bar{\rho}|\Psi|^2\right]\Psi, \tag{A.1}$$

where Ψ is a spinor order parameter, $\boldsymbol{\sigma}_\perp = (\sigma_x, \sigma_y)$, σ_i are the Pauli matrices, Q is the SOC

strength, $g = 4\pi\hbar^2 a/m$ (a is the scattering length), and $\bar{\rho}$ is the average density of the state.

The dispersion of this system consists of two energy branches given by

$$E_{R,\pm}(\boldsymbol{q}) = \epsilon_Q \left\{ \left(\frac{|\boldsymbol{q}|}{Q} \pm 1 \right)^2 + \frac{1}{2} \frac{g\bar{\rho}}{\epsilon_Q} \right\}, \tag{A.2}$$

with $\epsilon_Q = \frac{\hbar^2 Q^2}{2m}$. The branch $E_{R,-}$ possesses a Mexican-hat shape whose degenerate minima lie along the circle $|\boldsymbol{q}| = Q$ in the two-dimensional momentum space [Fig. A.1(a)]. The corresponding states are

$$\psi_{\pm,\boldsymbol{q}} = e^{i\boldsymbol{q}\cdot\boldsymbol{r}} \xi_{\pm,\boldsymbol{q}} = \frac{e^{i\boldsymbol{q}\cdot\boldsymbol{r}}}{\sqrt{2}} \begin{pmatrix} 1 \\ \mp e^{i\phi(\boldsymbol{q})} \end{pmatrix}, \tag{A.3}$$

where $\phi(\boldsymbol{q}) = \mathrm{Arg}(q_x + i\, q_y)$. (Unlike the periodically time-modulated lattices we discuss in Chapters 3, 4 and 5, the states $\psi_{\pm,\boldsymbol{q}}$ in the Rashba system have uniform and time-independent density.)

To determine the stability of bosons condensed at the single-momentum mean-field state $\psi_{-,\boldsymbol{q}}$ for arbitrary values of $\boldsymbol{q}$, we expand the perturbations $\delta\psi$ around $\psi_{-,\boldsymbol{q}}$ in the following way

$$\begin{aligned} \delta\psi = e^{-i[E_{R,-}(\boldsymbol{q})+g\bar{\rho}/2]t/\hbar} e^{+i\boldsymbol{q}\cdot\boldsymbol{r}} \times \\ \sum_{\boldsymbol{k}} \Big[e^{+i\boldsymbol{k}\cdot\boldsymbol{r}} \left(u^{(-)}_{\boldsymbol{q}+\boldsymbol{k}}(t)\, \xi_{-,\boldsymbol{q}+\boldsymbol{k}} + u^{(+)}_{\boldsymbol{q}+\boldsymbol{k}}(t)\, \xi_{+,\boldsymbol{q}+\boldsymbol{k}} \right) + \\ e^{-i\vec{k}\cdot\vec{r}} \left({v^{(-)}_{\boldsymbol{q}+\boldsymbol{k}}}^{*}(t)\, \xi_{-,\boldsymbol{q}-\boldsymbol{k}} + {v^{(+)}_{\boldsymbol{q}+\boldsymbol{k}}}^{*}(t)\, \xi_{+,\boldsymbol{q}-\boldsymbol{k}} \right) \Big], \end{aligned} \tag{A.4}$$

and insert the perturbed order parameter $\psi_{-,\vec{q}} + \delta\psi$ in equation (A.1). This leads to the

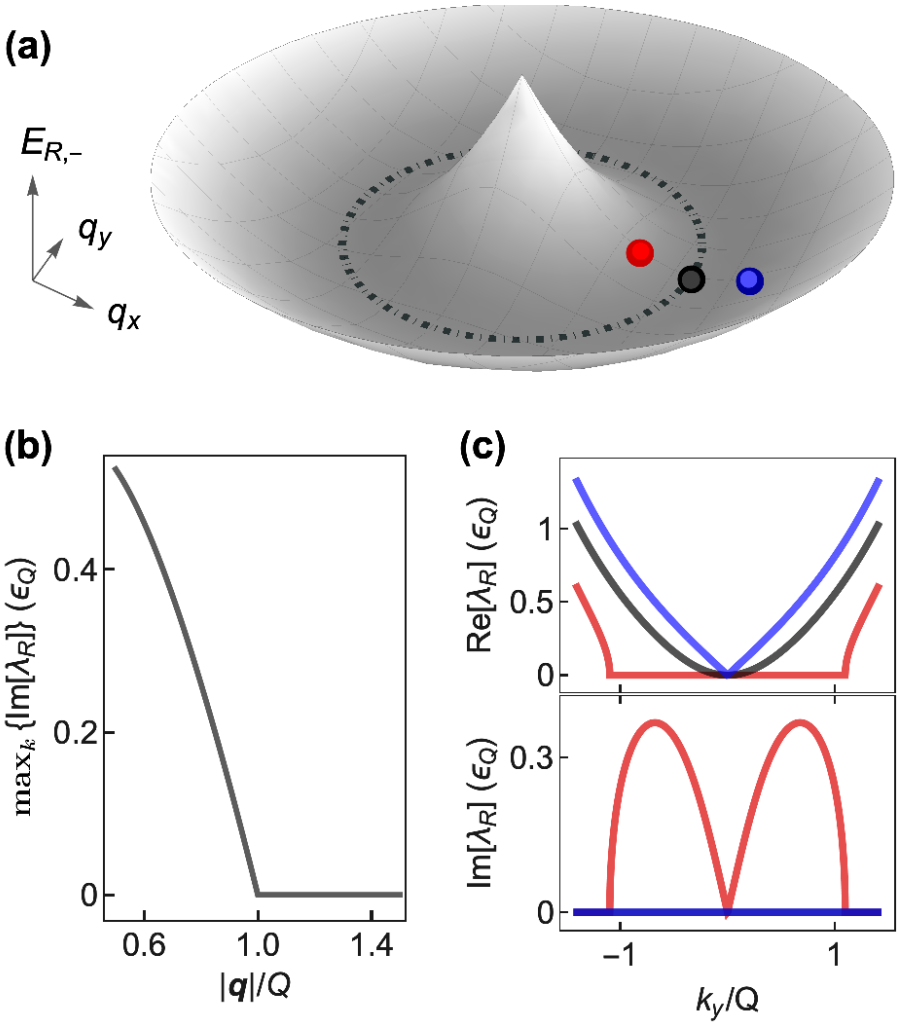

Figure A.1: (a) Lower branch $E_{R,-}$ of the Rashba energy spectrum. Dash-dotted line indicates the degenerate minima of $E_{R,-}$, located at $|\boldsymbol{q}| = Q$. The red, black and blue markers indicate points with $Q^{-1}\boldsymbol{q} = Q^{-1}(q_x, q_y)$ = (0.7, 0), (1.0, 0) and (1.3, 0), respectively. (b) Dependence of the largest value of $\mathrm{Im}[\lambda_R(\boldsymbol{k};\boldsymbol{q})]$ (at a given $\boldsymbol{q}$) on $|\boldsymbol{q}|$, for $g\bar{\rho} = \epsilon_Q$. (c) Real and imaginary parts of gapless $\lambda_R(\boldsymbol{k};\boldsymbol{q})$ as a function of k_y (with $k_x = 0$) for the three different values of the condensate momentum $\boldsymbol{q}$ indicated by the red, black and blue markers in (a), and for $g\bar{\rho} = \epsilon_Q$.

Bogoliubov-de Gennes (BdG) equations

$$i\hbar\frac{\partial}{\partial t}\begin{pmatrix} u^{(-)}_{\vec{q}+\vec{k}} \\ v^{(-)}_{\vec{q}-\vec{k}} \\ u^{(+)}_{\vec{q}+\vec{k}} \\ v^{(+)}_{\vec{q}-\vec{k}} \end{pmatrix} = \Sigma_z M_{\vec{k},\vec{q}} \begin{pmatrix} u^{(-)}_{\vec{q}+\vec{k}} \\ v^{(-)}_{\vec{q}-\vec{k}} \\ u^{(+)}_{\vec{q}+\vec{k}} \\ v^{(+)}_{\vec{q}-\vec{k}} \end{pmatrix} . \tag{A.5}$$

In Eq. (A.5), the matrix Σ_z is defined as

$$\Sigma_z = I_2 \otimes \sigma_z = \begin{pmatrix} +1 & 0 & 0 & 0 \\ 0 & -1 & 0 & 0 \\ 0 & 0 & +1 & 0 \\ 0 & 0 & 0 & -1 \end{pmatrix} , \tag{A.6}$$

(I_2 is the identity matrix of order 2) and the matrix $M_{\boldsymbol{k},\boldsymbol{q}}$ is given by

$$M_{\boldsymbol{k},\boldsymbol{q}} = \Delta_{\boldsymbol{k},\boldsymbol{q}} + g\bar{\rho} W^{\dagger}_{\boldsymbol{k},\boldsymbol{q}} \otimes W_{\boldsymbol{k},\boldsymbol{q}} \, , \tag{A.7}$$

where $\Delta_{\boldsymbol{k},\boldsymbol{q}}$ is

$$\Delta_{\boldsymbol{k},\boldsymbol{q}} = \begin{pmatrix} \delta E^{(a)}_{-} & 0 & 0 & 0 \\ 0 & \delta E^{(b)}_{-} & 0 & 0 \\ 0 & 0 & \delta E^{(a)}_{+} & 0 \\ 0 & 0 & 0 & \delta E^{(b)}_{+} \end{pmatrix} , \tag{A.8}$$

with the terms $\delta E_{\pm}^{(a)}$ and $\delta E_{\pm}^{(b)}$ defined by the expressions

$$\delta E_{\pm}^{(a)} = E_{R,\pm}(\boldsymbol{q}+\boldsymbol{k}) - E_{R,-}(\boldsymbol{q}), \qquad \delta E_{\pm}^{(b)} = E_{R,\pm}(\boldsymbol{q}-\boldsymbol{k}) - E_{R,-}(\boldsymbol{q}), \tag{A.9}$$

and the vectors $W_{\boldsymbol{k},\boldsymbol{q}}$ used in the Kronecker product $W_{\boldsymbol{k},\boldsymbol{q}}^{\dagger} \otimes W_{\boldsymbol{k},\boldsymbol{q}}$ are given by

$$W_{\boldsymbol{k},\boldsymbol{q}} = \begin{pmatrix} \xi_{-,a}^{\dagger}\xi_0 \\ \\ \xi_0^{\dagger}\xi_{-,b} \\ \\ \xi_{+,a}^{\dagger}\xi_0 \\ \\ \xi_0^{\dagger}\xi_{+,b} \end{pmatrix}, \tag{A.10}$$

with the states ξ_0, $\xi_{\pm,a}$ and $\xi_{\pm,b}$ defined as follows

$$\xi_0 = \frac{1}{\sqrt{2}} \begin{pmatrix} 1 \\ \\ +e^{i\phi(\boldsymbol{q})} \end{pmatrix}, \qquad \xi_{\pm,a} = \frac{1}{\sqrt{2}} \begin{pmatrix} 1 \\ \\ \mp e^{i\phi(\boldsymbol{q}+\boldsymbol{k})} \end{pmatrix}, \qquad \xi_{\pm,b} = \frac{1}{\sqrt{2}} \begin{pmatrix} 1 \\ \\ \mp e^{i\phi(\boldsymbol{q}-\boldsymbol{k})} \end{pmatrix}. \tag{A.11}$$

Explicitly, the elements of $\Sigma_z M_{\boldsymbol{k},\boldsymbol{q}}$ are the following

$$\Sigma_z M_{\boldsymbol{k},\boldsymbol{q}} = (I_2 \otimes \sigma_z)(\Delta_{\boldsymbol{k},\boldsymbol{q}} + g\bar{\rho} W_{\boldsymbol{k},\boldsymbol{q}}^{\dagger} \otimes W_{\boldsymbol{k},\boldsymbol{q}}) = \begin{pmatrix} \Lambda_1 & \Lambda_2 \\ \\ \Lambda_3 & \Lambda_4 \end{pmatrix}, \tag{A.12}$$

where

$$\Lambda_1 = \begin{pmatrix} +\delta E_-^{(a)} + g\bar{\rho}|\xi_0^\dagger \xi_{-,a}|^2 & +g\bar{\rho}(\xi_{-,b}^\dagger \xi_0)(\xi_{-,a}^\dagger \xi_0) \\ -g\bar{\rho}(\xi_0^\dagger \xi_{-,a})(\xi_0^\dagger \xi_{-,b}) & -\delta E_-^{(b)} - g\bar{\rho}|\xi_0^\dagger \xi_{-,b}|^2 \end{pmatrix}, \tag{A.13}$$

$$\Lambda_2 = \begin{pmatrix} +g\bar{\rho}(\xi_0^\dagger \xi_{+,a})(\xi_{-,a}^\dagger \xi_0) & +g\bar{\rho}(\xi_{+,b}^\dagger \xi_0)(\xi_{-,a}^\dagger \xi_0) \\ -g\bar{\rho}(\xi_0^\dagger \xi_{+,a})(\xi_0^\dagger \xi_{-,b}) & -g\bar{\rho}(\xi_{+,b}^\dagger \xi_0)(\xi_0^\dagger \xi_{-,b}) \end{pmatrix}, \tag{A.14}$$

$$\Lambda_3 = \begin{pmatrix} +g\bar{\rho}(\xi_0^\dagger \xi_{-,a})(\xi_{+,a}^\dagger \xi_0) & +g\bar{\rho}(\xi_{-,b}^\dagger \xi_0)(\xi_{+,a}^\dagger \xi_0) \\ -g\bar{\rho}(\xi_0^\dagger \xi_{-,a})(\xi_0^\dagger \xi_{+,b}) & -g\bar{\rho}(\xi_{-,b}^\dagger \xi_0)(\xi_0^\dagger \xi_{+,b}) \end{pmatrix}, \tag{A.15}$$

$$\Lambda_4 = \begin{pmatrix} +\delta E_+^{(a)} + g\bar{\rho}|\xi_0^\dagger \xi_{+,a}|^2 & +g\bar{\rho}(\xi_{+,b}^\dagger \xi_0)(\xi_{+,a}^\dagger \xi_0) \\ -g\bar{\rho}(\xi_0^\dagger \xi_{+,a})(\xi_0^\dagger \xi_{+,b}) & -\delta E_+^{(b)} - g\bar{\rho}|\xi_0^\dagger \xi_{+,b}|^2 \end{pmatrix}. \tag{A.16}$$

The stability of a condensate in the state $\psi_{-,\boldsymbol{q}}$ is inferred from the eigenvalues $\lambda_R(\boldsymbol{k};\boldsymbol{q})$ of $\Sigma_z M_{\boldsymbol{k},\boldsymbol{q}}$ [185]. Purely real eigenvalues represent the spectrum of excitations. On the other hand, complex eigenvalues with a positive imaginary part indicate the presence of an unstable mode with growth rate given by $\mathrm{Im}[\lambda_R(\boldsymbol{k},\boldsymbol{q})]$.

We find that the modes of condensates with $|\boldsymbol{q}| \geq Q$ are stable for all values of $\boldsymbol{k}$, $\mathrm{Im}[\lambda_R(\boldsymbol{k},\boldsymbol{q})] = 0$. By contrast, condensates with $|\boldsymbol{q}| < Q$ always have unstable modes with momenta $\boldsymbol{q}+\boldsymbol{k}$ in the neighborhood of $\boldsymbol{q}$. This result holds for any positive value of $g\bar{\rho}$ and is

illustrated in Figure A.1(b), where we present the growth rate of the most unstable mode (i.e., $\max_{\boldsymbol{k}} \mathrm{Im}[\lambda_R(\boldsymbol{k}, \boldsymbol{q})]$) as a function of $|\boldsymbol{q}|$ and for $g\bar{\rho} = \epsilon_Q$. The abrupt increase in maximum growth rate when $|\boldsymbol{q}| < Q$ has the same behavior as the single-band model for the Floquet-engineered moat band, shown in Fig 5.23 (open triangles).

The instabilities have the highest growth rate for $\boldsymbol{k} \perp \boldsymbol{q}$ [Fig. A.1(c)], which is the direction along which the band curvature is negative. For $\boldsymbol{k} \perp \boldsymbol{q}$, the pair of eigenvalues λ_R possessing a nonzero imaginary part are accurately described by a single-band model restricted to the $\mu_{R,-}$ branch. In this simplified description, the Bogoliubov excitations are found by diagonalizing the upper left quadrant of the 4×4 matrix representation of $\Sigma_z M_{\boldsymbol{k},\boldsymbol{q}}$, i.e., the matrix Λ_1. The eigenvalues of this 2×2 matrix are

$$\tilde{\lambda}_R(\boldsymbol{k}, \boldsymbol{q}) = \pm \sqrt{\delta\tilde{E}_- \left[\delta\tilde{E}_- + g\bar{\rho}\left(1 + \frac{|\boldsymbol{q}|}{\sqrt{|\boldsymbol{q}|^2 + |\boldsymbol{k}|^2}}\right)\right]}, \tag{A.17}$$

where $\delta\tilde{E}_-$ is defined as $\delta E_-^{(a)}$ $(= \delta E_-^{(b)})$. For $|\boldsymbol{q}| \geq Q$ and $g\bar{\rho} > 0$, the expression inside the radical in Eq. (A.17) is always positive if $|\boldsymbol{k}|$ is nonzero, and hence λ_R correspond to stable gapless modes [blue and black lines in Fig. A.1(c)]. For $|\boldsymbol{q}| < Q$ and $g\bar{\rho} > 0$, the same expression is always negative in some neighborhood of $\boldsymbol{k} = 0$ since $\delta\tilde{E}_- < 0$ when $\boldsymbol{k}$ is near 0. For those momenta, the eigenvalues λ_R are purely imaginary and correspond to unstable modes [red line in Fig. A.1(c)]. This instability argument holds for any Bogoliubov-like dispersion of the form $\sqrt{\delta E(\delta E + C)}$ where δE is the single particle dispersion.

Appendix B: Relation between the group velocity and the quasienergy

In a static lattice, the group velocity V_G of a Bloch state is related to the dispersion $E(\boldsymbol{q})$ according to the equation

$$V_G = \frac{1}{\hbar}\nabla_{\boldsymbol{q}} E(\boldsymbol{q}). \tag{B.1}$$

The purpose of this appendix is to formally derive the relation between the quasienergy ε and the group velocity v_g of the Floquet state. The group velocity is understood here as the expected value $\langle \hat{p} \rangle$ of the momentum operator divided by the mass m, which is what we can infer from time of flight diffraction images when the Floquet state is projected into the free-particle Hamiltonian by snapping-off the lattice. The appendix also includes the explicit form of the time-periodic micromotion term for v_g. Additionally, we discuss the form of this relation when accounting interactions via the time-modulated GP equation.

B.1 Free-particle case

Let's consider a Floquet-Bloch wavefunction $\tilde{\psi}$ as the solution to the modulated free-particle Schrödinger equation

$$\tilde{\psi} = e^{i\boldsymbol{q}\cdot\boldsymbol{r}-\varepsilon_{\boldsymbol{q}}t}u(\boldsymbol{r},t;\boldsymbol{q}), \tag{B.2}$$

where the Floquet mode u is a $\mathcal{B}$- and T- periodic function for every value of the crystal momentum $\boldsymbol{q}$ in the first Brillouin zone. [See Eq. (3.3), where this Floquet form was presented in the context of the Floquet theorem, and Eq. (3.34), where the Floquet-Bloch form was discussed as an ansatz to the GP equation which reduces to the Schrödinger equation in the absence of interactions.] The Schrödinger-like equation for the Floquet mode u alone is

$$\varepsilon_{\boldsymbol{q}}u(\boldsymbol{r},t;\boldsymbol{q}) + i\hbar\frac{\partial}{\partial t}u(\boldsymbol{r},t;\boldsymbol{q}) = \left[\frac{\hbar^2}{2m}(\boldsymbol{q}-i\nabla_{\boldsymbol{r}})^2 + V_{\text{latt}}(\boldsymbol{r},t)\right]u(\boldsymbol{r},t;\boldsymbol{q}), \tag{B.3}$$

which follows from Eq. (3.10), and where V_{latt} is the modulated lattice potential.

By performing the operation $\int d\boldsymbol{r}\ u^*(\boldsymbol{r},t;\boldsymbol{q})\times$Eq. (B.3) [i.e., projecting Eq. (B.3) onto $u(\boldsymbol{r},t;\boldsymbol{q})$], one gets

$$\begin{aligned}\varepsilon_{\boldsymbol{q}} + \int d\boldsymbol{r}\ u^*(\boldsymbol{r},t;\boldsymbol{q})i\hbar\frac{\partial}{\partial t}u(\boldsymbol{r},t;\boldsymbol{q}) = \\ = \int d\boldsymbol{r}\ u^*(\boldsymbol{r},t;\boldsymbol{q})\left[\frac{\hbar^2}{2m}(\boldsymbol{q}-i\nabla_{\boldsymbol{r}})^2 + V_{\text{latt}}(\boldsymbol{r},t)\right]u(\boldsymbol{r},t;\boldsymbol{q})\end{aligned} \tag{B.4}$$

In order to extract the difference $d\varepsilon = \varepsilon_{\boldsymbol{q}_2} - \varepsilon_{\boldsymbol{q}_1}$, let's now evaluate the terms highlighted in

blue and red in Eq. (B.4) at two nearby crystal momenta $\boldsymbol{q}_1$ and $\boldsymbol{q}_2$, whose difference is $\Delta\boldsymbol{q}$ (i.e., $\boldsymbol{q}_2 = \boldsymbol{q}_1 + \Delta\boldsymbol{q}$). In the following derivation, we will employ the approximate expansions

$$(\boldsymbol{q}_2 - i\nabla_{\boldsymbol{r}})^2 = (\boldsymbol{q}_1 + \Delta\boldsymbol{q} - i\nabla_{\boldsymbol{r}})^2 \approx (\boldsymbol{q}_1 - i\nabla_{\boldsymbol{r}})^2 + 2(\boldsymbol{q}_1 - i\nabla_{\boldsymbol{r}}) \cdot \Delta\boldsymbol{q}, \tag{B.5}$$

$$u(\boldsymbol{r}, t; \boldsymbol{q}_2) = u(\boldsymbol{r}, t; \boldsymbol{q}_1 + \Delta\boldsymbol{q}) \approx u(\boldsymbol{r}, t; \boldsymbol{q}_1) + \nabla_{\boldsymbol{q}} u(\boldsymbol{r}, t; \boldsymbol{q}_1) \cdot \Delta\boldsymbol{q}, \tag{B.6}$$

valid for small enough $\Delta\boldsymbol{q}$.

Term highlighted in blue

Using the approximation (B.6) and keeping terms up to first order in $\Delta\boldsymbol{q}$, the difference between the term with the time derivative (highlighted in blue) in Eq. (B.3) evaluated at crystal momenta $\boldsymbol{q}_1$ and $\boldsymbol{q}_2$ is approximated by

$$\begin{aligned}
&\int d\boldsymbol{r}\ \ u^*(\boldsymbol{r}, t; \boldsymbol{q}_2) i\hbar \frac{\partial}{\partial t} u(\boldsymbol{r}, t; \boldsymbol{q}_2) - \int d\boldsymbol{r}\ \ u^*(\boldsymbol{r}, t; \boldsymbol{q}_1) i\hbar \frac{\partial}{\partial t} u(\boldsymbol{r}, t; \boldsymbol{q}_1) \approx \\
&\qquad \approx \quad + \int d\boldsymbol{r}\ \left[\nabla_{\boldsymbol{q}} u^*(\boldsymbol{r}, t; \boldsymbol{q}_1) \cdot \Delta\boldsymbol{q}\right] i\hbar \frac{\partial}{\partial t} u(\boldsymbol{r}, t; \boldsymbol{q}_1) + \\
&\qquad\qquad + \int d\boldsymbol{r}\ u^*(\boldsymbol{r}, t; \boldsymbol{q}_1) i\hbar \frac{\partial}{\partial t} \left[\nabla_{\boldsymbol{q}} u(\boldsymbol{r}, t; \boldsymbol{q}_1) \cdot \Delta\boldsymbol{q}\right].
\end{aligned} \tag{B.7}$$

Term highlighted in red

Using the approximations (B.5) and (B.6), and keeping terms up to first order in $\Delta\boldsymbol{q}$, the difference between the term involving the lattice potential V_{latt} (highlighted in red) in Eq. (B.3)

evaluated at the nearby crystal momenta $\boldsymbol{q}_1$ and $\boldsymbol{q}_2$ is approximated by

$$\begin{aligned}
&\int d\boldsymbol{r}\; u^*(\boldsymbol{r},t;\boldsymbol{q}_2)\left[\frac{\hbar^2}{2m}(\boldsymbol{q}_2-i\nabla_{\boldsymbol{r}})^2+V_{\text{latt}}(\boldsymbol{r},t)\right]u(\boldsymbol{r},t;\boldsymbol{q}_2)\\
-&\int d\boldsymbol{r}\; u^*(\boldsymbol{r},t;\boldsymbol{q}_1)\left[\frac{\hbar^2}{2m}(\boldsymbol{q}_1-i\nabla_{\boldsymbol{r}})^2+V_{\text{latt}}(\boldsymbol{r},t)\right]u(\boldsymbol{r},t;\boldsymbol{q}_1)\approx\\
&\qquad+\boxed{\frac{\hbar^2}{m}\Delta\boldsymbol{q}\cdot\int d\boldsymbol{r}\;\; u^*(\boldsymbol{r},t;\boldsymbol{q}_1)\,(\boldsymbol{q}_1-i\nabla_{\boldsymbol{r}})\,u(\boldsymbol{r},t;\boldsymbol{q}_1)}+\\
&\qquad+\boxed{\int d\boldsymbol{r}\; u^*(\boldsymbol{r},t;\boldsymbol{q}_1)\left[\frac{\hbar^2}{2m}(\boldsymbol{q}_1-i\nabla_{\boldsymbol{r}})^2+V_{\text{latt}}(\boldsymbol{r},t)\right]\nabla_{\boldsymbol{q}}u(\boldsymbol{r},t;\boldsymbol{q}_1)\cdot\Delta\boldsymbol{q}}+\\
&\qquad+\boxed{\int d\boldsymbol{r}\;\nabla_{\boldsymbol{q}}u^*(\boldsymbol{r},t;\boldsymbol{q}_1)\cdot\Delta\boldsymbol{q}\left[\frac{\hbar^2}{2m}(\boldsymbol{q}_1-i\nabla_{\boldsymbol{r}})^2+V_{\text{latt}}(\boldsymbol{r},t)\right]u(\boldsymbol{r},t;\boldsymbol{q}_1)}. \qquad \text{(B.8)}
\end{aligned}$$

It is important to note that the term encircled by the square $\square$ in Eq. (B.8) is proportional to the (time-dependent periodic) weighted average of the momenta

$$\boxed{\frac{\hbar^2}{m}\Delta\boldsymbol{q}\cdot\int d\boldsymbol{r}\;\; u^*(\boldsymbol{r},t;\boldsymbol{q}_1)\,[(\boldsymbol{q}_1-i\nabla_{\boldsymbol{r}})]\,u(\boldsymbol{r},t;\boldsymbol{q}_1)=\frac{\hbar^2}{m}\Delta\boldsymbol{q}\cdot\left\{\boldsymbol{q}_1+\sum_{\boldsymbol{\mathcal{Q}}\in\tilde{\mathcal{B}}}\boldsymbol{\mathcal{Q}}|c_{\boldsymbol{\mathcal{Q}}}(t)|^2\right\}} \qquad \text{(B.9)}$$

where $\tilde{\mathcal{B}}$ is the reciprocal lattice, and $c_{\boldsymbol{\mathcal{Q}}}(t)$ are the **time-dependent periodic** coefficients of u when expanded in terms of plane waves.

Using Eq. (B.3), the last two terms in Eq. (B.8) can be written in terms of time derivatives (and also some terms involving the quasienergy $\varepsilon_{\boldsymbol{q}_1}$, but those terms will cancel out)

$$\int d\boldsymbol{r}\; u^*(\boldsymbol{r},t;\boldsymbol{q}_1)\left[\frac{\hbar^2}{2m}(\boldsymbol{q}_1 - i\nabla_{\boldsymbol{r}})^2 + V_{\text{latt}}(\boldsymbol{r},t)\right]\nabla_{\boldsymbol{q}} u(\boldsymbol{r},t;\boldsymbol{q}_1)\cdot\Delta\boldsymbol{q} +$$

$$+\int d\boldsymbol{r}\;\nabla_{\boldsymbol{q}} u^*(\boldsymbol{r},t;\boldsymbol{q}_1)\cdot\Delta\boldsymbol{q}\left[\frac{\hbar^2}{2m}(\boldsymbol{q}_1 - i\nabla_{\boldsymbol{r}})^2 + V_{\text{latt}}(\boldsymbol{r},t)\right] u(\boldsymbol{r},t;\boldsymbol{q}_1) =$$

$$= \int d\boldsymbol{r}\;\left[\varepsilon_{\boldsymbol{q}_1} u^*(\boldsymbol{r},t;\boldsymbol{q}_1) - i\hbar\frac{\partial}{\partial t}u^*(\boldsymbol{r},t;\boldsymbol{q}_1)\right]\nabla_{\boldsymbol{q}} u(\boldsymbol{r},t;\boldsymbol{q}_1)\cdot\Delta\boldsymbol{q} +$$

$$+\int d\boldsymbol{r}\;\nabla_{\boldsymbol{q}} u^*(\boldsymbol{r},t;\boldsymbol{q}_1)\cdot\Delta\boldsymbol{q}\left[\varepsilon_{\boldsymbol{q}_1} u(\boldsymbol{r},t;\boldsymbol{q}_1) + i\hbar\frac{\partial}{\partial t}u(\boldsymbol{r},t;\boldsymbol{q}_1)\right] =$$

$$= \varepsilon_{\boldsymbol{q}_1}\Delta\boldsymbol{q}\cdot\int d\boldsymbol{r}\;\left[u^*(\boldsymbol{r},t;\boldsymbol{q}_1)\nabla_{\boldsymbol{q}} u(\boldsymbol{r},t;\boldsymbol{q}_1) + u(\boldsymbol{r},t;\boldsymbol{q}_1)\nabla_{\boldsymbol{q}} u^*(\boldsymbol{r},t;\boldsymbol{q}_1)\right] +$$

$$+\Delta\boldsymbol{q}\cdot\int d\boldsymbol{r}\;\left[+\nabla_{\boldsymbol{q}} u^*(\boldsymbol{r},t;\boldsymbol{q}_1)i\hbar\frac{\partial}{\partial t}u(\boldsymbol{r},t;\boldsymbol{q}_1) - \nabla_{\boldsymbol{q}} u(\boldsymbol{r},t;\boldsymbol{q}_1)i\hbar\frac{\partial}{\partial t}u^*(\boldsymbol{r},t;\boldsymbol{q}_1)\right] =$$

$$= \varepsilon_{\boldsymbol{q}_1}\Delta\boldsymbol{q}\cdot\int d\boldsymbol{r}\;\nabla_{\boldsymbol{q}}\left[u^*(\boldsymbol{r},t;\boldsymbol{q}_1)u(\boldsymbol{r},t;\boldsymbol{q}_1)\right] +$$

$$+\Delta\boldsymbol{q}\cdot\int d\boldsymbol{r}\;\left[+\nabla_{\boldsymbol{q}} u^*(\boldsymbol{r},t;\boldsymbol{q}_1)i\hbar\frac{\partial}{\partial t}u(\boldsymbol{r},t;\boldsymbol{q}_1) - \nabla_{\boldsymbol{q}} u(\boldsymbol{r},t;\boldsymbol{q}_1)i\hbar\frac{\partial}{\partial t}u^*(\boldsymbol{r},t;\boldsymbol{q}_1)\right] =$$

$$= 0 + \Delta\boldsymbol{q}\cdot\int d\boldsymbol{r}\;\left[+\nabla_{\boldsymbol{q}} u^*(\boldsymbol{r},t;\boldsymbol{q}_1)i\hbar\frac{\partial}{\partial t}u(\boldsymbol{r},t;\boldsymbol{q}_1) - \nabla_{\boldsymbol{q}} u(\boldsymbol{r},t;\boldsymbol{q}_1)i\hbar\frac{\partial}{\partial t}u^*(\boldsymbol{r},t;\boldsymbol{q}_1)\right] \quad \text{(B.10)}$$

where in the last step we have used the fact that

$$\int d\boldsymbol{r}\;\nabla_{\boldsymbol{q}}\left[u^*(\boldsymbol{r},t;\boldsymbol{q}_1)u(\boldsymbol{r},t;\boldsymbol{q}_1)\right] = \nabla_{\boldsymbol{q}}\int d\boldsymbol{r}\;\left[u^*(\boldsymbol{r},t;\boldsymbol{q}_1)u(\boldsymbol{r},t;\boldsymbol{q}_1)\right] = \nabla_{\boldsymbol{q}}(1) = 0, \quad \text{(B.11)}$$

which follows from $\int d\boldsymbol{r} u^*(\boldsymbol{r},t;\boldsymbol{q}_1)u(\boldsymbol{r},t;\boldsymbol{q}_1) = 1$ being a constant (due to the normalization condition of u) and having no dependence on $\boldsymbol{q}$. Note that the time derivative has been highlighted in blue since similar terms appear in Eq. (B.7).

Evaluate difference between $\varepsilon_{\boldsymbol{q}_2}$ and $\varepsilon_{\boldsymbol{q}_1}$

To calculate the difference difference between $\varepsilon_{\boldsymbol{q}_2}$ and $\varepsilon_{\boldsymbol{q}_1}$, let's use Eq. (B.4) along with the derived expansions (B.7), (B.8) for the *blue* and *red* terms, and the relations (B.9), (B.10)

$$\begin{aligned}
&\varepsilon_{\boldsymbol{q}_1+\Delta\boldsymbol{q}} - \varepsilon_{\boldsymbol{q}_1} + \Delta\boldsymbol{q}\cdot\int d\boldsymbol{r}\;\; \cancel{\nabla_{\boldsymbol{q}} u^*(\boldsymbol{r},t;\boldsymbol{q}_1) i\hbar \frac{\partial}{\partial t} u(\boldsymbol{r},t;\boldsymbol{q}_1)} + \\
&\qquad\qquad + \Delta\boldsymbol{q}\cdot\int d\boldsymbol{r}\;\; u^*(\boldsymbol{r},t;\boldsymbol{q}_1) i\hbar \frac{\partial}{\partial t}\nabla_{\boldsymbol{q}} u(\boldsymbol{r},t;\boldsymbol{q}_1) = \\
&= \frac{\hbar^2}{m}\Delta\boldsymbol{q}\cdot\left\{\boldsymbol{q}_1 + \sum_{\boldsymbol{\mathcal{Q}}\in\tilde{\mathcal{B}}}\boldsymbol{\mathcal{Q}}|c_{\boldsymbol{\mathcal{Q}}}(t)|^2\right\} + \\
&\qquad + \Delta\boldsymbol{q}\cdot\int d\boldsymbol{r}\;\; \left[\cancel{+\nabla_{\boldsymbol{q}} u^*(\boldsymbol{r},t;\boldsymbol{q}_1) i\hbar \frac{\partial}{\partial t} u(\boldsymbol{r},t;\boldsymbol{q}_1)} - \nabla_{\boldsymbol{q}} u(\boldsymbol{r},t;\boldsymbol{q}_1) i\hbar \frac{\partial}{\partial t} u^*(\boldsymbol{r},t;\boldsymbol{q}_1)\right],
\end{aligned} \tag{B.12}$$

$$\begin{aligned}
&\mu_{\boldsymbol{q}_1+\Delta\boldsymbol{q}} - \mu_{\boldsymbol{q}_1} + \Delta\boldsymbol{q}\cdot\int d\boldsymbol{r}\; u^*(\boldsymbol{r},t;\boldsymbol{q}_1) i\hbar \frac{\partial}{\partial t}\nabla_{\boldsymbol{q}} u(\boldsymbol{r},t;\boldsymbol{q}_1) = \\
&\qquad = \frac{\hbar^2}{m}\Delta\boldsymbol{q}\cdot\left\{\boldsymbol{q}_1 + \sum_{\boldsymbol{\mathcal{Q}}\in\tilde{\mathcal{B}}}\boldsymbol{\mathcal{Q}}|c_{\boldsymbol{\mathcal{Q}}}(t)|^2\right\} + \Delta\boldsymbol{q}\cdot\int d\boldsymbol{r}\;\; \left[-\nabla_{\boldsymbol{q}} u(\boldsymbol{r},t;\boldsymbol{q}_1) i\hbar \frac{\partial}{\partial t} u^*(\boldsymbol{r},t;\boldsymbol{q}_1)\right],
\end{aligned} \tag{B.13}$$

$$\mu_{\boldsymbol{q}_1+\Delta\boldsymbol{q}} - \mu_{\boldsymbol{q}_1} = \frac{\hbar^2}{m}\Delta\boldsymbol{q}\cdot\left\{\boldsymbol{q}_1 + \sum_{\boldsymbol{\mathcal{Q}}\in\tilde{\mathcal{B}}}\boldsymbol{\mathcal{Q}}|c_{\boldsymbol{\mathcal{Q}}}(t)|^2\right\}$$
$$- \Delta\boldsymbol{q}\cdot\int d\boldsymbol{r}\left[\nabla_{\boldsymbol{q}}u(\boldsymbol{r},t;\boldsymbol{q}_1)i\hbar\frac{\partial}{\partial t}u^*(\boldsymbol{r},t;\boldsymbol{q}_1) + u^*(\boldsymbol{r},t;\boldsymbol{q}_1)i\hbar\frac{\partial}{\partial t}\nabla_{\boldsymbol{q}}u(\boldsymbol{r},t;\boldsymbol{q}_1)\right] \tag{B.14}$$

which can be written as

$$\boxed{\varepsilon_{\boldsymbol{q}_1+\Delta\boldsymbol{q}} - \varepsilon_{\boldsymbol{q}_1} = \frac{\hbar^2}{m}\Delta\boldsymbol{q}\cdot\left\{\boldsymbol{q}_1 + \sum_{\boldsymbol{\mathcal{Q}}\in\tilde{\mathcal{B}}}\boldsymbol{\mathcal{Q}}|c_{\boldsymbol{\mathcal{Q}}}(t)|^2\right\} - \Delta\boldsymbol{q}\cdot i\hbar\frac{\partial}{\partial t}\int d\boldsymbol{r}u^*(\boldsymbol{r},t;\boldsymbol{q}_1)\nabla_{\boldsymbol{q}}u(\boldsymbol{r},t;\boldsymbol{q}_1)} \tag{B.15}$$

If we integrate over a single period T of the modulation, the last term in the previous equation, namely,

$$i\hbar\frac{\partial}{\partial t}\int d\boldsymbol{r}\ u^*(\boldsymbol{r},t;\boldsymbol{q}_1)\nabla_{\boldsymbol{q}}u(\boldsymbol{r},t;\boldsymbol{q}_1), \tag{B.16}$$

(which can be termed as a *residual* or *micromotion* term), we get

$$i\hbar\int_{\tau}^{\tau+T}dt\ \ \frac{\partial}{\partial t}\int d\boldsymbol{r}\ \ u^*(\boldsymbol{r},t;\boldsymbol{q}_1)\nabla_{\boldsymbol{q}}u(\boldsymbol{r},t;\boldsymbol{q}_1) =$$
$$= i\hbar\left[u^*(\boldsymbol{r},\tau+T;\boldsymbol{q}_1)\nabla_{\boldsymbol{q}}u(\boldsymbol{r},\tau+T;\boldsymbol{q}_1) - u^*(\boldsymbol{r},\tau;\boldsymbol{q}_1)\nabla_{\boldsymbol{q}}u(\boldsymbol{r},\tau;\boldsymbol{q}_1)\right]$$
$$= 0, \tag{B.17}$$

where the last equality follows from the time-periodicity of the Floquet mode u. Finally, we obtain the result

$$\varepsilon_{\boldsymbol{q}_1+\Delta\boldsymbol{q}} - \varepsilon_{\boldsymbol{q}_1} = \frac{\hbar^2}{m}\Delta\boldsymbol{q}\cdot\left\{\boldsymbol{q}_1 + \sum_{\boldsymbol{\mathcal{Q}}\in\tilde{\mathcal{B}}}\boldsymbol{\mathcal{Q}}\frac{1}{T}\int_{\tau}^{\tau+T} dt\ \ |c_{\boldsymbol{\mathcal{Q}}}(t)|^2\right\}, \tag{B.18}$$

which relates the quasienergy ε to the expected value of the "momentum". Since the red part of Eq. (B.18) determines how much $\varepsilon_{\boldsymbol{q}}$ changes with $\Delta\boldsymbol{q}$, it represents the gradient of the quasienergy, namely,

$$\frac{1}{\hbar}\nabla_{\boldsymbol{q}}\varepsilon_{\boldsymbol{q}} = \langle v_g(\boldsymbol{q})\rangle_T, \tag{B.19}$$

where the symbol $\langle\cdots\rangle_T$ indicates average over a single period of the modulation.

B.2 Relation derived from the GP equation

If we now use the Floquet-Bloch form (B.2) for the condensate order parameter as an ansatz for the GP equation (3.30) [or Eq (3.35)], instead of the Schrödinger equation with no nonlinear term, we obtain

$$\varepsilon_{\boldsymbol{q}}u_c(\boldsymbol{r},t;\boldsymbol{q}_c) + i\hbar\frac{\partial}{\partial t}u_c(\boldsymbol{r},t;\boldsymbol{q}_c) = \left[\frac{\hbar^2}{2m}(\boldsymbol{q}_c - i\nabla_{\boldsymbol{r}})^2 + V_{\text{latt}}(\boldsymbol{r},t) + g\bar{n}|u_c|^2\right]u_c(\boldsymbol{r},t;\boldsymbol{q}_c), \tag{B.20}$$

which possesses the same form as Eq. (B.3) with the effective time-periodic lattice $\tilde{V}_{\text{latt}}(\boldsymbol{r}, t; \boldsymbol{q}_c) = V_{\text{latt}}(\boldsymbol{r}, t) + g\bar{n}|u_c(\boldsymbol{r}, t; \boldsymbol{q}_c)|^2$. Since the form of the lattice was arbitrary in the derivation of Eq. (B.18), it would seem plausible to conclude that it remains valid with the effecive potential $\tilde{V}_{\text{latt}}(\boldsymbol{r}, t)$. However, the $\boldsymbol{q}$- dependence of u_c (and, hence, $\tilde{V}_{\text{latt}}$) produces, in the derivation outlined above, the additional term

$$g\bar{n} \int d\boldsymbol{r}\, u_c^* \left[u_c^* \nabla_{\boldsymbol{q}} u_c + u_c \nabla_{\boldsymbol{q}} u_c\right] u_c = \frac{g\bar{n}}{2} \nabla_{\boldsymbol{q}} \int d\boldsymbol{r}\, |u_c|^4. \tag{B.21}$$

Hence, the relation between v_g and the (nonlinear) quasienergy when using the GP equation is now

$$\nabla_{\boldsymbol{q}} \left(\mu_c - \frac{1}{2} g\bar{n} \left\langle \int d\boldsymbol{r}\, |u_c|^4 \right\rangle \right) = \hbar \left\langle v_g \right\rangle_T . \tag{B.22}$$

Bibliography

[1] William D. Phillips. Nobel lecture: Laser cooling and trapping of neutral atoms. *Rev. Mod. Phys.*, 70:721–741, Jul 1998. [Cited on page 1.]

[2] Immanuel Bloch. Ultracold quantum gases in optical lattices. *Nature Physics*, 1(1):23–30, 2005. [Cited on page 1.]

[3] Immanuel Bloch. Exploring quantum matter with ultracold atoms in optical lattices. *Journal of Physics B: Atomic, Molecular and Optical Physics*, 38(9):S629, 2005. [Cited on page 1.]

[4] Maciej Lewenstein, Anna Sanpera, Veronica Ahufinger, Bogdan Damski, Aditi Sen(De), and Ujjwal Sen. Ultracold atomic gases in optical lattices: mimicking condensed matter physics and beyond. *Advances in Physics*, 56(2):243–379, 03 2007. [Cited on page 1.]

[5] Maciej Lewenstein, Anna Sanpera, and Verònica Ahufinger. *Ultracold Atoms in Optical Lattices : Simulating Quantum Many-body Systems*, volume 1st ed. OUP Oxford, Oxford, U.K., 2012. [Cited on page 1.]

[6] P. Verkerk, B. Lounis, C. Salomon, C. Cohen-Tannoudji, J.-Y. Courtois, and G. Grynberg. Dynamics and spatial order of cold cesium atoms in a periodic optical potential. *Phys. Rev. Lett.*, 68:3861–3864, Jun 1992. [Cited on page 1.]

[7] A. Hemmerich and T. W. Hänsch. Two-dimesional atomic crystal bound by light. *Phys. Rev. Lett.*, 70:410–413, Jan 1993. [Cited on page 1.]

[8] Jayadev Vijayan, Pimonpan Sompet, Guillaume Salomon, Joannis Koepsell, Sarah Hirthe, Annabelle Bohrdt, Fabian Grusdt, Immanuel Bloch, and Christian Gross. Time-resolved observation of spin-charge deconfinement in fermionic Hubbard chains. *Science*, 367(6474):186–189, 2020. [Cited on page 1.]

[9] Manolo R. Lam, Natalie Peter, Thorsten Groh, Wolfgang Alt, Carsten Robens, Dieter Meschede, Antonio Negretti, Simone Montangero, Tommaso Calarco, and Andrea Alberti. Demonstration of quantum brachistochrones between distant states of an atom. *Phys. Rev. X*, 11:011035, Feb 2021. [Cited on page 1.]

[10] Ruwan Senaratne, Danyel Cavazos-Cavazos, Sheng Wang, Feng He, Ya-Ting Chang, Aashish Kafle, Han Pu, Xi-Wen Guan, and Randall G. Hulet. Spin-charge separation

in a one-dimensional Fermi gas with tunable interactions. *Science*, 376(6599):1305–1308, 2022. [Cited on page 1.]

[11] Gabriele Natale, Thomas Bland, Simon Gschwendtner, Louis Lafforgue, Daniel S. Grün, Alexander Patscheider, Manfred J. Mark, and Francesca Ferlaino. Bloch oscillations and matter-wave localization of a dipolar quantum gas in a one-dimensional lattice. *Communications Physics*, 5(1):227, 2022. [Cited on page 1.]

[12] Roshan Sajjad, Jeremy L. Tanlimco, Hector Mas, Alec Cao, Eber Nolasco-Martinez, Ethan Q. Simmons, Flávio L. N. Santos, Patrizia Vignolo, Tommaso Macrì, and David M. Weld. Observation of the quantum boomerang effect. *Phys. Rev. X*, 12:011035, Feb 2022. [Cited on page 1.]

[13] D. Jaksch, C. Bruder, J. I. Cirac, C. W. Gardiner, and P. Zoller. Cold bosonic atoms in optical lattices. *Phys. Rev. Lett.*, 81:3108–3111, Oct 1998. [Cited on page 1.]

[14] Markus Greiner, Olaf Mandel, Tilman Esslinger, Theodor W. Hänsch, and Immanuel Bloch. Quantum phase transition from a superfluid to a Mott insulator in a gas of ultracold atoms. *Nature*, 415(6867):39–44, 2002. [Cited on page 1.]

[15] Robert Jördens, Niels Strohmaier, Kenneth Günter, Henning Moritz, and Tilman Esslinger. A Mott insulator of fermionic atoms in an optical lattice. *Nature*, 455(7210):204–207, 2008. [Cited on page 1.]

[16] U. Schneider, L. Hackermüller, S. Will, Th. Best, I. Bloch, T. A. Costi, R. W. Helmes, D. Rasch, and A. Rosch. Metallic and insulating phases of repulsively interacting fermions in a 3d optical lattice. *Science*, 322(5907):1520–1525, 2022/11/08 2008. [Cited on page 1.]

[17] Tilman Esslinger. Fermi-Hubbard physics with atoms in an optical lattice. *Annual Review of Condensed Matter Physics*, 1(1):129–152, 2022/11/08 2010. [Cited on page 1.]

[18] Philipp M. Preiss, Ruichao Ma, M. Eric Tai, Alexander Lukin, Matthew Rispoli, Philip Zupancic, Yoav Lahini, Rajibul Islam, and Markus Greiner. Strongly correlated quantum walks in optical lattices. *Science*, 347(6227):1229–1233, 2022/11/08 2015. [Cited on page 1.]

[19] S. Baier, M. J. Mark, D. Petter, K. Aikawa, L. Chomaz, Z. Cai, M. Baranov, P. Zoller, and F. Ferlaino. Extended Bose-Hubbard models with ultracold magnetic atoms. *Science*, 352(6282):201–205, 2016. [Cited on page 1.]

[20] Guillaume Salomon, Joannis Koepsell, Jayadev Vijayan, Timon A. Hilker, Jacopo Nespolo, Lode Pollet, Immanuel Bloch, and Christian Gross. Direct observation of incommensurate magnetism in Hubbard chains. *Nature*, 565(7737):56–60, 2019. [Cited on page 1.]

[21] Toshiya Kinoshita, Trevor Wenger, and David S. Weiss. Observation of a one-dimensional Tonks-Girardeau gas. *Science*, 305(5687):1125–1128, 2022/11/08 2004. [Cited on page 1.]

[22] Belén Paredes, Artur Widera, Valentin Murg, Olaf Mandel, Simon Fölling, Ignacio Cirac, Gora V. Shlyapnikov, Theodor W. Hänsch, and Immanuel Bloch. Tonks–Girardeau gas of ultracold atoms in an optical lattice. *Nature*, 429(6989):277–281, 2004. [Cited on page 1.]

[23] M. Girardeau. Relationship between systems of impenetrable bosons and fermions in one dimension. *Journal of Mathematical Physics*, 1(6):516–523, 1960. [Cited on page 1.]

[24] Zoran Hadzibabic, Peter Krüger, Marc Cheneau, Baptiste Battelier, and Jean Dalibard. Berezinskii–Kosterlitz–Thouless crossover in a trapped atomic gas. *Nature*, 441(7097):1118–1121, 2006. [Cited on page 1.]

[25] S. Tung, G. Lamporesi, D. Lobser, L. Xia, and E. A. Cornell. Observation of the presuperfluid regime in a two-dimensional Bose gas. *Phys. Rev. Lett.*, 105:230408, Dec 2010. [Cited on page 1.]

[26] Georg Wirth, Matthias Ölschläger, and Andreas Hemmerich. Evidence for orbital superfluidity in the P-band of a bipartite optical square lattice. *Nature Physics*, 7(2):147–153, 2011. [Cited on pages 1 and 2.]

[27] Parvis Soltan-Panahi, Dirk-Sören Lühmann, Julian Struck, Patrick Windpassinger, and Klaus Sengstock. Quantum phase transition to unconventional multi-orbital superfluidity in optical lattices. *Nature Physics*, 8(1):71–75, 2012. [Cited on page 1.]

[28] Hirokazu Miyake, Georgios A. Siviloglou, Colin J. Kennedy, William Cody Burton, and Wolfgang Ketterle. Realizing the Harper Hamiltonian with laser-assisted tunneling in optical lattices. *Phys. Rev. Lett.*, 111:185302, Oct 2013. [Cited on pages 1 and 4.]

[29] M. Aidelsburger, M. Atala, M. Lohse, J. T. Barreiro, B. Paredes, and I. Bloch. Realization of the Hofstadter Hamiltonian with ultracold atoms in optical lattices. *Phys. Rev. Lett.*, 111:185301, Oct 2013. [Cited on page 1.]

[30] G. E. Astrakharchik, J. Boronat, J. Casulleras, and S. Giorgini. Beyond the Tonks-Girardeau gas: Strongly correlated regime in quasi-one-dimensional Bose gases. *Phys. Rev. Lett.*, 95:190407, Nov 2005. [Cited on page 2.]

[31] Elmar Haller, Mattias Gustavsson, Manfred J. Mark, Johann G. Danzl, Russell Hart, Guido Pupillo, and Hanns-Christoph Nägerl. Realization of an excited, strongly correlated quantum gas phase. *Science*, 325(5945):1224–1227, 2009. [Cited on page 2.]

[32] Pablo Solano, Yiheng Duan, Yu-Ting Chen, Alyssa Rudelis, Cheng Chin, and Vladan Vuletić. Strongly correlated quantum gas prepared by direct laser cooling. *Phys. Rev. Lett.*, 123:173401, Oct 2019. [Cited on page 2.]

[33] André Eckardt. Colloquium: Atomic quantum gases in periodically driven optical lattices. *Rev. Mod. Phys.*, 89:011004, Mar 2017. [Cited on pages 2 and 39.]

[34] Takashi Oka and Sota Kitamura. Floquet engineering of quantum materials. *Annual Review of Condensed Matter Physics*, 10(1):387–408, 2019. [Cited on page 2.]

[35] Christof Weitenberg and Juliette Simonet. Tailoring quantum gases by Floquet engineering. *Nature Physics*, 17(12):1342–1348, 2021. [Cited on page 2.]

[36] Gregor Jotzu, Michael Messer, Rémi Desbuquois, Martin Lebrat, Thomas Uehlinger, Daniel Greif, and Tilman Esslinger. Experimental realization of the topological Haldane model with ultracold fermions. *Nature*, 515(7526):237–240, 2014. [Cited on page 2.]

[37] N. Fläschner, B. S. Rem, M. Tarnowski, D. Vogel, D.-S. Lühmann, K. Sengstock, and C. Weitenberg. Experimental reconstruction of the Berry curvature in a Floquet Bloch band. *Science*, 352(6289):1091–1094, 2016. [Cited on page 2.]

[38] Frederik Görg, Michael Messer, Kilian Sandholzer, Gregor Jotzu, Rémi Desbuquois, and Tilman Esslinger. Enhancement and sign change of magnetic correlations in a driven quantum many-body system. *Nature*, 553(7689):481–485, 2018. [Cited on page 2.]

[39] J. Struck, C. Ölschläger, M. Weinberg, P. Hauke, J. Simonet, A. Eckardt, M. Lewenstein, K. Sengstock, and P. Windpassinger. Tunable gauge potential for neutral and spinless particles in driven optical lattices. *Phys. Rev. Lett.*, 108:225304, May 2012. [Cited on page 2.]

[40] J. Struck, M. Weinberg, C. Ölschläger, P. Windpassinger, J. Simonet, K. Sengstock, R. Höppner, P. Hauke, A. Eckardt, M. Lewenstein, and L. Mathey. Engineering Ising-XY spin-models in a triangular lattice using tunable artificial gauge fields. *Nature Physics*, 9(11):738–743, 2013. [Cited on page 2.]

[41] Tigran A. Sedrakyan, Victor M. Galitski, and Alex Kamenev. Statistical transmutation in Floquet driven optical lattices. *Phys. Rev. Lett.*, 115:195301, Nov 2015. [Cited on pages 2, 3, 4, 6, 94, 95, 96, 101, 109, 143, and 145.]

[42] T. Kock, M. Ölschläger, A. Ewerbeck, W.-M. Huang, L. Mathey, and A. Hemmerich. Observing chiral superfluid order by matter-wave interference. *Phys. Rev. Lett.*, 114:115301, Mar 2015. [Cited on page 2.]

[43] Colin V. Parker, Li-Chung Ha, and Cheng Chin. Direct observation of effective ferromagnetic domains of cold atoms in a shaken optical lattice. *Nature Physics*, 9(12):769–774, 2013. [Cited on pages 2, 4, 46, 95, 96, and 107.]

[44] Y. J. Lin, K. Jiménez-García, and I. B. Spielman. Spin–orbit-coupled bose–einstein condensates. *Nature*, 471(7336):83–86, 2011. [Cited on page 3.]

[45] Victor Galitski and Ian B. Spielman. Spin–orbit coupling in quantum gases. *Nature*, 494(7435):49–54, 2013. [Cited on page 3.]

[46] Andika Putra, F. Salces-Cárcoba, Yuchen Yue, Seiji Sugawa, and I. B. Spielman. Spatial coherence of spin-orbit-coupled Bose gases. *Phys. Rev. Lett.*, 124:053605, Feb 2020. [Cited on page 3.]

[47] Horst L. Stormer, Daniel C. Tsui, and Arthur C. Gossard. The fractional quantum Hall effect. *Rev. Mod. Phys.*, 71:S298–S305, Mar 1999. [Cited on page 3.]

[48] Sebastian D. Huber and Ehud Altman. Bose condensation in flat bands. *Phys. Rev. B*, 82:184502, Nov 2010. [Cited on page 3.]

[49] Kai Sun, Zhengcheng Gu, Hosho Katsura, and S. Das Sarma. Nearly flatbands with nontrivial topology. *Phys. Rev. Lett.*, 106:236803, Jun 2011. [Cited on page 3.]

[50] Titus Neupert, Luiz Santos, Claudio Chamon, and Christopher Mudry. Fractional quantum hall states at zero magnetic field. *Phys. Rev. Lett.*, 106:236804, Jun 2011. [Cited on page 3.]

[51] Daniel Leykam, Alexei Andreanov, and Sergej Flach. Artificial flat band systems: from lattice models to experiments. *Advances in Physics: X*, 3(1):1473052, 01 2018. [Cited on page 3.]

[52] Erez Berg, Mark S. Rudner, and Steven A. Kivelson. Electronic liquid crystalline phases in a spin-orbit coupled two-dimensional electron gas. *Phys. Rev. B*, 85:035116, Jan 2012. [Cited on page 3.]

[53] Jonathan Ruhman and Erez Berg. Ferromagnetic and nematic non-Fermi liquids in spin-orbit-coupled two-dimensional Fermi gases. *Phys. Rev. B*, 90:235119, Dec 2014. [Cited on page 3.]

[54] P. G. Silvestrov and O. Entin-Wohlman. Wigner crystal of a two-dimensional electron gas with a strong spin-orbit interaction. *Phys. Rev. B*, 89:155103, Apr 2014. [Cited on page 3.]

[55] Lianyi He and Xu-Guang Huang. BCS-BEC crossover in 2D Fermi gases with Rashba spin-orbit coupling. *Phys. Rev. Lett.*, 108:145302, Apr 2012. [Cited on page 3.]

[56] Sarang Gopalakrishnan, Austen Lamacraft, and Paul M. Goldbart. Universal phase structure of dilute Bose gases with Rashba spin-orbit coupling. *Phys. Rev. A*, 84:061604, Dec 2011. [Cited on pages 3 and 143.]

[57] Qi Zhou and Xiaoling Cui. Fate of a Bose-Einstein condensate in the presence of spin-orbit coupling. *Phys. Rev. Lett.*, 110:140407, Apr 2013. [Cited on pages 3 and 143.]

[58] Shouvik Sur and Kun Yang. Metallic state in bosonic systems with continuously degenerate dispersion minima. *Phys. Rev. B*, 100:024519, Jul 2019. [Cited on pages 3 and 143.]

[59] Tigran A. Sedrakyan, Alex Kamenev, and Leonid I. Glazman. Composite fermion state of spin-orbit-coupled bosons. *Phys. Rev. A*, 86:063639, Dec 2012. [Cited on pages 3, 4, and 143.]

[60] Tigran A. Sedrakyan, Leonid I. Glazman, and Alex Kamenev. Absence of Bose condensation on lattices with moat bands. *Phys. Rev. B*, 89:201112, May 2014. [Cited on pages 3, 4, and 143.]

[61] Tigran A. Sedrakyan, Leonid I. Glazman, and Alex Kamenev. Spontaneous formation of a nonuniform chiral spin liquid in a moat-band lattice. *Phys. Rev. Lett.*, 114:037203, Jan 2015. [Cited on pages 3, 4, and 143.]

[62] Hui Zhai. Degenerate quantum gases with spin–orbit coupling: a review. *Reports on Progress in Physics*, 78(2):026001, feb 2015. [Cited on page 3.]

[63] Tomoki Ozawa and Gordon Baym. Stability of ultracold atomic Bose condensates with Rashba spin-orbit coupling against quantum and thermal fluctuations. *Phys. Rev. Lett.*, 109:025301, Jul 2012. [Cited on pages 4, 137, and 146.]

[64] Ryan Barnett, Stephen Powell, Tobias Graß, Maciej Lewenstein, and S. Das Sarma. Order by disorder in spin-orbit-coupled Bose-Einstein condensates. *Phys. Rev. A*, 85:023615, Feb 2012. [Cited on pages 4, 137, and 146.]

[65] E. McCann, D. S. L. Abergel, and V. I. Fal'ko. The low energy electronic band structure of bilayer graphene. *The European Physical Journal Special Topics*, 148(1):91–103, 2007. [Cited on page 4.]

[66] Yuanbo Zhang, Tsung-Ta Tang, Caglar Girit, Zhao Hao, Michael C. Martin, Alex Zettl, Michael F. Crommie, Y. Ron Shen, and Feng Wang. Direct observation of a widely tunable bandgap in bilayer graphene. *Nature*, 459(7248):820–823, 2009. [Cited on page 4.]

[67] Georgy Alymov, Vladimir Vyurkov, Victor Ryzhii, and Dmitry Svintsov. Abrupt current switching in graphene bilayer tunnel transistors enabled by van Hove singularities. *Scientific Reports*, 6(1):24654, 2016. [Cited on page 4.]

[68] D. Marchenko, D. V. Evtushinsky, E. Golias, A. Varykhalov, Th. Seyller, and O. Rader. Extremely flat band in bilayer graphene. *Science Advances*, 4(11):eaau0059, 2018. [Cited on page 4.]

[69] Darshana Wickramaratne, Ferdows Zahid, and Roger K. Lake. Electronic and thermoelectric properties of van der Waals materials with ring-shaped valence bands. *Journal of Applied Physics*, 118(7):075101, 2015. [Cited on page 4.]

[70] G D Mahan and J O Sofo. The best thermoelectric. *Proceedings of the National Academy of Sciences*, 93(15):7436–7439, 2022/10/06 1996. [Cited on page 4.]

[71] T. Stauber, N. M. R. Peres, F. Guinea, and A. H. Castro Neto. Fermi liquid theory of a Fermi ring. *Phys. Rev. B*, 75:115425, Mar 2007. [Cited on page 4.]

[72] Eduardo V. Castro, N. M. R. Peres, T. Stauber, and N. A. P. Silva. Low-density ferromagnetism in biased bilayer graphene. *Phys. Rev. Lett.*, 100:186803, May 2008. [Cited on page 4.]

[73] Cheng Gong and Xiang Zhang. Two-dimensional magnetic crystals and emergent heterostructure devices. *Science*, 363(6428):eaav4450, 2019. [Cited on page 4.]

[74] L. Seixas, A. S. Rodin, A. Carvalho, and A. H. Castro Neto. Multiferroic two-dimensional materials. *Phys. Rev. Lett.*, 116:206803, May 2016. [Cited on page 4.]

[75] H. Lignier, C. Sias, D. Ciampini, Y. Singh, A. Zenesini, O. Morsch, and E. Arimondo. Dynamical control of matter-wave tunneling in periodic potentials. *Phys. Rev. Lett.*, 99:220403, Nov 2007. [Cited on pages 4, 39, 40, and 84.]

[76] Zhendong Zhang, Kai-Xuan Yao, Lei Feng, Jiazhong Hu, and Cheng Chin. Pattern formation in a driven Bose–Einstein condensate. *Nature Physics*, 16(6):652–656, 2020. [Cited on page 4.]

[77] Luca D'Alessio and Marcos Rigol. Long-time behavior of isolated periodically driven interacting lattice systems. *Phys. Rev. X*, 4:041048, Dec 2014. [Cited on page 5.]

[78] Marin Bukov, Sarang Gopalakrishnan, Michael Knap, and Eugene Demler. Prethermal Floquet steady states and instabilities in the periodically driven, weakly interacting Bose-Hubbard model. *Phys. Rev. Lett.*, 115:205301, Nov 2015. [Cited on pages 5, 59, and 91.]

[79] Elena Canovi, Marcus Kollar, and Martin Eckstein. Stroboscopic prethermalization in weakly interacting periodically driven systems. *Phys. Rev. E*, 93:012130, Jan 2016. [Cited on page 5.]

[80] S. Lellouch, M. Bukov, E. Demler, and N. Goldman. Parametric instability rates in periodically driven band systems. *Phys. Rev. X*, 7:021015, May 2017. [Cited on pages 5, 59, 72, 73, 74, 75, and 91.]

[81] Jun-Ru Li, Boris Shteynas, and Wolfgang Ketterle. Floquet heating in interacting atomic gases with an oscillating force. *Phys. Rev. A*, 100:033406, Sep 2019. [Cited on page 5.]

[82] Krishnanand Mallayya and Marcos Rigol. Heating rates in periodically driven strongly interacting quantum many-body systems. *Phys. Rev. Lett.*, 123:240603, Dec 2019. [Cited on page 5.]

[83] M. Weinberg, C. Ölschläger, C. Sträter, S. Prelle, A. Eckardt, K. Sengstock, and J. Simonet. Multiphoton interband excitations of quantum gases in driven optical lattices. *Phys. Rev. A*, 92:043621, Oct 2015. [Cited on pages 5 and 84.]

[84] Martin Reitter, Jakob Näger, Karen Wintersperger, Christoph Sträter, Immanuel Bloch, André Eckardt, and Ulrich Schneider. Interaction dependent heating and atom loss in a periodically driven optical lattice. *Phys. Rev. Lett.*, 119:200402, Nov 2017. [Cited on pages 5 and 77.]

[85] Citlali Cabrera-Gutiérrez, Eric Michon, Maxime Arnal, Gabriel Chatelain, Vincent Brunaud, Tomasz Kawalec, Juliette Billy, and David Guéry-Odelin. Resonant excitations of a Bose Einstein condensate in an optical lattice. *The European Physical Journal D*, 73(8):170, 2019. [Cited on page 5.]

[86] T. Boulier, J. Maslek, M. Bukov, C. Bracamontes, E. Magnan, S. Lellouch, E. Demler, N. Goldman, and J. V. Porto. Parametric heating in a 2d periodically driven bosonic system: Beyond the weakly interacting regime. *Phys. Rev. X*, 9:011047, Mar 2019. [Cited on pages 5, 6, 73, 84, 88, and 91.]

[87] K. Wintersperger, M. Bukov, J. Näger, S. Lellouch, E. Demler, U. Schneider, I. Bloch, N. Goldman, and M. Aidelsburger. Parametric instabilities of interacting bosons in periodically driven 1d optical lattices. *Phys. Rev. X*, 10:011030, Feb 2020. [Cited on pages 5 and 76.]

[88] Konrad Viebahn, Joaquín Minguzzi, Kilian Sandholzer, Anne-Sophie Walter, Manish Sajnani, Frederik Görg, and Tilman Esslinger. Suppressing dissipation in a Floquet-Hubbard system. *Phys. Rev. X*, 11:011057, Mar 2021. [Cited on pages 5 and 92.]

[89] Christopher D. Mink, Axel Pelster, Jens Benary, Herwig Ott, and Michael Fleischhauer. Variational truncated Wigner approximation for weakly interacting Bose fields: Dynamics of coupled condensates. *SciPost Phys.*, 12:051, 2022. [Cited on page 5.]

[90] Thomas Bilitewski and Nigel R. Cooper. Scattering theory for Floquet-Bloch states. *Phys. Rev. A*, 91:033601, Mar 2015. [Cited on pages 5 and 77.]

[91] Servando López-Aguayo, Yaroslav V. Kartashov, Victor A. Vysloukh, and Lluis Torner. Method to generate complex quasinondiffracting optical lattices. *Phys. Rev. Lett.*, 105:013902, Jun 2010. [Cited on page 5.]

[92] Charles J. M. Mathy, David A. Huse, and Randall G. Hulet. Enlarging and cooling the Néel state in an optical lattice. *Phys. Rev. A*, 86:023606, Aug 2012. [Cited on page 5.]

[93] Patrick Windpassinger and Klaus Sengstock. Engineering novel optical lattices. *Reports on Progress in Physics*, 76(8):086401, jul 2013. [Cited on pages 5 and 7.]

[94] T. Macrì and T. Pohl. Rydberg dressing of atoms in optical lattices. *Phys. Rev. A*, 89:011402, Jan 2014. [Cited on page 5.]

[95] Y. Wang, S. Subhankar, P. Bienias, M. Łacki, T-C. Tsui, M. A. Baranov, A. V. Gorshkov, P. Zoller, J. V. Porto, and S. L. Rolston. Dark state optical lattice with a subwavelength spatial structure. *Phys. Rev. Lett.*, 120:083601, Feb 2018. [Cited on page 5.]

[96] M. McDonald, B. H. McGuyer, G. Z. Iwata, and T. Zelevinsky. Thermometry via light shifts in optical lattices. *Phys. Rev. Lett.*, 114:023001, Jan 2015. [Cited on page 5.]

[97] L. Duca, T. Li, M. Reitter, I. Bloch, M. Schleier-Smith, and U. Schneider. An Aharonov-Bohm interferometer for determining Bloch band topology. *Science*, 347(6219):288–292, 2015. [Cited on page 5.]

[98] Christian Gross and Immanuel Bloch. Quantum simulations with ultracold atoms in optical lattices. *Science*, 357(6355):995–1001, 2017. [Cited on page 5.]

[99] Luca Asteria, Henrik P. Zahn, Marcel N. Kosch, Klaus Sengstock, and Christof Weitenberg. Quantum gas magnifier for sub-lattice-resolved imaging of 3D quantum systems. *Nature*, 599(7886):571–575, 2021. [Cited on page 5.]

[100] Charles D. Brown, Shao-Wen Chang, Malte N. Schwarz, Tsz-Him Leung, Vladyslav Kozii, Alexander Avdoshkin, Joel E. Moore, and Dan Stamper-Kurn. Direct geometric probe of singularities in band structure. *Science*, 377(6612):1319–1322, 2022. [Cited on page 5.]

[101] P. J. Lee, M. Anderlini, B. L. Brown, J. Sebby-Strabley, W. D. Phillips, and J. V. Porto. Sublattice addressing and spin-dependent motion of atoms in a double-well lattice. *Phys. Rev. Lett.*, 99:020402, Jul 2007. [Cited on pages 5, 14, and 78.]

[102] N. Lundblad, J. M. Obrecht, I. B. Spielman, and J. V. Porto. Field-sensitive addressing and control of field-insensitive neutral-atom qubits. *Nature Physics*, 5(8):575–580, 2009. [Cited on page 5.]

[103] J. Sebby-Strabley, M. Anderlini, P. S. Jessen, and J. V. Porto. Lattice of double wells for manipulating pairs of cold atoms. *Phys. Rev. A*, 73:033605, Mar 2006. [Cited on pages 5, 14, 16, 78, and 80.]

[104] N. Lundblad, M. Schlosser, and J. V. Porto. Experimental observation of magic-wavelength behavior of $^{87}\mathrm{Rb}$ atoms in an optical lattice. *Phys. Rev. A*, 81:031611, Mar 2010. [Cited on page 5.]

[105] E. A. Goldschmidt, D. G. Norris, S. B. Koller, R. Wyllie, R. C. Brown, J. V. Porto, U. I. Safronova, and M. S. Safronova. Magic wavelengths for the $5s$–$18s$ transition in rubidium. *Phys. Rev. A*, 91:032518, Mar 2015. [Cited on page 5.]

[106] E. Magnan, J. Maslek, C. Bracamontes, A. Restelli, T. Boulier, and J. V. Porto. A low-steering piezo-driven mirror. *Review of Scientific Instruments*, 89(7):073110, 2018. [Cited on pages 5, 28, and 29.]

[107] C. A. Bracamontes, J. Maslek, and J. V. Porto. Realization of a Floquet-engineered moat band for ultracold atoms. *Phys. Rev. Lett.*, 128:213401, May 2022. [Cited on page 94.]

[108] Graham P. Collins. Gaseous Bose–Einstein condensate finally observed. *Physics Today*, 48(8):17–20, 1995. [Cited on page 7.]

[109] D. M. Stamper-Kurn, M. R. Andrews, A. P. Chikkatur, S. Inouye, H.-J. Miesner, J. Stenger, and W. Ketterle. Optical confinement of a Bose-Einstein condensate. *Phys. Rev. Lett.*, 80:2027–2030, Mar 1998. [Cited on page 7.]

[110] Anthony J. Leggett. Bose-Einstein condensation in the alkali gases: Some fundamental concepts. *Rev. Mod. Phys.*, 73:307–356, Apr 2001. [Cited on page 7.]

[111] M. D. Barrett, J. A. Sauer, and M. S. Chapman. All-optical formation of an atomic Bose-Einstein condensate. *Phys. Rev. Lett.*, 87:010404, Jun 2001. [Cited on page 7.]

[112] Barbara Goss Levi. Magnetic forces need not apply: Bose–Einstein condensates can be made in an optical trap. *Physics Today*, 54(7):20–22, 2001. [Cited on page 7.]

[113] P. S. Jessen and I. H. Deutsch. Optical Lattices. In Benjamin Bederson and Herbert Walther, editors, *Advances In Atomic, Molecular, and Optical Physics*, volume 37, pages 95–138. Academic Press, 1996. [Cited on page 7.]

[114] Oliver Morsch and Markus Oberthaler. Dynamics of Bose-Einstein condensates in optical lattices. *Rev. Mod. Phys.*, 78:179–215, Feb 2006. [Cited on page 7.]

[115] W. Ketterle, D. S. Durfee, and D. M. Stamper-Kurn. Making, probing and understanding Bose-Einstein condensates. In *Proceedings of the International School of Physics "Enrico Fermi", Course CXL, edited by M. Inguscio, S. Stringari and C.E. Wieman (IOS*, pages 67–176. Press, 1999. [Cited on pages 8 and 12.]

[116] Roger C. Brown. *Nonequilibrium manybody dynamics with ultracold atoms in optical lattices and selected problems in atomic physics*. PhD thesis, University of Maryland, College Park, 2014. [Cited on pages 8 and 14.]

[117] John H. Huckans. *Optical lattices and quantum degenerate $^{8}7$Rb in reduced dimensions*. PhD thesis, University of Maryland, College Park, 2006. [Cited on page 8.]

[118] Y.-J. Lin, A. R. Perry, R. L. Compton, I. B. Spielman, and J. V. Porto. Rapid production of ^{87}Rb Bose-Einstein condensates in a combined magnetic and optical potential. *Phys. Rev. A*, 79:063631, Jun 2009. [Cited on page 8.]

[119] S. C. Bell, M. Junker, M. Jasperse, L. D. Turner, Y.-J. Lin, I. B. Spielman, and R. E. Scholten. A slow atom source using a collimated effusive oven and a single-layer variable pitch coil Zeeman slower. *Review of Scientific Instruments*, 81(1):013105, 2010. [Cited on pages 8 and 10.]

[120] D. Alpert. New developments in the production and measurement of ultra high vacuum. *Journal of Applied Physics*, 24(7):860–876, 1953. [Cited on page 8.]

[121] William D. Phillips and Harold Metcalf. Laser deceleration of an atomic beam. *Phys. Rev. Lett.*, 48:596–599, Mar 1982. [Cited on page 10.]

[122] John F. O'Hanlon. *Getter and Ion Pumps*, pages 247–262. John Wiley & Sons, Ltd, 2003. [Cited on page 10.]

[123] E. L. Raab, M. Prentiss, Alex Cable, Steven Chu, and D. E. Pritchard. Trapping of neutral sodium atoms with radiation pressure. *Phys. Rev. Lett.*, 59:2631–2634, Dec 1987. [Cited on page 10.]

[124] Roger C. Brown, S. Olmschenk, Saijun Wu, A. M. Dyckovsky, R. Wyllie, and J. V. Porto. Note: Pneumatically actuated and kinematically positioned optical mounts compatible with laser-cooling experiments. *Review of Scientific Instruments*, 84(9):096101, 2013. [Cited on page 10.]

[125] Alan L. Migdall, John V. Prodan, William D. Phillips, Thomas H. Bergeman, and Harold J. Metcalf. First observation of magnetically trapped neutral atoms. *Phys. Rev. Lett.*, 54:2596–2599, Jun 1985. [Cited on page 11.]

[126] T. Bergeman, Gidon Erez, and Harold J. Metcalf. Magnetostatic trapping fields for neutral atoms. *Phys. Rev. A*, 35:1535–1546, Feb 1987. [Cited on page 11.]

[127] T. H. Bergeman, Patrick McNicholl, Jan Kycia, Harold Metcalf, and N. L. Balazs. Quantized motion of atoms in a quadrupole magnetostatic trap. *J. Opt. Soc. Am. B*, 6(11):2249–2256, Nov 1989. [Cited on page 11.]

[128] Charles S. Adams, Heun Jin Lee, Nir Davidson, Mark Kasevich, and Steven Chu. Evaporative cooling in a crossed dipole trap. *Phys. Rev. Lett.*, 74:3577–3580, May 1995. [Cited on page 11.]

[129] U. Schünemann, H. Engler, R. Grimm, M. Weidemüller, and M. Zielonkowski. Simple scheme for tunable frequency offset locking of two lasers. *Review of Scientific Instruments*, 70(1):242–243, 1999. [Cited on page 11.]

[130] K. B. MacAdam, A. Steinbach, and C. Wieman. A narrow-band tunable diode laser system with grating feedback, and a saturated absorption spectrometer for Cs and Rb. *American Journal of Physics*, 60(12):1098–1111, 1992. [Cited on page 12.]

[131] Marco Anderlini, Jennifer Sebby-Strabley, Jens Kruse, James V Porto, and William D Phillips. Controlled atom dynamics in a double-well optical lattice. *Journal of Physics B: Atomic, Molecular and Optical Physics*, 39(10):S199–S210, may 2006. [Cited on page 14.]

[132] G. Grynberg, B. Lounis, P. Verkerk, J.-Y. Courtois, and C. Salomon. Quantized motion of cold cesium atoms in two- and three-dimensional optical potentials. *Phys. Rev. Lett.*, 70:2249–2252, Apr 1993. [Cited on page 16.]

[133] Leticia Tarruell, Daniel Greif, Thomas Uehlinger, Gregor Jotzu, and Tilman Esslinger. Creating, moving and merging Dirac points with a Fermi gas in a tunable honeycomb lattice. *Nature*, 483(7389):302–305, 2012. [Cited on page 16.]

[134] L. E. Radford. Equal rights for the reciprocal lattice. *American Journal of Physics*, 43(8):697–700, 1975. [Cited on page 20.]

[135] Anthony Michael Glazer. The reciprocal lattice. In *A Journey into Reciprocal Space (Second Edition)*, 2053-2563, pages 2–1 to 2–11. IOP Publishing, 2021. [Cited on page 20.]

[136] Felix Bloch. Über die quantenmechanik der elektronen in kristallgittern. *Zeitschrift für Physik*, 52(7):555–600, 1929. [Cited on page 21.]

[137] David J. Griffiths and Darrell F. Schroeter. *Introduction to Quantum Mechanics*. Cambridge University Press, 3 edition, 2018. [Cited on page 21.]

[138] Carmen Chicone. *Ordinary Differential Equations with Applications*. Springer, New York, NY, 2006. [Cited on pages 30 and 56.]

[139] Dominic Jordan and Peter Smith. *Nonlinear Ordinary Differential Equations : An Introduction for Scientists and Engineers*, volume 4th ed of *Oxford Applied and Engineering Mathematics*. OUP, Oxford, 2007. [Cited on page 30.]

[140] Walter G. Kelley and Allan C. Peterson. *The Theory of Differential Equations*. Springer, New York, NY, 2010. [Cited on page 30.]

[141] S. R. Barone, M. A. Narcowich, and F. J. Narcowich. Floquet theory and applications. *Phys. Rev. A*, 15:1109–1125, Mar 1977. [Cited on page 31.]

[142] André Nauts and Robert E. Wyatt. Theory of laser-molecule interaction: The recursive-residue-generation method. *Phys. Rev. A*, 30:872–883, Aug 1984. [Cited on page 31.]

[143] T. P. Grozdanov and M. J. Raković. Quantum system driven by rapidly varying periodic perturbation. *Phys. Rev. A*, 38:1739–1746, Aug 1988. [Cited on page 31.]

[144] Martin Holthaus. Floquet engineering with quasienergy bands of periodically driven optical lattices. *Journal of Physics B: Atomic, Molecular and Optical Physics*, 49(1):013001, Nov 2015. [Cited on pages 31, 32, 36, 39, and 115.]

[145] C. M. Dai, Z. C. Shi, and X. X. Yi. Floquet theorem with open systems and its applications. *Phys. Rev. A*, 93:032121, Mar 2016. [Cited on page 31.]

[146] Saar Rahav, Ido Gilary, and Shmuel Fishman. Effective hamiltonians for periodically driven systems. *Phys. Rev. A*, 68:013820, Jul 2003. [Cited on page 33.]

[147] Marin Bukov, Luca D'Alessio, and Anatoli Polkovnikov. Universal high-frequency behavior of periodically driven systems: from dynamical stabilization to Floquet engineering. *Advances in Physics*, 64(2):139–226, 2015. [Cited on page 33.]

[148] André Eckardt and Egidijus Anisimovas. High-frequency approximation for periodically driven quantum systems from a Floquet-space perspective. *New Journal of Physics*, 17(9):093039, sep 2015. [Cited on pages 33, 36, 115, and 127.]

[149] Lichung Ha. *Bose-Einstein condensates in a shaken optical lattice*. PhD thesis, University of Chicago, 2016. [Cited on page 33.]

[150] Kenichi Konishi and Giampiero Paffuti. *Quantum Mechanics: A New Introduction*. Oxford University Press, 2009. [Cited on page 33.]

[151] Kleinert Hagen. *Path Integrals In Quantum Mechanics, Statistics, Polymer Physics, And Financial Markets (5th Edition).*, volume 5th ed. World Scientific, 2009. [Cited on page 33.]

[152] J.J. Sakurai and J.J. Napolitano. *Modern Quantum Mechanics: Pearson New International Edition PDF eBook*. Pearson Education, 2013. [Cited on page 33.]

[153] Masuo Suzuki. General decomposition theory of ordered exponentials. *Proceedings of the Japan Academy, Series B*, 69(7):161–166, 1993. [Cited on page 34.]

[154] Siu A. Chin and C. R. Chen. Gradient symplectic algorithms for solving the Schrödinger equation with time-dependent potentials. *The Journal of Chemical Physics*, 117(4):1409–1415, 2002. [Cited on page 34.]

[155] Naomichi Hatano and Masuo Suzuki. Finding exponential product formulas of higher orders. In Arnab Das and Bikas K. Chakrabarti, editors, *Quantum Annealing and Other Optimization Methods*, pages 37–68. Springer, Berlin, Heidelberg, 2005. [Cited on pages 34 and 35.]

[156] Viktor Novičenko, Egidijus Anisimovas, and Gediminas Juzeliūnas. Floquet analysis of a quantum system with modulated periodic driving. *Phys. Rev. A*, 95:023615, Feb 2017. [Cited on page 36.]

[157] Hideo Sambe. Steady states and quasienergies of a quantum-mechanical system in an oscillating field. *Phys. Rev. A*, 7:2203–2213, Jun 1973. [Cited on page 36.]

[158] Michael Vogl, Martin Rodriguez-Vega, and Gregory A. Fiete. Effective Floquet Hamiltonian in the low-frequency regime. *Phys. Rev. B*, 101:024303, Jan 2020. [Cited on page 36.]

[159] D. H. Dunlap and V. M. Kenkre. Dynamic localization of a charged particle moving under the influence of an electric field. *Phys. Rev. B*, 34:3625–3633, Sep 1986. [Cited on page 40.]

[160] André Eckardt, Martin Holthaus, Hans Lignier, Alessandro Zenesini, Donatella Ciampini, Oliver Morsch, and Ennio Arimondo. Exploring dynamic localization with a bose-einstein condensate. *Phys. Rev. A*, 79:013611, Jan 2009. [Cited on page 40.]

[161] J. Struck, C. Ölschläger, R. Le Targat, P. Soltan-Panahi, A. Eckardt, M. Lewenstein, P. Windpassinger, and K. Sengstock. Quantum simulation of frustrated classical magnetism in triangular optical lattices. *Science*, 333(6045):996–999, 2011. [Cited on page 40.]

[162] Gregor Jotzu, Michael Messer, Frederik Görg, Daniel Greif, Rémi Desbuquois, and Tilman Esslinger. Creating state-dependent lattices for ultracold fermions by magnetic gradient modulation. *Phys. Rev. Lett.*, 115:073002, Aug 2015. [Cited on page 40.]

[163] W. V. Houston. Acceleration of electrons in a crystal lattice. *Phys. Rev.*, 57:184–186, Feb 1940. [Cited on page 40.]

[164] Martin Holthaus and Daniel W. Hone. Localization effects in ac-driven tight-binding lattices. *Philosophical Magazine B*, 74(2):105–137, 08 1996. [Cited on pages 40 and 42.]

[165] Ennio Arimondo, Donatella Ciampini, André Eckardt, Martin Holthaus, and Oliver Morsch. Chapter 10 - Kilohertz-driven Bose–Einstein condensates in optical lattices. In Paul Berman, Ennio Arimondo, and Chun Lin, editors, *Advances in Atomic, Molecular, and Optical Physics*, volume 61 of *Advances In Atomic, Molecular, and Optical Physics*, pages 515–547. Academic Press, 2012. [Cited on page 40.]

[166] Li-Chung Ha, Logan W. Clark, Colin V. Parker, Brandon M. Anderson, and Cheng Chin. Roton-maxon excitation spectrum of Bose condensates in a shaken optical lattice. *Phys. Rev. Lett.*, 114:055301, Feb 2015. [Cited on page 46.]

[167] Eugene P. Gross. Hydrodynamics of a superfluid condensate. *Journal of Mathematical Physics*, 4(2):195–207, 1963. [Cited on page 49.]

[168] Lev P Pitaevskii. Vortex lines in an imperfect Bose gas. *Sov. Phys. JETP*, 13(2):451–454, 1961. [Cited on page 49.]

[169] Franco Dalfovo, Stefano Giorgini, Lev P. Pitaevskii, and Sandro Stringari. Theory of Bose-Einstein condensation in trapped gases. *Rev. Mod. Phys.*, 71:463–512, Apr 1999. [Cited on page 49.]

[170] Nick P Proukakis and Brian Jackson. Finite-temperature models of Bose–Einstein condensation. *Journal of Physics B: Atomic, Molecular and Optical Physics*, 41(20):203002, Oct 2008. [Cited on page 49.]

[171] P. A. Ruprecht, Mark Edwards, K. Burnett, and Charles W. Clark. Probing the linear and nonlinear excitations of Bose-condensed neutral atoms in a trap. *Phys. Rev. A*, 54:4178–4187, Nov 1996. [Cited on page 50.]

[172] D. S. Jin, J. R. Ensher, M. R. Matthews, C. E. Wieman, and E. A. Cornell. Collective excitations of a Bose-Einstein condensate in a dilute gas. *Phys. Rev. Lett.*, 77:420–423, Jul 1996. [Cited on page 50.]

[173] J. Denschlag, J. E. Simsarian, D. L. Feder, Charles W. Clark, L. A. Collins, J. Cubizolles, L. Deng, E. W. Hagley, K. Helmerson, W. P. Reinhardt, S. L. Rolston, B. I. Schneider, and W. D. Phillips. Generating solitons by phase engineering of a Bose-Einstein condensate. *Science*, 287(5450):97–101, 2000. [Cited on page 50.]

[174] Emil Lundh, C. J. Pethick, and H. Smith. Vortices in Bose-Einstein-condensed atomic clouds. *Phys. Rev. A*, 58:4816–4823, Dec 1998. [Cited on page 50.]

[175] Alexander L Fetter and Anatoly A Svidzinsky. Vortices in a trapped dilute Bose-Einstein condensate. *Journal of Physics: Condensed Matter*, 13(12):R135–R194, mar 2001. [Cited on page 50.]

[176] J. R. Abo-Shaeer, C. Raman, J. M. Vogels, and W. Ketterle. Observation of vortex lattices in Bose-Einstein condensates. *Science*, 292(5516):476–479, 2001. [Cited on page 50.]

[177] P.G. Kevrekidis, D.J. Frantzeskakis, and R. Carretero-González. *Emergent Nonlinear Phenomena in Bose-Einstein Condensates: Theory and Experiment*. Springer Series on Atomic, Optical, and Plasma Physics. Springer Berlin Heidelberg, 2007. [Cited on page 50.]

[178] G. J. Milburn, J. Corney, E. M. Wright, and D. F. Walls. Quantum dynamics of an atomic Bose-Einstein condensate in a double-well potential. *Phys. Rev. A*, 55:4318–4324, Jun 1997. [Cited on page 50.]

[179] A. Smerzi, S. Fantoni, S. Giovanazzi, and S. R. Shenoy. Quantum coherent atomic tunneling between two trapped Bose-Einstein condensates. *Phys. Rev. Lett.*, 79:4950–4953, Dec 1997. [Cited on page 50.]

[180] Michael Albiez, Rudolf Gati, Jonas Fölling, Stefan Hunsmann, Matteo Cristiani, and Markus K. Oberthaler. Direct observation of tunneling and nonlinear self-trapping in a single bosonic Josephson junction. *Phys. Rev. Lett.*, 95:010402, Jun 2005. [Cited on page 50.]

[181] Biao Wu and Qian Niu. Landau and dynamical instabilities of the superflow of Bose-Einstein condensates in optical lattices. *Phys. Rev. A*, 64:061603, Nov 2001. [Cited on pages 50, 51, and 137.]

[182] L. Fallani, L. De Sarlo, J. E. Lye, M. Modugno, R. Saers, C. Fort, and M. Inguscio. Observation of dynamical instability for a Bose-Einstein condensate in a moving 1d optical lattice. *Phys. Rev. Lett.*, 93:140406, Sep 2004. [Cited on pages 50, 75, and 137.]

[183] M. Modugno, C. Tozzo, and F. Dalfovo. Role of transverse excitations in the instability of bose-einstein condensates moving in optical lattices. *Phys. Rev. A*, 70:043625, Oct 2004. [Cited on page 50.]

[184] Dmitri Diakonov, L. M. Jensen, C. J. Pethick, and H. Smith. Loop structure of the lowest Bloch band for a Bose-Einstein condensate. *Phys. Rev. A*, 66:013604, Jul 2002. [Cited on page 50.]

[185] Biao Wu and Qian Niu. Superfluidity of Bose–Einstein condensate in an optical lattice: Landau–Zener tunnelling and dynamical instability. *New Journal of Physics*, 5:104–104, jul 2003. [Cited on pages 50, 133, and 151.]

[186] B. T. Seaman, L. D. Carr, and M. J. Holland. Nonlinear band structure in Bose-Einstein condensates: Nonlinear Schrödinger equation with a Kronig-Penney potential. *Phys. Rev. A*, 71:033622, Mar 2005. [Cited on page 50.]

[187] Hoi-Yin Hui, Ryan Barnett, J. V. Porto, and S. Das Sarma. Loop-structure stability of a double-well-lattice bose-einstein condensate. *Phys. Rev. A*, 86:063636, Dec 2012. [Cited on page 50.]

[188] Q. Guan, M. K. H. Ome, T. M. Bersano, S. Mossman, P. Engels, and D. Blume. Nonexponential tunneling due to mean-field-induced swallowtails. *Phys. Rev. Lett.*, 125:213401, Nov 2020. [Cited on page 50.]

[189] J. A. Armstrong, N. Bloembergen, J. Ducuing, and P. S. Pershan. Interactions between light waves in a nonlinear dielectric. *Phys. Rev.*, 127:1918–1939, Sep 1962. [Cited on page 72.]

[190] T. J. Kippenberg, H. Rokhsari, T. Carmon, A. Scherer, and K. J. Vahala. Analysis of radiation-pressure induced mechanical oscillation of an optical microcavity. *Phys. Rev. Lett.*, 95:033901, Jul 2005. [Cited on page 72.]

[191] Markus Aspelmeyer, Tobias J. Kippenberg, and Florian Marquardt. Cavity optomechanics. *Rev. Mod. Phys.*, 86:1391–1452, Dec 2014. [Cited on page 73.]

[192] André Eckardt, Christoph Weiss, and Martin Holthaus. Superfluid-insulator transition in a periodically driven optical lattice. *Phys. Rev. Lett.*, 95:260404, Dec 2005. [Cited on pages 77 and 84.]

[193] Sayan Choudhury and Erich J. Mueller. Stability of a Floquet Bose-Einstein condensate in a one-dimensional optical lattice. *Phys. Rev. A*, 90:013621, Jul 2014. [Cited on page 77.]

[194] Christoph Sträter and André Eckardt. Interband heating processes in a periodically driven optical lattice. *Zeitschrift für Naturforschung A*, 71(10):909–920, 2016. [Cited on page 84.]

[195] D. L. Campbell, G. Juzeliūnas, and I. B. Spielman. Realistic Rashba and Dresselhaus spin-orbit coupling for neutral atoms. *Phys. Rev. A*, 84:025602, Aug 2011. [Cited on pages 94 and 109.]

[196] Lianghui Huang, Zengming Meng, Pengjun Wang, Peng Peng, Shao-Liang Zhang, Liangchao Chen, Donghao Li, Qi Zhou, and Jing Zhang. Experimental realization of two-dimensional synthetic spin–orbit coupling in ultracold Fermi gases. *Nature Physics*, 12(6):540–544, 2016. [Cited on pages 94 and 109.]

[197] Junpeng Hou, Haiping Hu, Kuei Sun, and Chuanwei Zhang. Superfluid-quasicrystal in a Bose-Einstein condensate. *Phys. Rev. Lett.*, 120:060407, Feb 2018. [Cited on pages 94 and 109.]

[198] A. Valdés-Curiel, D. Trypogeorgos, Q. Y. Liang, R. P. Anderson, and I. B. Spielman. Topological features without a lattice in Rashba spin-orbit coupled atoms. *Nature Communications*, 12(1):593, 2021. [Cited on pages 94 and 109.]

[199] Shanchao Zhang and Gyu-Boong Jo. Recent advances in spin-orbit coupled quantum gases. *Journal of Physics and Chemistry of Solids*, 128:75–86, 2019. [Cited on page 95.]

[200] A Valdés-Curiel, D Trypogeorgos, E E Marshall, and I B Spielman. Fourier transform spectroscopy of a spin–orbit coupled Bose gas. *New Journal of Physics*, 19(3):033025, 2017. [Cited on page 118.]

[201] Karen Wintersperger, Christoph Braun, F. Nur Ünal, André Eckardt, Marco Di Liberto, Nathan Goldman, Immanuel Bloch, and Monika Aidelsburger. Realization of an anomalous Floquet topological system with ultracold atoms. *Nature Physics*, 16(10):1058–1063, 2020. [Cited on page 118.]

[202] J Hecker Denschlag, J E Simsarian, H Häffner, C McKenzie, A Browaeys, D Cho, K Helmerson, S L Rolston, and W D Phillips. A Bose-Einstein condensate in an optical lattice. *Journal of Physics B: Atomic, Molecular and Optical Physics*, 35(14):3095–3110, jul 2002. [Cited on page 118.]

[203] D. McKay, M. White, and B. DeMarco. Lattice thermodynamics for ultracold atoms. *Phys. Rev. A*, 79:063605, Jun 2009. [Cited on page 121.]

[204] Stephan Arlinghaus and Martin Holthaus. Generalized acceleration theorem for spatiotemporal Bloch waves. *Phys. Rev. B*, 84:054301, Aug 2011. [Cited on page 127.]

[205] A. R. Kolovsky and H. J. Korsch. Bloch oscillations of cold atoms in two-dimensional optical lattices. *Phys. Rev. A*, 67:063601, Jun 2003. [Cited on page 131.]

[206] Qizhong Zhu, Chuanwei Zhang, and Biao Wu. Exotic superfluidity in spin-orbit coupled Bose-Einstein condensates. *EPL (Europhysics Letters)*, 100(5):50003, Dec 2012. [Cited on pages 138 and 146.]

[207] Jonas Larson and Erik Sjöqvist. Jahn-Teller-induced Berry phase in spin-orbit-coupled Bose-Einstein condensates. *Phys. Rev. A*, 79:043627, Apr 2009. [Cited on page 146.]